Ph.D. Thesis

Studies on Pristine Graphene and Nitrogen Doped Graphene Films Grown by Chemical Vapor Deposition for Electronic and Sensing Applications

Submitted to the

University of Hyderabad

Towards partial fulfilment for the degree of

Doctor of Philosophy in Physics

By

Naresh Shyaga

Reg. No: 15PHPH11



Under the supervision of

Dr. Jayeeta Lahiri

Prof. M. Ghanashyam Krishna

School of Physics,

University of Hyderabad

Hyderabad-500 046.

Telangana, India.

(February-2023)

Declaration

I, Naresh Shyaga, hereby declare that the matter embodied in this thesis titled "Studies on Pristine Graphene and Nitrogen Doped Graphene films Grown by Chemical Vapor Deposition for Electronic and Sensing Applications" submitted to the University of Hyderabad for the award of Doctor of Philosophy in physics. It is a record of original research work carried out by me under the supervision of Dr. Jayeeta Lahiri and Prof. M. Ghanashyam Krishna in the School of Physics, University of Hyderabad. This thesis is free from plagiarism. To the best of my knowledge, this thesis has not been submitted partially or completely to any university or institute for award of any degree.

(Naresh Shyaga)

Reg. No. 15PHPH11

Date: 03-02-23
Place: Hyderabad



Certificate

This is to certify that the thesis titled "Studies on Pristine Graphene and Nitrogen Doped Graphene films grown by Chemical Vapor Deposition for Electronic and Sensing Applications" submitted by Naresh Shyaga bearing Reg. No. 15PHPH11, in fulfilment of the requirements for the award of Doctor of Philosophy in Physics, is a bonafide work carried out by him under my direct supervision.

This thesis is free from plagiarism and has not been submitted previously in part or in full to this or any other university or institution for the award of any degree or diploma.

Further, the student has the following publications before the submission of the thesis for adjudication.

1. **Shyaga N**, Sharma R, Hassan N, Alam B and Parmar A S 2022 Influence of growth parameters on the dopant configuration of nitrogen-doped graphene synthesized from phthalocyanine molecules J. Mater. Sci. Mater. Electron 33, 19361-19375 (2022).

Further, the student has passed the following courses towards the fulfilment of coursework required for a Ph.D.

S. No.	Course Code	Name	Credits	Pass/Fail
I.	PY801	Advanced Quantum Mechanics	4	Pass
2.	PY803	Advanced Statistical mechanics	4	Pass
3.	PY804	Advanced Electromagnetic Theory	4	Pass
4.	PY821	Research Methodology	4	Pass

Dr.Jayeeta Lahiri

Supervisor

Dr. Jayeeta Lahiri Assistant Professor Department of Physics Banaras Hindu University Varanasi-221005 Prof. M.Ghanasyam Krishna

Prof. M. UGHANASHYAM KRISHNA Centre for Advanced Studies in Electronics Science & Technology School of Physics, University of Hyderabad HYDERABAD-500 046. Telangana, India.

Prof. K.C. James Raju

Dean

School Of Physics

DEFN
School of Physics
University of Hyderabad
HYDERABAD - 500 046

Place: Hyderabad

Date: 03-02-23

Acknowledgments

First of all, I want to express my gratitude to those who fought for and still fight for human rights.

I would like to express my gratitude towards my supervisor **Dr. Jayeeta Lahiri** for her consistent and constructive guidance throughout my research. She motivated me to have patience and perseverance to obtain the expected results. I am thankful to her for our long discussions in our group meetings. I am always indebted to my co-supervisor, **Prof M. Ghanashyam Krishna** for his supervision during the last three years of my research. I will never forget his invaluable suggestions and encouragement during this period. I am grateful to him for his patience and kindness toward me.

I am very thankful to my doctoral review committee members, Prof S.V.S. Nageswara Rao and Dr. Venkataiah Gorige, for their suggestions and comments during my DRC meetings. I would also like to thank Prof. Srinath for his valuable advice during the DRC presentations. I would like to thank the present Dean, Prof K.C. James Raju, and former deans, Prof. Ashok Chatterjee, Prof. V. Seshubai, Prof. Bindu A Bambha, and prof. R. Sing for providing the resources for the research.

I am obliged to Prof T. N. Narayanan, TIFR Hyderabad, for his unconditional support in providing the facilities. Most of the measurements were performed in his lab. I might not have completed my thesis without his help and encouragement. He is a source of inspiration for many Ph. D. scholars like me who aspire to be in academics.

I wish to thank the school of physics office staff, Mr. Abraham, Mr. Prasad, Ms. Deepika, Mr. Sudarshan, and Ms. Shashikala, for their help in administrative matters. I am thankful to operators Ms. Sunitha, Mr. Santosh, and Mr. Naresh for assisting me in characterizing my samples.

I am grateful to the UOH BBL NON-NET fellowship for financial assistance.

I am thankful to my labmates, Dr. Nilanjan Basu and Nurul Hassan, for their help academically and non-academically. I am grateful to my dearest friend Dr. Leelashree Rajeswari for her caring and concern toward me. I would also like to thank my friends from Ph.D. batchmates Dr. Manasa

Kalla, Dr. Rajesh Y, Dr. Sujai Matta, Mr. Avishek Das, Dr. Md Abu Taher, Mr. Bappa, Dr. Rasi, and Dr. Zahid for their support during my research. I would like to express my gratitude to my beloved friend Rashmi Ranjan for our memorable discussions until his last days. Your death reminds me that our lives are uncertain, and I always miss you.

I am very thankful to TNN's lab students Dr. Rahul Sharma, Dr. Krishan Rani Sahoo, Dr. Sumit, Dr. Pallavi, Dr. Anku, Mr. Amar, and Mr. Deepak for their welcoming and friendly nature and for assisting me with measurements.

I am very indebted to my dearest friends Jyothi Yarram, Bhanu, Chaitanya, Sivaraju, Gangiredla, Vijay, Shankar, Ashok Patel, Krishna, Ashokanna, Harishanna, Narendranna, Devarajanna, Vasavi for their constant caring and unconditional support. I am thankful to other friends of Navodaya, Integrated, and Ph.D. courses.

I am very grateful to my maternal grandmother, whose love and care cannot be forgotten. I would also like to express my gratitude to my sisters, maternal uncles, and relatives for their care and support. Lastly, I am incredibly grateful to my parents for their eternal love and unconditional support. They value education so much that it allowed me to reach this far.

To

Amma & Nanna for giving life;

Ammamma for showing what life is.

Abbreviations

AFM Atomic Force Microscopy

Ag Silver

APCVD Atmospheric Pressure Chemical Vapor

Deposition

Ar Argon

Au Gold

CH₄ Methane

CVD Chemical Vapor Deposition

Cu Copper

CuPc Copper Phthalocyanine

DIW Deionized Water

EBSD Electron Back Scattered Diffraction

EHT Extra High Tension

FE field Emission

FeCl₃ Iron Chloride

FESEM Field Emission Scanning Electron Microscopy

FETs Field Effect Transistors

GO Graphite/Graphene Oxide

h-BN Hexagonal Boron Nitride

HOPG Highly Ordered Pyrolytic Graphite

H₂ Hydrogen

H₃PO₄ Orthophosphoric Acid

ICs Integrated Circuits

IPA Isopropyl Alcohol

Ir Iridium

ITO Iridium Tin Oxide

LPCVD Low Pressure CVD

MoS₂ Molybdenum Disulfide

NDG Nitrogen Doped Graphene

Ni Nickel

NO₂ Nitrogen Dioxide

Pc Phthalocyanine

PG Pristine Graphene

PMMA Polymethylmethacrylate

Pt Platinum

rGO reduced Graphene Oxide

R Resolution

RT Room Temperature

SCs Supercapacitors

SERS Surface Enhanced Raman Spectroscopy

Si Silicon

SiC Silicon Carbide

SiO₂ Silicon dioxide

TE Transparent Electrode

TMDs Transition Metal Dichalcogenides

UHV Ultra-High Vacuum

UV-Vis Ultra Violet- Visible

XPS X-ray Photoelectron Spectroscopy

XRD X-ray Diffraction

Table of Contents

Declaration	ii
Certificate	iii
Acknowledgement	v
Abbreviations	viii
Chapter 1: Introduction	01
Chapter 2: Literature Review	11
2.1 Overview of Pristine Graphene.	11
2.1.1 Introduction.	11
2.1.2 Structure of pristine of graphene	12
2.2 Physical properties of Graphene	13
2.2.1 Electronic Properties	13
2.2.2 Optical Properties.	15
2.2.3 Mechanical Properties.	15
2.2.4 Thermal properties.	15
2.3 Limitations of Graphene	19
2.4 Doping of Pristine Graphene	19
2.4.1 Nitrogen-Doped Graphene	20
2.5 Synthesis techniques for pristine and nitrogen doped graphene	22
2.5.1 Top-Down Methods	23
2.5.2 Bottom-Up methods	25
2.6 Applications of pristine and nitrogen doped graphene	31
2.7 Future Scope	37
2.8 Motivation and Objectives.	38
2.9 References	40
Chapter 3: Experimental Methods & Characterization techniques	51
3.1 Synthesis and Device fabrication	51
3.1.1 Cleaning & Electropolishing of Copper (Cu) foil	51
3.1.2 Synthesis Technique	52
3.1.3 Transferring the graphene onto target substrates	56
3.1.4 Device Fabrication	58

3.2 Characterization Techniques	59
3.2.1 Optical Microscopy	59
3.2.2 Field Emission Scanning Electron Microscopy	62
3.2.3 Atomic Force Microscopy	64
3.2.4 Raman Spectroscopy	68
3.2.5 X-ray photoelectron spectroscopy	71
3.2.6 Ultraviolet-visible-Near Infrared (UV-Vis-NIR) spectrophotometry	74
3.2.7 Electron Backscattered Diffraction	75
3.2.8 X-ray diffraction	77
3.3 Materials used	79
3.4 References	79
Chapter 4: Growth of pristine graphene by chemical vapor deposition	83
4.1 Introduction.	83
4.2 Growth of pristine graphene using APCVD	83
4.2.1 Copper substrate Preparation	83
4.2.2 Atmospheric pressure CVD grown graphene from PMMA	87
4.3 Results and Discussion.	89
4.3.1 Optimizing the evaporation temperature of PMMA	89
4.3.2 Optimizing the flow rate	93
4.3.3 Optimizing the growth time	95
4.3.4 Optimizing the amount of PMMA precursor	102
4.3.5 Temperature- dependent growth of graphene	106
4.4 Conclusion.	108
4.5 References.	108
Chapter 5: Synthesis of nitrogen doped graphene by CVD	111
5.1 Introduction	11
5.2 Atmospheric pressure CVD grown Nitrogen doped graphene from Pc and CuPc.	114
5.3 Results and Discussion.	115
5.3.1 Temperature-dependent nitrogen doped graphene Pc	115
5.3.2 Time-dependent nitrogen doped graphene from Pc	124
5.3.3 Nitrogen doped graphene from CuPc	129

5.5 References	
Chapter 6: Applications of pristine graphene & nitrogen doped graphene f	ilms136
6.1 Introduction.	136
6.2 Applications	137
6.2.1 Transparency of the graphene and NDG films	137
6.2.2 Graphene and NDG field effect transistors	138
6.2.3 Graphene/MoS2 heterostructure as a photodetector	144
6.2.4 Surface-enhanced Raman spectroscopy of graphene and NDG	147
6.3 Conclusion.	160
6.4 References.	161
Chapter 7: Conclusion and Future Scope	167
7.1 Summary & conclusion	167
7.2 Scope for future work	170
List of publications	171

Chapter-1

Introduction

Science has been an indispensable part of human civilization. Science built the modern world, that in turn shaped modern culture. The founder of the history of science discipline said that science was only a truly cumulative and progressive activity of humankind. It has impacted all aspects of human life, such as healthcare, communication, travel, food, etcetera. In the process of evolution of the scientific revolution, physics was the one branch of science that played a vital role among others. Physics saw a paradigm shift during this period as it delved into quantum physics from classical physics to understand the quantum phenomena in nature. However, simultaneously, the usage of materials also contributed to human civilization. In the early days, humans prepared material from natural deposits like iron, copper, and many more. Moreover, the evolution of human civilization occurred through the stone, bronze, and iron ages and finally arrived at the silicon age, which began with the discovery of semiconductors.

After the discovery of semiconductors and advancements in fabrication technology, transistors are built into smaller places. Understanding the transistor's functionalities assisted with the technology led to the exponential growth of integrated circuits (ICs), electronic devices, and other relevant applications. Millions of transistors were fabricated onto the same IC to increase the efficiency and speed of the devices. However, Moore's law predicts the number of transistors on a Si chip to double every year, and this was followed till the device started to scale down to the nanoscale [1–3]. When the channel width of the FET made of existing three dimensional material is reduced to the nanoscale results in low device performance due to the quantum effects. The source to drain tunneling would also be high, leading to less gate control. Thus, it is difficult to use conventional materials for the high performance of devices when they are scaled down to the nanoscale. There was a need to search for alternative materials to overcome these limitations.

In the context of modern science and engineering, understanding material systems is important for broadening the horizons of technology. The physicochemical properties of bulk or macroscopic materials are determined mostly by their chemical constituents. However, when the material's dimensions are reduced to the nanoscale, the size and shape play an essential role in determining the properties. It is often said that the materials properties depend on what the material is made up

of. However, it has been proven that a material's behavior relies on its size and dimensionality. It is true for some materials when their size is reduced to the nanoscale. There will be a Paradigm shift in the properties at the nanoscale compared to the counter bulk parts. This unique behavior of materials and being able to observe these characteristics with advanced technology made us dive into nanomaterials; currently, we are in the nano age.

Nanoscale refers to the object's size that has a length of a nanometer (10^{-9} meters). The materials having at least one of the dimensions at the nanoscale are called nanomaterials. The scientific study that deals with nanomaterials are termed nanoscience. Based on their dimensionality, materials are divided into zero-dimensional (0D), one-dimensional (1D), and two-dimensional (2D) materials. Bulk material has three dimensions (3D), having more than the nanoscale range. If one of the dimensions is restrained to nanometers out of three dimensions produces a 2D material similar to a sheet structure. Similarly, when the two dimensions are restrained, called 1D material, and if the three of them are confined to the nanoscale, called 0D materials [4].

Nanomaterials are alternative materials for addressing the limitations produced by 3D materials. 2D materials are the potential candidates among the nanomaterials as they can easily integrate into devices. However, until the 20th century, scientists believed that 2D materials cannot exist due to their instability because thermal fluctuations arrest long-range crystallinity at a finite temperature [5]. Geim and Novasolev discovered graphene in 2004 [6] for which they were awarded the Nobel Prize in 2010 [7]. Graphene has become the first 2D material to be discovered that consists of a sheet of carbon atoms with atomic thickness. It was isolated with scotch tape from highly ordered pyrolytic graphite (HOPG), as shown in figure 1.1. Usage of Graphite as a source material for exfoliation because it is a layered material in which many graphene layers are stacked vertically with van der Waals forces.

The valence and conduction bands of graphene being in contact result in the semi-metallic behavior, and its charge carriers act as Dirac fermions with zero effective mass. This characteristic feature resulted in unique properties such as high charge carrier mobility, half-integer quantum hall effect, micrometer-scale ballistic transport, and more than 97% optical transmittance [9–12]. Because of these properties, graphene is expected to replace silicon for ultra-fast nanoelectronics. Indeed, it is the thinnest material, flexible, and mechanically strong. Consequently, graphene has

become a suitable candidate for flexible electronics, medicine, defence, and consumer goods, among others.

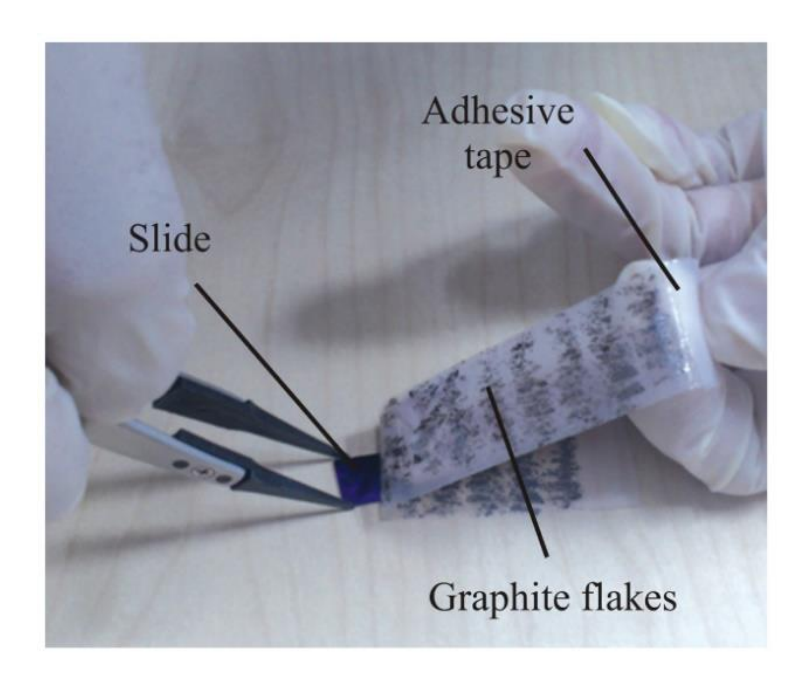


Figure 1.1 Isolation of graphene from graphite flakes using the scotch tape technique [8].

The intriguing properties and easy isolation of graphene stimulated the researchers to find other 2D materials from the existing layered materials. The family of 2D materials is shown in figure 1.2. An exponential rise in 2D materials discovery has occurred, and a recent prediction is that there are about 5600 layered compounds in which more than 1800 can be potentially exfoliable [13]. Some of the 2D materials of different groups that have undergone intensive research besides graphene are hexagonal BN, Mxenes, transitional metal dichalcogenides (TMDs), and black phosphorous. This family of 2D materials covers the whole spectrum of properties from metallic to insulator, superconductivity to magnetism, etc. New physical effects also have been observed for the same layers when they are arranged with some twist angle. Synthetic materials can be fabricated by stacking the different 2D crystals might lead to unpredictable properties.

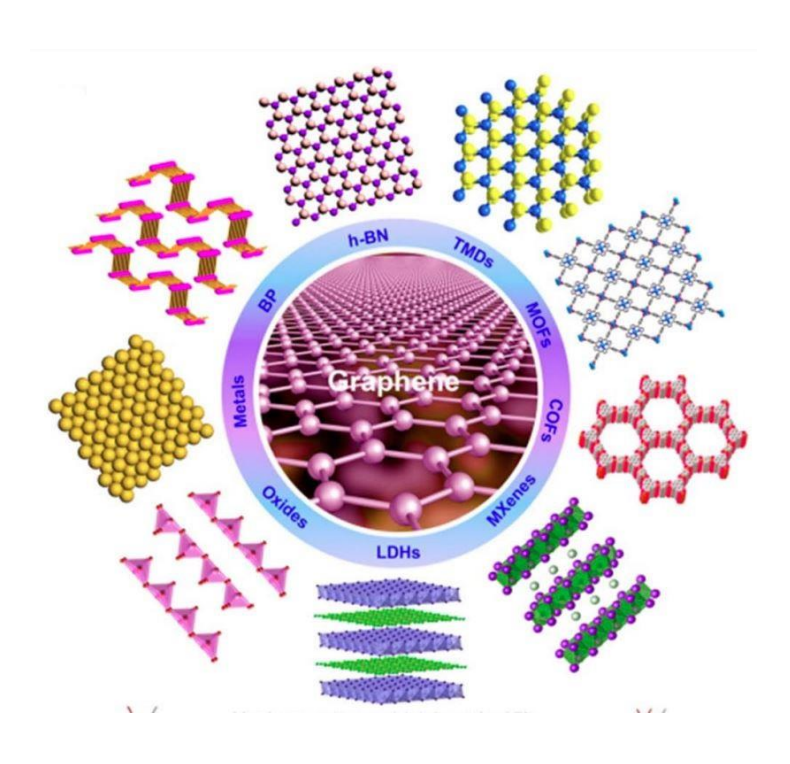


Figure 1.2 Schematic representation of the rise of various 2D materials after graphene discovery [14].

The wide range of unique properties broadened the applications of 2D compounds in various fields. The energy crisis in the world has increased the demand for efficient energy storage devices (ESDs). The global rise in energy sought for highly efficient ESDs. The properties found in 2D materials paved the path for satisfying these requirements. High specific surface area, high electrochemical activity, and electrical conductivity are characteristics of 2D materials that ensure the betterment of supercapacitors, batteries, and also for electrocatalysts. The high environmental sensitivity and surface area-to-volume ratios of 2D compounds are important features for chemical sensing applications. The fabricating of tunable channel sizes precisely with 2D materials can be utilized in the nanofluidics field. The achievable electrostatic gate control in FETs of 2D materials, having intrinsic properties of electric dipoles and magnetic moment can be used in nanoelectronics and flash memory devices [15]. Figure 1.3 displays the various other applications of the 2D materials.

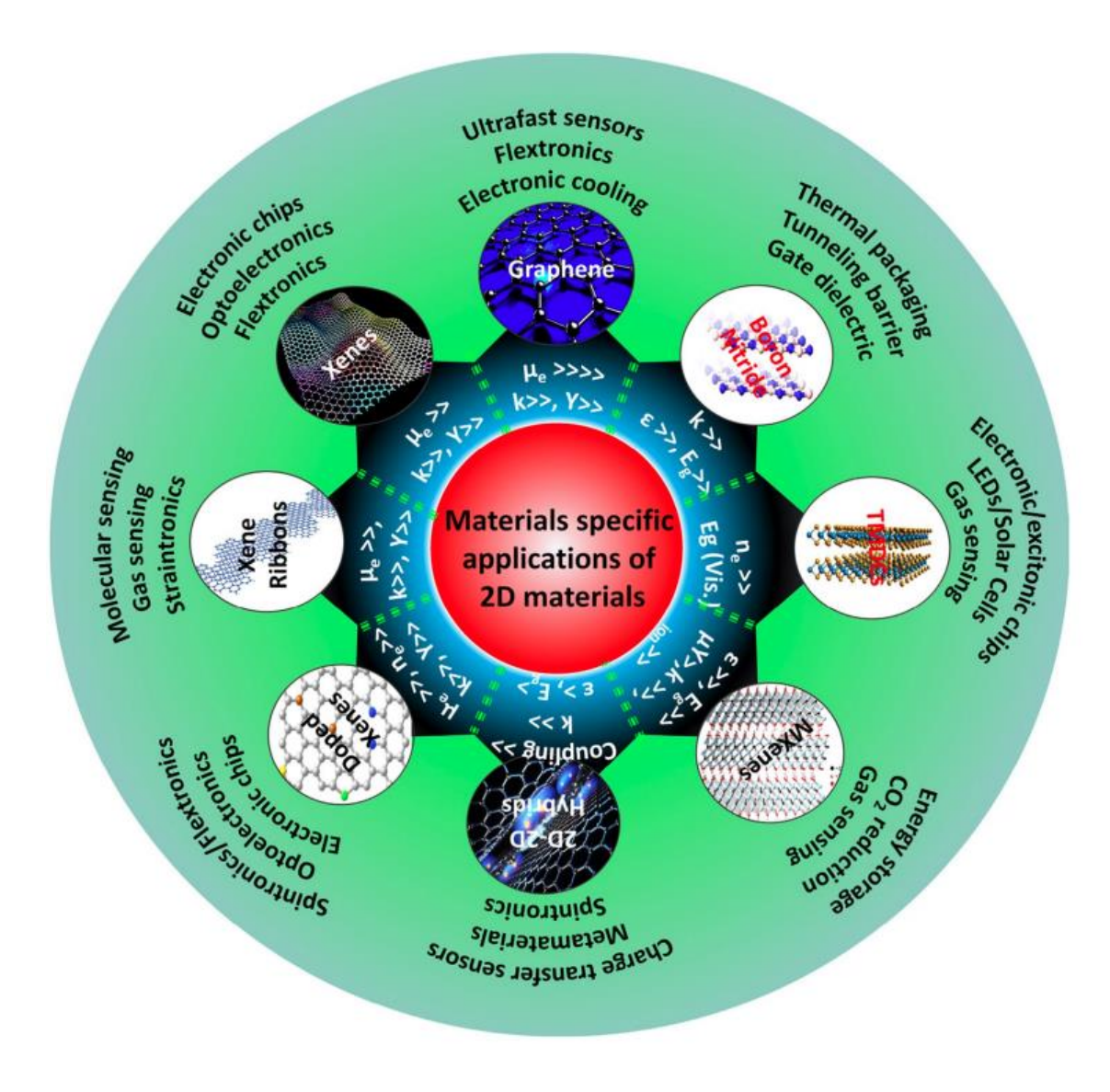


Figure 1.3 Applications of various 2D materials [15].

The major challenge of 2D materials is the synthesis of defect-free large-area crystals. High-quality 2D materials can be exfoliated from their bulk counterparts, but their yield is very low, and crystal sizes are very small. Chemical vapor deposition (CVD) can overcome some of these limitations, where large area 2D films can be obtained, but this method does not produce high quality compared to mechanical exfoliation. Synthesizing high-quality 2D materials on target substrates is a challenging aspect. Transferring the 2D materials onto desired substrates without degradation has not been resolved yet. Growing or transferring 2D crystals onto target substrates itself is a challenge. Doping 2D materials is necessary to obtain synergistic physicochemical properties, which is not straightforward. Uniformity in doping has not been established till now.

The research community's bottleneck is producing high quality 2D materials at a large scale to meet industrial needs and realize potential applications. As a result, new techniques must be developed. So, the CVD approach is suitable for synthesizing large-area continuous films with enhanced quality by choosing the right precursors and process parameters.

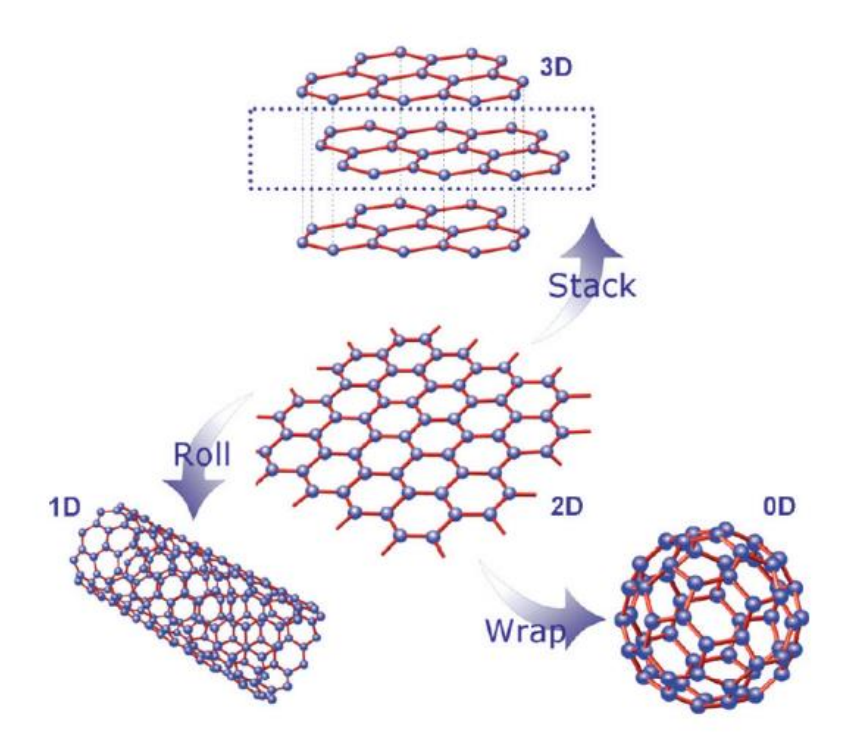


Figure 1.3 structure of the graphene. Graphene is a backbone for all sp² carbon allotropes [16].

My thesis work mainly focuses on graphene systems and their doping. Graphene is a 2D material comprising sp² hybridized carbon atoms, arranged in a honeycomb lattice structure, as displayed in figure 1.3. Graphene is the backbone for all sp² hybridized carbon structures (i.e., graphitic materials) irrespective of their dimensionalities. Rolled graphene produces carbon nanotubes (1D material), enfolded graphene gives rise to fullerene (0D material), and the stacked graphene sheets one on another lead to graphite (3D material). Graphene exhibits novel properties like high mechanical strength and carrier mobility, room-temperature quantum Hall effect, flexibility, catalytic and photoelectric activity. Due to its distinct properties, it has gained attention from the research community and industrialists. Graphene has become a suitable candidate for flexible electronics, medicine, defence, and consumer goods, among others. But, the limitation of graphene is that it does not have a band gap which reduces its scope in the digital nanoelectronics field,

where it requires a bandgap. This limitation can be overcome by functionalizing graphene with foreign atoms. Substitutional doping of graphene is a promising method to create a band gap and hence modify physicochemical properties. Controlled doping of graphene is also a challenge till today. Production of graphene at an industrial scale faces many problems because of technological immaturity and costly synthesis. The industrialization of graphene is a delicate process as the quality and the physicochemical properties mostly depend on the synthesis conditions and processing facilities. Thus, there is a demand for facile synthesis techniques for obtaining large-area graphene systems at a large scale without compromising the quality.

This thesis employed chemical vapor deposition technique of synthesizing pristine graphene and nitrogen-doped graphene at atmospheric pressure. CVD has been employed because of its ability to synthesize large-area films. But, CVD brings challenges, such as using hazardous precursors, difficulty controlling the thickness and twisting angles between layers, and growing graphene at low temperatures and also on insulating substrates. The most used precursor for graphene's CVD growth is methane gas which is poisonous and highly explosive. Solid precursors were found to be alternative precursors that pose less threat than methane gas. In the case of doping nitrogen of graphene, depending on concentration of nitrogen dopants, a band gap is induced. The selection of the precursor and growth parameters, like temperature, flow rate, time, and pressure, affect the nitrogen doping concentration and configurations. Therefore, it is crucial to investigate innovative precursors and adjust growth conditions in order to achieve the necessary nitrogen concentrations and configurations. This thesis work's motivation is synthesizing large-area continuous nitrogendoped graphene and pristine graphene films using solid precursors. The novelty of the work lies in introducing the new solid precursor for synthesizing the nitrogen-doped graphene and controlling its dopant configuration. The effect of the nitrogen doping configuration and concentration on electronic properties is also studied. Synthesized films were utilized for the applications of sensors and electronics. The films were applied in surface-enhanced Raman spectroscopic (SERS) studies, which act as SERS substrates for the organic dye molecules.

This thesis is divided into seven chapters. The chapters in this thesis are organized as follows.

Chapter 1 introduces the thesis that discusses the glimpses of 2D materials (focusing on graphene), their synthesis, potential applications, and challenges. It introduces the motivation behind the thesis work. It also presents the categorization of chapters in the thesis.

Chapter 2 reviews graphene and nitrogen-doped graphene materials based on published experimental and theoretical findings. It presents an overview of pure and doped graphene structure and properties. The recent development in synthesis techniques has been discussed in this chapter. It also elaborates on the contemporary research that is taking place on graphene systems, such as characterization, heterostructures based on graphene, and doping of graphene and their challenges. Overall, it provides the information for laying the foundation related to the aims of the thesis.

Chapter 3 is about experimental and characterization techniques. This chapter introduces the basic concepts of the synthesis techniques and characterization tools that have been used for the research work.

Chapter 4 is the first chapter to contain the results of my research. This chapter discusses the graphene growth on copper using polymethylmethacrylate (PMMA), a solid precursor using atmospheric pressure chemical vapor deposition (APCVD). Generally, the Spin-coated or deposited films of solid precursors on substrates are annealed at higher temperatures in a reduced atmosphere to obtain the graphene films. This approach does not have any control over the nucleating sites and the crystal's coalescence. Therefore, the PMMA was evaporated and transported to the substrate, and further process is similar to the graphene growth from methane. We optimized the different synthesis parameters such as evaporation temperature, growth time, and PMMA amount for obtaining the defect-free large-area continuous graphene films. Graphene films were also grown at various temperatures. The synthesized films were characterized by Optical microscopy, FESEM, Raman spectroscopy, and AFM for the morphology, crystallinity, and thickness studies.

Chapter 5 discusses growth of nitrogen-doped graphene using solid precursors. It can be doped in two ways: direct synthesis (foreign atoms are doped during graphene's growth) or post-treatment of graphene is the other method. We employed the APCVD technique as it comes under the direct synthesis method for doping graphene with nitrogen atoms. As mentioned earlier, the doping concentration and configuration strongly depend on the precursor and processing parameters, so we used the solid precursor phthalocyanine (containing carbon and nitrogen atoms) for the first time to synthesize nitrogen-doped graphene. We studied the effect of duration of growth time, growth temperature, and carrier gas on nitrogen doping configurations and its concentration. The

synthesized films were characterized using XPS for determining the nitrogen content and its configurations. Raman, FESEM, AFM, and optical measurements were performed on these films to get information about the morphology, thickness, and defects. We compared nitrogen-doped graphene films synthesized from phthalocyanine and copper phthalocyanine.

Chapter 6 is about the applications of synthesized films for electronics and sensing. FET measurements were performed for both pristine and nitrogen-doped graphene films to obtain the electronic properties. We studied the effect of the nitrogen dopant configuration on the Dirac point and charge carriers. The transmittance measurements were also performed for these films. For sensing applications, the films were utilized as surface-enhanced Raman spectroscopic (SERS) substrates. 2D materials are emerging as SERS substrates and have a greater edge than conventional materials. Graphene, nitrogen-doped graphene and, hexagonal boron nitride, etc., have proved to be effective SERS substrates for an array of probe materials. We used the probe molecules for sensing organic dyes like methylene blue, crystal violet, and Nile blue. The effect of doping on SERS behavior was studied and compared with pristine graphene SERS. Graphene has been utilized in the graphene/ MoS₂ heterostructre for photoconductivity studies.

Chapter 7 summarizes the conclusions and future scope. The key findings of the thesis work are summarized in this chapter. Based on the arrived conclusions, the future scope also was proposed.

References:

- [1] Moore G E 2009 Progress in digital integrated electronics [Technical literaiture, Copyright 1975 IEEE. Reprinted, with permission. Technical Digest. International Electron Devices Meeting, IEEE, 1975, pp. 11-13.] *IEEE Solid-State Circuits Soc. Newsl.* 11 36–7
- [2] Moore G E 1998 Cramming more components onto integrated circuits (Reprinted from Electronics *Proc. Ieee* **86** 82–5
- [3] Moore G E 1995 Lithography and the future of Moore's law *Integr. Circuit Metrol. Insp. Process Control IX* **2439** 2
- [4] Singh S, Verma K and Prakash C Materials Horizons: From Nature to Nanomaterials Advanced Applications of 2D Nanostructures Emerging Research and Opportunities
- [5] Illing B, Fritschi S, Kaiser H, Klix C L, Maret G and Keim P 2017 Mermin-Wagner fluctuations in 2D amorphous solids *Proc. Natl. Acad. Sci. U. S. A.* **114** 1856–61

- [6] K. S. Novoselov et al 2016 Electric Field Effect in Atomically Thin Carbon Films **306** 666–9
- [7] Gerstner E 2010 Nobel Prize 2010: Andre Geim & Konstantin Novoselov *Nat. Phys.* **6** 836–836
- [8] Randviir E P, Brownson D A C and Banks C E 2014 A decade of graphene research: Production, applications and outlook *Mater. Today* **17** 426–32
- [9] Chen J H, Jang C, Xiao S, Ishigami M and Fuhrer M S 2008 Intrinsic and extrinsic performance limits of graphene devices on SiO 2 *Nat. Nanotechnol.* **3** 206–9
- [10] Bolotin K I, Ghahari F, Shulman M D, Stormer H L and Kim P 2009 Observation of the fractional quantum Hall effect in graphene *Nature* **462** 196–9
- [11] Mayorov A S, Gorbachev R V., Morozov S V., Britnell L, Jalil R, Ponomarenko L A, Blake P, Novoselov K S, Watanabe K, Taniguchi T and Geim A K 2011 Micrometer-scale ballistic transport in encapsulated graphene at room temperature *Nano Lett.* **11** 2396–9
- [12] Nair R R, Blake P, Grigorenko A N, Novoselov K S, Booth T J, Stauber T, Peres N M R and Geim A K 2008 Fine structure constant defines visual transparency of graphene *Science* (80-.). **320** 1308
- [13] Mounet N, Gibertini M, Schwaller P, Campi D, Merkys A, Marrazzo A, Sohier T, Castelli I E, Cepellotti A, Pizzi G and Marzari N 2018 Two-dimensional materials from high-throughput computational exfoliation of experimentally known compounds *Nat. Nanotechnol.* **13** 246–52
- [14] Bo Guo B G 2018 2D noncarbon materials-based nonlinear optical devices for ultrafast photonics [Invited] vol 16
- [15] Ranjan P, Gaur S, Yadav H, Urgunde A B, Singh V, Patel A, Vishwakarma K, Kalirawana D, Gupta R and Kumar P 2022 2D materials: increscent quantum flatland with immense potential for applications *Nano Converg.* **9**
- [16] Wan X, Huang Y and Chen Y 2012 Focusing on energy and optoelectronic applications: A journey for graphene and graphene oxide at large scale *Acc. Chem. Res.* **45** 598–607

Chapter-2

Literature Review

This chapter presents an overview and the recent advancements in graphene systems. It briefly discusses graphene's structure, properties, and limitations. Doping graphene, especially focusing nitrogen-doped graphene, which was introduced in this chapter, addresses overcoming the limitations of pristine graphene. Then, fabrication techniques (special attention given to the CVD technique) were reviewed for pristine and nitrogen-doped graphene. Recent achievements of graphene utilization in different fields were also discussed. At last, after an intensive literature review, we provided the motivation and objectives of my research work.

2.1 Overview of pristine Graphene

2.1.1 Introduction

Before their discovery, it was argued that 2D structures cannot exist independently due to their thermodynamical instability. They were considered the basic constituents of 3D structures, such as layered materials, until the discovery of Graphene by Andre Geim and Konstantin Novoselov in 2004. Graphene is a single sheet of carbon atoms organized in a honeycomb lattice structure [1]. It is an allotrope of carbon, and its siblings are carbon nanotubes, fullerenes, and graphite. The graphene's carbon atoms are sp² hybridized, which is distinguished from diamond's sp3 hybridized carbon atoms. Graphene is a true 2D structure as it is one atom in thickness. This thesis deals with doped graphene, so undoped graphene is labeled as pristine graphene to contrast with doped graphene.

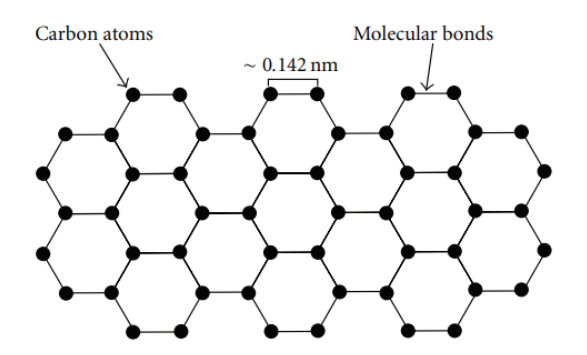


Figure 2.1 schematics of graphene structure [1].

2.1.2 Structure of pristine Graphene

The sp² hybridized carbon atoms allowed them to bond to three other carbon atoms, giving rise to the honeycomb lattice structure. The honeycomb lattice is formed by interpenetrating two triangular lattices mentioned as A and B, as shown in figure 2.2. The unit cell comprises two atoms, each from one sublattice. The two unit vectors of lattice cell a_1 and a_2 are written as

$$a_1 = \frac{a_{c-c}}{2} (3, \sqrt{3}), \qquad a_2 = \frac{a_{c-c}}{2} (3, -\sqrt{3})$$

Where a_{c-c} is the C-C bond length, which is about 0.142 nm. The corresponding reciprocal lattice vectors are written as

$$b_1 = \frac{2\pi}{3a_{c-c}} (1, \sqrt{3}), \qquad b_2 = \frac{2\pi}{3a_{c-c}} (1, -\sqrt{3})$$

The Brillouin zone was constructed by using reciprocal lattice vectors in k-space, as depicted in figure 2.2. The two vertices of two Brillouin zone, K and K', are Dirac points and are crucial in determining graphene's physics. The K and K' are written as

$$K = \frac{2\pi}{3a_{c-c}} \left(1, \frac{\sqrt{3}}{3} \right), \qquad K' = \frac{2\pi}{3a_{c-c}} \left(1, -\frac{\sqrt{3}}{3} \right)$$
(a)
$$\begin{pmatrix} \mathbf{b} \end{pmatrix}$$

$$\delta_{3}$$

$$\delta_{1}$$

$$\delta_{2}$$

$$\delta_{1}$$

$$\delta_{2}$$

$$\delta_{3}$$

$$\delta_{3}$$

$$\delta_{1}$$

$$\delta_{2}$$

$$\delta_{3}$$

$$\delta_{3}$$

$$\delta_{1}$$

$$\delta_{2}$$

$$\delta_{3}$$

$$\delta_{3}$$

$$\delta_{4}$$

$$\delta_{5}$$

$$\delta_{5}$$

$$\delta_{7}$$

$$\delta_{8}$$

$$\delta_{8}$$

Figure 2.2 (a) Graphene honeycomb lattice structure with two triangle-shaped sublattices is

depicted. The two lattice unit vectors of the unit cell are a_1 and a_2 , and δ_i are the nearest neighbors where i represents the 1,2 and 3. (b) Brillouin zone of graphene [2].

2.2. Physical properties of Graphene

2.2.1 Electronic properties of graphene

Band structures of materials determine their electronic properties. The energy band is derived for graphene by the tight-binding approximation method [3]. This technique involves expanding an electron's wave function while subjecting it to periodic crystal potential. The atomic orbits (LCAO) around all of the lattice atoms are combined linearly in this expansion. The electron wave function of the graphene lattice is represented as the sum of the wavefunctions of electrons from two sublattices because it is made up of two triangular sublattices (A and B).

$$\psi = C_A \psi^A + C_B \psi^B$$

Where ψ^A and ψ^B are linear combination of electron orbits around the sublattice A atoms and sublattice B atoms. The Schrodinger equation $H\Psi=E\Psi$, where E is the eigenvalue and H is the Hamiltonian function, can be used to derive the combination coefficients C_A and C_B . In this approximation, the overlap between the nearest and next-nearest neighbors is given greater weight than the distant orbits. The approximate solution for the energy bands results from this assumption is .

$$\begin{split} E_{\pm}(\vec{k}) &= \pm \gamma \sqrt{1 + 4\cos^2\left(\frac{\sqrt{3}k_y a_{c-c}}{2}\right) + 4\cos\left(\frac{\sqrt{3}k_y a_{c-c}}{2}\right)\cos\left(\frac{3k_x a_{c-c}}{2}\right)} \\ &- \gamma'\left(4\cos^2\left(\frac{\sqrt{3}k_y a_c - c}{2}\right) + 4\cos\left(\frac{\sqrt{3}k_y a_c}{2} - c\right)\cos\left(\frac{3k_x a_{c-c}}{2}\right) - 2\right) \end{split}$$

here k is the wave vector, - is the lower band, and + is the upper band. γ and γ' are the nearest neighbor hopping energy ($\approx 2.7 \text{ eV}$) and the next nearest-neighbor hopping energy, respectively. The contribution for γ comes from hopping between two different lattices, while for γ' comes from hopping within the same sub-lattice. Fig. 2.3 (a) displays the complete energy spectrum within the Brillouin zone [2]. The lower and upper bands are symmetric about zero energy if γ' is

neglected. Most importantly, the energy values at K' and K are same for the lower and upper bands, indicating no energy gap at the six corners of the Brillouin zone. These points are called Dirac points. E(K) expansion about the Dirac points results in an approximate linear dispersion relation (LDR).

$$E_+(\vec{q}) \approx \pm \nu |(\vec{q})|$$

Here (\vec{q}) is the wave vector measured with respect to Dirac points (DPs) and $v = \frac{3\gamma a_{c-c}}{2} \approx 1 \times 10^6 \ m/s$. Indeed, v is a fermi velocity v_f , as the DPs represent the largest wave number within the Brillouin zone. This LDR shows that the graphene's fermi velocity is not dependent on the energy. Contrary to the well-accepted parabolic relation $E(q) = q^2/2m$, signifying that fermi velocity varies with energy [2]. In fact, the LDR of the graphene resembles a photon equation, signifying that the holes and electrons close to the DPs act as massless fermions. Theoretically, the effective mass of particles tends to be zero leading to infinite carrier mobilities. In contrast, actual graphene samples have defects, finite mass of charge carriers, and phonons, that opposes motion of charge carriers. As a consequence, the mobility measured at room temperature has a finite value and is achieved in the order of $10^4 \ \text{cm}^2 \text{V}^{-1} \text{s}^{-1}$, when graphene is on SiO₂ [4]. As a matter of fact, the mobility of graphene is > the electron mobility of silicon, around ~1400 cm² V⁻¹ s⁻¹. The mobility of graphene has been achieved in the order of $10^5 \ \text{cm}^2 \text{V}^{-1} \text{s}^{-1}$ on hexagonal boron nitride encapsulation [5].

The graphene's charge carriers can be tuned constantly adjusted between holes and electrons by applying the external gate voltage due to its zero band gap, as shown in figure 2.3 (b). The change in the Fermi energy (E_F) level in the energy spectrum E(K) is shown in the inset of fig.2.3 (b). The E_F has moved away from the DP due to applying the gate voltage with holes (electrons) induced by negative (positive) voltage [6]. Therefore graphene provides an ambipolar behavior which is a potential character for electronic applications. Graphene has been demonstrated as a semi-conducting channel in field effect transistors (FETs) [7,8]. Fabricating an array of graphene FETs with uniform electrical properties demonstrates the integration of graphene into extensive electronic circuitry [9].

2.2.2 Optical properties

The theoretical calculations showed that the optical transmittance and reflectance for single-layer graphene are $(1 + \pi\alpha/2)^{-2} \approx 97.7\%$ and $\frac{\pi^2\alpha^2\left(1+\frac{\pi\alpha}{2}\right)^{-2}}{4}$ approximately 0.01% for normally incident light, respectively, where $\alpha\approx 1/137$ is the fine structure constant [10,11]. For CVD-grown graphene, the obtained transmittance of different layers has been shown in figure 2.4.a. Transmittance value at 550 nm wavelength is 97.7% for monolayer graphene, which matches the theoretical value mentioned earlier, and it is almost constant in the visible region [12]. The layer dependent up to four layers on the optical transmittance is shown in the inset of figure 2.4. a and it is almost linear, up to four layers. The high conductivity and transmittance properties make graphene a potential candidate for transparent conductive films [13,14].

2.2.3 Mechanical properties:

Both experimental methods and numerical simulations have explored the mechanical properties of graphene [15–17]. Figure 2.4 (b) illustrates a typical measuring technique called nano-indentation, in which graphene is hung above a substrate cavity with a micrometer-sized opening. An AFM tip is placed in the middle of the trench for performing the force-displacement measurement. The obtained young's modulus of defect-free single-layer graphene is ~1.0 TPa, and the fracture strength is ~130 GPa [16]. This indicates that graphene is a strong material because of the sp² covalent bonding among the carbon atoms. Indeed, to break the graphene, 48,000 kNmkg⁻¹ of specific strength is required, which is much higher than that of steel (~ 154 kNmkg⁻¹) [18]. These properties imply graphene is a suitable candidate for flexible nanoelectronics [19,20]. Most importantly, graphene can be utilized as an enforcer to lightweight polymers to increase their mechanical properties [18].

2.2.4 Thermal properties:

Graphene is also a good thermal conductor. The main contribution to thermal conductivity is from phonon transport, but the electronic contribution is minimal because of the low carrier density of pristine graphene. Thus, understanding of lattice vibrational modes (phonons) of graphene is crucial to gain insights into its thermal properties [21]. The unit cell of graphene has two atoms (N=2), as shown in figure 2.2 (a). This results in forming 3N-3 optical (O), and three acoustic (A)

phonon modes, with dispersions, as shown in figure 2.4 (c) [22]. The phonon dispersion links the phonon energy or frequency and the reduced phonon wave vector. The atomic displacements are defined as Longitudinal (L) modes along the direction of wave propagation; in contrast, transverse (T) modes relate to the in-plane lattice displacements orthogonal to the propagation direction.

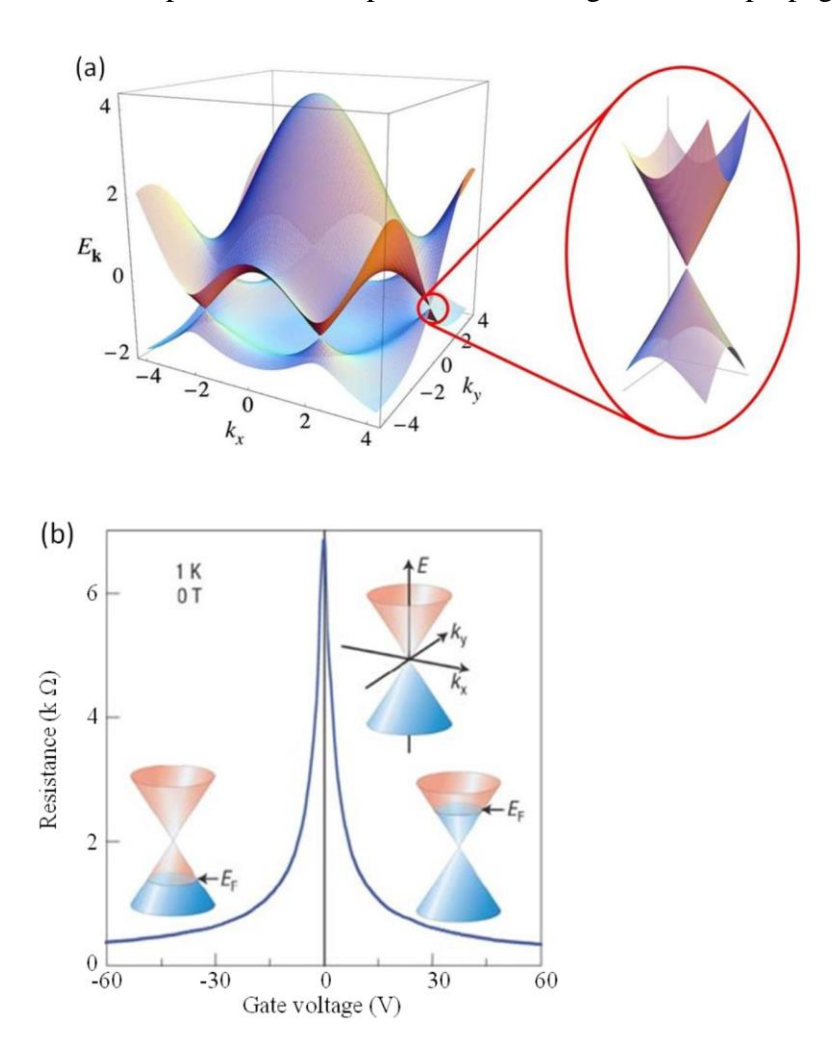


Figure 2.3 (a) Energy bands (in γ units) of honeycomb lattice of graphene obtained using tight binding approximation for γ =2.7 eV and γ '=-0.2 γ . Also shown on the right is the enlarged image of the energy bands about the DPs depicting linear dispersion [2]. (b) Graphene resistance depends on the applied gate voltage measured at 1K and zero magnetic field [6].

These phonons interact inelastically with photons that manifest in the Raman spectra of pristine monolayer graphene, as shown in figure 2.4d. They comprise characteristics of the Raman G-band at ~1580 cm⁻¹ and 2D band at ~2700 cm⁻¹ [23]. Besides these peaks, a D-band at 1350 cm⁻¹, is assigned to graphene with defects [24] and a G-peak is assigned to the in-plane vibration modes

of the carbon atom and vibrates in directions opposite to its nearest atoms (doubly degenerate iTO) and LO phonon mode at the Brillouin zone center) [25–27]. This is the only band that arises from the first-order Raman scattering process. This peak is prominent in all Raman spectra of graphitic materials. The 2-D band is a 2nd order Raman scattering process that involves the two iTO phonons near the K point. A double resonance process comes from the inter-valley scattering of the electrons by the k-point phonons. The D peak is associated with an electron scattering process that involves both a defect state and a Brillouin zone boundary phonon. This corresponding vibration mode of the D band is attributed to the breathing mode of the six-membered ring, that is constrained by the closely packed neighboring rings and thus occurs only at defects [26]. Hence, the D-band is not present in the defect-free graphene. The Raman bands of graphene are useful to characterize the crystalline quality. The 2D peak's high intensity compared to the G peak, weak D band, and narrowed width of the 2D peak indicate the high crystallinity of graphene. The number of layers up to five is determined by the ratio I(2D)/I(G), derived from the integrated intensity of the 2D peak to the G peak. [25]. The I(2D)/I(G) ratio is inversely proportional to the layer number increases and directly proportional to the broadening of the 2D peak which is asymmetric and blues shifts, as shown in figure 2.4 (d). The origin of asymmetry of the 2D peak is the many resonance modes in multilayer graphene, since the energy bands of multilayer graphene split into multiple bands due to interaction between them [25]. Charge doping via the electron-phonon coupling in turn, affects positions of the 2D and G bands [28,29].

The setup for thermal conductivity is shown in figure 2.4 (e) [30]. The monolayer graphene flake has been suspended over a micron-sized substrate cavity. A laser is focused over the graphene center, and heat radially flows through the graphene. When heated with low laser power, the red shift in the Raman G-band is caused. Its amplitude is linearly related to the temperature of the graphene flake being heated[31]. The slope of the shift in the G-peak position with excitation power can be used to calculate the thermal conductivity value. The value for the pure monolayer graphene is ~5000 Wm⁻¹K⁻¹. When graphene is placed on substrates like SiO₂, its thermal conductivity drops to about ~600 Wm⁻¹K⁻¹. Its decrease is attributed to the phonons that leak over the substrate-graphene interface and the scattering of flexural modes at the interface [32]. However, compared to copper's 385 Wm⁻¹K⁻¹ thermal conductivity, graphene's value is high. This high graphene thermal conductivity helps solve nanoelectronic architecture heat dissipation problems [32].

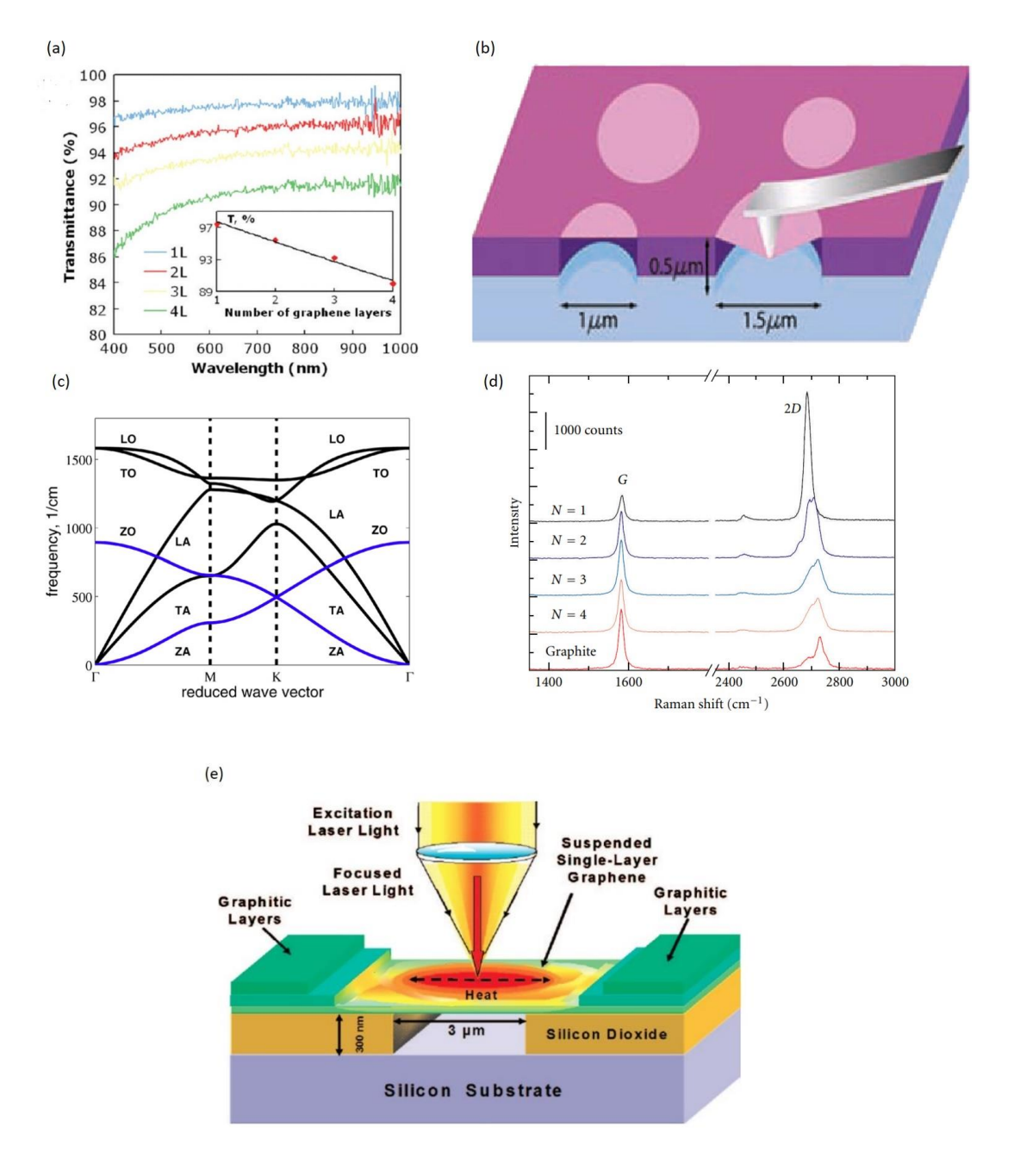


Figure 2.4. (a) Optical transmittance of graphene with different layers. It has been shown up to four layers. Inset figure shows the linear dependence of transmittance with layer numbers up to four layers [12]. (b) schematic representation for measurements of mechanical properties of the suspended graphene by an AFM tip [16]. (c) phonon dispersion of graphene [22]. (d) Raman spectroscopy for graphene with different thicknesses (layer number) on SiO₂(300nm)/Si and bulk graphite [23]. (e) schematic representation of thermal conductivity measurement setup for suspended graphene [30].

2.3. Limitations of Pristine Graphene:

Graphene has some major limitations, even though it has exceptional properties. The availability of free charge carriers for electronic transport in pristine graphene is absent as the valance electrons fill the electronic bands up to the DP. As a consequence, transport measurements show a minimum conductivity near the DP. The minimum conductivity at this point does not go to zero but reaches $4e^2/\hbar$ even for the cleanest graphene samples [2,7,33]. This minimum conductivity decreases the efficiency of the electronic transport that must be increased for applications such as electrodes. The transport can be increased by introducing free charge carriers that cause it to move away from the neutrality point. The electric field effect is one way to introduce either hole or electron carriers into graphene by changing the polarity of the gate voltage.

The other limitation of graphene is its semimetal nature. As can be seen from figure 2.3 (a) that there is no band gap in the energy band structure. However, the bandgap is needed for electronics where the flow of electrons controlling is required to attain an on or off state. The band gap in graphene can be created in many ways, such as by applying the electric field, functionalizing or doping the pristine graphene, and quantum confinement [34–36][37]. It has been shown that a tunable band gap can be achieved in AB stacked bilayer graphene through a dual gating technique, which breaks inversion symmetry [38]. However, compared to single-layer graphene, producing large-area AB stacked bilayer graphene sheets is difficult. [39]. Additionally, it has been demonstrated that the interaction of the graphene with the substrate causes the band gap creation. The graphene synthesized on h-BN that had been synthesized on Ni(111) showed a 0.5 eV bandgap measured using STM [40]. The doping of graphene also produces changes in physicochemical properties besides inducing bandgap. Substitutional doping is the primary method used in the doping of conventional semiconductors. In graphene lattice, n-type and p-type can be obtained by substituting carbon with nitrogen, boron, or other atoms [41]. One of my thesis's focussed works is the doping of graphene with nitrogen atoms. Poor solubility and low reactivity are additional shortcomings of pristine graphene.

2.4. Doping of pristine Graphene:

Chemically doping with heteroatoms into graphene's honeycomb lattice structure has been an effective way to tailor the graphene properties that further broaden graphene applications. This

technique has been widely utilized for electron/hole doping to silicon in the modern semiconductor industry. The suitable species with an excess or depletion of electrons will be doped into graphene films to introduce free charge carriers. The heteroatoms similar in size to carbon atoms are boron (one less electron than the carbon atom) and nitrogen (one more electron than the carbon atom) atoms. Intuitively, when the boron atoms are embedded in the carbon framework, they withdraw some amount of electrons from carbons as they have one less electron than the carbon atoms. As a consequence, boron-doped graphene films exhibit hole-doped behavior. Similarly, when the nitrogen atoms are doped into the graphene framework, they are expected to be electron-doped as the nitrogen atom contains one more electron than the electrons in the carbon atom. However, the theoretical calculations predicted that there is much physics beyond the intuitions[42,43].

Moreover, depending on the chemistry of heteroatoms, they bond differently to the carbon atoms, thus giving rise to the distinct dopant bonding configurations within the graphene. The contribution of electrons or holes of dopants to the graphene depends on the doping form of the dopants. There are typically two methods for chemically doping graphene: (1) gas or organic molecules containing the appropriate dopants are adsorbed to the graphene surface (2) Heteroatoms, such as boron and nitrogen atoms, are substituted for carbon atoms in substitutional doping. These two techniques can change the electrical characteristics of graphene [44]. Mostly, substitutional doping has been addressed under which nitrogen doping is focussed during my thesis work.

2.4.1. Nitrogen-Doped Graphene (NDG):

In a honeycomb lattice structure, nitrogen atoms can easily replace carbon atoms due to their identical atomic size and length of chemical bonds. In nitrogen doping graphene, nitrogen atoms create vacancies besides substituting carbon atoms, thus producing different bonding configurations. Nitrogen atoms majorly bond to carbon atoms in three bonding configurations: pyridinic-N, graphitic-N (or quarternary-N), and pyrrolic-N, as shown in figure 2.5 (a) [45]. Each configuration significantly impacts doped graphene's electrical and transport characteristics. Graphitic-N doping configuration refers to the direct substitution in which nitrogens replace carbons without breaking the hexagonal ring. In this configuration, three valance electrons of nitrogen make three sigma bonds. The 4th electron occupies the π band, and the 5th electron moves into the π * band. The donation of one electron to the conduction band indicates an n-type doping [46]. On the other hand, the situation becomes more complex for pyridinic-N and pyrrolic-N

configurations. Pyridinic-N configuration exists when the nitrogen atom is bonded to 2 carbon atoms in a 6-membered ring and accompanied by a vacancy. Pyrrolic-N configuration is when the nitrogen atom bonds to 2 carbon atoms in a 5-membered ring, which is sp³ hybridized [47]. The contribution of pyrrolic-N to the graphene's electrical properties is p-doped behavior [48]. Other than these common configurations, N-oxides of pyridinic-N and nitrilic-N are also observed.

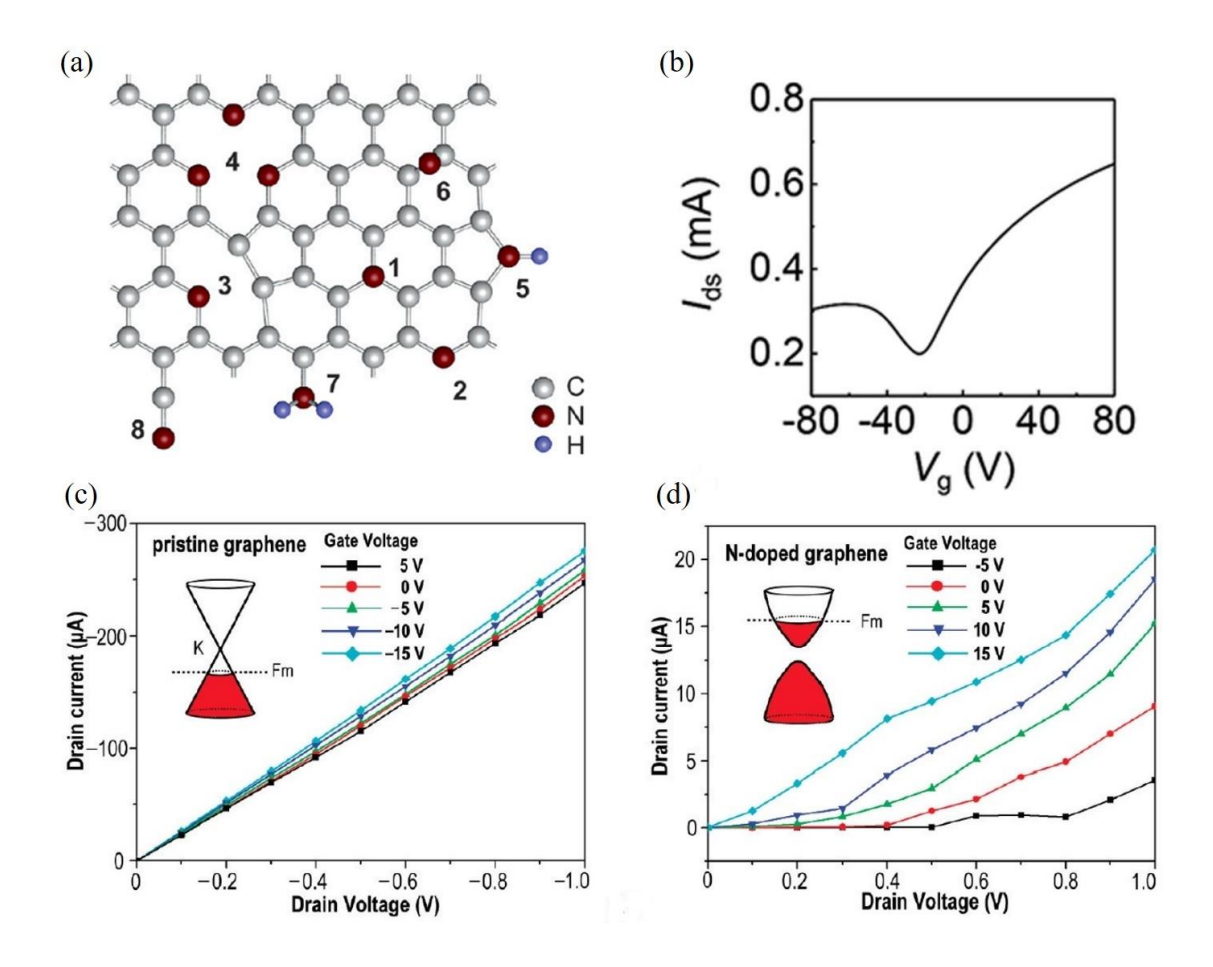


Figure 2.5 (a). Possible configurations of nitrogen-doped graphene: (1) graphitic-N or substitutional-N, (2) pyridinic-like-N, (3) mono N pyridinic vacancy, (4) triple N pyridinic vacancy, (5) Pyrrolic-N, (6) adatom, (7) amine and (8) nitrile [45]. (b) I_{ds} -V_g characteristics of NDG FET device [49]. (c) and (d) I_{ds} vs V_{ds} characteristics of the pristine graphene and Nitrogen-doped graphene films at different Vg, where I_{ds} , V_g , and V_{ds} represent the source-drain current, the gate voltage, and source-drain voltage, respectively. The predicted band structures for pure and nitrogen-doped graphene films are shown in the insets in figures (c) and (d) [35].

The N-dopants in NDG opened a band gap whose exact value depends on the dopant concentration, dopant configurations, and the sites of the dopants [50]. The NDG-based FETs devices exhibit lower turn-on fields and larger on/off current ratios than pristine graphene [50]. It was reported that NDG films showed lower mobility and conductivity compared to pristine graphene due to dopants acting as scattering centers [51]. The I_{ds} vs V_g curve is shown in figure 2.5 (b), for which the obtained highest mobility for graphitic-N NDG film is 1400 cm²/Vs for the FET device by Son et al. [49]. Lin et al. showed the highest mobility for graphitic nitrogen cluster-doped graphene films is 13,000 cm²/Vs measured using the hall device [52]. Figure 2.5 (c) and (d) show typical Ids vs Vds characteristics at different Vg. Pure graphene has higher conductivity and linear behavior than the NDG films, but the NDG film exhibited a larger on-off ratio. Inset figures in 2.5 (c) and (d) show the predicted band structures for NDG films and pure graphene. The band structure of the pure graphene demonstrates 2 bands contacting each other, which implies no band gap and exhibits the p-type behaviour as a result of the absorption of oxygen and water in the air. The density of states of graphene around the fermi energy (F_m) level is suppressed in NDG films because N dopants bond covalently to the carbon atoms and break the symmetry. As a result, a bandgap appears [35]. NDG is more suitable for anode material in batteries than pristine graphene, as the dopants produce active sites for adsorption, substitution, and intercalation capabilities [53]. NDG has been used in the field of ultracapacitors, and it has shown long cycle life than pristine graphene [54].

2.5 Synthesis techniques for Pristine and Nitrogen-Doped graphene:

The industrialization of graphene can be realized when synthesis methods are inexpensive and can produce large scale with tailored required properties for target applications. Various techniques have been used for graphene syntheses that include mechanical exfoliation, chemical vapor deposition (CVD), epitaxial growth, arc discharge method, chemical synthesis, and many other methods, as shown in figure 2.6 [55]. All these various techniques can be summarized into top-down and bottom-up methods. As demonstrated in figure 2.6, chemical synthesis, mechanical and chemical exfoliation come under the top-down methods. Methods including epitaxial growth, CVD, and pyrolysis are classified as bottom-up. Every method has its pros and cons in the synthesis of graphene.

2.5.1. Top-Down Methods:

Top-down approaches involve the breaking down of the bulk materials (3D materials) into nanostructures or particles. Graphite as the source material would be thinned down to a single or few layers of graphene using various techniques. Some of the methods are discussed in this section.

Mechanical Exfoliation: The birth of graphene took place in the real world using the scotch tape method. This technique separates graphene layers from the bulk HOPG (Highly Ordered Pyrolytic Graphite) surface using adhesive tape. Scotch tape is applied to the surface of HOPG and thus exerts a normal force, as shown in figure 2.7 (a). The graphitic layers are made thinner and thinner by applying normal force numerous times until it eventually transforms into monolayer graphene. The force is sufficient to cleave the graphene layers as the graphite comprises graphene layers stacked with Van Der Waals interactions. This technique is suitable for preparing high-quality graphene flakes. However, the disadvantages of this method are labor intensive, noncontrollable thickness, time-consuming, and low yield.

Another mechanical exfoliation process is the ball milling method in which graphene is prepared using a high-speed vibrating ball mill and grinding balls (stainless steel balls). The motor rotates the cylinder containing the graphite powder and grinding balls at high speed and vibrates. During this process, the kinetic energy attained by the grinding balls gets transferred to the graphite, which gives rise to graphene's exfoliation [56].

Chemical exfoliation: Liquid-phase exfoliation is one method that comes under chemical exfoliation. This method produces graphene flakes by ultrasonication of natural graphite in organic solvents and aqueous solutions, shown in figure 2.7b [57]. As the graphite does not dissolve in aqueous solutions, thus the addition of surfactants is necessary. Due to sonication, there is a strong interaction between the graphitic basal planes and the solvent molecules that lead to exfoliation. The solvents that can minimize interfacial tension between the graphene flakes and liquid are considered suitable solvents.

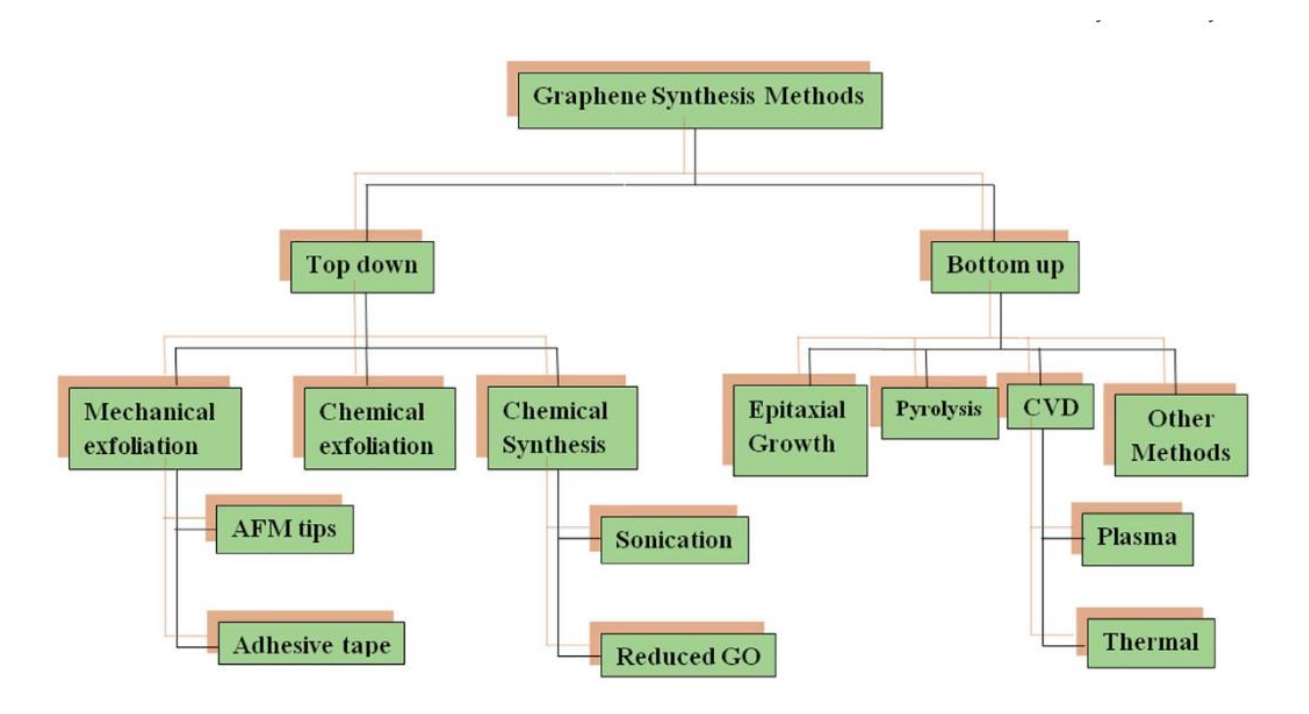


Figure 2.6 Schematics of different fabrication techniques that are categorized into top-down and bottom-up methods for graphene production [55].

Chemical synthesis: Oxidant exfoliation of graphite is a promising method for preparing graphite oxide (GO). It is commonly used as a raw material in the industrial manufacturing of reduced graphene or graphene. During the oxidation process, the oxygen moieties are covalently bonded to the carbon structure to overcome the Van der Waals forces between layers. The interlayer spacing between layers increases because of the oxygen functionalities. The graphite precursor, oxidizing agents, selected synthesis process, and reaction conditions determine the chemical content and structure of graphite oxide(GO).

Further, the prepared GO is dispersed in suitable solvents by ultrasonication, producing well-dispersed mono, bi, or few-layer GO flakes, as shown in figure 2.67 (c) [59]. Later on, the GO flakes can be transformed into reduced graphene oxide (rGO) using various reduction methods like chemical, thermal, microwave hydrothermal, and photoreduction methods [58]. Chemical exfoliation and synthesis methods are suitable for large production, but they are defective, and the size of the flakes is in microns.

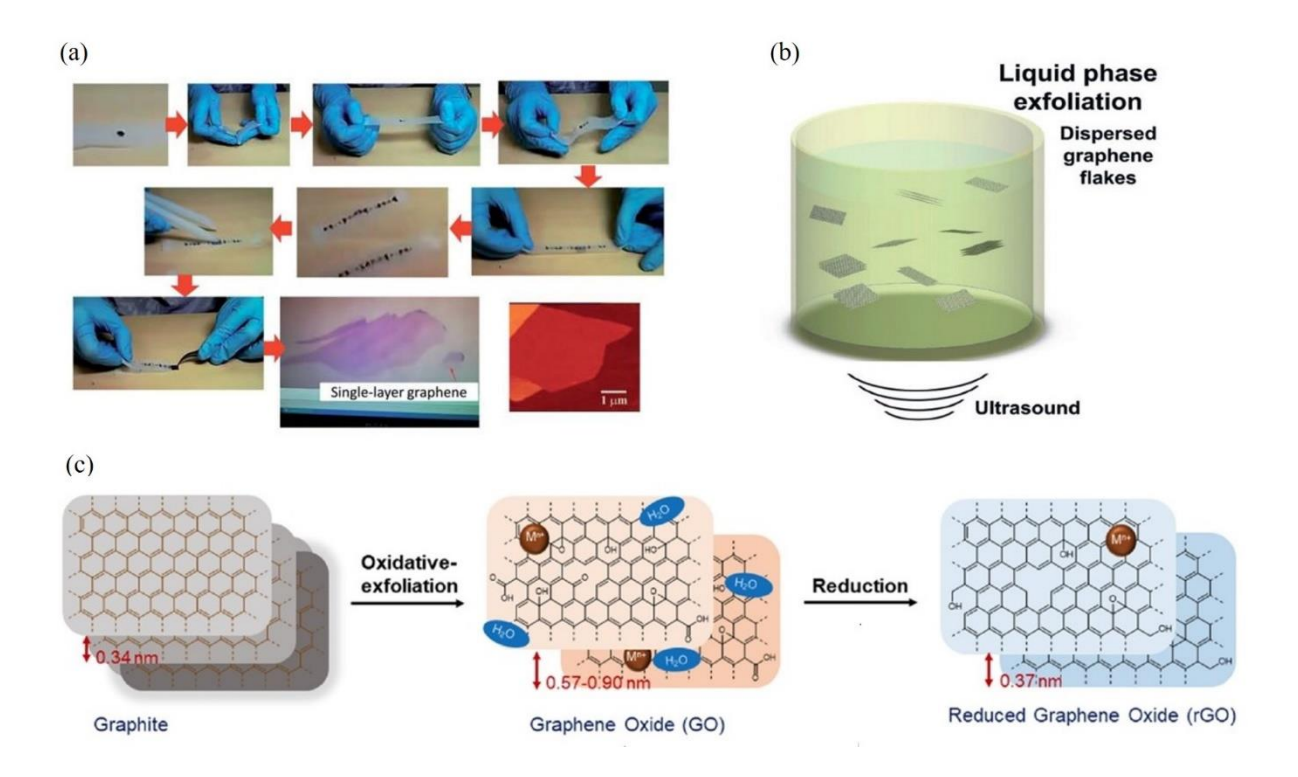


Figure 2.7 a. illustration of the mechanical exfoliation of graphite using the scotch-tape method [55]. b liquid phase exfoliation of graphene using ultrasonication [57]. c schematics of the oxidation-reduction method to synthesize rGO from graphite [58]

2.5.2. Bottom-Up Methods:

The bottom-up approach refers to the preparation of material (nanostructures) from atoms or molecules. It involves atom-by-atom or cluster-by-cluster manipulation for nanostructure synthesis. This approach is suitable for producing large-area graphene at a large scale. Prominent bottom-up methods used for the growth of graphene are discussed below.

Epitaxial Growth: Graphene is grown epitaxially through the sublimation of silicon (Si) from the source material, silicon carbide (SiC), and the schematics of the growth are shown in figure 2.8 a. The graphene growth is possible because of the sublimation of Si atoms over C atoms. Meanwhile, the leftover carbon atoms on SiC form graphene while the process proceeds at a high temperature of around 1200 °C in an ultra-high vacuum (UHV). The grown graphene contains monolayer to few-layer graphene. The graphene growth is sensitive to the crystallographic orientation of SiC, and the process of it is needed before the growth [60]. The percentage of the monolayer areas is increased by using a stronger Si vapor pressure over the SiC to avoid substrate pitting, higher

temperatures (2000 °C), and argon (Ar) to decrease the sublimation rate [61]. The graphene grown via this technique produced small grains around 30 -200 nm.

The mobility of graphene grown on SiC has mobility of $> 3400 \, \text{cm}^2 \text{V}^{-1} \text{s}^{-1}$ [62]. Epitaxy of graphene on 4H-SIC(0001) subjected to H₂ intercalation, showing the mobility measured at a temperature of 0.3K is $> 11000 \, \text{cm}^2 \text{V}^{-1} \text{s}^{-1}$ [63]. The film produced with the process can not be used for targeted applications as the transfer from SiC is difficult and detrimental. However, no transfer is needed to measure the transport and thermal characteristics of graphene/SiC as SiC is an insulating material (band gap 3 eV) [64].

Chemical Vapor Deposition (CVD):. CVD combines the gas molecules with a substrate surface inside a reaction chamber under pressure, temperature, rate conditions, and gas flow. A typical CVD instrument includes a quartz reaction chamber, a pump, a mass flow controller, a vacuum system, thermocouples for measuring temperature, a gas delivery system, and a furnace, as shown in figure 2.8 (b) [65]. CVD is a bottom-up synthesis approach utilized to produce large-area graphene films on a large-scale basis [66]. The CVD has been discussed in detail below, as this technique was utilized during the research.

Heating a gas flow consisting of carbon (C) based precursors, typically hydrocarbons, such as methane (CH₄), Ethene (C₂H₄), Acetylene (C₂H₂), and Ethane (C₂H₆) to elevated temperatures in the range of 300 to 1100 °C has resulted in successful synthesis of graphene using CVD on transition metal substrates[67,68]. The morphology of CVD-grown graphene is heavily dependent upon the growth substrate. The grain orientation, grain boundary density, grain size, and the number of layers are affected due to the substrate. C dissolves into the substrate surface at elevated temperature and pressure during CVD, and the amount of C taken by the substrate is defined as solubility. The C solubility is a crucial factor for optimizing the graphene growth as it determines the number of layers of graphene due to the C atoms precipitating out during cooling down.

Role of Substrate: The substrates with low C solubility suppress the formation of a few graphene layers, as C adatoms are mostly restricted to the substrate surface. Graphene growth takes place by forming the small nucleations that coalesce to cover the surface fully, at that point, the precursor no longer dissociates at the catalyst surface and, therefore, no more C will be added to the system, leading to the self-terminating of graphene growth. Minimal bi-layer formation was observed on

very low C solubility materials, such as Copper (Cu), in which the monolayer graphene coverage is around 95% [69–72]. However, this is variable with other CVD parameters such as C concentration, pressure, temperature, and growth time.

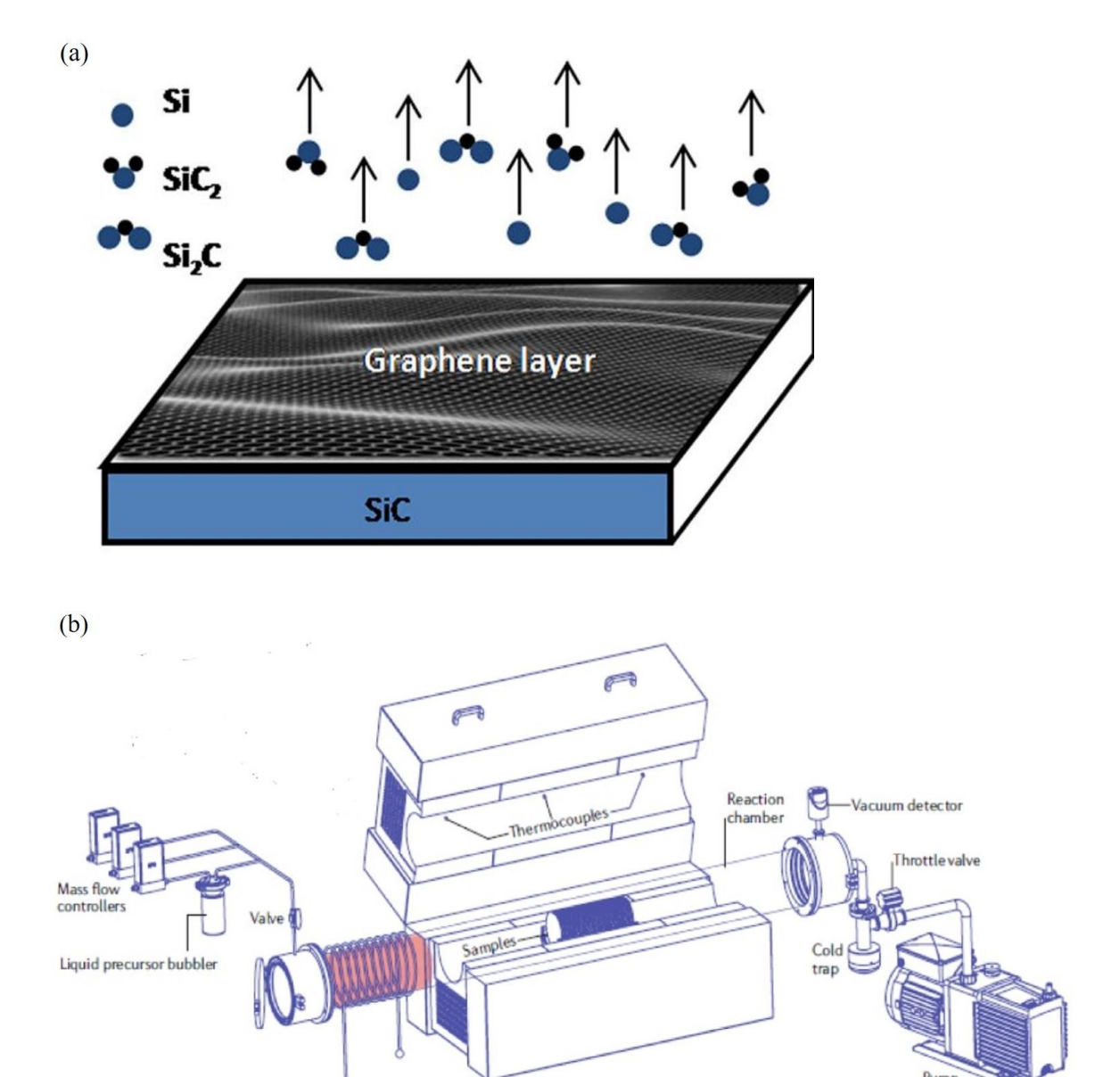


Figure 2.8 a schematics of epitaxial growth of graphene on SiC. b schematics of chemical vapor deposition (CVD) system.

Plasma source

The graphene's 2pz orbital volume is out of the graphene lattice plane. It is expected that the 2pz electron couples with the outermost d-subshell electrons of the transition metal on which it sits

[73]. However, metals such as group 11, Platinum (Pt), and Iridium (Ir) have weak interfacial interaction with graphene bonded to graphene Via Van der Waals forces [74]. The outermost d subshell is filled, and the s subshell is filled with a single electron, causing the Cu, gold (Au), and silver (Ag) to have weak surface interaction with graphene. Among the transition metals, Pt, Ir, Cu, Ag, and Au have the greatest bond separation. These are suitable candidates for the growth substrates due to their weak interfacial bonding. They also have the lowest C solubility, contributing to the monolayer graphene's greater coverage on the substrate.

Nickel (Ni) as the catalytic substrate has been studied extensively for graphene growth. It was considered an ideal growth substrate because it has a close lattice match with the graphene, and therefore, the graphene can create a commensurate graphene lattice on Ni(111). However, it forms graphene multilayers due to Ni having more C solubility at elevated temperatures, and the diffused C gets segregated from the bulk substrate while cooling down [75,76]. The growth process is from C precipitation more than CVD.

Carbon Source or Precursor: The precursor flow in the CVD contains a C source, H₂, and a buffer gas. The buffer gas is a neutral gas, such as Ar, that is not involved in the growth mechanisms but helps keep the viscous flow. H₂ gas acts as an etching agent and an activator of surface-bound carbon [77]. It cleans the oxide species on the Cu surface by reducing the Cu₂O and CuO contaminating surface species. The type of C source is very important as it has proportionalities with graphene growth kinetics at the Cu surface. The activation energy of precursors at different temperatures and pressures to dissociate into C atoms determines the graphene film's growth rate. Thus, appropriate starting materials (precursors) and efficient synthesis need to be identified to meet the potential applications and industrial level.

The gaseous hydrocarbon source has been investigated intensively among all carbon precursors. CH₄ is a less susceptible hydrocarbon to get dissociated into its constituents at the Cu surface but exhibits the most consistent results so far [67,71,78]. Other precursors liquids include benzene and solids like polymers such as polystyrene (PS), polymethylmethacrylate (PMMA), etc. [79,80].

Even though methane has been studied extensively as a precursor and produced reproducible results, it has limitations, such as it is a flammable gas, costly, and complex to use. It dissociates into C radicles at a higher temperature of around 1200 °C. Alcohols as precursors, such as 1-

propanol, ethanol, and methanol, are comparatively less flammable than methane. They decompose at lower temperatures, synthesizing graphene at lower temperatures. The quality of the graphene films derived from these precursors is comparable to methane-derived graphene. Synthetic polymers such as PMMA, waste plastic, and polyimide are used as precursors. They are also easier to handle and decompose at lower temperatures than methane. Sun et al. synthesized graphene from PMMA by spin-coating it on a metal catalyst substrate [80]. As it is post-annealing of the deposited precursor film on the substrate, the controlled growth of graphene can be obtained by tuning the thickness of the PMMA and controlling the hydrogen flow rate. PMMA-derived graphene showed comparable quality with methane-derived graphene and was also synthesized at a lower temperature [81].

Current Scenario of CVD on Cu: CVD currently provides the means of large-scale fabrication of monolayer graphene with recent advances in deposition on the scale of 100 m² per day [13,82]. Even though the industrialization of graphene is rapidly increasing using CVD, the physics behind the growth process is flagging [18].

The electrical properties of CVD-synthesized graphene on Cu using CH₄ have been shown to have significant mobilities. The mobilities measured at room temperature have shown up to 69000 cm²V⁻¹s⁻¹ and at 1.6 K 350,000 cm²V⁻¹s⁻¹, comparable to the exfoliated graphene [83]. CVD-produced graphene has shown a young's modulus value of ~1 TPa for both small-grain and large-grain polycrystalline graphene [84].

The study of the growth of graphene on copper took intensive research but lacked a definite model of growth kinetics. Many published works showed that trial and error approaches are needed to determine the ideal recipe for monolayer graphene with decreased grain boundaries or large domain size and continuous growth. These studies laid a path for growth, but a large discrepancy still exists in reported values, and reproducibility is a prime issue. So further theoretical and empirical investigation is needed [18,85]. A general consensus was attained from empirical studies for the conditions of the monolayer graphene growth on Cu are low pressures (mbar scale), a low surface roughness Cu, high temperatures of > 900 °C, and a CH₄ H₂ flow ratio less than 1.

Synthesis of Nitrogen-Doped graphene (NDG): NDG films are synthesized through the CVD technique by employing a large range of C and N-containing precursors, by in-situ growth or ex-

situ treatment as shown in figure 2.9 [86]. Till now, the content of the nitrogen dopant of NDG synthesized by both methods ranges from 0.2 to 16 at% [44,47]. The CVD approach for doping N atoms to graphene occurs through substitutional doping or surface charge transfer. Gas molecules or metal atoms are adsorbed to the graphene; however, the electrical properties of resulted doping suffer from long-term instability[87]. In substitutional doping, N dopants are bonded covalently to the graphene network, stabilizing the material but degrading the original pristine graphene properties. In in-situ growth, the nitrogen gets doped to graphene during its growth. The NDG is commonly produced on a transition-metal catalyst. Similar to the CVD graphene synthesis, a reactive mixture consisting of C and N precursors is injected into the reaction chamber at a growth temperature of around 700-1000 °C. The precursors decompose on the substrate surface, and NDG is deposited through the precipitation /organization of the C and N atoms on the substrate. NDG has been synthesized using gaseous, liquid, and solid precursors such as NH₃, pyridine, melamine, Dimethylformamide, and Acetonitrile [86]. In ex-situ growth, NDG is grown by post-treatment of pristine graphene at elevated temperatures and pressures.

Imammura et al. studied the impact of the choice of precursor on the growth of NDG. This report used two different N and C containing precursors, pyridine (C5H5N) and acrylonitrile (C_3H_3N), for NDG synthesis [88]. Pyridine only produced NDG, but acrylonitrile produced pristine graphene, even though both precursors contain C and N atoms. The authors proposed that the growth mechanism for producing pristine and ND graphene films depends on molecule dissociation and diffusion on the growth substrate. The molecular structure of acrylonitrile has C=C double, C-C single, and C=N triple bonds. High temperatures cause the weak C-C single bonds to break, releasing fragments of C=N. These fragments form volatile compounds C_2N_2 or HCN molecules on a catalytic substrate, and they are removed by the flowing gas, forming pristine graphene. When pyridine was used, this did not happen, and NDG was produced. The precursors, which have lower activation energies for breaking the bonds, form volatile compounds like HCN, which draw N away from the substrate and result in a reduced N-dopant configuration. Therefore, it is very important to choose the right precursor to obtain the required configuration and concentration of nitrogen atoms in a graphene network [47].

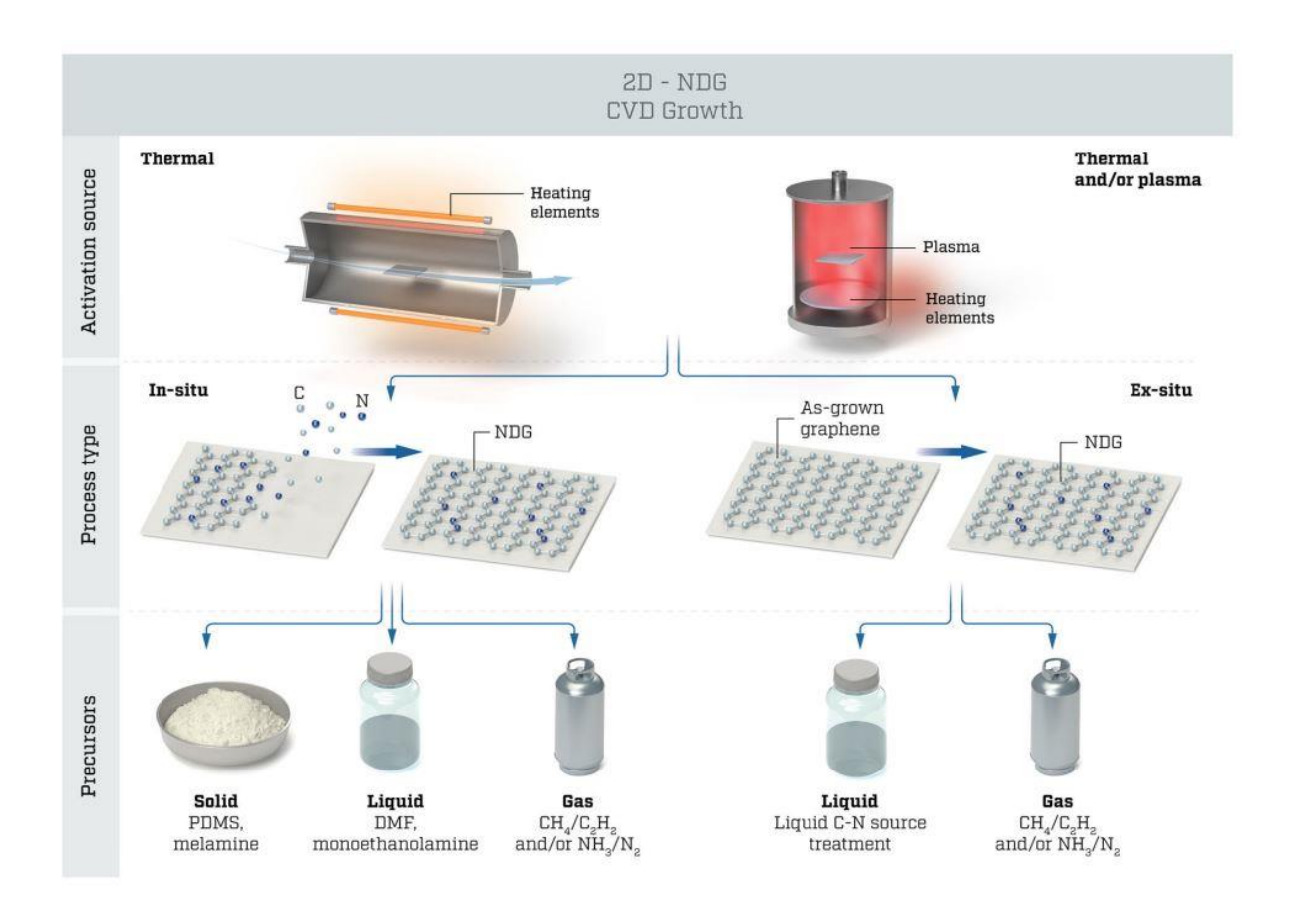


Figure 2.9 NDG film growth as depicted in a tree diagram utilizing different CVD techniques. They are divided by the kind of (1) source activation, (2) type of procedure (ex-situ or in-situ), and (3) type of precursor material (gas, liquid, solid) [86].

2.6 Applications of Pristine and Nitrogen-Doped Graphene:

Graphene's fascinating properties have led to various applications, like electronics, lithium-ion batteries, solar cells, fuel cells, and other energy sources. It is also used in biosciences, water purification membranes, and sensor applications, indicating graphene's versatility.

Field Effect Transistors (FETs): The distinct band structure and high carrier mobility of graphene make it useful for FETs applications. Studies have investigated stable FETs with higher carrier mobility and better miniaturization of the devices. Graphene as the channel in FETs has overcome the obstacles created by silicon (Si) nanowires, Carbon nanotubes, and so on. The schematics of Graphene FETs (GFETs) have shown in figure 2.10 a [89]. Moreover, the GFETs will continue to obey Moore's law to realize the further miniaturization of integrated circuits (ICs).

In GFETs, the Dirac fermion can be converted from hole to electron (electron to hole) continuously under the electric field due to graphene's semi-metallic and linear band structure. First reported by the Novosolev that FETs showed ambipolar properties with electron and hole concentrations of around 10^{13} cm⁻² and mobilities up to ~10000 cm² V⁻¹s⁻¹ at 300 K as well as ballistic transport up to sub-micron distances [33]. Graphene should be in strips laterally confined to nanometers called graphene nanoribbons to integrate with the FETs. They introduce bandgap because of the quantum confinement effect, which is useful for room-temperature FET applications [90]. It is expected that in the absence of ripples and charged impurities, mobilities can reach up to 200,000 cm² V⁻¹s⁻¹ [91]. Hexagonal boron nitride encapsulated graphene showed mobilities of 140,000 cm² V⁻¹s⁻¹ [92]. Ultrahigh mobilities of CVD-grown graphene have been measured by Banszerus et al., and the values are up to 150,000 cm² V⁻¹s⁻¹ [83].

Nitrogen-doped graphene FETs generally showed lower conductivity and mobilities than pristine graphene. Generally, pyridinic-N and pyrrolic-N configurations have higher defect densities than graphitic-N configurations; therefore, the former configurations have lower mobilities than the latter. Lin et al. demonstrate that the nitrogen cluster doped graphene was grown by liquid precursor acetonitrile using CVD, in which nitrogen dopants were doped graphically. The carrier mobilities measured for this film are 8600 cm² V⁻¹s⁻¹ and 13500 cm² V⁻¹s⁻¹ at room temperature and 1.9 K, respectively [52].

Field Emission (**FE**): In field emission application, the electrons are emitted from a material by applying a high electric field to it. In order to obtain a larger electric field, the object should be made into a sharp tip. Thus, the electric fields are produced at the tip of sharp objects. The graphene sheets are placed on the substrates where the patterns are available. This is due to the fact that at graphene's sharp edges, the work function is reduced. Vertically stacked few layers of graphene FE cathodes were synthesized on silicon and titanium by Malesevic et al. The graphene cathodes clearly showed a local field of the emitter of 1V/um, current density (I) of 14 mA/cm^2 , and field enhancement (β) of ~7500. The growth of graphene on metallic substrates is desirable for FE applications because of the formation of ohmic contact between them [93].

Transparent electrodes(**TE**): TEs are films with strong electrical conductivity and optical transmittance, making them suited for prospects in optical and optoelectronic features. Fluorine tin oxide and Indium Tin Oxide (ITO) are metal oxides that are well-established examples of TEs.

Researchers are searching for alternative materials as these oxides have disadvantages, such as being less abundant, having weak chemical resistance towards base or acids, and being brittle when used on flexible substrates [94]. Graphene has become an alternative next-generation TE for photovoltaic applications because of its stability against water and oxygen, high surface area, and high carrier mobility. Graphene-based TEs used for dye-sensitized solar cells (DSSC) synthesized from graphite oxide showed a transparency of 70% between 1000 to 3000 nm and 550 S cm⁻¹ electrical conductivity. The DSSC exhibited a 1.01 mA/cm² short circuit photocurrent density and open circuit voltage of 0.7 V. The total power conversion efficiency of DSSC was 0.26 %, and the low efficiency was attributed to the low-quality graphene film [95]. There are still some challenges to the synthesis of graphene directly on transparent substrates.

Photodetectors: Photodetectors measure optical power or photon flux by transforming the absorbed photon energy into an electrical current. These photodetectors are commonly used in many devices, such as televisions, DVD players, and remote controls. When the material absorbs the photons, the electrons are excited from the valence band to the conduction band, producing an electric current. The schematics of a photodetector are shown in figure 10 (b) [96]. The material becomes transparent when the incident photon energy is less than the bandgap energy. Therefore, the material's absorption usually sets a limit on the spectral bandwidth. Graphene absorbs the light from ultraviolet to the terahertz range.

Consequently, graphene-based photodetectors (GPDs) can work in a much broader wavelength range. GPDs can be ultrafast as the response time depends on carrier mobility, whereas graphene has huge mobility. The photoelectrical response of graphene at different wavelengths of 0.514, 0.633, 1.5, and 2.5 um have been reported [96]. Xia et al. showed that a GPD is capable of a photoresponse up to 40 GHz.

Sensors: Graphene-based gas and biological sensors have various uses in environmental monitoring and public safety. The underlying mechanisms of graphene-based sensors are based on the change in the electrical resistivity of graphene upon the adsorption of molecules on the graphene's surface. The variation in resistivity has been attributed to the change in the carrier concentration of graphene due to the charge transfer between the adsorbed molecules and graphene. As a fact of the matter, the adsorbed molecules serve as electron acceptors or donors. Graphene is a potential candidate for sensors because it exhibits high thermal and electrical

conductivities, high surface area, and high sensitivity due to atomic thickness. These properties have improved the detection limit for gas molecules down to a single atom. [99]. The graphene-based gas sensor has been tested for NO₂ gas detection, as shown in figure 10 (c) [97]. The hole-induced conduction caused by the removal of one electron from graphene served as the basis for the sensing mechanism. Enzymatic biosensors have also been developed using graphene [55].

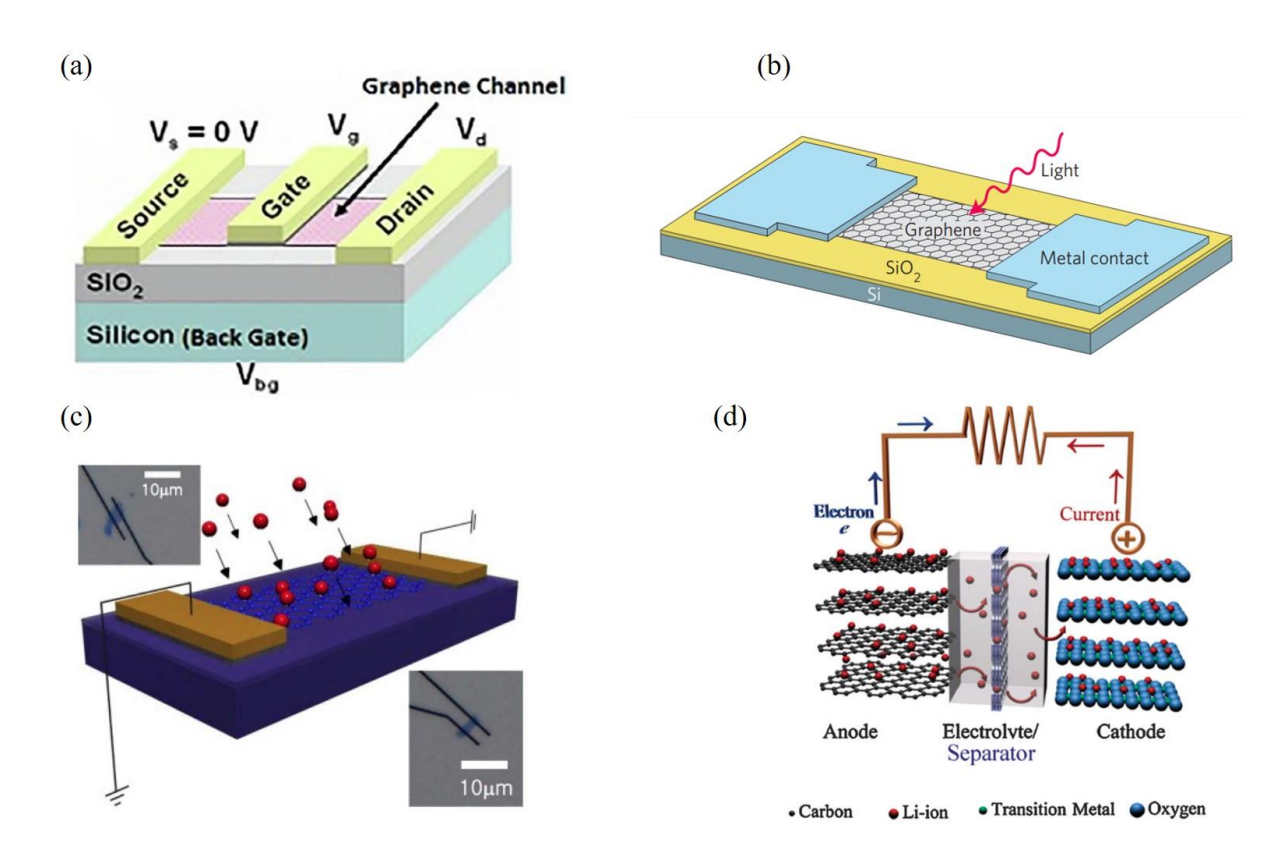


Figure 10 schematics of (a) 3D vies of graphene FETs, [89] (b) graphene photodetector [96], (c)graphene-based sensor for NO2 gas molecule, [97] and (d) a typical lithium-ion battery where lithium cobalt oxide and graphite are used as cathode and anode, respectively [98].

Energy Storage Devices: Batteries: Lithium-ion battery technology is the best energy source available on the global market for mobile electronic applications. Graphite is employed as an anode material in Li-ion batteries because of its reversibility and acceptable specific capacity. Researchers were inspired to discover novel electrode materials by the rise in demand for high energy density and long-lasting systems. Graphene-based materials have been found to be potential alternatives in batteries because of their higher surface area, higher chemical stability, and higher

conductivity in comparison to that graphite. Graphene is a suitable candidate as the segregation of nanoparticles can be prevented by it, and ionic and electronic capacity can be improved. This can cause a decrease in the amount of active material and enhances the electrode's mechanical integrity, which could achieve that perform well in terms of high flexibility and high capacity throughout the charge-discharge process. Sole graphene as an electrode has shown some disadvantages, such as a high charge-discharge platform, poor cycle stability, and low coulombic efficiency. But, graphene composites showed good results than pristine graphene as an electrode [100]. Recently, Liu et al. developed a unique integrated 3D mesostructure graphene and vanadium oxide (V_2O_5) composites. It was reported that at 5C, after 200 cycles, electrode capacity is ca.230 mA h g⁻¹; after 200 cycles, it is about 203 mA h g⁻¹.

In nitrogen-doped graphene (NDG), the N dopants alter the electronic structures and produce the active sites in the graphene network while enhancing the interlayer distance between graphene layers. Therefore the NDG is a more suitable candidate as an anode material that increases the battery capacity by increasing the adsorption, intercalation capabilities, and substitution. Reddy et al. investigated the directly grown NDG in a Li-ion battery assembly [101]. The NDG-based LIB's reversible discharge capacity was twice as compared to the graphene-based LIB's. The higher capacity results from surface defects induced by the N dopants. The theoretical storage capacity for an NDG-based K-ion battery (KIB) is 350 mA h/g and for a graphene-based K-ion battery is 278 mA h/g [102]. The NDG-based KIB has more storage capacity than graphene-based KIB because the pyridinic-N configuration induces a local electron deficiency that draws electrons from nearby K atoms [103].

Supercapacitors (SCs): The rapid increase in mobile technologies increases the demand for energy storage devices to act as efficient energy storage units or as power sources for energy harvesting systems. Supercapacitors are regarded as one of the most suitable electrochemical energy storage devices for future electronics because of their quick charge/discharge rates, high power density, and long cycle life. Supercapacitors are divided into two categories based on their energy storage mechanism. They are pseudocapacitors and electric double-layer capacitors (EDLCs). The charges accumulated at the electrolyte-electrode junctions determine the capacitance for EDLCs. Materials with high specific surface area, high electrical conductivity, and large pore size are needed to attain high storage capacity.

Graphene and its composites are more appealing for supercapacitors because of their outstanding physicochemical properties. When the entire surface of graphene is used, its theoretical specific capacitance is 500 F/g [104]. However, the practical capacitance did not reach the theoretical value because of the aggregation during the preparation or application processes. Therefore, the functionalization of graphene is useful to prevent agglomeration during the reduction process and to increase graphene capacitance. Recently, Adenine functionalized graphene has been utilized as EDLCs with a specific capacitance of 333 F/g at a scan rate of 1 mV/s [105]. It was reported that after 1000 cycles at 200 mV/s, it had good cycling retention with a 102% rate. It exhibited 64.42 Wh/Kg energy density with a power density of 599.8 W/kg at 1A/g.

Desalination applications: Graphene-based materials provide an excellent remedy to current desalination technologies' drawbacks. They offer the benefit of utilizing size-selective separation membranes. The structure on the graphene surface can support extraordinarily high water flux besides low biofouling potential. Graphene's primary sieving mechanism is comparable to carbon nanotubes' water permeation mechanism. Although graphene is impermeable to water, functional groups like epoxy and hydroxyl cause the creation of nano capillaries. The schematic diagram is depicted in figure 2.11, where a single-layer graphene-based membrane has been used [55]. These groups aggregate to produce a cluster with substantial percolating regions between graphene layers that have not been oxidized. These nano-capillaries allow only low friction of monolayer of water to transport similar to water molecules pass through an open aperture.

Kou et al. investigated graphyne for water desalination application. It is a carbon allotrope of graphene [106]. By substituting acetylene connections for some of the carbon-carbon bonds in graphene, graphyne is created. It was reported that graphyne has two orders of higher permeability than the currently available RO membranes and 100 % elimination of the common ions present in seawater.

Surface-enhanced Raman spectroscopy (SERS): Graphene has been proven to be a fascinating SERS substrate because of its advantages over traditional enhancement materials. Graphene properties such as large surface area, quenching the photoluminescence of fluorescent dyes, superior molecule adsorption ability, and rapidly eliminating the fluorescence background made graphene suitable for application as a SERS substrate [107]. Above all, graphene makes a great charge transfer SERS substrate for understanding the precise role of the charge transfer

mechanism. The charge transfer between the graphene and various molecules occurs because of the presence of the molecular enrichment effect, possibly through π - π interactions. It was reported that the NDG could find the Raman signals of rhodamine concentrations of $5x10^{-11}$ M, which is the lowest LOD reported among graphene-based SERS [108]. However, the effect of different configurations of NDG on the Raman enhancement signals has not been addressed much.

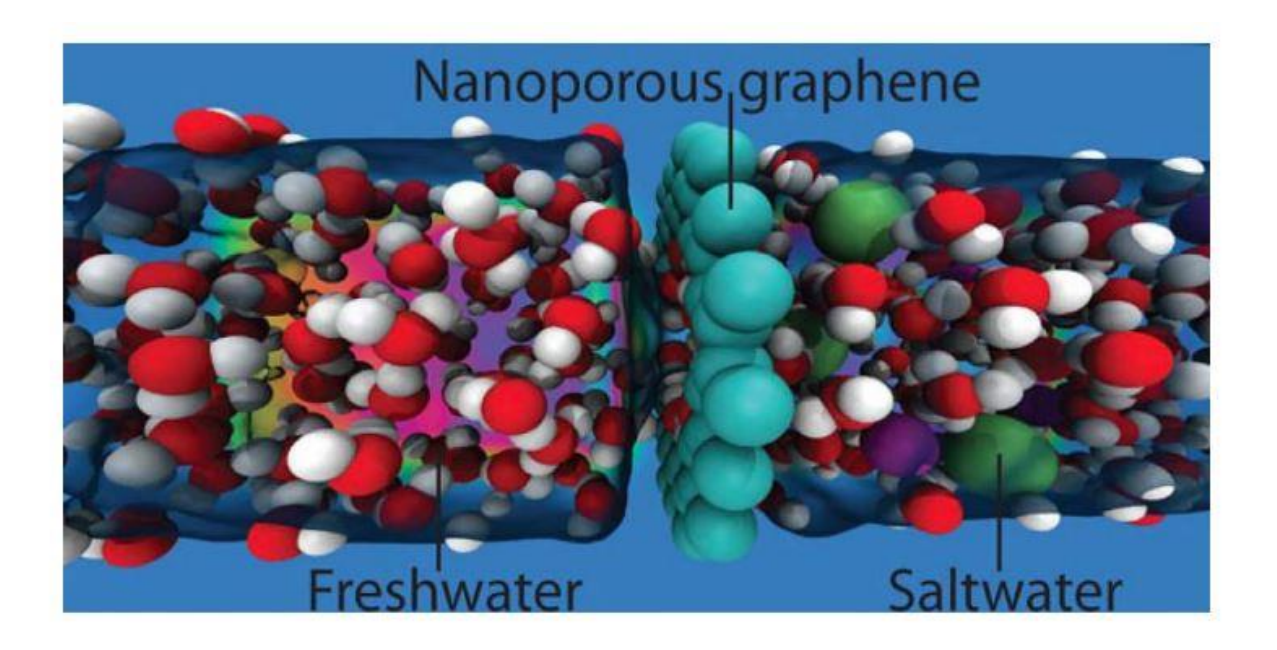


Figure 2.11 Schematic diagram illustrates the filtration process of NaCl from water through monolayer graphene-based membranes [55].

2.7. Future Scope: 2D materials have come a long way ever since the arrival of graphene in 2004 has occurred. The discovery of other 2D materials after graphene broadens applications such as emerging fields of quantum computing, artificial intelligence, quantum informatics, etcetera. Twisted bilayer graphene showed superconductivity behavior that is unexpected and surprised researchers. Synthetic materials produced from 2D heterostructures may exhibit synergistic physicochemical properties that increase the scope of these 2D materials for different applications.

2.8 Motivation and Objectives:

This thesis work is the outcome of intensive experiments in conjugation with a literature review. This thesis work attempts to fill the research gaps regarding the synthesis and application of graphene systems. The main motivation of the current work is to synthesize graphene and nitrogendoped graphene using solid precursors via CVD and use them in electronic and sensing applications.

The motivations for the research work undertaken are-

- Methane as a gaseous precursor has been intensively studied for the growth of graphene systems in CVD. However, methane poses a threat in research and at industrial levels as it is a poisonous gas and decomposes at a higher temperature (~ 1200 °C). More safety precautions are needed at the laboratory stage, and for industrialization, the graphene should be grown at low temperatures. Therefore, alternative precursors, such as liquid and solid precursors, have emerged and been utilized for graphene synthesis to overcome the problems. Predominantly, solid precursors have been used for graphene growth. But, most of the synthesis is taken place by post-annealing the pre-deposited solid precursor film on the substrate. This kind of growth does not have any control over the nucleation and the grain's size. The studies also reported only continuous graphene films with this method. This can be overcome by evaporating and transporting the precursors onto the metallic substrate. There are only a few studies where the solid precursors (PMMA, camphor) are evaporated and transported to the metal substrate to grow only continuous graphene film. Therefore, this thesis work addresses the optimizing growth conditions for graphene which was synthesized from solid precursor PMMA where the nucleations, grains, and continuous film are obtained.
- The scope for the applications of pristine graphene can be increased further by doping it with nitrogen atoms. Generally, nitrogen-doped graphene (NDG) has been synthesized in situ via CVD utilizing a variety of precursors that contain both carbon and nitrogen, as mentioned in the synthesis section. It was also reported that all precursors might not produce NDG, even though they might contain carbon and nitrogen species. Moreover, the choice of precursor affects the nitrogen dopant concentrations and configurations. Therefore, the novel precursor phthalocyanines have been synthesized for NDG films in

- this thesis work. The growth conditions have been optimized for studying the nitrogen configurations and concentrations.
- The grown films via CVD were subjected to various applications. The motivation behind their use is as follows.
 - (a) Electronic applications: The mobility of the films is investigated and compared with the methane-grown graphene films, as the electronic measurements indicate the quality of the grown film. The effect of the nitrogen configurations and concentrations on the electrical properties needs to be studied. So, here we tried to address the mobility and doping type due to nitrogen dopants.
 - (b) Surface-enhanced Raman spectroscopy: The utilization of 2D materials as SERS substrates has attracted in recent years. Graphene has been the most researched 2D material as a SERS substrate, and few reports have discussed the utilization of NDG films as SERS substrates. The literature compares the graphene and NDG films' sensing ability and enhancement factor. The effect of the dopant configurations on the SERS behavior has not been addressed clearly. Here, we tried to address the doping effect on the sensing behavior of NDG films.

After establishing motivations, the major objectives of this study are given below:

- The synthesis of pristine graphene on copper using solid precursor PMMA is studied via CVD. We optimize the growth conditions, such as the evaporation temperature of PMMA, gas flow rate, growth time, and powder amount, to obtain continuous films. Low-temperature growth of graphene is to be investigated.
- Another objective is synthesizing nitrogen-doped graphene films using solid precursor
 phthalocyanines via CVD. The time-dependent and temperature-dependent growth of
 NDG is to be investigated. We try to control the dopant configuration as the growth time
 increases.
- Study the graphene's electronic properties to investigate the film's quality and compare it with existing literature. The effect of the nitrogen doping configuration on electronic properties is to be studied.
- SERS behavior of graphene and NDG films on organic dye molecules is investigated. The effect of the doping configuration on Raman enhancement will be studied.

2.9 References:

- [1] Clemons C B, Roberts M W, Wilber J P, Young G W, Buldum A and Quinn D D 2010 Continuum plate theory and atomistic modeling to find the flexural rigidity of a graphene sheet interacting with a substrate *J. Nanotechnol.* **2010**
- [2] Castro Neto A H, Guinea F, Peres N M R, Novoselov K S and Geim A K 2009 The electronic properties of graphene *Rev. Mod. Phys.* **81** 109–62
- [3] Wallace P.R. 1947 The Band Theory Of Graphite *Phys. Rev.* **71** 622–34
- [4] Ni Z H, Ponomarenko L A, Nair R R, Yang R, Anissimova S, Grigorieva I V., Schedin F, Blake P, Shen Z X, Hill E H, Novoselov K S and Geim A K 2010 On resonant scatterers as a factor limiting carrier mobility in graphene *Nano Lett.* **10** 3868–72
- [5] Mayorov A S, Gorbachev R V., Morozov S V., Britnell L, Jalil R, Ponomarenko L A, Blake P, Novoselov K S, Watanabe K, Taniguchi T and Geim A K 2011 Micrometer-scale ballistic transport in encapsulated graphene at room temperature *Nano Lett.* **11** 2396–9
- [6] Geim A K and Novoselov K S 2009 The rise of graphene *Nanosci. Technol. A Collect.*Rev. from Nat. Journals 11–9
- [7] Novoselov K S, Geim A K, Morozov S V., Jiang D, Katsnelson M I, Grigorieva I V., Dubonos S V. and Firsov A A 2005 Two-dimensional gas of massless Dirac fermions in graphene *Nature* **438** 197–200
- [8] Heersche H B, Jarillo-Herrero P, Oostinga J B, Vandersypen L M K and Morpurgo A F 2007 Bipolar supercurrent in graphene *Nature* **446** 56–9
- [9] Levendorf M P, Ruiz-Vargas C S, Garg S and Park J 2009 Transfer-free batch fabrication of single layer graphene transistors *Nano Lett.* **9** 4479–83
- [10] Zhu S E, Yuan S and Janssen G C A M 2014 Optical transmittance of multilayer graphene *Epl* **108** 1–4
- [11] Falkovsky L A 2008 Optical properties of graphene J. Phys. Conf. Ser. 129

- [12] Li X, Zhu Y, Cai W, Borysiak M, Han B, Chen D, Piner R D, Colomba L and Ruoff R S 2009 Transfer of large-area graphene films for high-performance transparent conductive electrodes *Nano Lett.* **9** 4359–63
- [13] Kobayashi T, Bando M, Kimura N, Shimizu K, Kadono K, Umezu N, Miyahara K, Hayazaki S, Nagai S, Mizuguchi Y, Murakami Y and Hobara D 2013 Production of a 100-m-long high-quality graphene transparent conductive film by roll-to-roll chemical vapor deposition and transfer process *Appl. Phys. Lett.* 102 1–5
- [14] Kim K S, Zhao Y, Jang H, Lee S Y, Kim J M, Kim K S, Ahn J H, Kim P, Choi J Y and Hong B H 2009 Large-scale pattern growth of graphene films for stretchable transparent electrodes *Nature* **457** 706–10
- [15] Frank I W, Tanenbaum D M, van der Zande A M and McEuen P L 2007 Mechanical properties of suspended graphene sheets *J. Vac. Sci. Technol. B Microelectron. Nanom. Struct.* **25** 2558
- [16] Lee C, Wei X, Kysar J W and Hone J 2008 of Monolayer Graphene *Science* (80-.). **321** 385–8
- [17] Reddy C D, Rajendran S and Liew K M 2006 Equilibrium configuration and continuum elastic properties of finite sized graphene *Nanotechnology* **17** 864–70
- [18] Ferrari A C, Bonaccorso F, Fal'ko V, Novoselov K S, Roche S, Bøggild P, Borini S, Koppens F H L, Palermo V, Pugno N, Garrido J A, Sordan R, Bianco A, Ballerini L, Prato M, Lidorikis E, Kivioja J, Marinelli C, Ryhänen T, Morpurgo A, Coleman J N, Nicolosi V, Colombo L, Fert A, Garcia-Hernandez M, Bachtold A, Schneider G F, Guinea F, Dekker C, Barbone M, Sun Z, Galiotis C, Grigorenko A N, Konstantatos G, Kis A, Katsnelson M, Vandersypen L, Loiseau A, Morandi V, Neumaier D, Treossi E, Pellegrini V, Polini M, Tredicucci A, Williams G M, Hee Hong B, Ahn J H, Min Kim J, Zirath H, Van Wees B J, Van Der Zant H, Occhipinti L, Di Matteo A, Kinloch I A, Seyller T, Quesnel E, Feng X, Teo K, Rupesinghe N, Hakonen P, Neil S R T, Tannock Q, Löfwander T and Kinaret J 2015 Science and technology roadmap for graphene, related two-dimensional crystals, and hybrid systems *Nanoscale* 7 4598–810

- [19] Kim K S, Zhao Y, Jang H, Lee S Y, Kim J M, Kim K S, Ahn J H, Kim P, Choi J Y and Hong B H 2009 Large-scale pattern growth of graphene films for stretchable transparent electrodes *Nature* **457** 706–10
- [20] Geng H Z, Ki K K, Kang P S, Young S L, Chang Y and Young H L 2007 Effect of acid treatment on carbon nanotube-based flexible transparent conducting films *J. Am. Chem. Soc.* **129** 7758–9
- [21] Pop E, Varshney V and Roy A K 2012 Thermal properties of graphene: Fundamentals and applications *MRS Bull.* **37** 1273–81
- [22] Anon symmetry constraints on phonon dispersion of graphene.pdf
- [23] Yu V 2010 Optics and Chemical Vapour Deposition of Graphene Monolayers on Various Substrates
- [24] Cançado L G, Jorio A, Ferreira E H M, Stavale F, Achete C A, Capaz R B, Moutinho M V O, Lombardo A, Kulmala T S and Ferrari A C 2011 Quantifying defects in graphene via Raman spectroscopy at different excitation energies *Nano Lett.* 11 3190–6
- [25] Ferrari A C, Meyer J C, Scardaci V, Casiraghi C, Lazzeri M, Mauri F, Piscanec S, Jiang D, Novoselov K S, Roth S and Geim A K 2006 Raman spectrum of graphene and graphene layers *Phys. Rev. Lett.* **97** 1–4
- [26] Ferrari A C 2007 Raman spectroscopy of graphene and graphite: Disorder, electron-phonon coupling, doping and nonadiabatic effects *Solid State Commun.* **143** 47–57
- [27] Ferrari A C and Basko D M 2013 Raman spectroscopy as a versatile tool for studying the properties of graphene *Nat. Nanotechnol.* **8** 235–46
- [28] Pisana S, Lazzeri M, Casiraghi C, Novoselov K S, Geim A K, Ferrari A C and Mauri F 2007 Breakdown of the adiabatic Born-Oppenheimer approximation in graphene *Nat. Mater.* 6 198–201
- [29] Yan J, Zhang Y, Kim P and Pinczuk A 2007 Electric field effect tuning of electronphonon coupling in graphene *Phys. Rev. Lett.* **98** 1–4

- [30] Balandin A A, Ghosh S, Bao W, Calizo I, Teweldebrhan D, Miao F and Lau C N 2008 Superior thermal conductivity of single-layer graphene *Nano Lett.* **8** 902–7
- [31] Calizo I, Balandin A A, Bao W, Miao F and Lau C N 2007 Temperature dependence of the raman spectra of graphene and graphene multilayers *Nano Lett.* **7** 2645–9
- [32] Seol J H, Jo I, Moore A L, Lindsay L, Aitken Z H, Pettes M T, Li X, Yao Z, Huang R, Broido D, Mingo N, Ruoff R S and Shi L 2010 Two-dimensional phonon transport in supported graphene *Science* (80-.). **328** 213–6
- [33] K. S. Novoselov et al 2016 Electric Field Effect in Atomically Thin Carbon Films **306** 666–9
- [34] Sahu S and Rout G C 2017 Band gap opening in graphene: a short theoretical study *Int. Nano Lett.* **7** 81–9
- [35] Wei D, Liu Y, Wang Y, Zhang H, Huang L and Yu G 2009 Synthesis of n-doped graphene by chemical vapor deposition and its electrical properties *Nano Lett.* **9** 1752–8
- [36] Chen Q, Ma L and Wang J 2016 Making graphene nanoribbons: A theoretical exploration *Wiley Interdiscip. Rev. Comput. Mol. Sci.* **6** 243–54
- [37] Jariwala D, Srivastava A and Ajayan P M 2011 Graphene synthesis and band gap opening *J. Nanosci. Nanotechnol.* **11** 6621–41
- [38] Zhang Y, Tang T T, Girit C, Hao Z, Martin M C, Zettl A, Crommie M F, Shen Y R and Wang F 2009 Direct observation of a widely tunable bandgap in bilayer graphene *Nature* **459** 820–3
- [39] Havener R W, Zhuang H, Brown L, Hennig R G and Park J 2012 Angle-resolved raman imaging of interlayer rotations and interactions in twisted bilayer graphene *Nano Lett.* **12** 3162–7
- [40] Kawasaki T, Ichimura T, Kishimoto H, Akbar A A, Ogawa T and Oshima C 2002 Double atomic layers of graphene/monolayer h-BN on Ni(111) studied by scanning tunneling microscopy and scanning tunneling spectroscopy *Surf. Rev. Lett.* **9** 1459–64

- [41] Ullah S, Shi Q, Zhou J, Yang X, Ta H Q, Hasan M, Ahmad N M, Fu L, Bachmatiuk A and Rümmeli M H 2020 Advances and Trends in Chemically Doped Graphene *Adv. Mater. Interfaces* 7 1–23
- [42] Pereira V M, Nilsson J and Castro Neto A H 2007 Coulomb impurity problem in graphene *Phys. Rev. Lett.* **99** 2–5
- [43] Zheng B, Hermet P and Henrard L 2010 Scanning tunneling microscopy simulations of nitrogen- and boron-doped graphene and single-walled carbon nanotubes *ACS Nano* **4** 4165–73
- [44] Wang H, Maiyalagan T and Wang X 2012 Review on recent progress in nitrogen-doped graphene: Synthesis, characterization, and its potential applications *ACS Catal.* **2** 781–94
- [45] Usachov D, Vilkov O, Grüneis A, Haberer D, Fedorov A, Adamchuk V K, Preobrajenski A B, Dudin P, Barinov A, Oehzelt M, Laubschat C and Vyalikh D V. 2011 Nitrogendoped graphene: Efficient growth, structure, and electronic properties *Nano Lett.* 11 5401–7
- [46] Haberer D, Fedorov A and Adamchuk V K 2011 Nitrogen-Doped Graphene: Efficient Growth, Structure, and Electronic Properties 5401–7
- [47] Granzier-Nakajima T, Fujisawa K, Anil V, Terrones M and Yeh Y T 2019 Controlling nitrogen doping in graphene with atomic precision: Synthesis and characterization *Nanomaterials* **9** 1–18
- [48] Lu Y F, Lo S T, Lin J C, Zhang W, Lu J Y, Liu F H, Tseng C M, Lee Y H, Liang C Te and Li L J 2013 Nitrogen-doped graphene sheets grown by chemical vapor deposition:

 Synthesis and influence of nitrogen impurities on carrier transport *ACS Nano* **7** 6522–32
- [49] Son M, Chee S S, Kim S Y, Lee W, Kim Y H, Oh B Y, Hwang J Y, Lee B H and Ham M H 2020 High-quality nitrogen-doped graphene films synthesized from pyridine via two-step chemical vapor deposition *Carbon N. Y.* **159** 579–85
- [50] Gao H, Song L, Guo W, Huang L, Yang D, Wang F, Zuo Y, Fan X, Liu Z, Gao W, Vajtai R, Hackenberg K and Ajayan P M 2012 A simple method to synthesize continuous large

- area nitrogen-doped graphene Carbon N. Y. 50 4476–82
- [51] Capasso A, Dikonimos T, Sarto F, Tamburrano A, De Bellis G, Sarto M S, Faggio G, Malara A, Messina G and Lisi N 2015 Nitrogen-doped graphene films from chemical vapor deposition of pyridine: Influence of process parameters on the electrical and optical properties *Beilstein J. Nanotechnol.* 6 2028–38
- [52] Lin L, Li J, Yuan Q, Li Q, Zhang J, Sun L, Rui D, Chen Z, Jia K, Wang M, Zhang Y, Rummeli M H, Kang N, Xu H Q, Ding F, Peng H and Liu Z 2019 Nitrogen cluster doping for high-mobility/conductivity graphene films with millimeter-sized domains *Sci. Adv.* 5
- [53] Ikram R, Jan B M, Pervez S A, Papadakis V M, Ahmad W, Bushra R, Kenanakis G and Rana M 2020 Recent advancements of n-doped graphene for rechargeable batteries: A review *Crystals* **10** 1–27
- [54] Jeong H M, Lee J W, Shin W H, Choi Y J, Shin H J, Kang J K and Choi J W 2011 Nitrogen-doped graphene for high-performance ultracapacitors and the importance of nitrogen-doped sites at basal planes *Nano Lett.* **11** 2472–7
- [55] Ghany N A A, Elsherif S A and Handal H T 2017 Revolution of Graphene for different applications: State-of-the-art *Surfaces and Interfaces* **9** 93–106
- [56] Huang G, Jiang P, Zhang X, Zhou C, Zhou J, Huang Y, Yang P, Yang L, Tian X and Hao Y 2022 Efficient preparation and characterization of graphene based on ball milling *Diam*. *Relat. Mater.* **130**
- [57] Feng C, Zhu D, Wang Y and Jin S 2020 Electromechanical behaviors of graphene reinforced polymer composites: A review *Materials (Basel)*. **13**
- [58] Kumar N, Salehiyan R, Chauke V, Joseph Botlhoko O, Setshedi K, Scriba M, Masukume M and Sinha Ray S 2021 Top-down synthesis of graphene: A comprehensive review FlatChem 27 100224
- [59] Muzyka R, Kwoka M, Smędowski Ł, Díez N and Gryglewicz G 2017 Oxidation of graphite by different modified Hummers methods *Xinxing Tan Cailiao/New Carbon Mater.* 32 15–20

- [60] Virojanadara C, Zakharov A A, Yakimova R and Johansson L I 2010 Buffer layer free large area bi-layer graphene on SiC(0 0 0 1) *Surf. Sci.* **604** L4
- [61] Johansson L I, Watcharinyanon S, Zakharov A A, Iakimov T, Yakimova R and Virojanadara C 2011 Stacking of adjacent graphene layers grown on C-face SiC *Phys. Rev. B Condens. Matter Mater. Phys.* **84** 1–8
- [62] Robinson J A, Hollander M, Labella M, Trumbull K A, Cavalero R and Snyder D W 2011 Epitaxial graphene transistors: Enhancing performance via hydrogen intercalation *Nano Lett.* 11 3875–80
- [63] Pallecchi E, Lafont F, Cavaliere V, Schopfer F, Mailly D, Poirier W and Ouerghi A 2014 High electron mobility in epitaxial graphene on 4H-SiC(0001) via post-growth annealing under hydrogen *Sci. Rep.* **4** 1–7
- [64] Abderrazak H and Hadj Hmi E S B 2011 Silicon Carbide: Synthesis and Properties *Prop. Appl. Silicon Carbide*
- [65] Campbell S A and Smith R C 2003 Chemical vapour deposition *High-K Gate Dielectr*. **0123456789** 65–88
- [66] Bae S, Kim H, Lee Y, Xu X, Park J S, Zheng Y, Balakrishnan J, Lei T, Ri Kim H, Song Y II, Kim Y J, Kim K S, Özyilmaz B, Ahn J H, Hong B H and Iijima S 2010 Roll-to-roll production of 30-inch graphene films for transparent electrodes *Nat. Nanotechnol.* **5** 574–8
- [67] Saeed M, Alshammari Y, Majeed S A and Al-Nasrallah E 2020 Chemical Vapour Deposition of Graphene—Synthesis, Characterisation, and Applications: A Review *Molecules* **25**
- [68] Shi Q, Tokarska K, Ta H Q, Yang X, Liu Y, Ullah S, Liu L, Trzebicka B, Bachmatiuk A, Sun J, Fu L, Liu Z and Rümmeli M H 2020 Substrate Developments for the Chemical Vapor Deposition Synthesis of Graphene *Adv. Mater. Interfaces* **7**
- [69] Sun J, Lindvall N, Cole M T, Angel K T T, Wang T, Teo K B K, Chua D H C, Liu J and Yurgens A 2012 Low partial pressure chemical vapor deposition of graphene on copper

- IEEE Trans. Nanotechnol. 11 255–60
- [70] Liu L, Zhou H, Cheng R, Chen Y, Lin Y C, Qu Y, Bai J, Ivanov I A, Liu G, Huang Y and Duan X 2012 A systematic study of atmospheric pressure chemical vapor deposition growth of large-area monolayer graphene *J. Mater. Chem.* **22** 1498–503
- [71] Gao L, Ren W, Zhao J, Ma L P, Chen Z and Cheng H M 2010 Efficient growth of high-quality graphene films on Cu foils by ambient pressure chemical vapor deposition *Appl. Phys. Lett.* **97** 1–4
- [72] Liu W, Li H, Xu C, Khatami Y and Banerjee K 2011 Synthesis of high-quality monolayer and bilayer graphene on copper using chemical vapor deposition *Carbon N. Y.* **49** 4122–30
- [73] N'Diaye A T, Bleikamp S, Feibelman P J and Michely T 2006 Two-dimensional Ir cluster lattice on a graphene moiré on Ir(111) *Phys. Rev. Lett.* **97** 1–4
- [74] Sutter P, Sadowski J T and Sutter E 2009 Graphene on Pt(111): Growth and substrate interaction *Phys. Rev. B Condens. Matter Mater. Phys.* **80** 1–10
- [75] Sung C M and Tai M F 1997 Reactivities of Transition Metals with Carbon: Implications to the Mechanism of Diamond Synthesis Under High Pressure *Int. J. Refract. Met. Hard Mater.* **15** 237–56
- [76] Li X, Cai W, Colombo L and Ruoff R S 2009 Evolution of graphene growth on Ni and Cu by carbon isotope labeling *Nano Lett.* **9** 4268–72
- [77] Xu Y, Liu J, Zuo C, Cai H, Wu P, Huang Z, Lai F, Lin L, Zheng W and Qu Y 2019 The Role of Hydrogen on the Growth of Graphene Nanostructure Using a Two-Step Method *J. Nanosci. Nanotechnol.* **19** 7294–300
- [78] Li X, Magnuson C W, Venugopal A, Tromp R M, Hannon J B, Vogel E M, Colombo L and Ruoff R S 2011 Large-area graphene single crystals grown by low-pressure chemical vapor deposition of methane on copper *J. Am. Chem. Soc.* **133** 2816–9
- [79] Li Z, Wu P, Wang C, Fan X, Zhang W, Zhai X, Zeng C, Li Z, Yang J and Hou J 2011

- Low-temperature growth of graphene by chemical vapor deposition using solid and liquid carbon sources *ACS Nano* **5** 3385–90
- [80] Sun Z, Yan Z, Yao J, Beitler E, Zhu Y and Tour J M 2010 Growth of graphene from solid carbon sources *Nature* **468** 549–52
- [81] Yan Y, Nashath F Z, Chen S, Manickam S, Lim S S, Zhao H, Lester E, Wu T and Pang C H 2020 Synthesis of graphene: Potential carbon precursors and approaches *Nanotechnol*. *Rev.* 9 1284–314
- [82] Polsen E S, McNerny D Q, Viswanath B, Pattinson S W and John Hart A 2015 High-speed roll-to-roll manufacturing of graphene using a concentric tube CVD reactor *Sci. Rep.* **5** 1–12
- [83] Banszerus L, Schmitz M, Engels S, Dauber J, Oellers M, Haupt F, Watanabe K, Taniguchi T, Beschoten B and Stampfer C 2015 Ultrahigh-mobility graphene devices from chemical vapor deposition on reusable copper *Sci. Adv.* **1** 1–7
- [84] Lee G H, Cooper R C, An S J, Lee S, Van Der Zande A, Petrone N, Hammerberg A G, Lee C, Crawford B, Oliver W, Kysar J W and Hone J 2013 High-strength chemical-vapor-deposited graphene and grain boundaries *Science* (80-.). **340** 1074–6
- [85] Hao Y, Bharathi M S, Wang L, Liu Y, Chen H, Nie S, Wang X, Chou H, Tan C, Fallahazad B, Ramanarayan H, Magnuson C W, Tutuc E, Yakobson B I, McCarty K F, Zhang Y W, Kim P, Hone J, Colombo L and Ruoff R S 2013 The role of surface oxygen in the growth of large single-crystal graphene on copper *Science* (80-.). **342** 720–3
- [86] Deokar G, Jin J, Schwingenschlögl U and Costa P M F J 2022 Chemical vapor deposition-grown nitrogen-doped graphene's synthesis, characterization and applications *npj 2D Mater. Appl.* **6** 1–17
- [87] Plutnar J, Pumera M and Sofer Z 2018 The chemistry of CVD graphene *J. Mater. Chem. C* **6** 6082–101
- [88] Imamura G and Saiki K 2011 Synthesis of nitrogen-doped graphene on Pt(111) by chemical vapor deposition *J. Phys. Chem. C* **115** 10000–5

- [89] Krsihna B V, Ravi S and Prakash M D 2021 Recent developments in graphene based field effect transistors *Mater. Today Proc.* **45** 1524–8
- [90] Choi W, Lahiri I, Seelaboyina R and Kang Y S 2010 Synthesis of graphene and its applications: A review *Crit. Rev. Solid State Mater. Sci.* **35** 52–71
- [91] Schwierz F 2010 Graphene transistors *Nat. Nanotechnol.* **5** 487–96
- [92] Shautsova V, Gilbertson A M, Black N C G, Maier S A and Cohen L F 2016 Hexagonal Boron Nitride assisted transfer and encapsulation of large area CVD graphene *Sci. Rep.* 6 1–8
- [93] Malesevic A, Kemps R, Vanhulsel A, Chowdhury M P, Volodin A and Van Haesendonck C 2008 Field emission from vertically aligned few-layer graphene *J. Appl. Phys.* **104** 1–6
- [94] Xu Y and Liu J 2016 Graphene as Transparent Electrodes: Fabrication and New Emerging Applications *Small* **12** 1400–19
- [95] Wang X, Zhi L and Müllen K 2008 Transparent, conductive graphene electrodes for dyesensitized solar cells *Nano Lett.* **8** 323–7
- [96] Bonaccorso F, Sun Z, Hasan T and Ferrari A C 2010 Graphene photonics and optoelectronics *Nat. Photonics* **4** 611–22
- [97] Ko G, Kim H Y, Ahn J, Park Y M, Lee K Y and Kim J 2010 Graphene-based nitrogen dioxide gas sensors *Curr. Appl. Phys.* **10** 1002–4
- [98] Bhatt M D and O'Dwyer C 2015 Recent progress in theoretical and computational investigations of Li-ion battery materials and electrolytes *Phys. Chem. Chem. Phys.* **17** 4799–844
- [99] Schedin F, Geim A K, Morozov S V., Hill E W, Blake P, Katsnelson M I and Novoselov K S 2007 Detection of individual gas molecules adsorbed on graphene *Nat. Mater.* **6** 652–5
- [100] Mazar Atabaki M and Kovacevic R 2013 Graphene composites as anode materials in lithium-ion batteries *Electron. Mater. Lett.* **9** 133–53

- [101] Leela A, Reddy M, Srivastava A, Gowda S R, Gullapalli H, Dubey M and Ajayan P M 2010 Synthesis Of Nitrogen-Doped Graphene **4** 6337–42
- [102] Share K, Cohn A P, Carter R, Rogers B and Pint C L 2016 Role of Nitrogen-Doped Graphene for Improved High-Capacity Potassium Ion Battery Anodes ACS Nano 10 9738–44
- [103] Wu X, Chen Y, Xing Z, Lam C W K, Pang S S, Zhang W and Ju Z 2019 Advanced Carbon-Based Anodes for Potassium-Ion Batteries *Adv. Energy Mater.* **9** 1–46
- [104] Xia J, Chen F, Li J and Tao N 2009 Measurement of the quantum capacitance of graphene *Nat. Nanotechnol.* **4** 505–9
- [105] El-Gendy D M, Ghany N A A, El Sherbini E E F and Allam N K 2017 Adenine-functionalized Spongy Graphene for Green and High-Performance Supercapacitors *Sci. Rep.* **7** 1–10
- [106] Kou J, Zhou X, Lu H, Wu F and Fan J 2014 Graphyne as the membrane for water desalination *Nanoscale* **6** 1865–70
- [107] Lai H, Xu F, Zhang Y and Wang L 2018 Recent progress on graphene-based substrates for surface-enhanced Raman scattering applications *J. Mater. Chem. B* **6** 4008–28
- [108] Feng S, Cristina dos Santos M, Carvalho B R, Lv R, Li Q, Fujisawa K, Elías A L, Lei Y, Perea-López N, Endo M, Pan M, Pimenta M A and Terrones M 2016 Ultrasensitive molecular sensor using N-doped graphene through enhanced Raman scattering *Sci. Adv.* 2 1–13

Chapter-3

Experimental Methods & Characterization techniques

This chapter introduces the details of the experimental protocols and characterization techniques used during the research work. Basic working principles of the synthesis methods and characterization techniques and their instrumentation are discussed briefly in this chapter. The first section of the chapter deals with the synthesis, and the second section is dedicated to the characterization tools.

3.1. Synthesis and Device Fabrication

3.1.1 Cleaning & Electropolishing of Copper (Cu) foil

Cleaning of copper: Copper is utilized as a substrate for graphene synthesis. Cleaning of the Cu foil plays a key role as the graphene synthesis strongly depends on the substrate surface properties. The Cu foil was purchased from Alfa Aesar (99.8 %, 25 µm thick). The 4 cm x 4 cm Cu foil was cut and cleaned with diluted (6.9%) nitric acid (HNO₃) for 25 seconds to remove the impurity particles and surface native oxide layers [1]. The reaction between the HNO₃ and Cu is given in equation 3.1.1.

$$Cu(s)+4HNO_3(aq) \rightarrow Cu(NO_3)_2(aq) + 2NO_2(g) + 2H_2O$$
 Eq 3.1.1

The reaction demonstrates that as the reaction takes place, the copper's surface is oxidized and dissolved in the solution. Simultaneously, the nitrogen dioxide (NO₂) gas is generated violently, pushing away the impurity particles from the surface. The original copper surface is removed in this way to obtain a newly cleaned surface, but it is found to be very rough. The roughness increased due to the etching of the Cu surface. The substrate was washed in deionized water (DIW) in order to eliminate the residual impurities that were left on the copper. These foils were subjected to electropolishing to reduce the surface roughness further.

Electropolishing of Copper: Electropolishing is an electrochemical process that requires an electrolyte and Direct (DC) current. When the current is applied, the high points of rough surfaces and burr areas hold a high current which dissolves at a greater rate than the rest of the surfaces. In

this way, the surface becomes smoother or deburring. While this process occurs, the oxygen gas is generated from the anode and the hydrogen from the cathode. Electropolishing occurs for a certain range of the voltage, as shown in figure 3.1, where a proper balance is required between the voltage and the current density [2]. When the current density enhances too high, the etching of the valleys and peaks of the metal surfaces occurs, resulting in pitting and gas evolution. The etching occurs for the low current density, resulting in the surface's uneven removal.

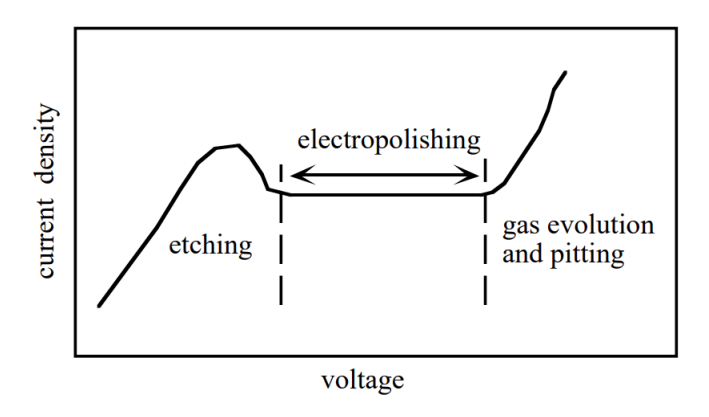


Figure 3.1 The relationship between voltage and current density.

A homemade electrochemical cell was used for electropolishing. The cleaned two copper foils are utilized as electrodes as anode and cathode, in which the anode is the working electrode, and the other is the counter electrode. The electrolyte solution is a mixture of 40 ml of orthophosphoric acid (H₃PO₄ 85%), and 10 ml of isopropyl alcohol (IPA 99%) is used for electropolishing [3]. Copper foils were placed in the solution with the support of alligator clips. A Keithley source meter is used for supplying the voltage/current. The voltage range of 1.5 V - 2.0 V was applied for 30 minutes. The electropolished copper foils were cleaned in DIW twice, rinsed in the Acetone, IPA, and DIW, and blown with nitrogen gas.

3.1.2 Synthesis Technique:

Pristine Graphene (PG) and Nitrogen Doped Graphene (NDG) have been synthesized using a chemical vapor deposition method.

Chemical Vapor Deposition (CVD): Chemical Vapor deposition is one of the key technologies in semiconductor processing [4]. It is a synthesis technique for depositing a solid film by the chemical components that react in the vapor phase next to or on a heated substrate. It is a bottom-

up approach where the film is prepared from atoms or molecules. The precursors are the volatile compounds used as a source for target material for deposition. The precursors are evaporated/sublimated at elevated temperatures. The carrier gases transport the evaporated reactant species towards the substrate, which is already set to the desired temperature. These reactant species diffuse through the boundary layer above the substrate. The species are transported to the surface via diffusion, and a chemical reaction occurs on or above the surface through adsorption or chemisorption, pyrolysis, disproportionation, oxidation, etc. [5]. The film deposition takes place after the chemical reaction. The byproducts that have been generated are diffused away from the substrate through the boundary layer.

All chemical reactions and precursor evaporation do not occur at room temperature. Hence some amount of energy is required to raise the temperature. The furnaces are used for raising the temperature and maintaining the constant heat. The high temperature at the substrate helps in breaking the precursor molecule's bonds into reactant species, and also it increases diffusion for the adsorbents on the substrate's surface, which enhances the wettability of the film. Constant feeding of the mass transport, constant heating zone at the substrate, and the proper venting of the byproducts are the minimum conditions for achieving the homogeneous and continuous film.

The processing parameters that affect the growth of a film in CVD include temperature, pressure, precursor type, flow rate, substrate/wall temperature, activation manner, and depositing time. CVD systems are categorized into seven main types of CVDs using these process parameters shown in figure 3.2. This figure shows the classification of CVD systems. It can be observed that there are 21 types of CVDs are there together. Some of the popular CVDs used for graphene growth shall be discussed here.

Low-pressure CVD (LPCVD): The Pressure in the CVD lies in the order of 10⁻³ mbar. This pressure is created by the rotary pump connecting the exhaust side of the furnace tube and another side, the precursors and carrier gases entry will be there.

Atmospheric pressure CVD (APCVD): The CVD is operated at the ambient pressure. The cost of the APCVD equipment is low compared to the LPCVD as it is not required any vacuum pumps to create a vacuum. The mean free path for the reactive species is less in APCVD compared to the

LPCVD. The limitation of the APCVD is that it is more susceptible to oxidation because of the greater gas density and ambient pressure working conditions [6].

Plasma Enhanced CVD (PECVD): This CVD comes under the activation manner/activation energy. It is similar to the LPCVD, where the molecule's chemical bonds are dissociated into reactive species using heat energy, but in PECVD, the plasma is used to break down the molecules. In PECVD, the plasma is used as activation energy besides heat energy reduces the reaction temperature. In this way, the PECVD is used to grow films at low temperatures.

Metal-organic CVD (MOCVD): This CVD comes under the nature of the precursor used for the coating of the film. In this MOCVD, the precursor is metal-organic compound which means that the organic molecules comprise metal atoms in addition to the organic ligands. The advantage of using metal-organic precursors is that the evaporation temperature of precursors can be decreased. In CVD, using the metals as precursors and their evaporation is not possible because of their high melting points for depositing the films. Thus, metal-organic compounds are suitable candidates for evaporation as they are volatile compounds.

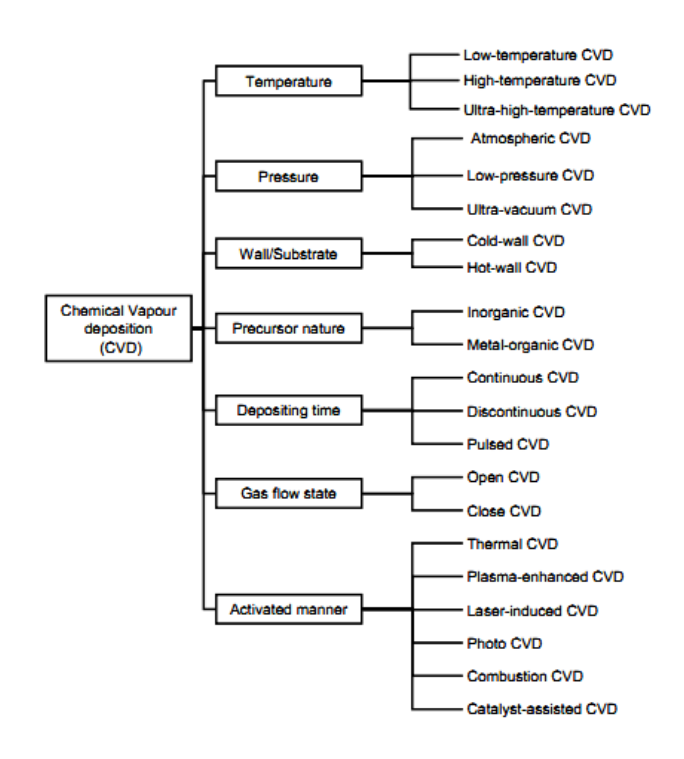


Figure 3.2 classification of Chemical Vapor deposition systems [7].

PG and NDG have been synthesized by using a homemade atmospheric pressure chemical vapor deposition system. The schematics of APCVD are shown in figure 3.3 for the growth of PG and NDG. The precursors used are polymethyl methacrylate (PMMA) and phthalocyanine (Pc) or copper Phthalocyanine (CuPc) molecules for the growth of PG and NDG, respectively. APCVD equipment consists of a furnace, quartz tube, flanges, gas connections, mass flow controllers, control valves, and gas cylinders.

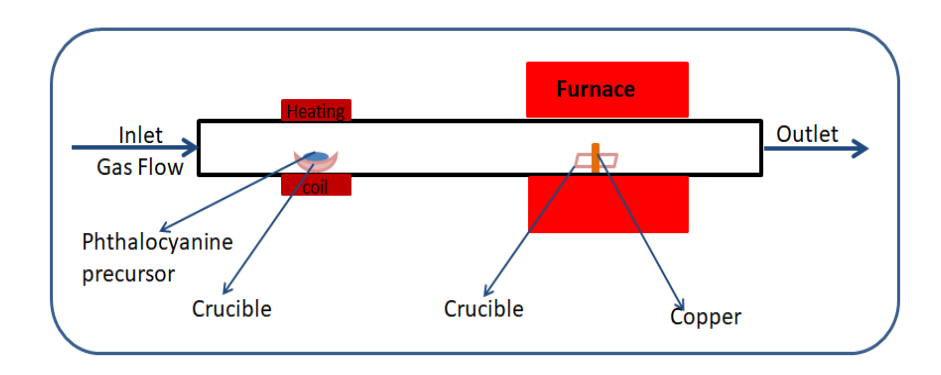


Figure 3.3 Schematics of the APCVD used for PG and NDG synthesis.

MTI single zone sliding furnace was used. The dimensions of the quartz tube used for the growth are 100 cm in length and 60 mm in diameter. The ends of the tube are sealed with stainless steel flanges which were connected to the stainless steel gas pipelines. Mass flow controllers were attached between these connections to control the gas flow rate. An electropolished 2.5 cm x 1 cm copper substrate was kept on the alumina crucible and placed in the quartz tube at the center of the furnace, where the constant heating zone exists. The placing of the copper is perpendicular to the line of gas flow, as shown in the schematics. In this configuration, most of the area of the copper substrate attains the 111 plane orientation. In order to evaporate the precursor, a nichrome heating tape was wound around the quartz tube at 40 cm upstream from the center of the furnace (where the Cu sample was kept), as illustrated in the schematics. It was connected to a variac and temperature controller for controlling the heat and temperature, respectively. The precursor powder was placed inside the quartz tube, where the position lies at the center of the heating tape. The PMMA and Pc or CuPc were sublimated/evaporated in the range of 400- 250 °C and 525-545 °C, respectively. In order to get rid of the oxides in the quartz tube, the system was purged

with 200 SCCM of argon gas for 30 minutes at room temperature (RT) before the experiment started. Then, the temperature was increased to 1050 °C at a ramp rate of 8°C/min in the presence of at same flow rate. 200 SCCM of Ar: H₂ gas mixture (90:10) was introduced, and argon was stopped once the temperature reached 1050 °C, and the substrate was annealed for 30 minutes. The different flow rates and growth time were used for the PG and NDG growth. Ar gas was introduced in place of the Ar:H2 gas flow after the growth process was finished, and it has been flowed at a rate of 50 SCCM as the system cooled naturally. The as-grown samples were taken outside the furnace after cooling to room temperature.

3.1.3 Transferring the graphene onto target substrates:

Graphene growth using CVD on metallic substrates such as copper and nickel produces good quality, uniformity, and controllability, which is not observed for the dielectric substrates. This limitation requires transferring graphene onto destination substrates for further characterization, physical property measurements, and applications.

CVD graphene transfer can be broadly classified into two categories dry and wet transfer methods depending on the environment where graphene comes in contact with the target substrate [8]. The dry or wet transfer methods are determined by the process in which how the graphene is released onto the target substrate. In the wet transfer method, the supporting polymer layer assisted to the graphene is removed in a solvent to avoid mechanical damage to the graphene film. In the dry transfer method, the removal of the supporting layer can be executed by the differences in adhesion forces between the interfaces of polymer/graphene and graphene/substrate [9]. The wet transfer method in which PMMA-mediated transfer has been used during my research work.

The graphene can not self-support because of its thinness. Therefore, the graphene usually needs a supporting layer when the transfer is required from as grown substrate to the destination substrate. The polymers are used widely as a supporting layer because of their ability in self-supporting, strong adhesion between graphene and transfer medium, good chemical stability, and ease of being completely removed after transfer.

In the PMMA-mediated transfer, the PMMA is used as a supporting layer. The drawing of the transfer of process is shown in figure 3.4. The transfer process contains the following steps [10].

- 1. Spin coating/drop-casting of PMMA on the graphene surface and curing it at moderate temperature.
- 2. Removing the unwanted graphene grown on the copper's backside surface is usually done in Hcl or using oxygen plasma.
- 3. Etching the copper foil using copper etchants such as Ferri chloride, ammonium persulfate, etc.
- 4. Washing the PMMA/graphene in DIW multiple times and then transferring it onto the target substrate.
- 5. Dissolving the PMMA in organic solvents such as acetone.

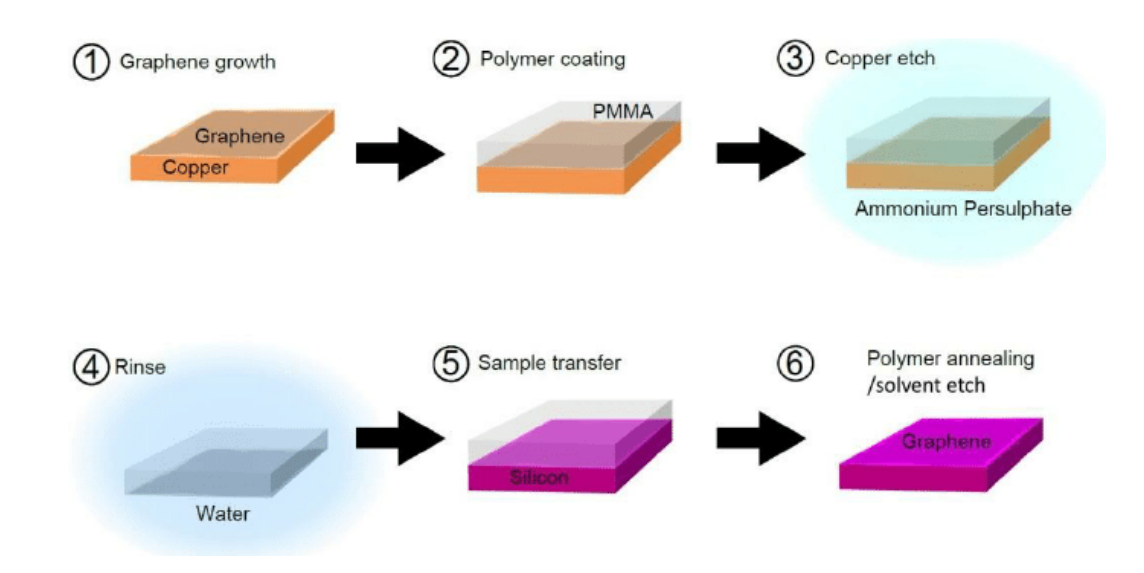


Figure 3.4 The representative is drawing for the transfer process using PMMA [11].

Similar steps have been used in transferring the PG and NDG onto $SiO_2(300 \text{ nm})/Si$ and quartz. $1\text{cm} \times 1\text{cm}$ film was cut from the as-grown graphene/Cu. The graphene was coated with 2ul of 1% solution of polymethyl methacrylate (PMMA) prepared in anisole, making sure that the PMMA covered the entire area of the film. To dry the PMMA, it was baked for five minutes on a hot plate. The PMMA/graphene/Cu was immersed in iron chloride or ammonium persulfate solution to etch the copper. The PMMA/graphene was transferred into the DIW twice after etching the copper in order to get rid of the FeCl₃ ions. Acetone, IPA, and DIW were used to clean the $SiO_2(300\text{nm})/Si$ substrate for 15 minutes each by ultra-sonication. The PMMA/graphene film was transferred onto the SiO_2 substrate followed by dring for 12hours. After this,

PMMA/graphene/SiO₂ was immersed in hot acetone (60 °C) for 2 hours to remove the PMMA from the film.

3.1.4 Device Fabrication:

The devices were fabricated using laser lithography. Lithography is the process by which patterns with different shapes and dimensions are transferred onto the wafer. Different lithographic methods are available depending on the radiation used for exposure, such as optical, e-beam, soft, ion beam, and x-ray lithography. The main component of any lithography process is a photoresist. It is a photosensitive material that changes its physical properties when it is exposed to light. Depending on whether it undergoes polymerization or depolymerization, the photoresist is classified as either positive or negative.

In the laser lithography process, we used the positive photoresist. The schematics of the laser lithography process are shown in figure 3.5. The photoresist was spin coated on the substrate. Then, the substrate was baked at 100 °C to polymerize the photoresist. The UV laser having a 365 nm wavelength was used to write the desired pattern on the polymer. The exposed region of the polymer has been depolymerized in that particular pattern. These substrates were immersed in the developer to remove the polymer from exposed regions, resulting in expected patterns. After this step, the substrates were deposited with metals using a thermal evaporator. Then, the substrates were dipped in acetone to lift off, forming metal patterns on the substrate.

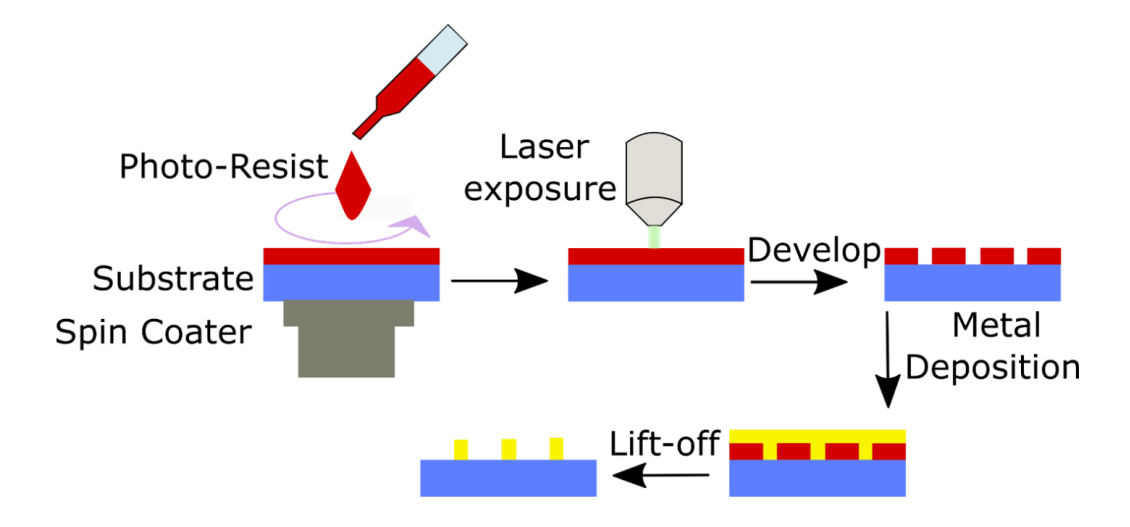


Figure 3.5 The flow of the process for the laser lithography [26].

3.2 Characterization techniques:

The raw materials and synthesized products must be characterized with microscopic and spectroscopic techniques to gain insight into the material's properties. No technique can give complete information about any system's chemical composition, crystal structure, and physical properties. Henceforth, we must use alternative and complementary techniques to get sufficient and supporting information about the characteristics of the synthesized materials, respectively.

Here, we employed various characterization techniques such as optical microscopy, micro Raman spectroscopy, Field Emission Scanning Electron Microscopy (FESEM), X-ray Photo Electron Spectroscopy (XPS), Atomic Force Microscopy (AFM), and Transmission Electron Microscopy (TEM), Electron Backscattered Diffraction (EBSD), X-ray Diffraction (XRD) for structural and physicochemical properties. The basic concepts of these characterization techniques are briefed in this section.

3.2.1. Optical Microscope:

The optical microscope has become an essential tool for examining the microstructure of various material systems besides biological systems since the 19th century. The basic principle of an optical microscope is the formation of a magnified image of a specimen by using an objective lens, and the image which formed is further viewed through the eyepiece. It can be understood in detail by invoking the optical principles of image formation, resolution, magnification, and contrast.

The image formation can be explained through a ray diagram, as shown in figure 3.6. An object (specimen) is kept between the focal length and radius of curvature of an objective lens, at position A shown in figure 3.6. The light rays from an object travel to the objective (first) lens at which these rays converge and focus onto position B, where it forms a magnified, real and inverted image. The image formed at position B acts as an object for the projector (second) lens. The rays from this object pass to the second lens further converge and give rise to the finally further magnified real image at position C. The image is formed at position C, where the camera film or screen will be kept for recording images. In an optical microscope, when we observe the microstructures with

our eyes through the eyepiece, the light path will go through an eyepiece instead of a second lens. These rays will form a virtual image on the retina of a human eye. The virtual image is adjusted at a minimum distance of 25 cm from the eyepiece, which comes under the eye's optimal focal length. The virtual image is inverted and magnified to the object.

Magnification is defined as the size of the image compared to the size of an object. It is taken as the ratio of image size to the size of an object. By applying linear optics, we can obtain a magnification (M) of the convergent lens as shown in equation 3.2.1

$$M = \frac{v - f}{f}$$
 Eq 3.2.1

Where v is image distance from the lens and f is the lens's focal length. From the above equation, it can be deduced that the focal length should be shorter for higher magnification. The total magnification is taken as the product of the two respective magnifications of an objective lens and projector lens, as shown in equation 3.2.2

$$M = M_1 M_2 = \frac{(v_1 - f_1)(v_2 - f_2)}{f_1 f_2}$$
 Eq-3.2.2

where subscripts 1 and 2 represent the objective lens and projector lens. When an object is observed through an eyepiece, the total magnification becomes the eyepiece's magnification multiplied with the magnification of an objective lens in place of the projector lens's magnification.

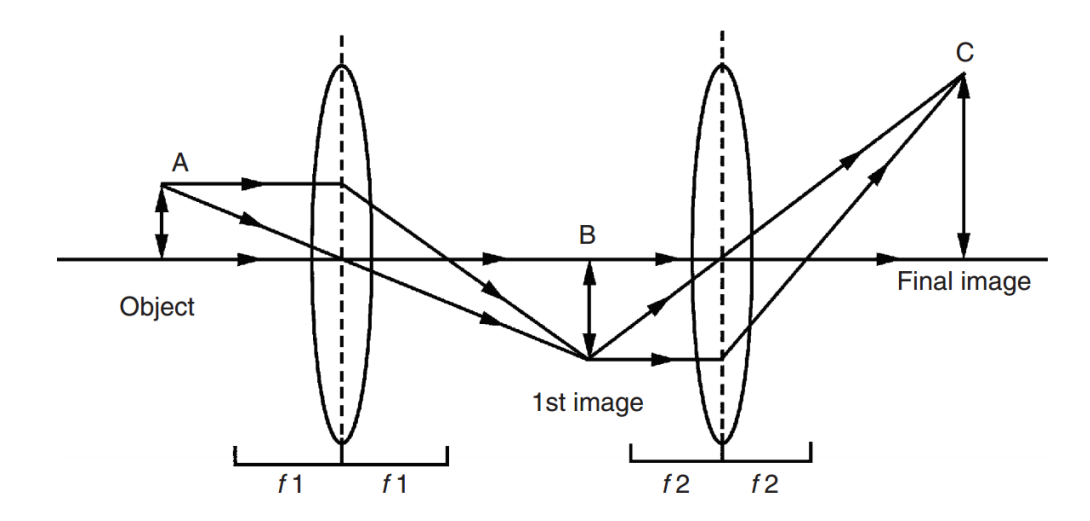


Figure 3.6 principles of magnification of an optical microscope [12].

Eq-3.2.2 indicates there is no limitation for the magnification of an optical microscope, but in reality, meaningful magnification is achieved when the magnified image is adequately resolved. It implies that the resolution limits the magnification of a microscope. The resolution is defined as the two closed points visibly distinguished as two separate points with a minimum distance. The diffraction of the light controls the resolution. An optical microscope's resolution (R) is given by equation 3.2.3

$$R = \frac{0.6\lambda}{\mu \sin \alpha}$$
 Eq-3.2.3

Where λ is the wavelength of the light, μ is the refractive index of the medium between the objective lens and specimen, and the α is the semi-angle of the light cone that has formed while entering the objective lens. The product of μ and $\sin\alpha$ defines as the numerical aperture (NA). It is inferred from equation 1.3 that the high resolution is achieved by increasing the numerical aperture and using the shorter wavelength of light.

The microscope requires to produce sufficient contrast and brightness from the specimen to look into the microscale features. It is essential at any magnification for viewing microscale objects. The brightness defines the light intensity, which depends on the numerical aperture and magnification. The contrast refers to the difference between the background intensity and the object's intensity.

Graphene visibility under an optical microscope is appreciated for the optical interference of the wavelength between the graphene and the underlying substrate SiO₂/Si. We all know that the appearance of SiO₂ film's color grown on Si quantifies its thickness is attributed to the interference between the two optical paths that emerged from air to SiO₂ and SiO₂ to Si [13]. The thickness variation produces the changes in the distances traveled by the optical paths, which interfere, giving rise to the phase shifts. This phase contrast induces different colors in the film. A similar mechanism is applied to graphene visibility, where the optical interference occurs between the air to graphene, graphene to SiO₂, and SiO₂ to Si[14]. The variation in the thickness of the graphene on SiO₂ produces different color contrast making us identify the number of layers to a certain precision.

We used the Olympus BX53M optical microscope for optical measurements. This instrument contains the objective lenses of 10X, 20X, 50X, 100X, long-distance 50X having numerical apertures 0.25, 0.40, 0.75, 0.90, and 0.50 respectively. We observed the graphene on SiO₂(300 nm)/Si and on the oxidized copper.

3.2.2. Field Emission Scanning Electron Microscope (FESEM):

For any microscope, the resolution depends inversely on the source's wavelength, which emphasizes using the lower wavelength to increase the resolution. In the optical microscope, the resolution has been limited by the visible light wavelength. Thus, a high-energy beam of electrons is used as an illumination source in an electron microscope to obtain a shorter wavelength. These electrons impinge onto the specimen and will undergo scattering that produces different signals. Specialized detectors are used to collect generated signals to form the image or to get other information. Therefore, it is vital to understand the interactions between the electron and the specimen's atoms.

A focussed electron beam that hits onto the surface is called primary electron. When these electrons interact, they undergo elastic and inelastic scattering, and they can even knock out the specimen's electrons. Figure 3.7 displays the interaction between the electron beam and the sample's surface [15]. The elastic scattering mostly happens by the coulombic interactions. In inelastic exchange, some of the energy of the primary electrons is transferred to the sample. The energy transferred to the specimen can cause different signals, as shown in figure 3.7, such as backscattered electrons (BSE), secondary electrons (SE), continuum x-ray, auger electrons, characteristic x-rays, and cathodoluminescence. The region from which the signals are generated is called the interaction volume. The interaction volume size depends on the electron penetration's depth and the excited volume's width. The various signals created from the different portions of the interaction volume and what kind of information they provide is illustrated in figure 3.7.

The schematics of the FESEM and its components are shown in figure 3.8 [16]. An emitter is the electron gun made up of a metallic filament or tip from which the electrons are emitted. There are two ways to eject the electrons from the filament. One is the thermionic emission in which a filament is heated to a high temperature where the electrons at the surface attain high kinetic energy to come out of the surface. We have to choose a metal filament with a high melting point, low

work function, abundant electrons, and stability. Tungsten is the metal filament that satisfies all these conditions. Another is the field emission gun, where the metal tip's surface is subjected to a high electric field for which the electrons can be sufficiently emitted from the surface by following the tunneling effect mechanism. We obtain high energy electrons with a narrow energy band from the field emission gun than the thermionic emission because of the tunneling effect. Consequently, the resolution is higher for the field emission gun than the thermionic emission. The emitted electrons are further accelerated by the accelerating anode. The accelerated beam of electrons can be converged into a point by the electrostatic and magnetic fields created by the electromagnetic lenses. The scanning coils job is to deflect the entire beam of electrons back and forth to scan the

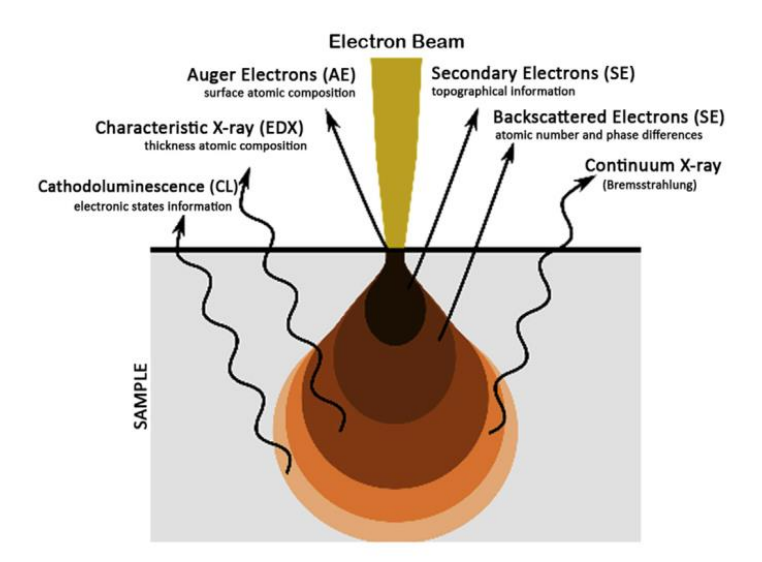


Figure 3.7 Interaction between the electron beam and the sample [15]. The interaction effects produced different signals, and interaction volume is also shown.

whole specimen's surface. Eventually, the focused electron beam spot strikes the sample and produces the signals mentioned earlier.

The nature of the signals that were produced after interaction determines the information of the sample. Secondary electrons are those electrons that have come out of the surface and have energy less than 50 eV. The secondary electron yield is very high compared to the other signals as these electrons escape from the specimen's near surface region, as shown in figure 3.7. Abundant secondary electrons are used for imaging signals. The inlens or secondary electron detector collects these electrons. The image is obtained by mapping the intensity of the electrons through the

rastering specimen's surface. An inlens detector can give a better-resolved image than the secondary electron detector because the inlens is assembled around the line of the path of the electron beam, where the probability of finding the secondary electrons is high. Backscattered electrons are the elastically scattered electrons with the same energy range as the incident beam and are collected by the BSE detector. They are mainly used for diffraction and phase contrast images. The primary electron beam can knock out the localized electrons of the atoms. As a result, they get into an excited state. After some time, the empty electronic state is filled by other higher shell electrons to relax the atoms. In this process, the excess energy is released as a secondary effect in the form of characteristic x-rays, auger electrons, and cathodoluminescence.

The resolution is determined by accelerating voltage called extra high tension (EHT), and the working distance is defined as the distance between the gun and sample. The size of the beam spot reduces as the working distance decreases, and in effect, the resolution increases. We used the FESEM Zeiss ultra 55 to investigate the graphene-related films' surface morphology on copper foil. The working distance was between 1 mm and 3 mm, with an acceleration voltage of 2 kilovolts (KV) was utilized. We have used copper tape instead of carbon tape as adhesive and for the electrical conduction path for the sample as the copper tape has higher conductivity than carbon tape.

3.2.3. Atomic Force Microscope (AFM):

The atomic force microscopy produces the surface topographical images by utilizing the atomic forces between the tip (surface atoms) and the sample's surface atoms. It also comes under surface probe microscopy, where the sharp probe is brought in contact with the sample surface, and the raster scans over the surface to obtain an image. The governing principle for an AFM is atomic forces consisting of van der Waals forces, adhesive and capillary forces. The van der Waals force is the dominant force among all forces in AFM. When we get the two atoms together, the force between them is given by the Lennard- Jones potential. The mathematical description for this potential is given by equation 3.2.4.

$$U(r) = \frac{a}{r^{12}} - \frac{b}{r^6}$$
 Eq-3.2.4,

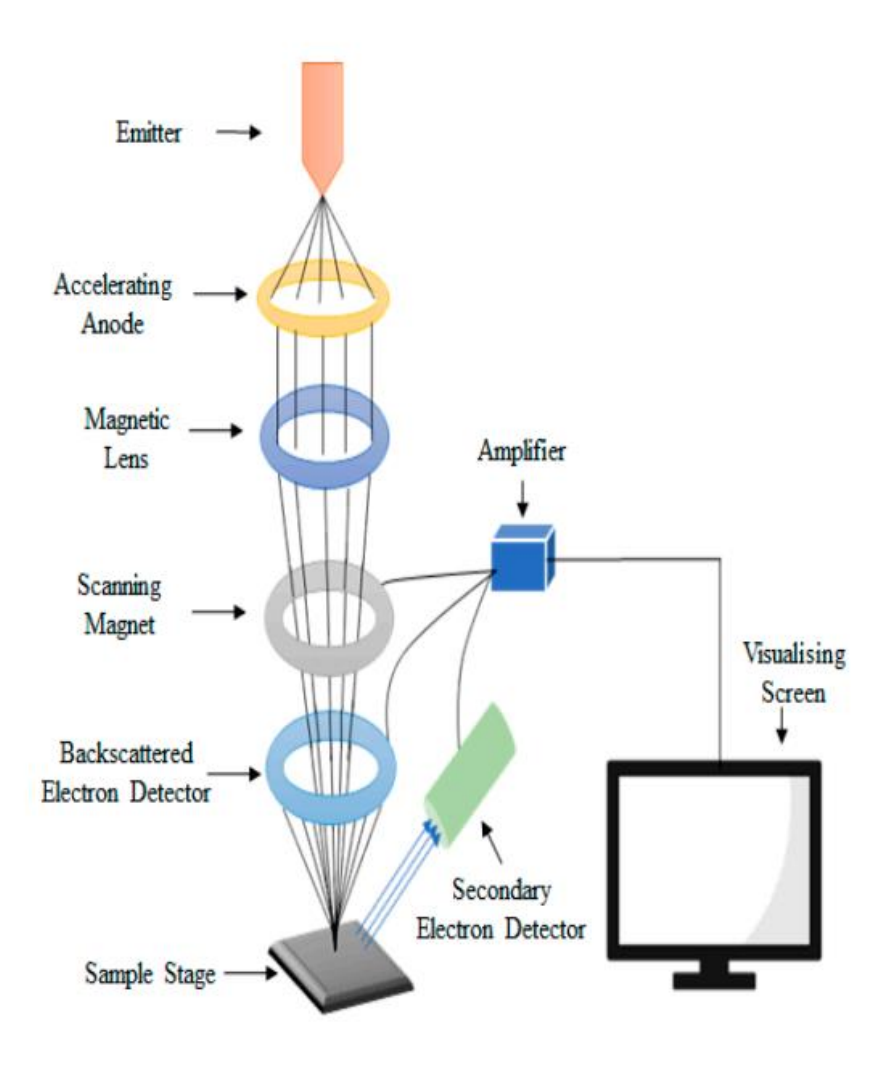


Figure 3.8 Schematics of the FESEM and its respective components [16].

where U is the potential, r is the distance between the two atoms, a, and b are the constants. It is known that the force can be derived by differentiating the potential with the r. The resultant plot f is shown in figure 3.9, the variation in the force as the distance between the tip surface and sample surface atoms changes. In the figure, the distance (r) at which the force is minimum is the equilibrium position is as r_0 . For r greater than r_0 , the force is dominated by the long-range attractive interactions between the atoms. Short-range repulsive forces start dominating for shorter distances (less than r_0).

The schematics of standard AFM are represented in figure 3.10, which contains a sharp tip, a cantilever (holds tip at its free end), a laser, a scanner, and a four-quadrant photodiode. The cantilever is fabricated using silicon nitride or silicon with a low spring constant. The tip is also

prepared from silicon or silicon nitride. Nowadays, tips are also manufactured with diamonds and carbon nanotubes. Generally, the tip's radius of curvature is 10-60 nm, and the length is 100-200 um.

The tip does not encounter any force when it is far away from the sample surface. As it is brought near the surface, the tip experiences repulsive or attractive forces leading to a negative or positive bending of the cantilever. A laser is incident onto the top of the cantilever surface. The cantilever's lateral and vertical deflections are measured using an optical lever that operates by reflecting the laser beam. The reflected beam strikes the position-sensitive photodetector (PSPD) comprising four-quadrant photodetectors. As the tip rasters over the surface with uneven features will induce a varied amount of force on the cantilever that changes the position in the PSPD. The changes in the laser's position on the PSPD using the feedback loop are converted to electric voltage, and further quantification of it will accurately estimate the surface topography, height, and depth of the surface.

Generally, the tip does not move in AFM, so the sample is allowed to move in x, y, and z directions by utilizing the piezo scanners shown in the schematics of AFM. These are piezoelectric materials (obtained from ceramic materials), which will change their dimensions by application of the voltage. This mechanism helps move the sample precisely in the x,y, and z directions. The AFM uses false color to generate the image. The image is also accompanied by the sale bar that denotes the height profile.

An AFM acquires the images precisely in three modes. They are namely tapping mode, contact mode, and non-contact mode. Depending on the requirement, the mode will be chosen. Each mode has its pros and cons.

Tapping mode (dynamic mode): This mode eliminates the influence of the frictional force by intermittently contacting the surface. The cantilever oscillates at ample amplitude to not be trapped in the adhesive forces. This cantilever oscillates near its resonant frequency. The feedback loop provides the cantilever to maintain the oscillating amplitude constant during the scan so that a constant interaction between the tip and sample is conserved. This mode of operation is less destructive compared to the contact mode.

Contact mode: The tip is lightly in physical contact with the surface in the contact mode. It works in the repulsive force regime shown in the force-distance curve figure 3.9. The tip can move over the surface with constant force or at a fixed height. The spring constant of the tip should be lower than the sample, then the cantilever bends. Adhesive and frictional forces strongly influence the tip movement that damages the surface. This mode is suitable for hard surfaces.

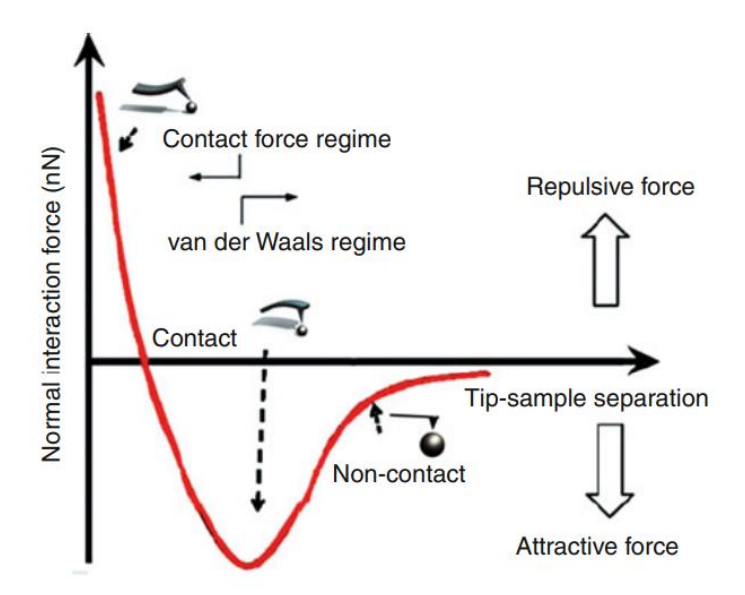


Figure 3.9 The force-distance (between tip and sample) curve [17].

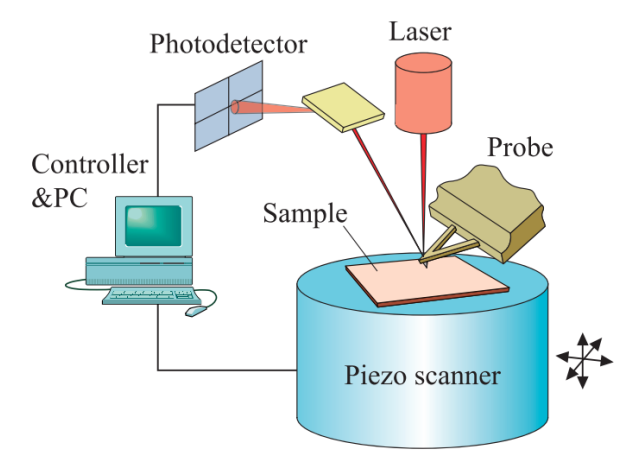


Figure 3.10 Schematics of Atomic force microscope [18].

Non-contact mode: The tip is not physically touching the sample in this mode. This mode is suitable for soft samples such as biological samples. The cantilever oscillates above the surface

with a frequency higher than its resonant frequency and lower amplitude. This mode works in the attractive region. The feedback loop tracks the variations in the amplitude because of the van der Waals attractive forces, so the topography is monitored. These forces can cause changes in the cantilever's phase, amplitude, and resonant frequency.

There are advantages of an AFM compared to electron microscopes. An AFM works in ambient conditions, whereas electron microscopes require a high vacuum for their operation. The sample preparation is also more laborious for electron microscopes than for the AFM. The samples (especially non-conducting) characterized with FESEM can not be characterized further by other instruments because the samples were coated with gold for conductivity. But in an AFM, there is no coating required for samples. It works for insulating samples too. The specific advantage of an AFM over an electron microscope is that it can obtain the height or depth profile of the surface. This feature does not exist in electron microscopes.

General applications of an AFM: It is used to get a high-resolution topographical image at the nanoscale. We can use AFM for various samples, from hard (metals) to soft samples such as polymers, DNA, and protein molecules. Besides obtaining the topography images, AFM is useful for getting information about the surface properties such as stiffness, friction, and hardness. AFM is used to measure the conductivity, magnetic properties, and other properties using specially designed tips.

The disadvantages of an AFM are that the scan rate is slow, and the scan size is less than the FESEM. The artifacts appear in the AFM images. The radius of curvature of the tip limits the resolution. If the dimensions of the surface features are less than the tip's radius of curvature are not appropriately resolved.

We used AFM to measure graphene films' thickness, surface roughness, and topography. We did the measurements on the graphene or NDG on copper and graphene on SiO₂. The scanning was performed at the edge of the film to measure the thickness. We used the Asylum AFM to perform the measurements. The images were acquired in intermittent (dynamic or tapping) mode. The obtained images were processed using WSxM software.

3.2.5. Raman Spectroscopy:

Raman spectroscopy is a nondestructive analytical technique that deals with light-matter interactions in which the vibrational modes of the molecules are studied by employing light. It is vastly used in many fields, from biology to physics, because it can be applied to solids, gases, and liquids. This technique is used to identify materials owing to its characteristic Raman bands. It provides the structural, chemical, and physical information of materials.

When light impinges on the material, the light undergoes either absorption, transmission, or scattering. A large number of photons (more than 99.9%) will undergo elastic scattering called rayleigh scattering, for which the incident light wavelength and scattered wavelength are the same. A small proportion of the incident light is subjected to inelastic scattering, where the scattered light's wavelength is either increased or decreased. This phenomenon is called the Raman effect, as Raman discovered it. The probability of Raman scattering occurring is that one in 10⁷ photons undergo Raman scattering.

The Raman effect was explained in the classical domain that the molecule undergoes polarizability under a static electric field. In quantum theory, the molecules have quantized energy levels, as shown in figure 3.11, and the light is considered a stream of photons. When the molecule absorbs a photon, it excites the molecule to a virtual excited state, and immediately it returns to the same energy state. So, the photon emitted with no energy loss is defined as the rayleigh scattering shown in the figure. In another case, the photon is emitted with a varied wavelength while the molecule returns to the lower vibrational energy states is named Raman scattering. The transition in which the molecule gains energy by absorbing the incident photon and the scattered photon loses energy is called the Stokes scattering. The molecule resides at a higher vibrational energy level, shown in figure 3.11. The scattered photon gains energy if the molecule loses energy to the incident photon by returning to the lower energy state from the higher energy state. This transition is called as antistokes scattering. The difference in frequency between the scattered photon and incident photon refers to the vibrational energy state of the molecule, and it is generally called the Raman shift. When the Raman shift frequency is increased, it is called the blue shift, and if it decreases, it is called the red shift.

A micro-Raman spectrometer comprises of laser, a spectrometer, and the sampling interface. A monochromatic laser source is used as the excitation wavelengths. The advantage of using lasers is that they provide an intense and stable radiation beam. The intensity of the Raman peaks depends

on the fourth power of the excitation frequency of the laser. Some of the popular laser wavelengths are 532 nm, 633 nm, and 785 nm. The fluorescence also increases for the shorter wavelength of the laser. Fiber optics cables are used to transmit and collect the laser energy from the sample. An edge filter or notch is utilized to eliminate the anti-stokes or rayleigh scattered light, and the remaining stokes scattered light is dispersed onto the holographic grating. The light coming from the grating is captured by the charge-coupled device (CCD) that results in the Raman spectrum.

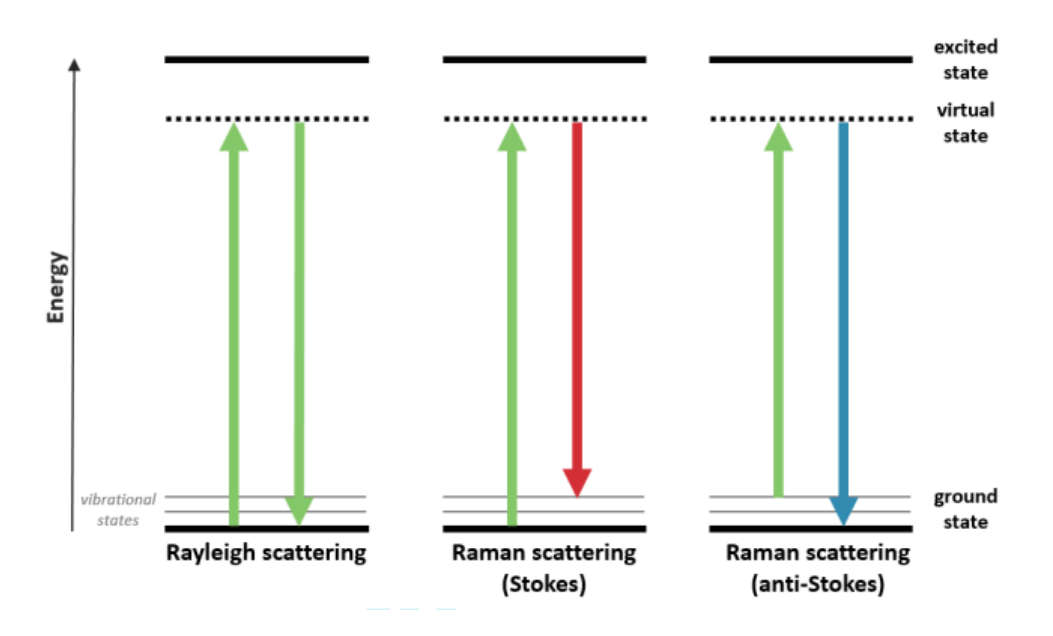


Figure 3.11 Schematics of energy transitions for Raman and rayleigh scattering [19].

The limitations of the Raman effect are that it is a weak phenomenon, as one photon in a million undergoes Raman scattering. The peak intensities are very low for poor Raman scatterers or low concentrations. The high fluorescence of molecules will hinder the intensity of the Raman peaks. Other modified Raman spectroscopies have increased the Raman signal, such as surface-enhanced Raman spectroscopy (SERS), tip-enhanced Raman spectroscopy, resonant Raman spectroscopy, and confocal Raman spectroscopy.

We used 532 nm and 633 nm excitation wavelengths for Raman measurements on graphene and nitrogen doped graphene. These measurements were performed on graphene/NDG on copper and transferred samples. Invia Renishaw micro Raman spectrometer was employed for the Raman measurements. We also applied SERS measurements for graphene and NDG films.

3.2.6. X-ray photoelectron spectroscopy:

X-ray photoelectron spectroscopy (XPS) has become one of the most used surface analytic techniques. The unique characteristics of the XPS are that it has surface sensitivity (~10 nm) and can distinguish the differences in the chemical environments of a material system. With a detection limit of roughly 0.1%-1%, it can detect all elements apart from hydrogen and helium. It is used to study the surfaces of all materials.

XPS works on the photoelectric effect principle in which the electrons are ejected from the surface of a material by x-rays irradiation. The surface is exposed to soft X-rays (less than 6 KeV), and the kinetic energy of the ejected electrons is measured. When the total energy of X-rays are transferred to the core level electrons, the electrons will be emitted. The mathematical form for this process is given in equation 3.2.5.

$$hv = BE + KE + \emptyset_{spec}$$
 Eq 3.2.5,

where hv is x-rays energy, BE is binding energy, KE is kinetic energy, and the \emptyset_{spec} is a spectrometer work function. The equation states that the x-rays' incident energy is equal to the sum of the kinetic energy, the binding energy of the ejected electrons, and the spectrometer work function (constant value). The binding energy can be determined by rearranging equation 3.2.5.

$$BE = hv - KE - \emptyset_{spec}$$
 Eq 3.2.6

This equation was illustrated schematically in the energy level diagram form in figure 3.12 (a). It can be noticed in the diagram that the photoelectron binding energy is measured with respect to the Fermi level of the sample. That is the reason \emptyset_{spec} is included in equation 3.2.6. The electron's binding energy is the intrinsic property of a material, and it is independent of the energy of the x-ray sources utilized for ejecting them.

Schematics of X-ray photoelectron spectroscopy are shown in figure 3.12 (b), illustrating all instrument's major components. The XPS instrument consists of an x-ray source, analyzer, extraction lenses, and detector accommodated in an ultra-high vacuum environment. Electron sources create the x-rays by hitting the x-ray anode. A Tungsten or LaB₆ heated filament provides a beam of electrons that are further accelerated towards an x-ray anode. Aluminum (Al) or magnesium (Mg) are the two materials used for the x-ray anodes. An instrument contains both as

a dual anode, which can be selected as one of them either. Many instruments use monochromators for obtaining monochromatic x-rays. For Al x-rays, Quartz crystal is positioned at a specific angle to allow only Al K alpha x-rays to get diffract and filter out all other Al x-ray lines. An advantage of using monochromatic x-rays is to increase the spectral resolution as it was limited by the x-ray linewidth. An electron optics exists between the sample and an analyzer called extractions lenses to provide the electron collection efficiency and control the sample area from which the electrons are collected. They also control the energy of the electrons that are traveling toward the analyzer to make it specific energy before entering the analyzer, called pass energy.

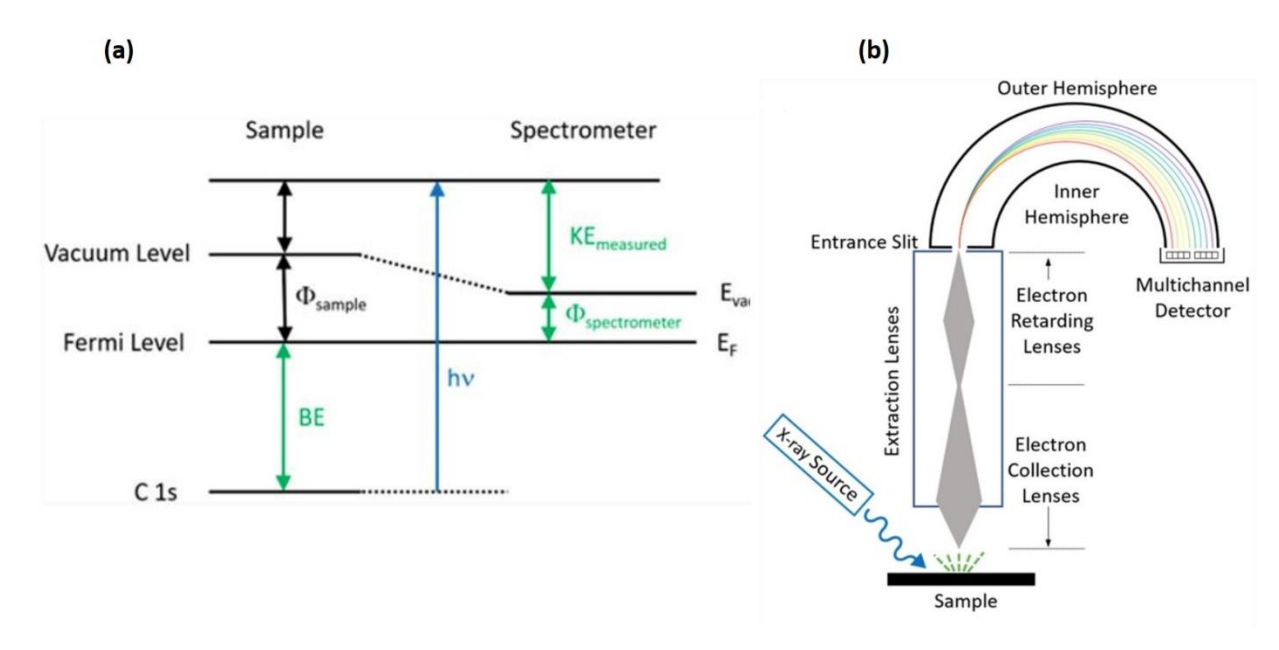


Figure 3.12 (a) Energy level diagram illustrating the binding energy equation (b) schematics of the components of an X-ray photoelectron spectroscopy [20].

XPS systems have primarily two types of analyzers: concentric hemispherical analyzers and cylindrical mirror analyzers. The former is better as its energy resolution and throughput are high. The concentric hemispherical analyzer comprises two hemispheres, as shown in figure 3.12 (b). Both hemispheres are subjected to the voltage in which the outer hemisphere has more negative than the inner sphere. Through a slit, electrons enter the analyzer. Only electrons with a certain amount of energy are permitted to move through the analyzer. The lower energy electrons collide with the inner hemisphere, and the higher energy electrons hit the outer hemisphere. The radius of the analyzer determines the analyzer resolution, as it is proved larger the radius higher the

resolution. XPS instruments use electron multipliers as detectors. These multipliers are kept along the exit slit for more electron collection.

In XPS spectra, besides the photoelectron peaks, there are auger lines and satellite peaks shown in figure 3.13. The reasons for arising these peaks are discussed below.

Photoelectron lines: These peaks are the primary peaks in the XPS spectra. These come from the core-shell electrons. The intensity and the sharpness of these peaks are very high.

Auger lines: The ejection of the core electron creates the hole there. The excited ionized atom gets relaxed by filling the hole with another electron that has come from the valance orbital. This relaxation process produces the auger electron. These lines are used for the qualitative analysis of materials. The notation of these lines, are K, L, and M, indicates the atomic orbitals from which the electrons have filled holes. They are denoted by the KLL, KLM, etc. For example, KLL indicates that the core electron is ejected from the K shell, the L shell electron filled the core hole, and the auger electron also came from the L shell. It indicates that the three different electronic transitions are occurring for the ejection of auger electron.

Satellite peaks: Satellite peaks appear in XPS spectra due to a nonmonochromaticity in x-ray source. These sources produce x-ray lines with varying energies leading to the appearance of satellite peaks.

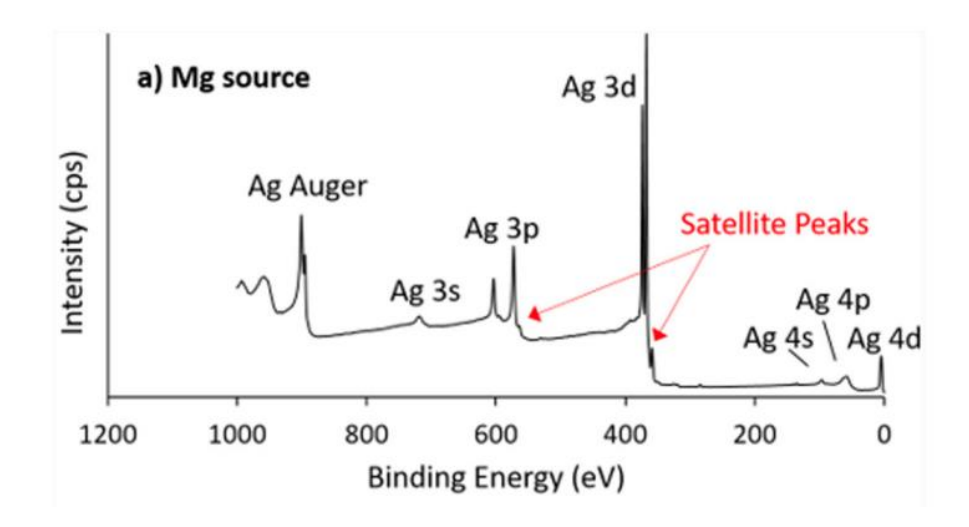


Figure 3.13 survey spectrum of silver with nonmonochromatic Mg source. The presence of photoelectric lines, auger lines, and satellite peaks can be seen in the figure [20].

In this thesis work, XPS has been performed on the nitrogen doped graphene on copper. We used it for the nitrogen content and its configurations in the carbon lattice.

3.2.7. UV-Vis spectroscopy:

Uv-vis spectroscopy is an important physical tool in obtaining the information on transmittance, the concentration of an absorbing species, and band gap using a Tauc plot. It exploits the interaction of ultraviolet, visible, and near-infrared light with the matter. An instrument utilized for UV-Vis spectroscopy is called a UV-Vis-NIR spectrometer. The wavelength range used for Uv is 200-400 nm, visible 400-800 nm, and the near-infrared region 800- 1200 nm. Samples are measured using three modes, transmittance, absorbance, and reflectance in UV-Vis spectroscopy. When the energy of the photons of UV -visible light is sufficient to cause the transitions in electronic energy levels, the molecules absorb the photons to excite the electron from a lower electronic energy level to a higher electronic energy level. These transitions are characteristic due to the specific energy between the levels for every material.

The schematic of the UV-vis spectrometer is illustrated in figure 3.14. The diagram here is the double beam instrument. A light beam in the visible and ultraviolet regions is obtained from the tungsten lamp and D2 (deuterium arc) lamp, respectively. This light is passed through a monochromator to disperse the lights into individual wavelengths. The monochromator consists of a prism or a diffraction grating. The monochromatic light beam is split into two halves in equal intensities by a beam splitter. In these two light beams, one is sent through the reference sample, and the other is passed through the sample under examination. After passing through the reference and sample, both light rays can travel toward the detectors. These detectors compare their intensities as the light intensity ratio through the sample to the reference.

UV-Vis spectroscopy uses the Beer-Lambart law for the solutions. It manifests that the absorbance of light by the solution (sample) is directly proportional to the path length through the sample and the concentration of the sample. This law helps to find a solution's concentration as it is a characteristic of every compound. We used UV-Vis spectroscopy for transmittance measurements in my thesis work. We transferred the graphene and nitrogen doped graphene samples onto quartz substrates using the wet transfer method. Quartz is used as a substrate because of its transparency. UV (200–400 nm) and visible light wavelengths were used (400-800 nm) for measurements.

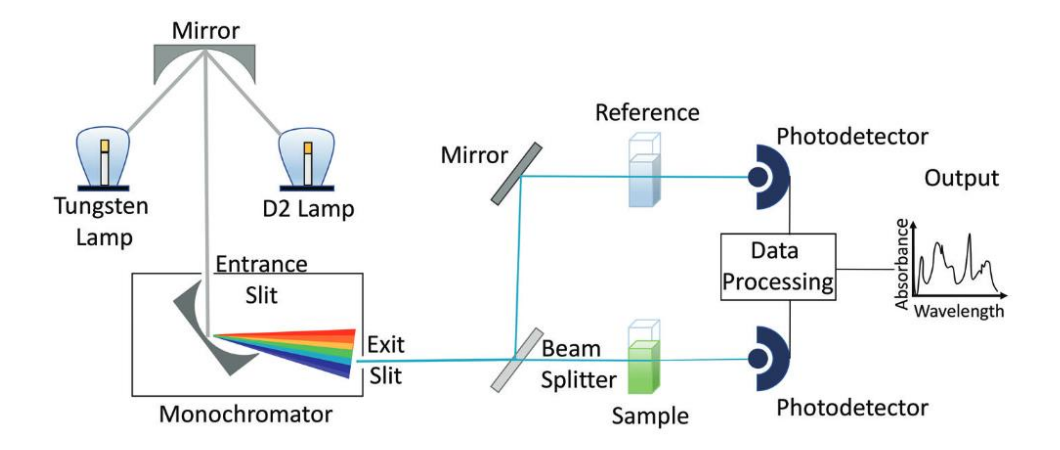


Figure 3.14 Schematics of double beam instrument of UV-Vis spectrometer [21].

3.2.8. Electron Backscatter Diffraction (EBSD):

Electron backscatter diffraction is an important technique that obtains electron diffraction patterns from polycrystalline materials. These patterns are utilized to determine crystallographic orientation, grain boundaries, and phase identification. This characterization is employed as an additional tool in FESEM. The advantage of EBSD being attached to FESEM is that the area where the morphology is obtained is the same place EBSD acquires information about the grain's orientation and distribution.

When the electron beam impinges onto the tilted crystalline sample, it can generate non-elastically scattered or elastically scattered electrons. The scattered electrons that satisfy Bragg's condition produce diffraction patterns. These diffracted electrons hit the phosphorus screen and generate the visible lines called electron backscatter patterns or Kikuchi bands, shown in figure 3.15 (b). The characteristic feature of Kikuchi bands is bright parallel bands regularly arranged on a steep continuous background rather than a series of diffraction spots. The position where the kikuchi bands intersect appears prominent and indicates the zone axis. The kikuchi pattern geometry can be interpreted as the gnomonic projection of the crystal lattice on the phosphorous screen.

The placing the sample stage with respect to the electron beam is depicted in figure 3.15 (a). The specimen is placed in FESEM and is inclined 70° relative to the normal incidence of the electron beam. Accelerating voltage of 10-30 KV and incident beam current in the 1-50 nA range produce

the EBSD patterns. The detector is a camera containing a phosphorous screen that resides on a mounted motorized carriage.

Kikuchi bands are detected using the Hough transform in which the Kikuchi lines recorded from the image are converted into a point in the hough space. The detected bands' width is a function of the spacing of the diffracting planes, and it can be comparable to the theoretical list of diffracting planes.

An EBSD data is interpreted in inverse pole figure (IPF) to illustrate grains (planes) orientation. A pole figure is an illustration of three-dimensional space in a graphical representation of two dimensions. It shows the orientation of a selected plane which is normal with respect to the sample frame. The inverse pole figure complements the pole figure in that it represents the location of a sample direction relative to the crystal reference system [23]. This IPF can be used as a color code for crystal orientation maps (COMs), as shown in figure 3.15 (c). This figure has three corners. Standard colors assigned to the IPF are blue (111), green (101), and red (001) at the three corners. The measurement of an individual orientation is related to the single point in an IPF.

I have performed EBSD measurements on the electropolished copper foil. We tried to understand the copper plane orientation on the effect of graphene and nitrogen doped graphene films.

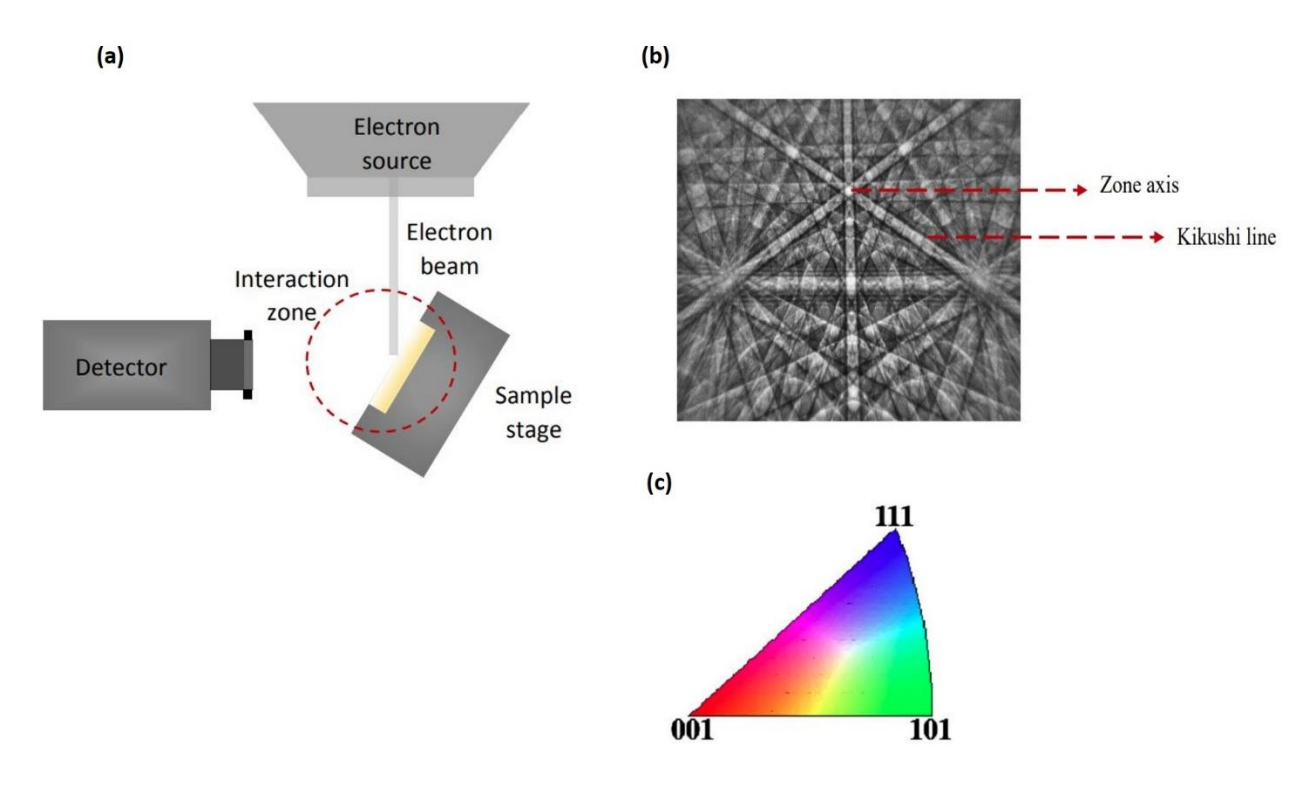


Figure 3.15 (a)schematics of the EBSD instrument [22]. (b) Representation of kikuchi patterns. The bands are Kikuchi bands. Each band indicates the family of diffracted planes. The intersection of bands is ascribed to the zone axis. (c) color key of inverse pole figure (IPF).

3.2.9. X-ray Diffraction (XRD)

X-ray diffraction is an essential and nondestructive technique in determining the crystalline phases that exist in materials. Structural properties such as strain state, defect structure, and grain size can be measured using XRD. In XRD, a parallel beam of x-rays with a wavelength of around 0.5-2.0 angstroms is incident on a specimen. These x-rays are diffracted by the crystal planes satisfying Bragg's condition given in equation 3.2.7.

$$2d\sin\Theta = n\lambda$$
 Eq 3.2.7

Where λ is the wavelength of X-rays, d is the distance between crystal planes, Θ is the angle of x-ray incidence with respect to the atomic planes, and n is the order of diffraction (first-order diffraction is considered). The graphical diagram is shown in figure 3.16 for equation 3.2.7. The diffracted rays undergo constructive interference when the X-rays satisfy Bragg's condition. The points (in dark color) represent the crystal planes.

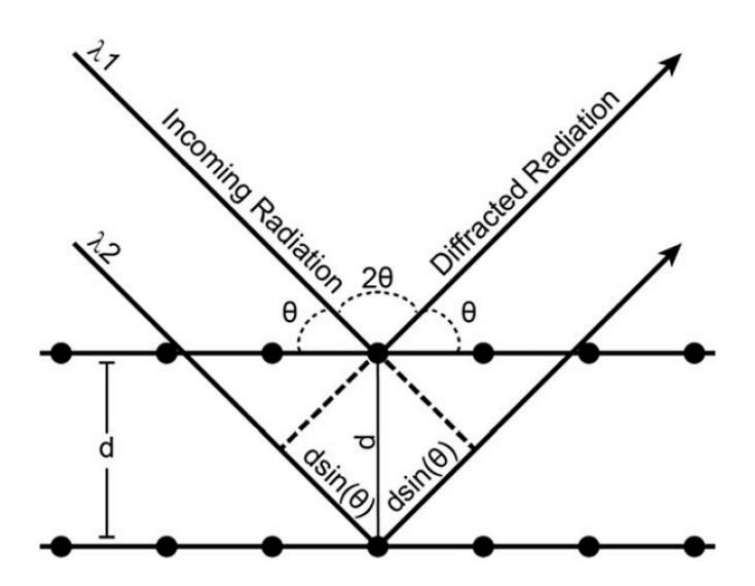


Figure 3.16 Schematics illustration of Bragg's law condition [24].

The X-ray diffractometer comprises of an X-ray source, sample holder, divergent slit, receiving slit, and X-ray detector, as shown in figure 3.17. The X-rays have been generated using various methods such as x-ray tubes, synchrotrons, and microfocus tubes. These rays are collimated and monochromatized by the monochromator slit. This narrowed wavelength thin beam is directed towards the specimen, where the rays get diffracted by the crystal in different directions. The specimen is held by the sample holder, which is aligned along the center of the beam. The detector is mounted on the arm and rotates at an angle of 2Θ , while the sample rotates at an angle Θ of in the x-ray beam's path. The diffracted rays are allowed to travel through the receiver slit to reach the X-ray detector. Detectors are fabricated by transducers that generate a signal when radiation hits them. For bulk materials, the powder XRD technique is utilized in which the x-rays source and detector are allowed to rotate simultaneously. The penetration depth of X-rays is around 50-200 µm. This method has the limitation of measuring thin films for which most of the x-rays should travel within the film instead of in the substrate. A glancing incidence XRD method overcomes the former technique. In this, the incidence angle is limited up to 1° with respect to the sample. The incident angle restriction reduces the X-rays' penetration depth and constrains most of the xrays within the film.

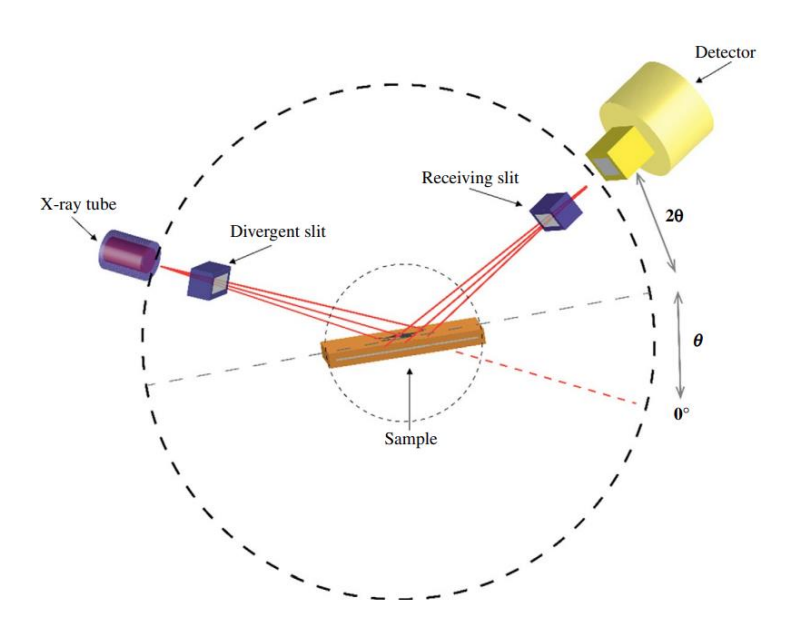


Figure 3.17 schematics representation of X-ray diffraction instrument [25].

We used a powder x-ray diffraction method on copper foil (considering it a bulk material) before and after annealing to determine its crystallographic nature. The copper crystal orientation affects the graphene growth; thus, orientation information is required.

3.3 Materials used

List of chemicals used for synthesising graphene and NDG, to clean the copper substrate and other miscellaneous chemicals:

Name	Purity	Make
PMMA Powder	99%	Sigma Aldrich
Phthalocyanine	98%	Sigma Aldrich
Copper	99.8%	Sigma Aldrich
phthalocyanine		
Isopropyl alcohol	Sisco research	99%
	laboratories	
Nitric acid	70%	FINAR
Ferric Chloride	98%	Avra
(anhydrous)		
Acetone	99.9%	SRL
25 micron thick	99.8%	Alfa Aesar
copper foil		
Ammonium	98%	Sigma Aldrich
Persulphate		
Ortho phosphoric	85%	SRL
acid		
Methylene Blue	82%	Sigma Aldrich
powder		
Crystal violet powder	95%	Sigma Aldrich
Anisole	99.7%	Sigma Aldrich

3.4 References:

[1] Kim S M, Hsu A, Lee Y H, Dresselhaus M, Palacios T, Kim K K and Kong J 2013 The effect of copper pre-cleaning on graphene synthesis *Nanotechnology* **24**

- [2] Chou P J, Bowden G B, Copeland M R, Farvid A, Kirby R E, Menegat A, Pearson C, Shere L, Siemann R H, Spencer J E and Whittum D H 2009 The fabrication of millimeter-wavelength accelerating structures 501–17
- [3] Kondrashov I, Komlenok M, Pivovarov P, Savin S, Obraztsova E and Rybin M 2021
 Preparation of copper surface for the synthesis of single-layer graphene *Nanomaterials* **11**1–10
- [4] Sohal R CVD growth of (001) and (111) 3C-SiC epilayers and their interface reactivity with praseodymium oxide dielectric layers High k dielectrics for mim application View project Defect states in nanocrystallized silicon View project
- [5] Anon chemical vapor deposition
- [6] Meyers L and P W 1999 Atmospheric Pressure Chemical Vapor Deposition of CdTe for High Efficiency Thin Film PV Devices Atmospheric Pressure Chemical Vapor Deposition of CdTe for High Efficiency Thin Film PV Devices Annual Report 4
- [7] Saeed M, Alshammari Y, Majeed S A and Al-Nasrallah E 2020 Chemical Vapour Deposition of Graphene—Synthesis, Characterisation, and Applications: A Review *Molecules* **25**
- [8] Chen Y, Gong X L and Gai J G 2016 Progress and Challenges in Transfer of Large-Area Graphene Films *Adv. Sci.* **3**
- [9] Yoon M-A, Kim C, Kim J-H, Lee H-J and Kim K-S 2022 Surface Properties of CVD-Grown Graphene Transferred by Wet and Dry Transfer Processes *Sensors* **22** 3944
- [10] Song Y, Zou W, Lu Q, Lin L and Liu Z 2021 Graphene Transfer: Paving the Road for Applications of Chemical Vapor Deposition Graphene *Small* **17** 1–14
- [11] Goniszewski S, Gallop J, Adabi M, Gajewski K, Shaforost O, Klein N, Sierakowski A, Chen J, Chen Y, Gotszalk T and Hao L 2015 Self-supporting graphene films and their applications *IET Circuits, Devices Syst.* **9** 420–7
- [12] Nichols G 2006 Light Microscopy *Polymorph. Pharm. Ind.* 167–209

- [13] Henrie J, Kellis S, Schultz S M and Hawkins A 2004 Electronic color charts for dielectric films on silicon *Opt. Express* **12** 1464
- [14] Roddaro S, Pingue P, Piazza V, Pellegrini V and Beltram F 2007 The optical visibility of graphene: Interference colors of ultrathin graphite on SiO2 *Nano Lett.* **7** 2707–10
- [15] Ezzahmouly M, Elmoutaouakkil A, Ed-Dhahraouy M, Khallok H, Elouahli A, Mazurier A, ElAlbani A and Hatim Z 2019 Micro-computed tomographic and SEM study of porous bioceramics using an adaptive method based on the mathematical morphological operations *Heliyon* **5** e02557
- [16] Sharma S, Jaiswal S, Duffy B and Jaiswal A K 2019 Nanostructured Materials for Food Applications: Spectroscopy, Microscopy and Physical Properties *Bioengineering* 6 1–17
- [17] Fundamentals S 2013 Encyclopedia of Tribology
- [18] Ishida N and Craig V S J 2019 Direct measurement of interaction forces between surfaces in liquids using atomic force microscopy *KONA Powder Part. J.* **36** 187–200
- [19] Moura C C, Tare R S, Oreffo R O C and Mahajan S 2016 Raman spectroscopy and coherent anti-Stokes Raman scattering imaging: Prospective tools for monitoring skeletal cells and skeletal regeneration *J. R. Soc. Interface* **13**
- [20] Stevie F A and Donley C L 2020 Introduction to x-ray photoelectron spectroscopy *J. Vac. Sci. Technol. A* **38** 063204
- [21] Rocha F S, Gomes A J, Lunardi C N, Kaliaguine S and Patience G S 2018 Experimental methods in chemical engineering: Ultraviolet visible spectroscopy—UV-Vis *Can. J. Chem. Eng.* **96** 2512–7
- [22] Saleh A A 2020 Anthony Abou Saleh Relation entre auto-organisation et création / résorption de défauts microstructuraux sous irradiation laser ultrabrèves
- [23] Wright S I 2005 Orientation Texture Encycl. Condens. Matter Phys. 221–33
- [24] Stan C V., Beavers C M, Kunz M and Tamura N 2018 X-ray diffraction under extreme conditions at the advanced light source *Quantum Beam Sci.* **2** 1–33

- [25] Falsafi S R, Rostamabadi H and Jafari S M 2020 X-ray diffraction (XRD) of nanoencapsulated food ingredients (Elsevier Inc.)
- [26] Rahul Sharma "Studies on the Vapor Transport Assisted Growth of Two-Dimensional Atomic Layers and Their Heterostructures for Optoelectronic Devices and Catalysis

Chapter-4

Growth of Pristine Graphene by Chemical Vapor Deposition

This chapter deals with the synthesis of pristine graphene on copper from a solid carbon precursor, polymethylmethacrylate (PMMA), by atmospheric pressure CVD (APCVD). A large area of continuous graphene films was obtained by optimizing the growth conditions such as evaporation temperature, amount of powder of PMMA, and growth time. The reduction of growth temperature for graphene growth is essential to meet industrial needs. Therefore, This chapter has also focused on graphene's temperature-dependent growth. AFM, FESEM, Raman, and optical measurements were performed on these films to get insights into the film's morphology, topography, crystallinity, and thickness.

4.1 Introduction

Graphene was discovered using mechanical exfoliation in which the graphene layers are peeled off from the graphite flakes using scotch tape [1]. Even though this method produces high-quality graphene flakes, their yield is very low, with no control over their thickness and size in microns. Researchers have focused on synthesizing large-area graphene films. Chemical vapor deposition has achieved this on metallic substrates such as Nickel (Ni) and copper (Cu). However, in the CVD technique, graphene synthesis has mostly been produced using gaseous precursor Methane (CH₄), which is poisonous, highly flammable, and has a high decomposition temperature. Alternative precursors like solid and liquid precursors have been utilized for synthesis. The graphene has been synthesized using solid precursors by post-annealing the deposited precursor film on copper. This method does not have control over the nucleations or grains. Therefore, the PMMA was evaporated and transported to the copper substrate to obtain the gains and continuous films depending on the growth conditions.

4.2 Growth of pristine graphene using APCVD

Pristine graphene has been synthesized in atmospheric pressure CVD on copper substrate. First of all, the copper substrate preparation is discussed for the growth of graphene.

4.2.1 Copper substrate preparation:

The thickness of the copper foil used as a substrate for graphene growth is 25 um. The copper was subjected to three processes before graphene growth. These processes are discussed below.

Step-I

Cleaning of copper foil: 4 cm x 1 cm was cut from the copper foil. This copper was rinsed in 6.9% of HNO₃ for 25 seconds, followed by cleaning with deionized water (DIW) three times. Wash with the acetone and isopropyl alcohol (IPA) and dry with an air blower.

Step-II

Electropolishing: As received, copper foil itself has a rough surface, and cleaning with HNO3 makes the copper surface roughness, besides removing the oxygen from the surface. This roughness creates a high nucleation density that reduces film grain size and consequently increases grain boundaries, adversely affecting film quality. Therefore, the cleaned foils were used for electropolishing to reduce the film's roughness. The procedure for electropolishing was mentioned in the experimental chapter. The parameters used for electropolishing are as follows:

The electropolishing solution is a mixture of Orthophosphoring acid and IPA in a 5:1 ratio, time-30 min, the distance between the anode and cathode is 2 cm, applied voltage 1.5-1.8 V, and electropolishing current- 20 mAor 4.6 mA/cm².

After the electropolishing, the samples were rinsed in DI water twice to remove the electrolyte solution. Further cleaning was performed with acetone and IPA to remove organic contaminants.



Figure 4.1 Placing the copper substrate on the alumina crucible.

Step-III

Post-annealing of copper: The annealing was done before the growth of graphene. The details are discussed below.

The electropolished copper was cut into 2.5 x 1 cm and used as a substrate. This substrate was kept on the rims of the alumina crucible, as shown in figure 4.1, to make the most of the area to be contact free from the crucible. The substrate was loaded into the CVD chamber. Then, the system was purged with Ar gas at 200 SCCM for 30 minutes to remove the ambient gases and moisture. The ramping rate was 8 °C/ min. The copper was annealed in the 200 SCCM of Argon (ar) + hydrogen (H₂) atmosphere having a 9:1 ratio for 30 minutes at 1050 °C. Allowed the furnace to cool naturally.

The growth of graphene by CVD on the catalytic single-crystal metallic substrate has attracted great attention due to certain planes having a small lattice mismatch with graphene [2]. Cu (111) orientation mismatch is ~3 to 4 %, and it is the least among all orientations of copper. This orientation of the substrate can be used for the heteroepitaxial growth of single-crystal graphene without grain boundaries. Therefore, Contact-free annealing (CFA) of copper foil is a suitable method to achieve a homogeneous and large grain-sized Cu (111) surface [3]. The copper (111) plane has the lowest surface energy. When the copper is annealed at its close melting temperatures under reduced atmospheres, the copper surface restructures itself into (111) orientation during recrystallization, achieving the highest packing fraction at the surface. The contact-free regions from the crucible are subjected to stress-free while under annealing, causing them to produce a (111) plane more homogeneously and simultaneously produce large grains.

To obtain crystallographic orientation, we investigated the annealed copper substrates using XRD and EBSD techniques (details explained in the experimental methods section). Figure 4.2. (a) shows the XRD diffractograms of contact-free and contact-annealed copper samples. It was found that (111) and (100) planes exist for copper, which has undergone contact annealing. However, the copper annealed with contact-free has shown only (111) plane. The information obtained from XRD is not restricted to the surface, as the X-ray beam in XRD penetrates the bulk of the sample. Thus it implies that the bulk of the copper is also subjected to the (111) plane. The inverse pole figure (IPF) color maps from EBSD are shown in figure 4.2 (b-d). The color code can be taken

from figure 4.2 (d), where blue denotes the (111) plane, red (001), and green (101) plane. Figure 4.2 (b) is the map obtained from the contact annealed copper area showing the mixed colors, with the major area covered with blue ((111) plane) and other colors denoting other planes. The IPF image of the contact-free annealed area of copper is shown in figure 4.2 (c), where only blue color is observed, which indicates the whole surface is (111) plane. The advantage of the copper surface being (111) plane is that it induces less stress on graphene due to the least lattice mismatch between them compared to the other orientations of copper. Moreover, copper annealing by flowing hydrogen (H₂) gas helps etch the intrinsic carbon that exists in the subsurface region of copper that diffuses during annealing.

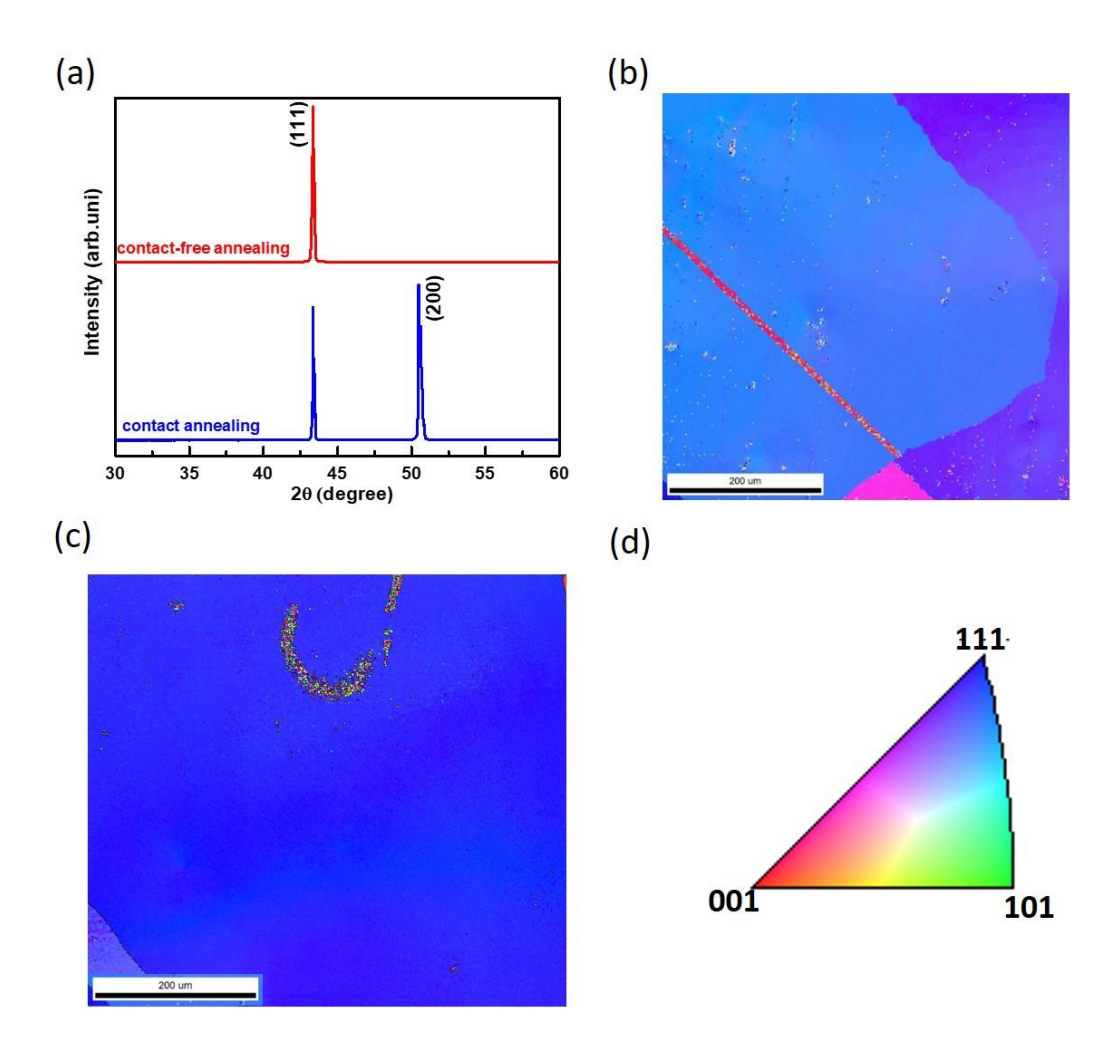


Figure 4.2 (a) XRD diffractogram of contact annealing and contact-free annealing of copper. EBSD map of contact annealing (b) and contact free-annealing (c) and Inverse pole figures of color coding (d).

4.2.2 Atompsheric pressure CVD grown graphene from PMMA

Pristine graphene has been synthesized by using polymethylmethacrylate (PMMAA) powder as a precursor material. Two independent heating zones were used for the graphene growth. The PMMA powder was placed upstream, 40 cm from the substrate, which was kept at the center of the furnace and is a constant zone. The schematics of CVD are shown in figure 4.3. A quartz tube with dimensions 100 cm in length and 50 mm in diameter. PMMA is a synthetic polymer that contains carbon, oxygen, and hydrogen atoms. The structure of PMMA is shown in figure 4.4 [4]. The nichrome coil assisted with a temperature controller used to evaporate the PMMA powder.

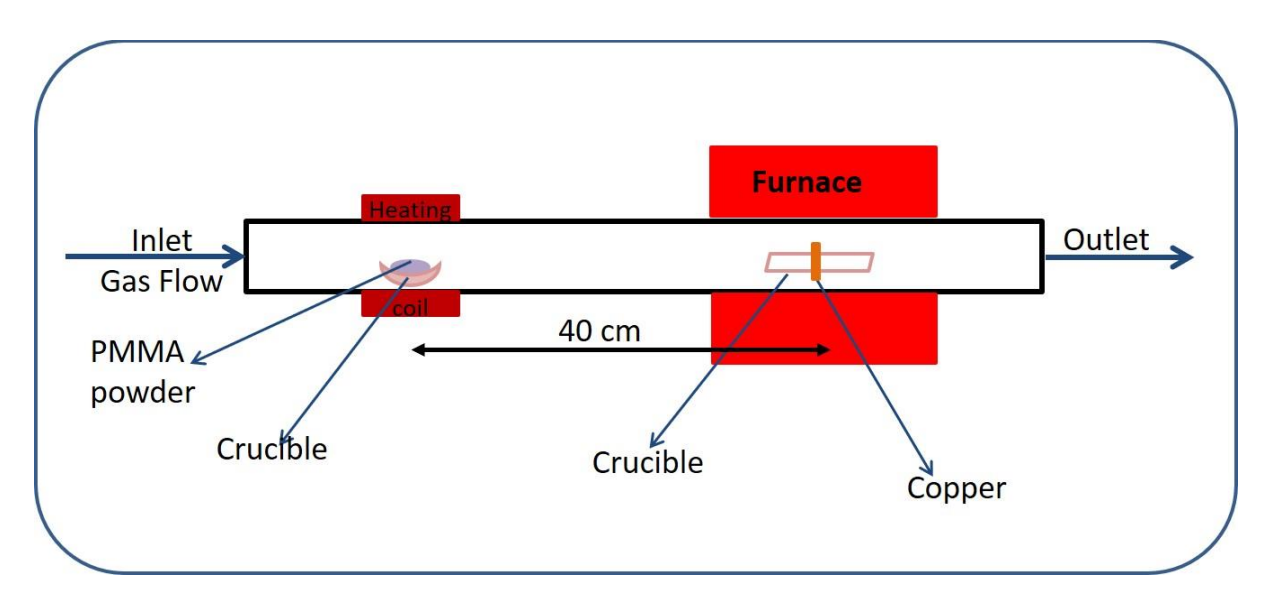


Figure 4.3 Schematics of CVD system for graphene growth.

Atmospheric pressure chemical vapor deposition (APCVD) has been employed for synthesizing graphene. Initially, at the beginning of the experiment, the system was purged with the Ar gas at 200 SCCM for 30 minutes to evacuate the atmospheric oxygen in the quartz tube. Purging is important as oxygen at high temperatures oxidizes the copper, which is detrimental to graphene growth.

Figure 4.5 shows the typical heat profile for graphene growth. Some of the parameters were kept constant for all our experiments. Those are ramp rates (8°C/min), pre-annealing parameters (temperature, time, and flow rate), and allowing the system to cool naturally after the growth. A mixture of Ar and H₂ gas was used as carrier gas during the growth process. The temperature of the precursor was ramped up when the pre-annealing started. The rate of ramping is maintained

such that it reaches the evaporation temperature of the precursor when the pre-annealing ends, as shown in the heating profile. The gas was switched from Ar+ H₂ to Ar while the system was cooling down. The used gas flow rate was 50 SCCM of Ar gas after the growth. Several growth parameters were optimized for obtaining continuous graphene films.

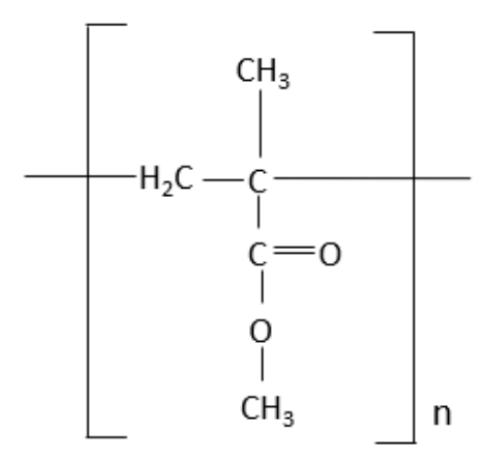


Figure 4.4 Structure of Polymethylmethacrylate (PMMA) [4].

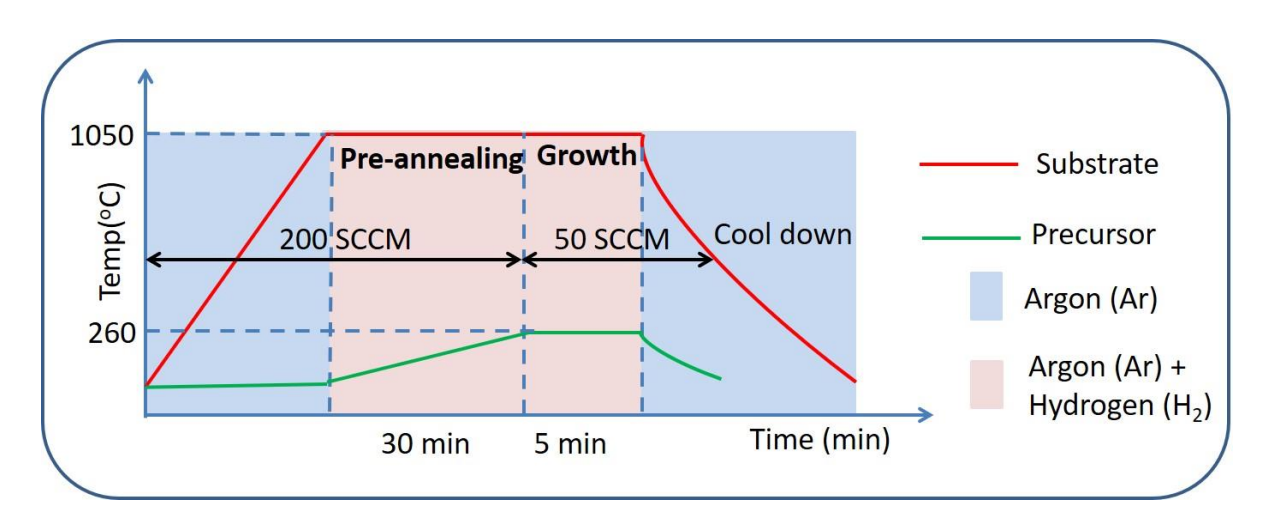


Figure 4.5 Typical heating profile for the graphene growth

The growth parameters that have been used for obtaining high-quality large-area continuous films are shown in Table 4.1

Growth parameters	values
Precursor Evaporation temperature (°C)	335, 285 & 260
Amount of Powder (mg)	1, 2, & 3
Growth Temperature (°C)	1050, 850 & 650
Growth time (min)	5,10, 15 & 20
Gas Flow rate (SCCM)	100, 50, 25 & 10

Table 4.1 Growth parameters employed for synthesizing graphene.

4.3 Results and Discussion:

The synthesized graphene films via APCVD on the copper substrate (2. 5 cm x 1 cm) were characterized with microscopic and spectroscopic techniques to investigate different aspects of the film, such as structural, morphological, surface homogeneity, etc. Optical microscopy, FESEM, AFM, and Raman spectroscope techniques were employed for film characterization. The film's various characteristics are discussed in detail in this section.

4.3.1 Optimizing the evaporation temperature of PMMA

The synthesis of graphene from solid precursor PMMA was first reported by sun et al. [5]. The PMMA was deposited on copper by spin coating, and graphene was synthesized by post-annealing the PMMA film/Cu in the reduced atmosphere. In this process, there is no requirement for finding the evaporation temperature of PMMA. Graphene has also been grown via low-pressure or atmospheric-pressure CVD by evaporating the PMMA, but the evaporation temperatures were mentioned over a range in the literature [6,7]. However, the evaporation temperature depends on the average molecular weight of the polymer. It also relies on what pressure the CVD experiment has been performed. Therefore, we tried to optimize the evaporation temperature of PMMA where it starts evaporation in APCVD. The amount of PMMA powder used for the growth of films is 1 mg. The films were grown at 1050 °C for 5 min at 50 SCCM of Ar/H₂ by employing the different evaporation temperatures of PMMA. We varied the evaporation temperature of PMMA from 335 °C to 260 °C.

FESEM images were taken on the as-grown films (graphene on copper). Optical images were captured on transferred graphene films that had been transferred onto Silicon dioxide (SiO₂) (300 nm) on a Silicon (Si) substrate. Raman measurements were performed on transferred films with 532 nm excitation wavelngth. Figure 4.6 shows the FESEM and optical micrographs and Raman spectra of all films. The FESEM image of figure 4.6 (a) is a graphene film that has been synthesized by evaporating the PMMA at 335 °C. The morphology in figure 4.6 (a) shows that the film has different contrast. The contrast in the image arises from the attenuation of secondary electrons (SE) emitted from the copper substrate by the film. The number of SE reaching the detector will be lower as the thickness of the film increases; as a result, the regions with higher thickness will be darker than the regions with lower thickness. In this image, the copper surface is completely covered with a thin graphene layer, and the Raman measurements confirmed that it was monolayer graphene which will be discussed in detail later. There are islands of graphene crystals that might have nucleated on top of monolayer graphene with different contrasts corresponding to different thicknesses. The white particles are SiO₂ may be deposited on top of the film or copper surface due to the aging or more usage of the quartz tube [8]. 1cm x 1 cm film was cut from the as-grown film and utilized for transferring onto the SiO₂ substrate. The transferring details have been mentioned in the experimental chapter.

Figure 4.6 (b) shows the optical micrograph of the graphene film transferred onto SiO₂, which had been grown by evaporating PMMA at 335 °C. Similar to the FESEM image, the optical micrograph shows a different contrast in the film. The varied contrast can be observed due to constructive interference between the air and film (different layers) interface and film and SiO₂ interface. As the thickness of the crystals increases, more contrast can be observed with respect to the substrate surface. The image has light contrast all over the area, indicating the thin layer covers the entire area. This thin layer was found to be monolayer graphene, confirmed by Raman measurements. On top of the monolayer, islands of crystals have dark contrast with varied contrast, indicating the different number of layers. The particles that were shown in red circles represent the leftover PMMA that has been used in the transfer process. The presence of more islands of multilayered crystals on monolayer graphene might be due to the higher evaporation temperature of PMMA that caused the conversion of PMMA into the vapor phase quickly. It leads to large mass transport of the PMMA vapor onto the substrate. Therefore, the evaporation temperature of PMMA has been reduced from 335 °C to 285 °C.

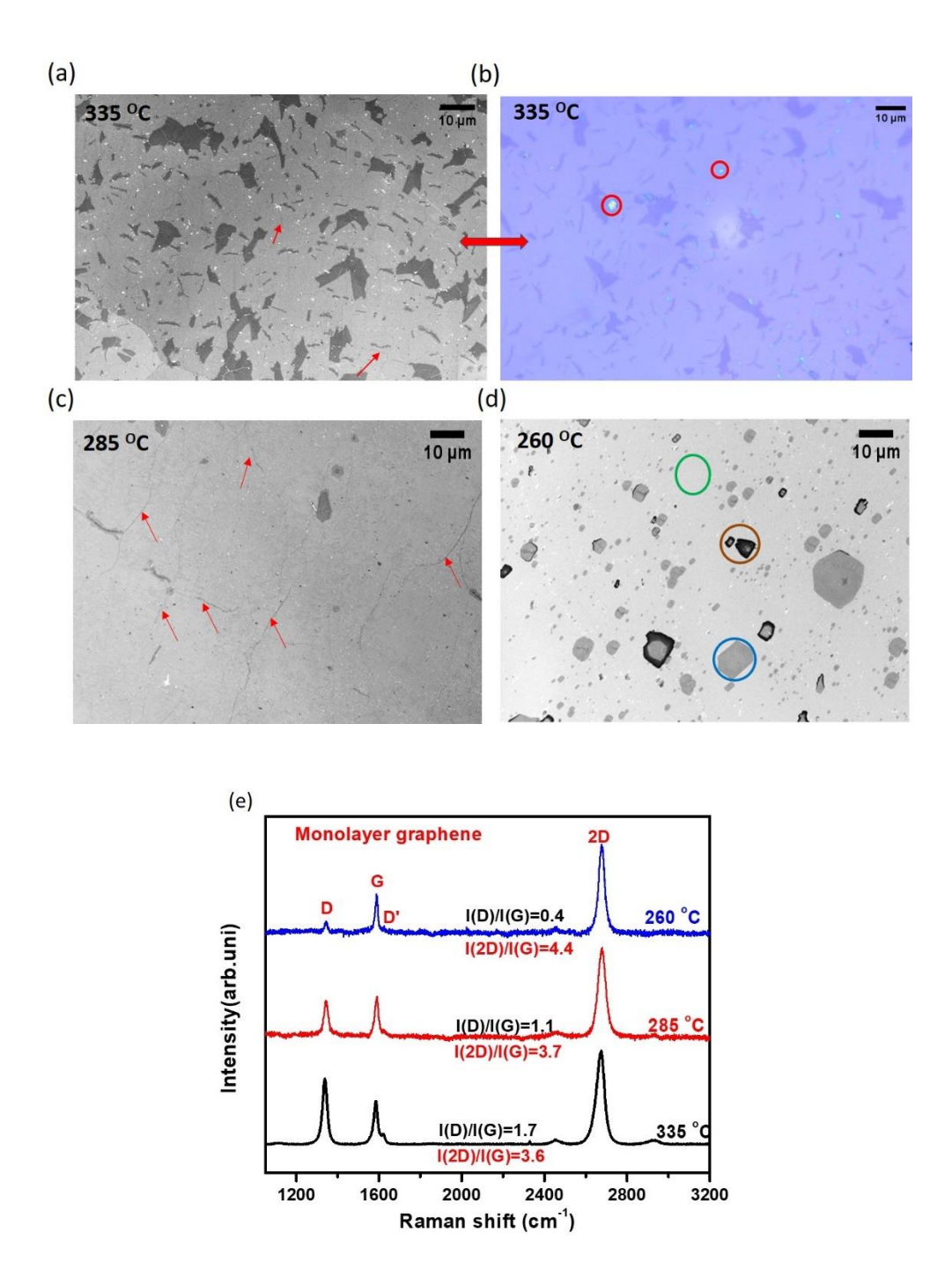


Figure 4.6 (a,c,d) FESEM and (b) optical images and Raman spectra of graphene films as a function of precursor temperature. FESEM micrographs of films grown by evaporating at (a) 335 °C, (c) 285 °C, (d) 260 °C. (b) An optical micrograph of film synthesized by evaporating at 335 °C. (e) Raman spectra of all films were recorded on only the thinnest layers, which were confirmed to be monolayers. Laser excitation used is 532 nm.

Figure 4.6 (c) shows the FESEM micrograph of graphene film grown by evaporating the PMMA at 285 °C. The image shows that the copper surface is completely covered by a thin layer of graphene film, which is a monolayer. The red arrows in the figures indicate the wrinkles on the film are the characteristic features that can be observed distinctly due to the different thermal expansion coefficients of Cu and graphene. It can be observed that the density of darker islands is very less compared to the film formed with PMMA evaporated at 335 °C. The decrease in the number of darker regions can be attributed to the low evaporation temperature of PMMA. The reduction in the evaporation temperature decreases the evaporation rate of PMMA. Consequently, fewer molecules were brought onto the copper substrate, reducing the film's growth rate. The evaporation temperature has been reduced further to 260 °C to obtain the individual grains or nucleations. Figure 4.6 (d) depicts the isolated graphene crystals with different contrast. The region in a green circle represents the bright regions that correspond to the bare copper. The blue circle denotes the light gray contrast, representing the thinnest layer, and the orange circle denotes the darker contrast indicating the thicker crystals. A huge distribution in crystal's lateral sizes is observed that varies from ~ 50 nm to ~ 15 μ m. The isolated crystals have been obtained due to the decrease in the rate of evaporation of PMMA further. An evaporation temperature of 260 °C produced the isolated crystals; therefore, it has been considered the minimum evaporation temperature for PMMA for all our experiments.

Raman measurements were performed after transferring the films to the SiO₂ substrate using a PMMA-wet transfer method to get information about the crystalline quality and number of layers. Only one optical image was shown in figure 4.6 (b) for reference that corresponds to the film grown by evaporating PMMA at 335 °C. Raman measurements were performed with a 532 nm laser excitation wavelength. Raman spectra were obtained on the thinnest layers of every film, as they covered a large part of the film and are common among all films. The Raman spectra of the thinnest layers of graphene film derived from PMMA are displayed in figure 4.6 (e). The two most prominent peaks, the G-band (in-plane vibrational E_{2g} mode) signature of the graphitic band and 2D-band second order of zone-boundary phonons, arises from a resonant second-order Raman process, are found in all spectra [9]. The peak positions of the G band and 2D bands are from 1585 cm⁻¹ to 1589 cm⁻¹ and 2673 cm⁻¹ to 2678 cm⁻¹, respectively. The shift in the positions can be attributed to the strain induced in the films due to the defective nature of the film. The number of layers can be determined by utilizing the ratio of the integrated intensity of the 2D band to the G

band (I(2D)/ I(G)), as well as the shape, position, and FWHM of the 2D band [10]. The bands were fitted with the Lorentzian function to obtain the FWHM, position, and area under the peaks. The I(2D)/I(G) ratios for films synthesized by evaporating PMMA at 335 °C, 285 °C, and 260 °C are 3.6, 3.7, and 4.4, which indicate the monolayer as the I(2D)/I(G) ratio greater than the 2.5 corresponds monolayer graphene [11]. We can observe that the ratio of I(2D)/I(G) increases as the evaporation temperature decreases can be attributed to the decrease in the D- band intensity. The reduction of defects also decreases the FWHM of 2D bands from 41.1 cm⁻¹ to 31.1 cm⁻¹. These numbers are within the range of reported values for monolayer graphene, which strongly confirms that the obtained spectra for the thinnest layers in the graphene film are monolayers.

The D and D' bands in Raman spectra are defect-induced, and the I(D)/I(G) ratio is used for defect density calculations. The peak position for the D band is at 1335 cm⁻¹, and the weak D' band's position is at 1625 cm⁻¹. The I(D)/ I(G) ratio for the film obtained by evaporating the PMMA at 335 °C is 1.7, which is higher than the films grown by the low evaporation temperatures of 285 °C and 260 °C. It is due to the film having more islands of crystals (varied in lateral sizes and thicknesses) on the monolayer, and their edges contribute to the D band. The ratio, I(D)/I(G), has reduced as the evaporation temperature of PMMA decreased owing to the decrease in the number of islands on monolayer graphene. At last, the isolated monolayer graphene crystals were obtained for 260 °C and showed the low D band. The D' band disappeared as the D peak decreased as it was a weak band.

We can corroborate from the FESEM micrographs and Raman spectra that the slowest growth rate for 5 minutes of graphene film is obtained when the precursor's evaporation temperature is at 260 °C. We obtained discontinuous graphene grains with low defects for this temperature, and a complete film was formed for different temperatures (285 °C & 335 °C). Hence, we have used 260 °C as an optimized evaporation temperature for the further optimization of other growth parameters to obtain high-quality large-area continuous graphene films.

4.3.2 Optimizing the flow rate

The large area of continuous graphene film should have minimum grain boundaries to be qualified as high-quality film. It implies that the film should have grown with low nucleation density and larger grains or crystals. The gaseous flow rate can control the nucleations and growth of graphene

grains/crystals [12]. Thus, we optimized the flow rate for graphene film grown at 1050 °C, 5 min, 1 mg PMMA evaporated at 260 °C to obtain the nucleations as low as possible. The flow rate was varied from 100 SCCCM of Ar/H₂ to 10 SCCM of Ar/H₂.

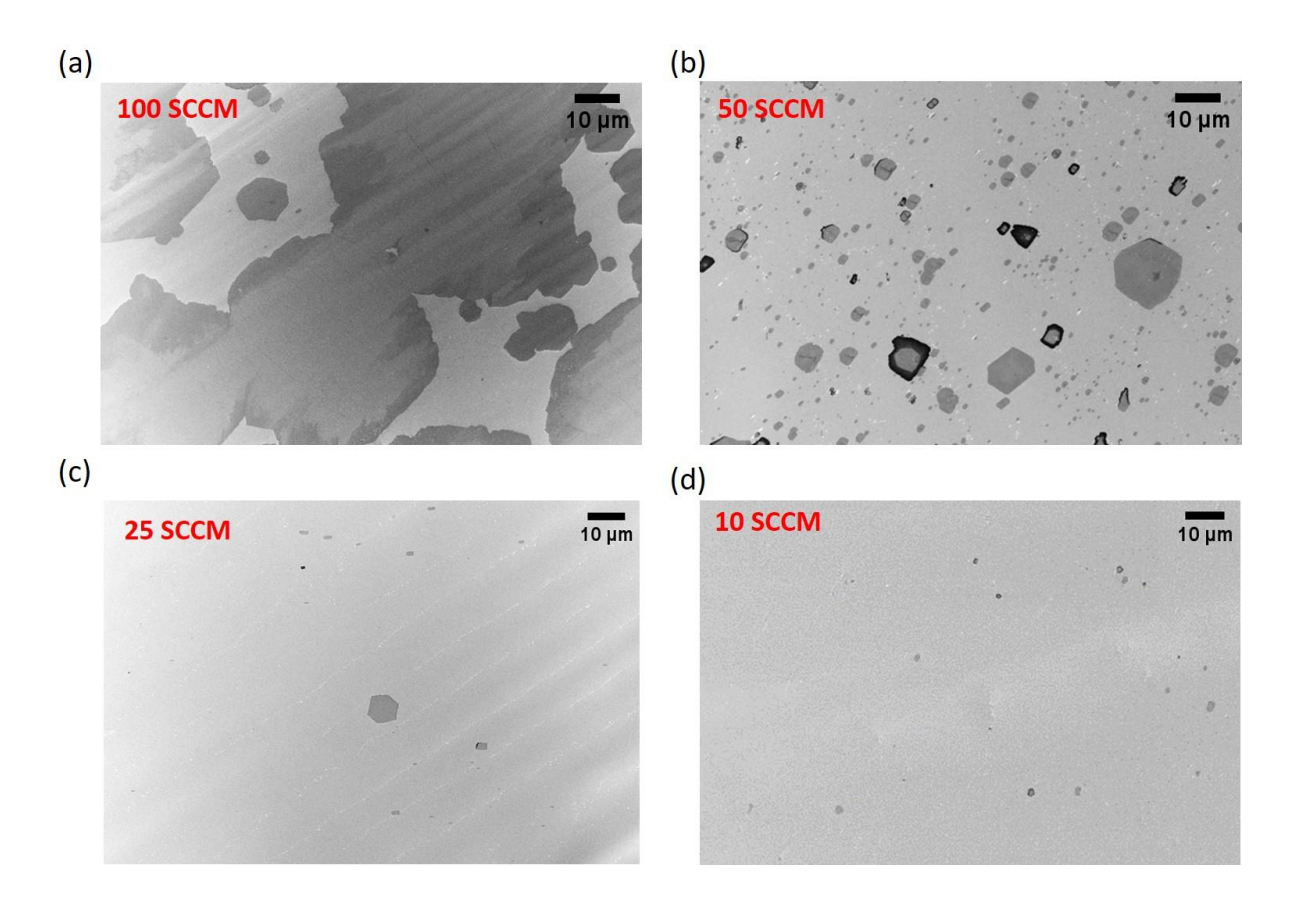


Figure 4.7 FESEM micrographs of graphene films synthesized at 1050 °C for **5 minutes** by evaporating the PMMA at 260 °C for different flow rates. (a) 100 SCCM, (b) 50 SCCM, (c) 25 SCCM, and (d) 10 SCCM of Ar/H₂.

The graphene films were synthesized for varied flow rates by using an optimized evaporation temperature of PMMA of 260 °C, and the FESEM micrographs are shown in figure 4.7. We can observe the graphene crystals having light gray contrast are monolayers with different lateral sizes in figure 4.7 (a), which was grown at 100 SCCM flow rate of Ar/H₂. The darker patches are on top of the edges of the monolayers, and it seems they have nucleated at the edges. These thicker layers grow toward the center of the monolayer from its edges. Most of these crystals have coalesced due to the high flow rate that increases the growth rate of the film. The flow rate was decreased to 50 SCCM of Ar/H₂ to obtain the isolated crystals. Figure 4.7 (b) shows that most of the crystals are

isolated, but the number of crystals is very high. To reduce the nucleation density, the flow rate was further decreased to 25 SCCCM of Ar/H₂. Figure 4.7 (c) shows that the number of nucleations has decreased compared to the 50 SCCM-grown films. The variation in the lateral sizes of the crystals has reduced compared to the crystals in the 50 SCCM film. Decreasing the flow rate from 25 to 10 SCCM produced nucleating sites that have similar in size, as shown in figure 4.7 (d). As the flow rate decreased, the crystals and their lateral size decreased due to the reduction in mass transport of precursor species toward the substrate. The flow rate also determines the shape of the crystals grown at high temperatures. The shapes of the crystals for 100 SCCM are close to the circle shapes. For 50 SCCM, the shapes of the crystals turned out to be truncated hexagonal structures. Further reduction in the flow rate produced the hexagonal and rectangular shapes. Obtaining the different shapes for varied flow rates is due to the competitive hydrogen etching effect [13]. The hydrogen assists in the chemical reaction of active carbon species for deposition on the metal and simultaneously etches deposited carbon atoms that lie at the edges of the domains/grains. As the 10 SCCM flow rate produced the minimum number of nucleating sites compared to all flow rates, thus it has been used as an optimized flow rate for the further growth of graphene film.

4.3.3. Optimizing the growth time:

The large-area continuous film with large-size graphene domains/crystals can be obtained by increasing the growth time while maintaining the low concentrations of both active carbon species and active sites on the Cu surface [14]. Here, we utilized the pre-annealing of electropolished copper, the low evaporation temperature of PMMA, and the low flow rate that produced the less active sites and active carbon species, resulting in a low number of nucleation sites. The graphene films were synthesized at 1050 °C, 10 SCCM flow rate, and 260 °C evaporation temperature of PMMA for various growth times. The different growth times used for graphene film growth are 5 minutes (min), 10 minutes, and 15 minutes. After the graphene growth on copper, the samples were oxidized in air at 250 °C on a hot plate for one minute to make the graphene crystals optically visible [15,16]. The graphene crystals covered sites were protected from oxidation, and bare copper got oxidized. Under an optical microscope, a clear contrast can be observed between the graphene-occupied sites and oxidized copper.

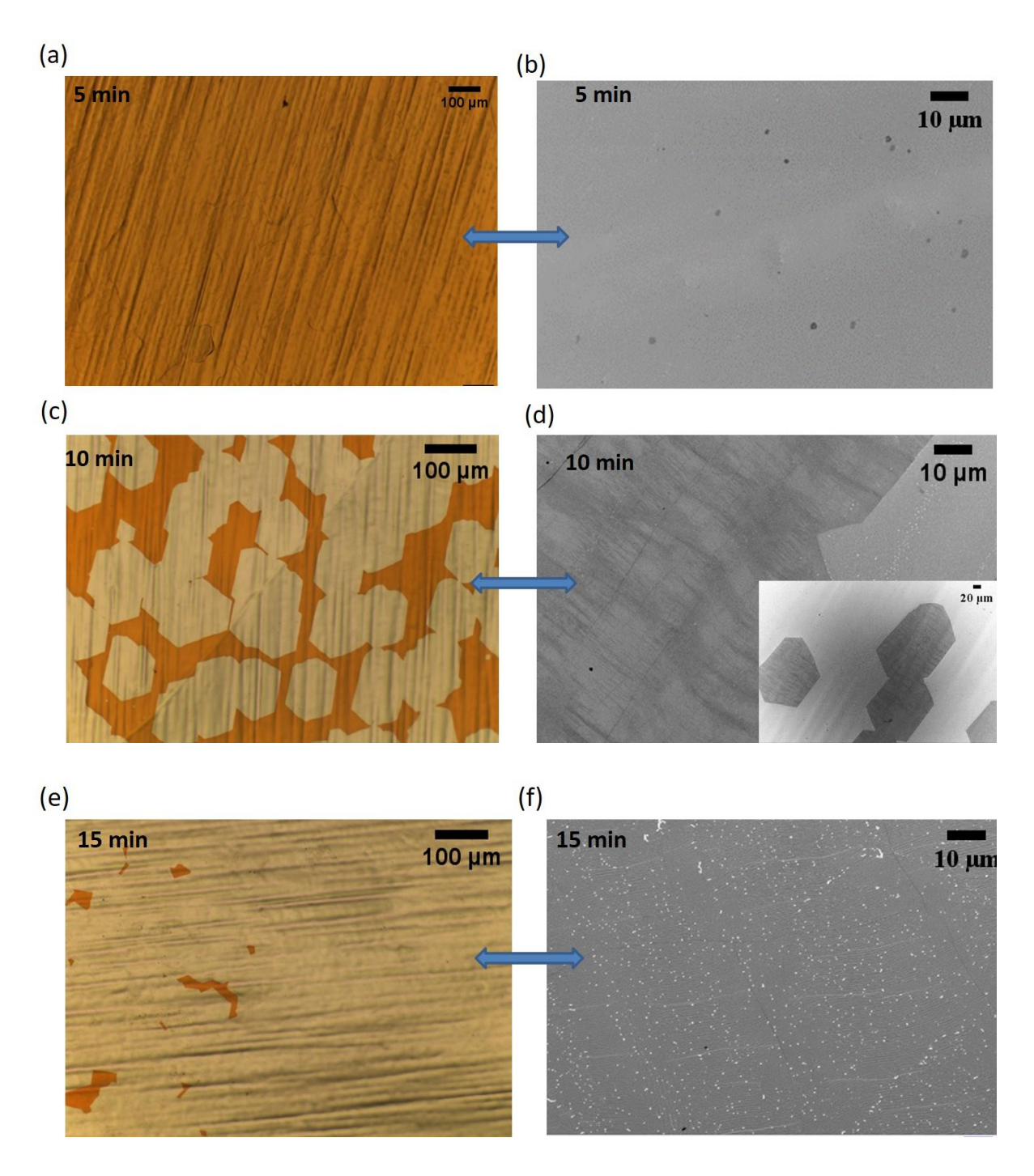


Figure 4.8 The optical and FESEM micrographs on copper of the graphene films synthesized at different growth times. The left panel images (a,c, and e) are optical images taken after the oxidation of the graphene/Cu, and the right (b,d, and f) are FESEM images. (a, b) 5 min, (c, d) 10 min, and (e,f) 15 min.

Figure 4.8 shows the optical and FESEM micrographs of the graphene film for different growth durations. Figures 4.8 (a) and (b) are the optical and FESEM images for 5 min film, respectively. The optical image shows that the copper surface is light brown, indicating it has been completely oxidized. It implies that there is no graphene over copper. But FESEM image figure 4.8 (b) shows that the graphene nucleations are on copper with lateral sizes of around nanometers. It can be inferred from the FESEM micrograph that the optical image could not resolve the nucleations as it has a low resolution compared to the FESEM. As mentioned in the flow rate section, the graphene grown with a 10 SCCCM flow rate for 5 minutes produced low nucleating sites with a size of around nanometers.

When the growth time was increased to 10 minutes, figure 4.8 (c), an optical image shows two contrasts in the film. The areas with brownish color indicate copper oxide where there is no graphene. The light yellowish color represents non-oxidized copper, in which the graphene is there. We can observe the hexagonal-shaped domains in these areas, some of which have coalesced together to become larger domains. The largest isolated single crystal size among isolated graphene crystals is 180 ±5 µm. The same film has been used to obtain the FESEM image, as shown in figure 4.8 (d). we can observe the two coalesced domains. On top of a graphene crystal, light dark shades indicate the presence of more layers. In the inset, the lower magnification image was shown, where we can observe graphene crystals similar to the optical image. The increase in crystal sizes for 10 min growth compared to the 5 min is due to the constant transport of active carbon reactive species to the substrate. The growth time was increased to 15 min to obtain the continuous graphene films by maintaining all other growth parameters constant. In an optical image figure, 4.8 (e), only a tiny area has been oxidized where we can observe the light brown color, and the remaining area is covered with graphene. The FESEM image from the same film is shown in figure 4.8 (f), where we can observe continuous graphene film. We can observe the wrinkles on the film. The bright particles on the film are of SiO2. Comparing the FESEM image of 15 min film to 10 min film, we can observe that there is no contrast on the film due to the etching of top layers by the H₂ gas. The constant flow of active carbon species towards the substrate occurs as time increases. These carbon adatoms attach to the carbon atoms at the edges of crystals, increasing the domains' size and merging to form a continuous film.

The films grown for 10 min and 15 min were transferred to the SiO₂ substrates for Raman measurements. Figure 4.9 (a) and (b) show optical images of graphene films of 10 min and 15 min, respectively. The hexagonal crystal can be seen in figure 4.9 (a), and it has been noticed from FESEM images in figure 4.8 (b) that isolated crystals were obtained for 10 min growth time. The PMMA residues with blue color lying on top of the crystal are denoted by the red arrow mark. The crystal size is around 180 µm. The continuous graphene film is observed in figure 4.9 (b) for 15 min growth time, which can be correlated with the FESEM image of figure 4.8 (d), where we observed the continuous film. The black arrows indicate the wrinkles on the film that exist on graphene films synthesized from CVD.

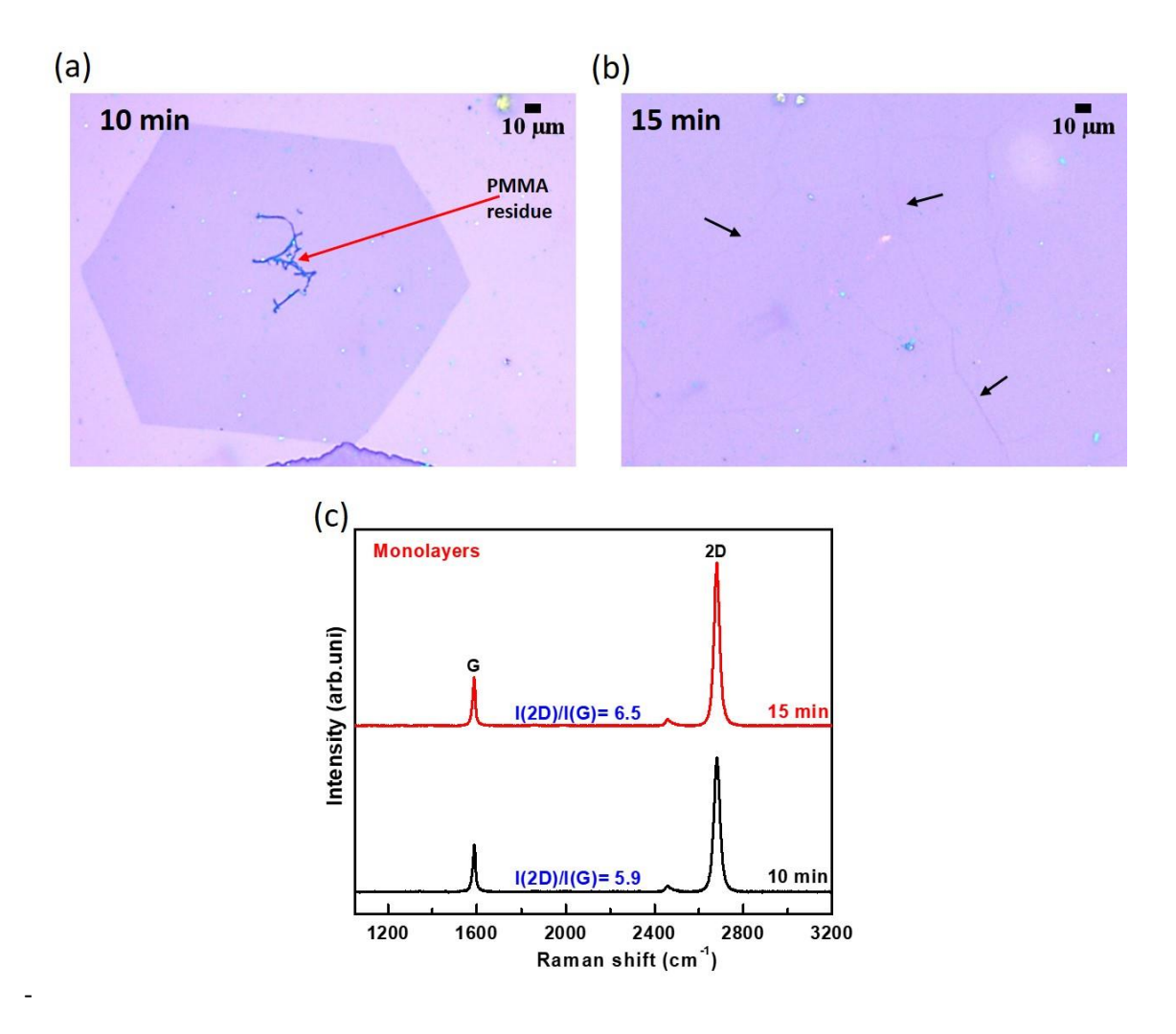


Figure 4.9 optical images of transferred graphene on SiO₂. (a) 10 min. (b) 15 min. (c) Raman spectra of both films of 10 min and 15 min.

Figure 4.9 (c) shows the Raman spectra of graphene film of 10 min and 15 min growth. The spectrum is the characteristics of five locations recorded over the cleanest positions of a sample. G and 2D bands are the characteristic bands of graphene. The peak positions of the G-band are 1587.9 cm⁻¹ and 1587.0 cm⁻¹ for 10 min and 15 min, respectively. For the 2D band, the peak positions are observed at 2681.2 cm⁻¹ and 2680.3 cm⁻¹ for 10 min and 15 min, respectively. The shift in the G and 2D bands to lower wave numbers as the growth time increases is due to the strain induced in the films by the substrate [17]. The ratio of I(2D)/I(G) for 10 min and 15 min graphene films are 5.9 and 6.5, respectively, indicating that they are monolayer graphene as their intensity is more than 2.5 [18]. The full width at half maximum (FWHM) of the 2D band for 10 min and 15 min films are 28.4 cm⁻¹ and 26 cm⁻¹, respectively, representing the monolayer. The absence of a D band in both films indicates they are high-quality films. The increase in the I(2D)/I(G) ratio and reduction in the FWHM of the 2D band from 10 min to 15 min film can be attributed to the increase in the crystallinity in the film.

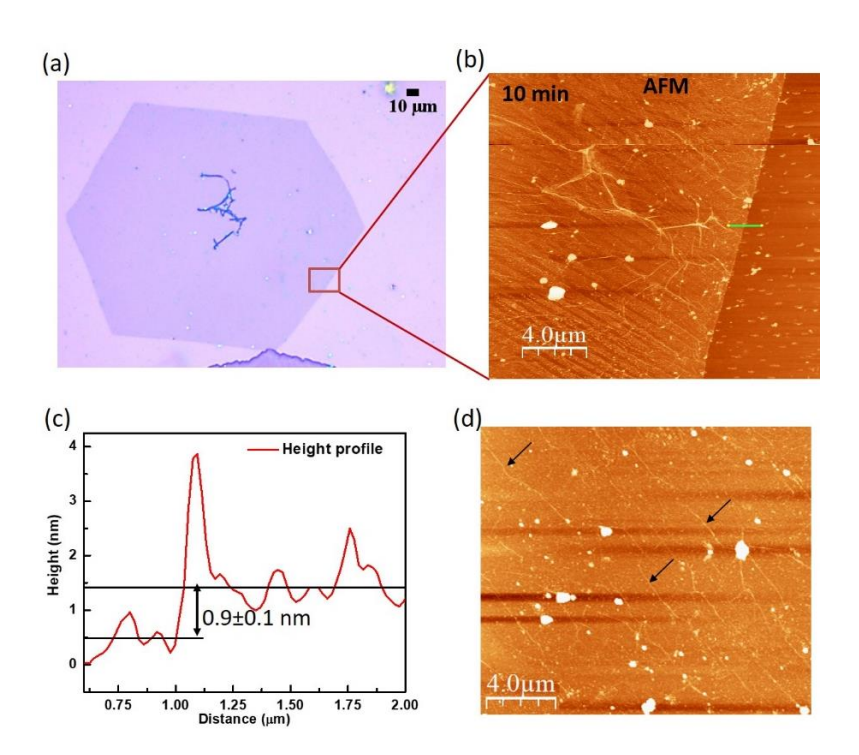


Figure 4.10 graphene film grown for 10 min and 15 min was used for AFM measurements. (a) optical image for 10 min and the area in the red box is used for thickness measurement. (b) Thickness was measured at the edge of the film using AFM. (c) The thickness profile of the film. (d) The topography of the film was measured on the basal plane of the crystal.

The transferred 10 min and 15 min film was utilized for AFM measurements to understand the topography and determine the thickness. Figure 4.10 shows the optical and AFM images of the 10 min graphene film that contains the crystals. The area where the AFM measurement was performed is shown in the red box drawn in the optical image shown in figure 4.10 (a). The AFM-obtained topography at the edge of the film is presented in figure 4.10 (b). The thickness measured for ten places at the edge is represented with one green line in figure 4.10 (b). The average thickness of the graphene crystal is displayed in figure 4.10 (c). The average thickness of the crystal is 0.9 ± 0.1 nm indicating that it is monolayer graphene [19]. Figure 4.10 (d) shows the topography of the monolayer graphene film grown for 15 min, which is continuous. The black arrows are shown toward the wrinkles. The bright particles are residues of PMMA left over after the transfer.

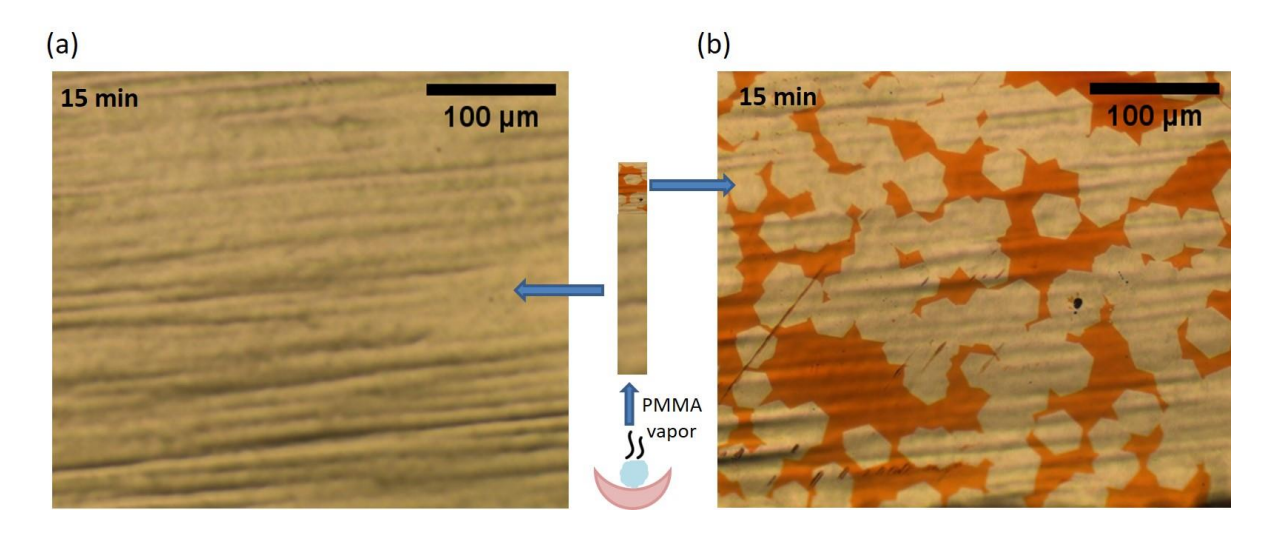


Figure 4.11 Optical images of the graphene film synthesized at 1050 °C, 15 min at 10 SCCM ar/H₂. A representative figure is shown between two images, (a) and (b), where the PMMA vapor is evaporated towards the copper substrate. The regions of copper are indicated with arrows. (a) continuous graphene film. (b) discontinuous graphene.

It was observed that the graphene film did not cover the portions of copper far away from the PMMA precursor, as shown in figure 4.11. The optical images shown in figure 4.11 are graphene on copper captured after oxidation. We notice that most of the area is covered with continuous graphene, and only the region far away from the PMMA has not been completely covered. The representative schematics are shown between two images where the PMMA vapor is directed

toward the copper, shown by the arrow mark. The region with the left arrow indicated is shown in Figure 4.11 (a), where it is a continuous graphene film as the copper has not been oxidized. The region with the right arrow indicated is shown in figure 4.11 (b), which has discontinuous graphene film, as some parts of the area have been oxidized. The oxidized areas have a brown color representing copper oxide, and non-oxidized areas are covered with graphene. We can notice in the film that some graphene crystals have coalesced, and a few are individual. The region far away from PMMA not covered with graphene completely implies that it has not obtained sufficient reactive carbon species to make a continuous film for a growth time of 15 minutes, and simultaneously etching is also occurring due to H_2 gas. Thus the growth has to be increased further to observe complete coverage.

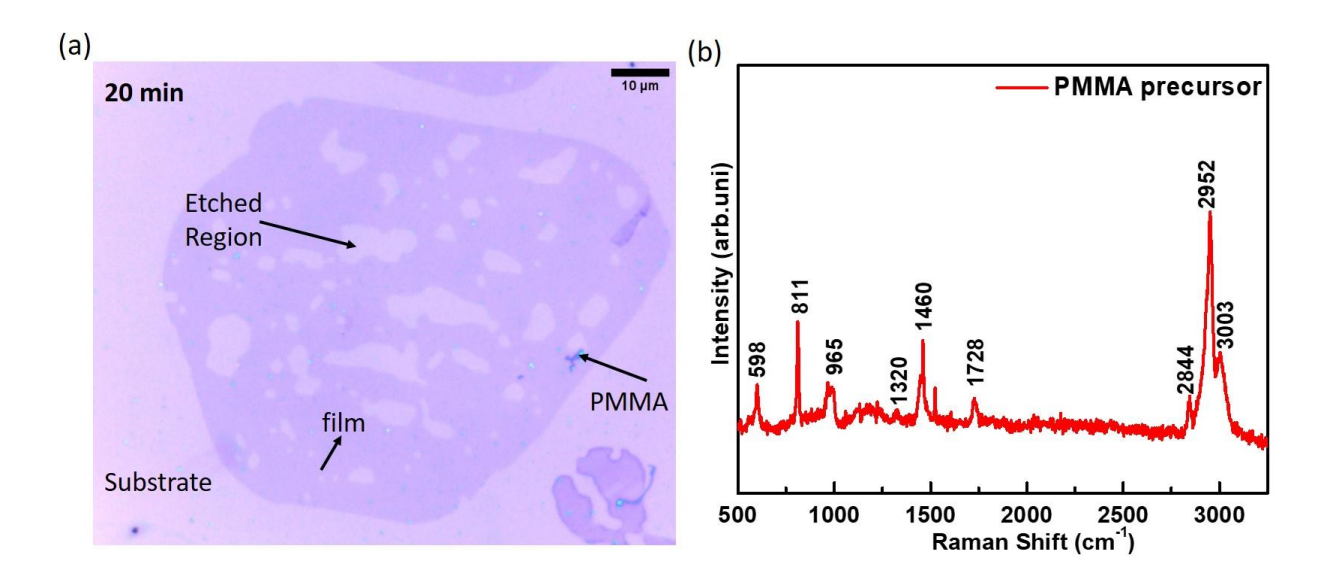


Figure 4.11 (a) an optical image of graphene film grown for 20 min. (b) Raman spectrum of leftover PMMA after 20 min growth.

The growth time was increased to 20 min to obtain the continuous film. It was observed that the film had been etched, as shown in figure 4.11 (a). The area with one contrast is represented by the substrate in the image, and the other contrast with the film is indicated by the arrow, as shown in figure 4.11 (a). The blue contrast indicated by the arrow is PMMA residue. The random etching is observed in the film. It can be inferred that the film had been etched due to the H₂ etching effect, and it became dominant as the carbon influx toward the substrate is arrested after 15 min growth time. However, the PMMA precursor powder has not evaporated completely after 20 min growth.

Therefore, it suggests that either PMMA might have turned into a carbonized form or polymerized further. To confirm that, the Raman measurements were carried out to obtain the chemical structure information of leftover PMMA. The Raman spectrum of leftover PMMA is shown in figure 4.11 (b). The obtained peak positions are 598, 811, 965, 1320, 460, 1728, 2844, 2952, and 3000 cm⁻¹. The strongest peak positions are 811 cm⁻¹, 1460 cm⁻¹, and 2952 cm⁻¹ match the existing literature on Raman bands of PMMA [20]. This indicates that the leftover precursor powder is PMMA, and it is polymerizing besides evaporating. The evaporation was arrested completely after the growth time of 15 minutes. The complete polymerization of PMMA with high molecular weight led to no evaporation at the same temperature. Therefore, the PMMA amount has been increased to increase the time for complete polymerization. By that time, the film will be covered completely.

4.3.4 Optimizing the amount of PMMA precursor

The amount of PMMA powder has been increased from 1 mg to 2mg and 3mg to obtain the continuous graphene films with the optimized growth parameters. The evaporation temperature of PMMA was maintained at 260 °C. The growth temperature was 1050 °C flow rate was 10 SCCM, and a growth time of 20 minutes was utilized for growth. The synthesized films were transferred onto SiO₂ for optical images and Raman measurements. Figure 4.12 displays the optical images and Raman spectra of all films. The graphene obtained for 20 min growth with 1mg PMMA, shown in figure 4.12 (a), has been subjected to etching, as it had been discussed already. The amount of PMMA powder was increased to 2 mg to obtain the continuous film for 20 min growth. The optical image shown in figure 4.12 (b) is of graphene film grown by 2mg. It shows that the film is continuous, with most of the area having the same color contrast. This continuous film was found to be a monolayer, confirmed by Raman spectroscopy. We can observe the wrinkles on the film, which are characteristic features of graphene. The hexagonal crystal having higher color contrast can be observed in the film, which is a second layer. These layers result from secondary nucleations that grow in the areas where the monolayer crystals grow and merge to form a continuous film. However, there are conflicting reports in the literature on the nature of nucleations. Robertson et al. reported that the secondary layers occur on top of the monolayer, as supported by atomic force microscopy (AFM) [21]. But, the same surface profile can also exist for the nucleation when they are under the first layer. Moreover, other groups have reported that the additional layers can grow

under the first layer, where copper can catalyze the growth with the support of the reactive carbon species diffusing through the edge of the first layer crystals [22,23].

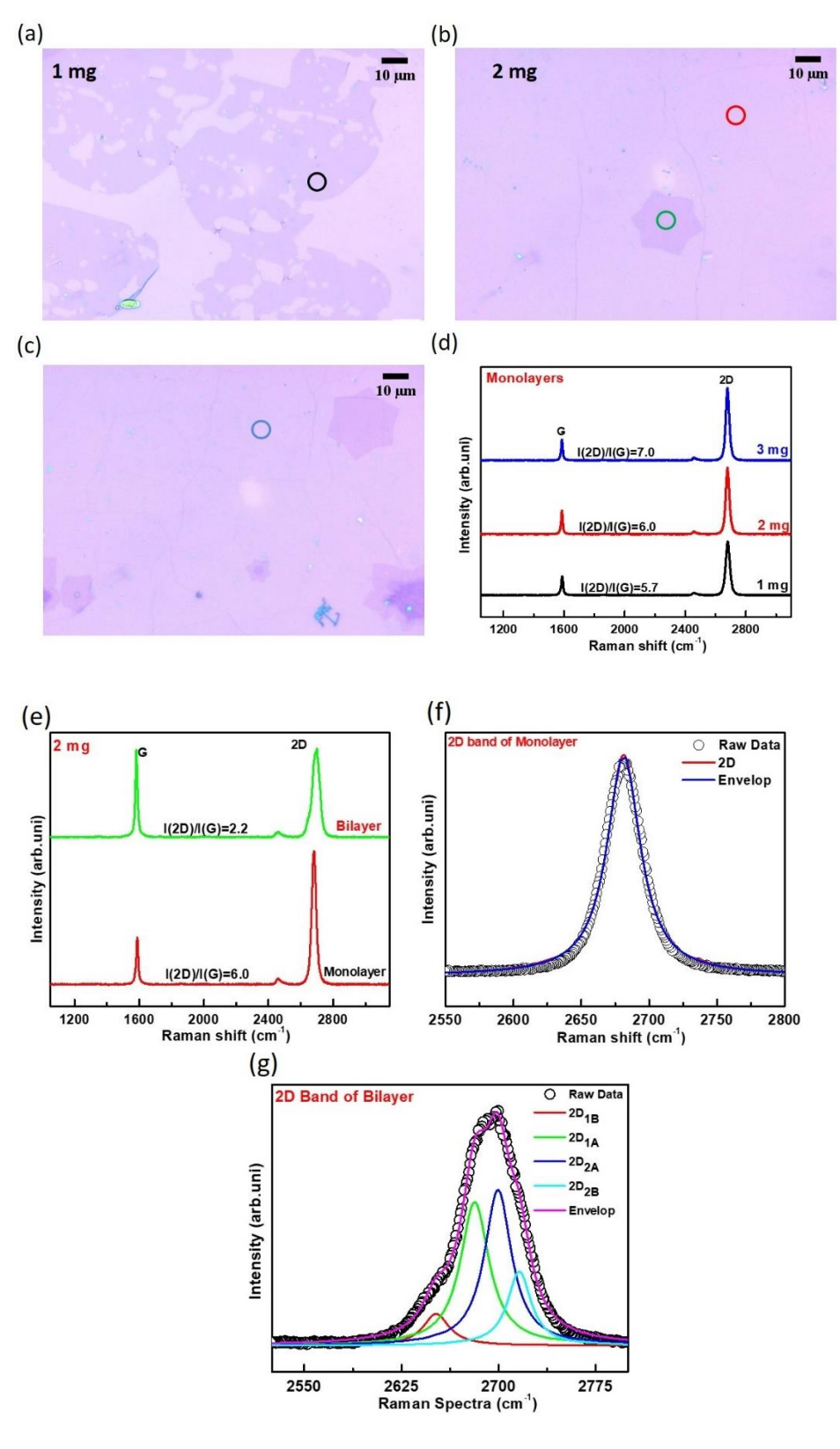


Figure 4.12 Optical images of graphene films synthesized with a varied amount of PMMA powder for optimized growth conditions. (a) 1mg. (b) 2 mg. (c) 3 mg. (d) Raman spectra of all graphene films synthesized at varied PMMA amounts. The black, red, blue, and green circles represent the positions where Raman measurements were taken and are shown in the optical image. (e) Raman spectra were obtained for the graphene film grown with 2 mg. Raman fittings for the layers obtained in the film were synthesized using 2 mg PMMA. 2D peak fitting of monolayer (f) and bilayer (g).

The second layer might have grown on top or below the first layer. The intake of carbon species has been arrested as the growth time has ended, leading to the growth of the second layer getting stopped. Therefore, the secondary nucleation results in smaller crystals. The obtained crystal size of the second layer of the film in figure 4.12 (b) is $20 \pm 4 \,\mu m$. Figure 4.12 (c) shows the optical micrograph of graphene film synthesized using 3 mg. The surface is covered completely by a single layer having wrinkles. The number of secondary nucleations grown into hexagonal crystals can be noticed in the figure, and they are more in number than the graphene grown using 2 mg. Tertiary nucleations are also observed under/above the second layer. The tertiary nucleation appears at the center of the secondary nucleated hexagonal crystal. The increase in the growth of adlayers under the first layer can be attributed to the increase in the amount of powder, as it increases the availability of active carbon species that will diffuse through the first layer crystals until they coalesce.

The Raman measurements were carried out on all the graphene films synthesized for different amounts of powder. The positions where Raman measurements were recorded are shown in circles (black, red, and blue) on all optical micrographs. Figure 4.12 (d) shows the Raman spectra of graphene films. The absence of the D band for all spectra indicates that they are high-quality graphene films. The quality of the graphene film synthesized for 1 mg is also high even though the graphene has been etched because the Raman measurements were performed on the non-etched regions of graphene. The peak positions of the 2D band are 2681.1 cm⁻¹, 2679.8 cm⁻¹, and 2679.5 cm⁻¹ for the monolayered graphene films synthesized at 1 mg, 2 mg, and 3 mg, respectively. The shift in the 2D band positions is attributed to the strain in the film that occurred due to transfer. The obtained I(2D)/I(G) ratios for graphene films synthesized from 1 mg, 2 mg, and 3 mg are 5.7,

6.0, and 7.0, respectively, and FWHM of the 2D band in the range of 24-29 cm⁻¹ indicates that the positions where Raman measurements were recorded are monolayers. It can be observed that these monolayers covered a large area of the film, as it has the same optical contrast in the film. On top of it or below, secondary or tertiary crystals can also be observed from optical micrographs. Thus, the Raman measurements were performed on the secondary nucleated crystal for 2 mg grown film and compared with the monolayer Raman spectrum of the same film.

The Raman fittings were shown for continuous film, and hexagonal crystal for the film synthesized using 2 mg PMMA in figure 4.12 (f) and (g). The red and green circle represents where Raman measurements were performed. Figure 4.12 (e) shows the Raman spectra of the graphene film measured for different layers. The Raman spectrum obtained from the red circle indicates the monolayer graphene as the I(2D)/I(G) ratio is 6.0, which is greater than 2.5. It was reported that the crystals nucleated under or above the monolayer graphene might sometimes not follow the Ab stacking order. They have different orientations than the monolayer, forming a twist angle between them. Suppose the twist angle is less than 8° between two layers. In that case, the strong coupling between layers is manifested in the 2D band of Raman spectra. For more than 13° the double layers depict the Raman spectra close to that of the single-layer Raman signature [24]. Here, the Raman spectrum on the hexagonal crystal produced I(2D)/I(G) ratio is 2.2, indicating that it is a bilayer graphene as the value is less than 2.5. and it follows the AB staking as the line shape of the 2D band is asymmetric that can be deconvoluted into four components. The peak positions of the 2D band of monolayer and bilayer are 2681.1 cm⁻¹ and 2693.9 cm⁻¹. The blue shift of the 2D band position is attributed to an increase in the number of layers [25]. Therefore, the 2D peak is upshifted from monolayer to bilayer. The electronic band structure of graphene layers strongly influences the 2D band due to the double resonance process. The shift in the 2D band is due to variations in the electronic band structure as the layer number increases.

The line shape of the 2D band also is utilized to determine the number of layers. The 2D peak is single, sharp and symmetric for the monolayer. It was fitted with a single Lorentzian function as shown in figure 4.12 (f). The FWHM of this band is around 28.3 cm⁻¹. This peak is roughly four times more intense than the G band in the spectrum. The 2D band of the bilayer is much broader and upshifted compared to the 2D band of the monolayer. It has asymmetry in the peak, which can be deconvoluted into four peaks, as shown in figure 4.12 (g). The components shown in the figure

are $2D_{1B}$, $2D_{1A}$, $2D_{2A}$, and $2D_{2B}$, in which $2D_{2A}$ and $2D_{1A}$ have higher relative intensities than the other two. The evolution of the four components in the 2D band for bilayer graphene can be attributed to the splitting of electronic bands occurring due to strong coupling between two layers and leading to π and π^* bands dividing into four bands. The possibility of four optical transitions gives rise to four components in the 2D band for bilayer graphene [26]. Therefore, It can be concluded that the hexagonal crystal is following AB stacking with the monolayer. We can conclude that the high-quality large-area continuous graphene film has been obtained at 1050 °C, 20 min, 10 SCCM for 2 mg as it has less number of secondary nucleated crystals.

4.3.5. Temperature-dependent growth of graphene

The graphene films were synthesized at different temperatures to investigate the formation of graphene as the PMMA decomposes at lower temperatures. The graphene films were grown at 850 °C and 650 °C with optimized growth conditions like the amount of precursor (2mg), growth time (20 min), and evaporation temperature of PMMA (260°C). The grown films are shown in figure 4.14, which contains optical images and Raman spectra. Figure 4.14 (a) is an optical image of the film grown at 850 °C. The film contrast in figure 4.14 (a) is much higher compared to the monolayer graphene contrast shown in figure 4.13 (a). This indicates that the grown film is of higher thickness. The contrast variation at different positions can be attributed to the not uniformity in the thickness of the film. The wrinkles in the film can be seen distinctively, and they are the distinctive aspects of the graphene film, as mentioned in earlier sections.

The growth temperature was reduced from 850 °C to 650 °C to understand the evolution of the graphene film. Figure 4.14 (b) shows the optical image of graphene film synthesized at 650 °C. Most of the area in the film has one contrast except a few positions where low contrast can be seen. It can be inferred that the film has nonuniformity in thickness. The particles with blue color are the PMMA residues on the film. The grown films were characterized with Raman spectroscopy to understand the chemical nature of the film. The Raman spectrum of 850 °C film shows that it is a completely graphitized film, as it has G and 2 Band with narrow FWHM. The peak positions of D, G, and 2D bands are around 1352.1 cm⁻¹, 1582.8 cm⁻¹, and 2692.8 cm⁻¹, respectively. The presence of the D band represents the film has defective nature that arises due to the edges of the

top layer that has not been completely covered. The film's I(2D)/I(G) ratio is 1.4 and can be considered trilayer graphene. The Raman spectrum of the graphene film that has been synthesized at 650 °C shows the broad D and G bands and suppressed 2D bands. The peak positions of the D and G bands of this film are around 1356 cm⁻¹ and 1590 cm⁻¹. The broadening of the G band and suppressed 2D band intensity can be ascribed to the decrease in the film's crystallinity. Therefore, this film represents the nanocrystalline graphene film, and the film's Raman bands are similar to the nanocrystalline film reported in the literature [27]. The nanocrystalline nature of the film caused more intensity to the D band. As the D band intensity increases and broadens, the 2D band's intensity gets suppressed. Further investigation is needed to understand the evolution of the crystallinity of the graphene film at 650 °C.

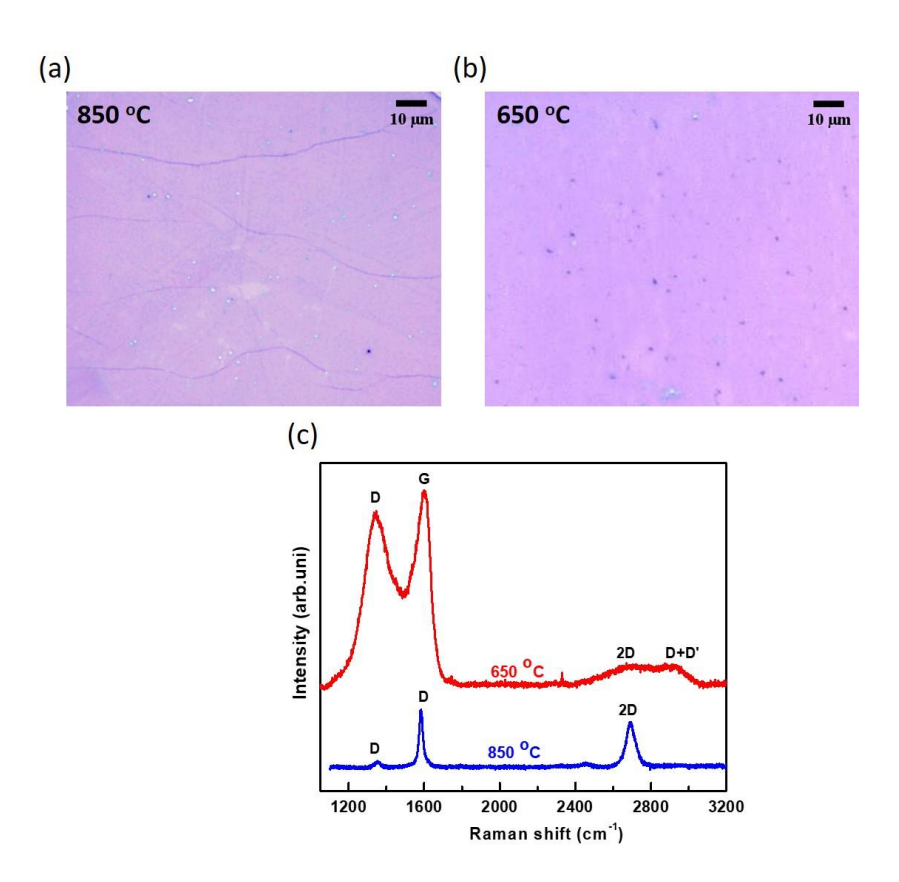


Figure 4.14 optical micrographs of graphene films synthesized at 850 °C (a) and 650 °C (b). (c) Raman spectra of both films.

4.4 Conclusion:

The pristine graphene has been synthesized successfully over copper foil at 1050 °C via APCVD using PMMA as a precursor. The evaporation temperature of PMMA has been optimized to get low evaporation. The growth parameters, such as flow rate and growth time, have been optimized to obtain the nucleations, crystals, and continuous film. The films were characterized with microscopic and spectroscopic techniques to gain insights into the film's morphology and physicochemical properties. A large-sized graphene crystal is around 200 µm obtained. It was found that the PMMA is evaporating and polymerizing simultaneously, leading to the cessation of PMMA vapor after some time. The amount of PMMA has been optimized to get the continuous film. The thickness of the monolayer graphene obtained around 0.5 nm. The temperature-dependent growth graphene has been investigated by employing APCVD. We have obtained nanocrystalline graphene film at 650 °C.

4.5 References:

- [1] K. S. Novoselov et al 2016 Electric Field Effect in Atomically Thin Carbon Films **306** 666–9
- [2] Luo D, Wang M, Li Y, Kim C, Yu K M, Kim Y, Han H, Biswal M, Huang M, Kwon Y, Goo M, Camacho-Mojica D C, Shi H, Yoo W J, Altman M S, Shin H J and Ruoff R S 2019 Adlayer-Free Large-Area Single Crystal Graphene Grown on a Cu(111) Foil *Adv. Mater.* **31** 1–13
- [3] Jin S, Huang M, Kwon Y, Zhang L, Li B W, Oh S, Dong J, Luo D, Biswal M, Cunning B V., Bakharev P V., Moon I, Yoo W J, Camacho-Mojica D C, Kim Y J, Lee S H, Wang B, Seong W K, Saxena M, Ding F, Shin H J and Ruoff R S 2018 Colossal grain growth yields single-crystal metal foils by contact-free annealing *Science* (80-.). **362** 1021–5
- [4] Mohd Farid D A, Zahari N A H, Said Z, Ghazali M I M, Hao-Ern L, Mohamad Zol S, Aldhuwayhi S and Alauddin M S 2022 Modification of Polymer Based Dentures on Biological Properties: Current Update, Status, and Findings *Int. J. Mol. Sci.* 23
- [5] Sun Z, Yan Z, Yao J, Beitler E, Zhu Y and Tour J M 2010 Growth of graphene from solid carbon sources *Nature* **468** 549–52
- [6] Growth L, Vapor C, Using D and Sources L C 2011 Low-Temperature Growth of Graphene by Chemical Vapor Deposition Using Solid and Liquid Carbon Sources 3385–90
- [7] Kairi M I, Khavarian M, Mohamed A R and Bakar S A 2018 Recent trends in graphene materials synthesized by CVD with various carbon precursors *J. Mater. Sci.* **53** 851–79

- [8] Lisi N, Dikonimos T, Buonocore F, Pittori M, Mazzaro R, Rizzoli R, Marras S and Capasso A 2017 Contamination-free graphene by chemical vapor deposition in quartz furnaces *Sci. Rep.* **7** 1–11
- [9] Malard L M, Pimenta M A, Dresselhaus G and Dresselhaus M S 2009 Raman spectroscopy in graphene *Phys. Rep.* **473** 51–87
- [10] Graf D, Molitor F, Ensslin K, Stampfer C, Jungen A, Hierold C and Wirtz L 2007 Spatially resolved raman spectroscopy of single- and few-layer graphene *Nano Lett.* **7** 238–42
- [11] Bhaviripudi S, Jia X, Dresselhaus M S and Kong J 2010 Role of kinetic factors in chemical vapor deposition synthesis of uniform large area graphene using copper catalyst *Nano Lett.* **10** 4128–33
- [12] Yan Y, Nashath F Z, Chen S, Manickam S, Lim S S, Zhao H, Lester E, Wu T and Pang C H 2020 Synthesis of graphene: Potential carbon precursors and approaches *Nanotechnol*. *Rev.* **9** 1284–314
- [13] Zhang X, Ning J, Li X, Wang B, Hao L, Liang M, Jin M and Zhi L 2013 Hydrogen-induced effects on the CVD growth of high-quality graphene structures *Nanoscale* **5** 8363–6
- [14] Yan Z, Lin J, Peng Z, Sun Z, Zhu Y, Li L, Xiang C, Loi E, Kittrell C and Tour J M 2012 Toward the Synthesis of Wafer-Scale *ACS Nano* **6** 9110–7
- [15] Chen S, Brown L, Levendorf M, Cai W, Ju S, Edgeworth J, Ruoff R S and Al C E T 2011 Oxidation Resistance of Graphene- Coated Cu and Cu / Ni Alloy 1321–7
- [16] Wang H, Wang G, Bao P, Yang S, Zhu W, Xie X and Zhang W J 2012 Erratum: Controllable synthesis of submillimeter single-crystal monolayer graphene domains on copper foils by suppressing nucleation. (Journal of the American Chemical Society (2012) 134 (3627-3630) (DOI: 10.1021/ja2105976)) *J. Am. Chem. Soc.* **134** 18476
- [17] Jafari A, Alipour R and Ghoranneviss M 2015 The effects of growth time on the quality of graphene synthesized by LPCVD *Bull. Mater. Sci.* **38** 707–10
- [18] Verguts K, Vermeulen B, Vrancken N, Schouteden K, Van Haesendonck C, Huyghebaert C, Heyns M, De Gendt S and Brems S 2016 Epitaxial Al2O3(0001)/Cu(111) Template Development for CVD Graphene Growth *J. Phys. Chem. C* **120** 297–304
- [19] Shearer C J, Slattery A D, Stapleton A J, Shapter J G and Gibson C T 2016 Accurate thickness measurement of graphene *Nanotechnology* **27**
- [20] Thomas K J, Sheeba M, Nampoori V P N, Vallabhan C P G and Radhakrishnan P 2008 Raman spectra of polymethyl methacrylate optical fibres excited by a 532 nm diode pumped solid state laser *J. Opt. A Pure Appl. Opt.* **10**
- [21] Robertson A W and Warner J H 2011 Hexagonal single crystal domains of few-layer graphene on copper foils *Nano Lett.* **11** 1182–9

- [22] Nie S, Wu W, Xing S, Yu Q, Bao J, Pei S S and McCarty K F 2012 Growth from below: Bilayer graphene on copper by chemical vapor deposition *New J. Phys.* **14**
- [23] Nie S, Walter A L, Bartelt N C, Starodub E, Bostwick A, Rotenberg E and McCarty K F 2011 Growth from below: Graphene bilayers on Ir(111) *ACS Nano* **5** 2298–306
- [24] Kim K, Coh S, Tan L Z, Regan W, Yuk J M, Chatterjee E, Crommie M F, Cohen M L, Louie S G and Zettl A 2012 Raman spectroscopy study of rotated double-layer graphene: Misorientation-angle dependence of electronic structure *Phys. Rev. Lett.* **108** 1–6
- [25] Yoon D, Moon H, Cheong H, Choi J S, Choi J A and Park B H 2009 Variations in the Raman spectrum as a function of the number of graphene layers *J. Korean Phys. Soc.* **55** 1299–303
- [26] Ferrari A C, Meyer J C, Scardaci V, Casiraghi C, Lazzeri M, Mauri F, Piscanec S, Jiang D, Novoselov K S, Roth S and Geim A K 2006 Raman spectrum of graphene and graphene layers *Phys. Rev. Lett.* **97** 1–4
- [27] Jerng S K, Yu D S, Kim Y S, Ryou J, Hong S, Kim C, Yoon S, Efetov D K, Kim P and Chun S H 2011 Nanocrystalline graphite growth on sapphire by carbon molecular beam epitaxy *J. Phys. Chem. C* **115** 4491–4

Chapter-5

Synthesis of Nitrogen-Doped Graphene by CVD

This chapter deals with the synthesis of nitrogen-doped graphene on copper from a solid carbon precursor, Phthalocyanine (Pc) and copper phthalocyanine (CuPc), by atmospheric pressure CVD (APCVD). The Pc as a precursor was used for the first time to grow Nitrogen-doped graphene (NDG). A large area of continuous Nitrogen-doped graphene (NDG) films was obtained. The study was conducted on the impact of the growth parameters (temperature, time, and carrier gas) on the NDG film's surface morphology, dopant configurations, and concentrations. The nitrogen-doped graphene films were grown at various temperatures of 1050 °C, 950 °C, and 850 °C for different growth times of 5 -15 minutes in the presence of an Ar+H₂ gas mixture. The presence of graphitic, pyrrolic, and pyridinic kinds of nitrogen dopant configuration was confirmed by X-ray photoelectron spectroscopy. AFM, FESEM, Raman, and optical measurements were performed on these films to get insights into the film's morphology, topography, crystallinity, and thickness.

5.1 Introduction

Since the discovery of graphene, it has attracted the scientific community and industrialists for its distinct physicochemical properties and potential applications[1–3]. Pristine graphene is semimetallic in nature in which the valence band and conduction band touch each other at K and K' points in reciprocal space. The absence of the bandgap is a hindrance to potential applications of graphene in nanoelectronics, which can be overcome by doping graphene. Substitutional doping of graphene is a feasible and promising way to induce bandgap and thus modify its electrical and chemical properties[4,5]. Nitrogen, being adjacent to carbon in the periodic table, can easily substitute carbon in the graphene lattice. Depending on the concentration of the nitrogen dopants, a small band gap can also be produced. In nitrogen-doped graphene (NDG), nitrogen is primarily found in the following configurations (i) substitutional configuration, where nitrogen is bonded to neighboring three carbon atoms (also known as graphitic or quaternary nitrogen) (ii) pyridinic configuration, where substitutional nitrogen is accompanied by a vacancy such that the nitrogen is bonded to only two carbon atoms in the six-membered ring, (iii) pyrrolic configuration where nitrogen is bonded to only two carbon atoms part of a five-membered ring as shown in figure 5.1.

These configurations affect the local charge distribution and local density of states differently, producing different electronic, magnetic, and chemical properties [6]. In addition, there can also be chemisorbed Nitrogen or physisorbed N₂. Graphitic nitrogen defects preserve graphene lattice symmetry and conjugation. Theoretical calculations have shown that over a wide range of temperatures and pressure, pyridinic nitrogen and graphitic nitrogen were the most stable nitrogen functionality, while pyrrolic nitrogen became the most stable structures at high pressures ($>10^4$ bar)[7]. It has been shown that the graphitic type of dopant induces n-type conductivity while the pyridinic configuration induces p-type conductivity, with the opening of a small band gap[8,9]. The magnitude of the band gap can be increased by increasing the number of dopants. Doping graphene with a high concentration of a graphitic type of nitrogen dopant (> 5.1 at %) induces ferromagnetism in graphene [10]. Pyrrolic nitrogen-doped graphene has been predicted to have the highest catalytic activity toward CO2RR[11]. These dopants act as scattering centers and reduce the high mobility /conductivity of films observed in monolayer graphene. Recently Lin et al. were able to increase the mobility by doping monolayer graphene with graphitic nitrogen clusters[12]. They were able to achieve this by removing the pyridinic nitrogen centers by oxidative etching during growth. The ability to synthesize nitrogen-doped graphene with specific properties by selectively tuning the chemical configuration and concentration of nitrogen dopants is important for developing NDG-based devices and sensors.

The type of nitrogen dopants and their concentration is strongly dependent on the synthesis method and/or the precursor used in synthesis. Nitrogen-doped graphene is usually synthesized in two ways. (1) Direct synthesis in which the nitrogen dopants are introduced during the graphene growth, and (2) Post-treatment of the graphene in which the graphene layer is doped after its growth. Specifically, Chemical vapor deposition (CVD), solvothermal, segregation method, and arc discharge approaches come under the direct synthesis method[13–16]. Graphene's post-treatment includes the plasma treatment and thermal treatment of the graphene film, where Nitrogen atoms replace C atoms [17–19]. This method reduces the quality of the graphene sheet tremendously. CVD is the most common technique among all because of its cost-effectiveness and ability to produce large-area continuous graphene films[20]. This technique involves the flow of carbon and nitrogen molecules containing precursors for the growth of NDG films. The carrier gas transports the evaporated/sublimated molecules through the furnace toward the target substrate held at the desired temperature. The precursors can be in the gas phase (NH₃), liquid phase (such

as pyridine, Dimethylformamide), and solid phase (like melamine, triazine, and urea)[21–25]. The nitrogen doping concentration and its configurations depend on the precursor choice and the growth parameters such as temperature, flow rate, time, and pressure. The selection of the precursor has been reported by Imumara et al. that the precursor should contain the carbon atoms bonding to nitrogen atoms and should be either sp³ hybridized or sp² hybridized[26]. The molecule acrylonitrile, which contains C-C and C≡N, produced pristine graphene instead of nitrogen-doped graphene. The proposed mechanism for this growth depends on the precursor molecule's decomposition and diffusion on the growth substrate. Thus, it is very important to explore the novel precursors and tune the growth parameters for attaining the required nitrogen concentration and configurations.

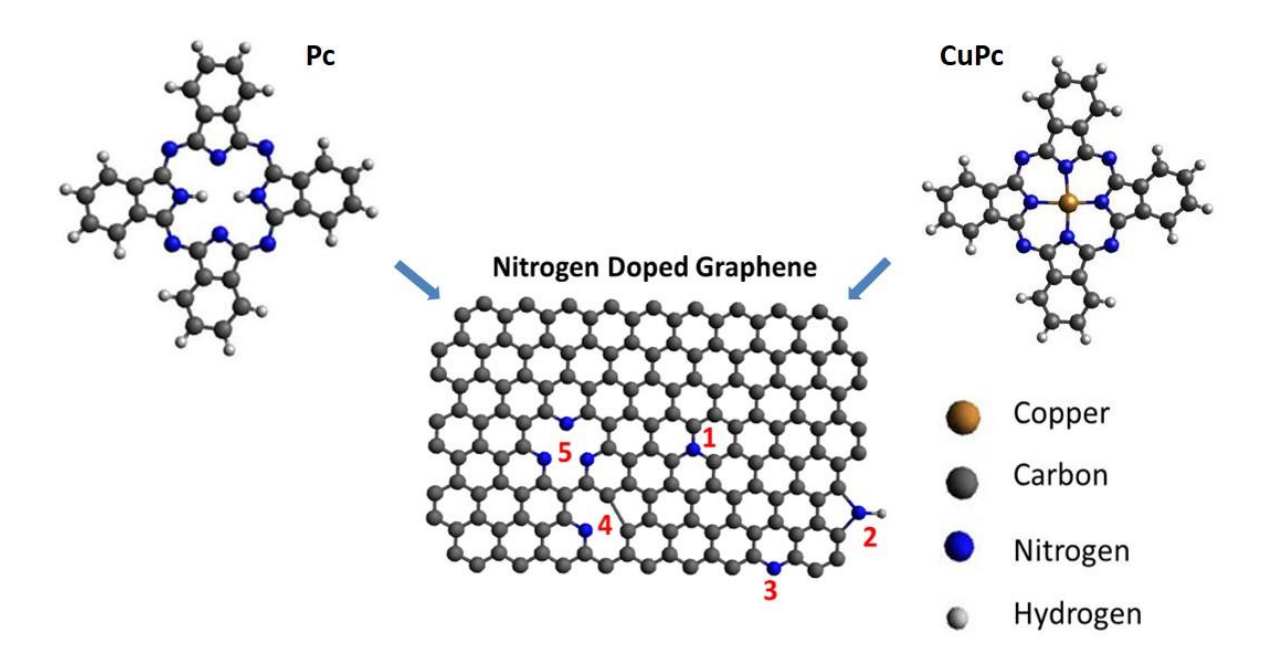


Figure 5.1 The possible configurations of NDG: (1) substitutional or graphitic N, (2) pyrrole-like (3) pyridine-like N, (4) single-N pyridinic vacancy, (5) triple-N pyridinic vacancy.

The novelty of the current work lies in the use of Phthalocyanine based precursors, free base phthalocyanine (Pc) and copper phthalocyanine (CuPc), in atmospheric pressure CVD to produce nitrogen-doped graphene (NDG). Previously, phthalocyanines (Pcs) and their complexes with 3d metals, such as FePc, CoPc, NiPc, etc., have been utilized to synthesize carbon nanotubes and carbon nanofibers[27,28]. However, they have not been used to synthesize nitrogen-doped

graphene sheets. It is shown to be a facile low, temperature and relatively rapid technique to realize NDG films using Pcs via CVD.

5.2. Atmospheric pressure CVD-grown Nitrogen-doped graphene from Pc and CuPc

Nitrogen-doped graphene has been synthesized on copper (Alfa Aesar, 25 μ m thickness, purity 99.8%) using APCVD. The as-received Cu foil (1cm \times 2.5 cm) was cleaned with diluted nitric acid (6.9%) for 25 seconds to remove the surface native oxide and rinsed with deionized water (DIW). Then, it was electropolished in the electrolyte consisting of orthophosphoric acid (40 ml) and isopropyl alcohol (IPA) (10 ml) for 30 minutes at 1.5V. This electropolished copper was cleaned with DIW and rinsed in acetone, IPA, and DIW. After this, the sample was loaded in the horizontal tubular furnace. Schematics of the CVD chamber for the growth of NDG are shown in figure 5.2 (a).

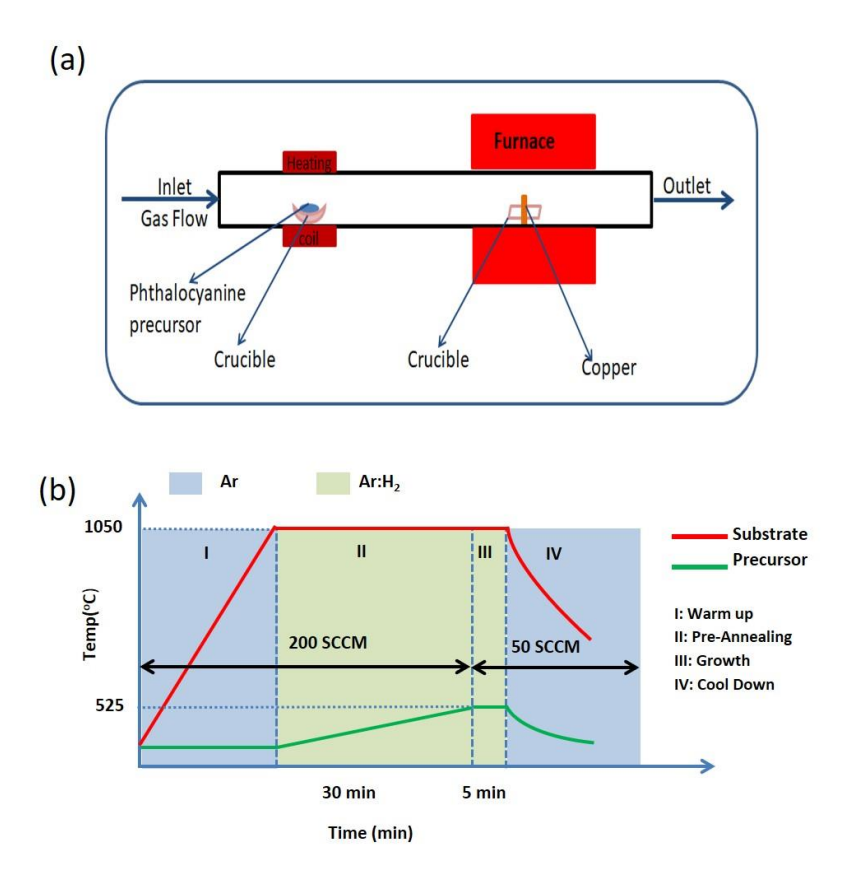


Figure 5.2 schematics of (a) APCVD system and (b) heating profile for the synthesis of the nitrogen-doped graphene (NDG).

The precursor powder (1 mg) was placed 40 cm upstream from the center of the tube (where the Cu sample was kept). Two different types of precursors were used for NDG growth (i) Phthalocyanine (Pc) and (ii) Copper Phthalocyanine (Pc). Phthalocyanine (Pc) molecules are aromatic macrocyclic compounds similar to porphyrins. The molecular structure of these precursors is shown in figure 5.1. A nichrome heating tape connected to a temperature controller is used to vaporize the precursor. The Phthalocyanine (Pc) and Copper Phthalocyanine (CuPc) were evaporated at 525 °C and 545 °C, respectively. Before the experiments started, the system was purged with 200 SCCM of Argon gas for 30 minutes at room temperature (RT), and then the temperature was increased to 1050 °C (heating rate 8°C/min). Once the temperature is reached 1050 °C, 200 SCCM of Ar: H₂ gas mixture (90:10) is introduced, and the substrate is annealed for 30 min in this reducing atmosphere. The heating profile of the substrate and precursor is shown in figure 5.2 (b). The NDG films were synthesized at different substrate temperatures of 1050 °C, 950 °C, and 850 °C to understand the effect of temperature on the film properties. To study the effect of the growth time, the films were synthesized at 1050 °C for different growth times of 5 minutes (min), 10 min, and 15 min. After the growth process was over, the Ar: H₂ gas flow was replaced with Ar gas which flowed at 50 SCCM while the system was cooling down naturally.

5.3 Results and Discussion

5.3.1 Temperature-dependent Nitrogen-doped graphene from Pc

Nitrogen-doped graphene films were synthesized at different growth temperatures for different time durations using solid Phthalocyanine precursor. We have investigated the evolution of the film morphology, thickness, and composition as a function of growth temperature (for fixed growth time). Figure 5.3 shows the FESEM image of the Nitrogen-doped graphene films synthesized at 850°C, 950°C, and 1050°C for 5 minutes, respectively. For the films synthesized at 850°C, we observe numerous quasi-rectangular grains of size ~ 2µm nucleated on the substrate. All the grains do not have the same contrast. The image contrast in SEM is due to the attenuation of secondary electrons (SEs) emitted from the Cu substrate by the overlayer/film. As the thickness of the overlayer increases, fewer SEs reach the detector, leading to low signal intensities, so the thicker areas of the films appear darker than thinner areas. Thus, the grains having darker contrast are of higher thickness. For the films at 950 °C shown in panel (c), we can observe that the sample is covered by bright and dark areas associated with films of different thicknesses. In the darker

regions of the film, we also observe bright wrinkles crisscrossing the dark and bright regions. These wrinkles are the characteristic feature of graphene, which arises due to the different thermal expansion coefficients of the graphene and Cu substrate. The brighter regions seem to be composed of coalesced hexagonal islands. The darker regions corresponding to higher thickness may be due to the nucleation of the second layers on top of the underlying layers. The films synthesized at 1050° C shown in panel (e) are continuous and appear to be more homogeneous with a relatively lesser number of dark patches.

Raman measurements were done after transferring the films on SiO2/Si substrate to get more information about the homogeneity and crystalline quality of the films. The as-grown NDG films on copper at different growth temperatures of 850 °C, 950 °C, and 1050 °C for 5 min were transferred onto SiO2/Si substrates using the PMMA wet transfer method. The optical micrographs of the transferred film are shown in Figures 5.4 (a), (c), and (e). The film's color contrast can be attributed to the variation in the NDG layer number. We observe that the NDG film is discontinuous for 850 °C and turns out to be a continuous film as the growth temperature is increased to 1050 °C. The PMMA residues can also be observed in all the films. The Raman measurements were taken at the cleanest positions where no PMMA is visible. The positions where measurements were carried are shown in the circles. Raman measurements were carried out at different positions on NDG films after transferring them onto SiO2 (300 nm)/Si substrates.

Raman spectra of the films are shown in figure 5.4 (b, d, and f), grown at 850° C, 950° C, and 1050° C, respectively. The representative Raman spectra for three positions representing three different thicknesses within the film are shown for each film. For all the films, we can observe the characteristic G band (in-plane vibrational E_{2g} mode), defect-mediated D and D' peak, and second-order 2D bands peak. The ratio of the integrated intensity of the 2D band to the G band (I(2D)/I(G)) and the FWHM of the 2D peak are used to estimate the number of layers in NDG. The ratio of the I(2D)/I(G) value is 2 or greater, indicating the monolayer NDG, which was reported earlier [23]. The values of I(2D)/I(G) for bilayer and trilayer NDG films vary from 1.6 to 1.9 and 1.0 to 1.5, respectively. In this study, thicknesses greater than 3 layers have been labeled as a few layers of film. From the I(2D)/I(G) ratios that were shown in the Raman spectra figure 5.4 (b), (d), and (f), we observe that the film synthesized at 850 °C has a wide variation in thickness from monolayer to few layers. The films synthesized at 950 °C have areas with monolayers, trilayers, and few

layers of thickness. The films synthesized at 1050°C is more uniform in thickness, with the film thickness varying from monolayer, bilayer, and trilayer. The position and the line shape of the G and 2D peaks depend strongly on the number of layers, strain, and doping[29,30].

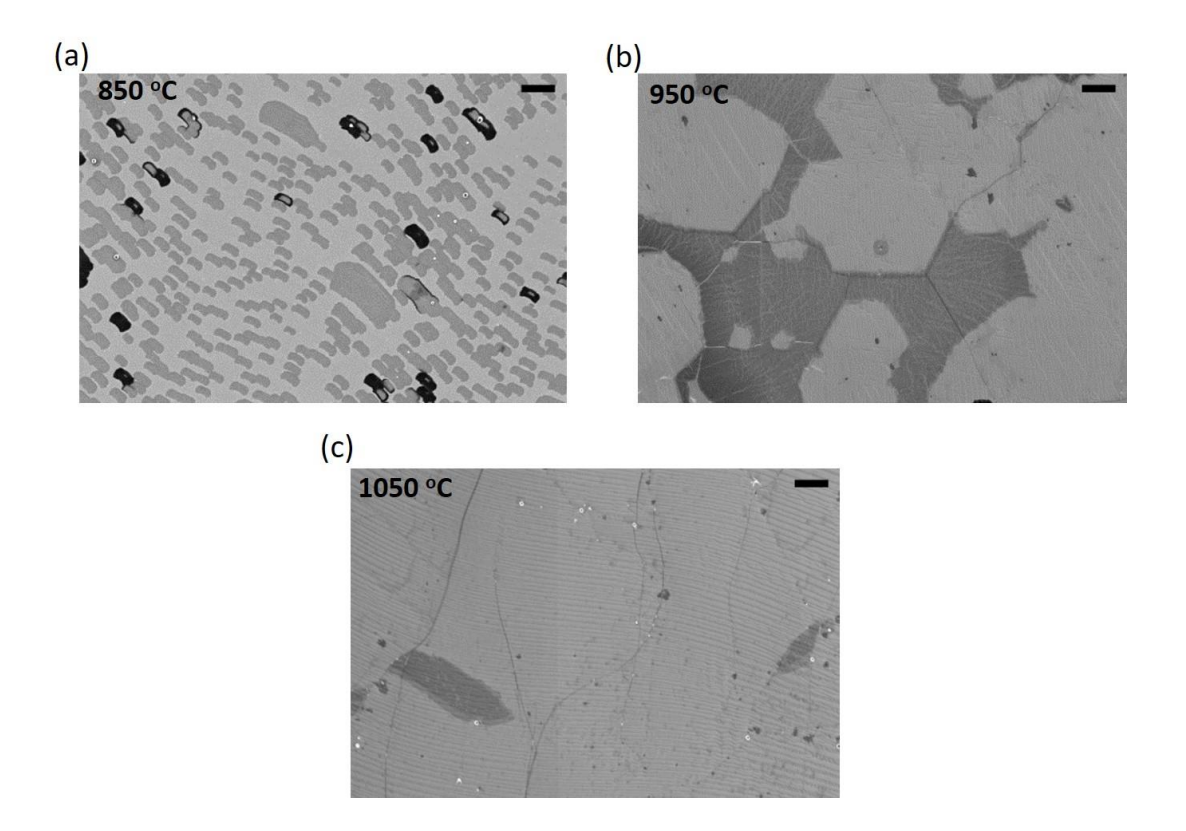


Figure 5.3 Temperature dependence for 5 min growth: (a), (b), (c) FESEM micrographs of films synthesized at temperatures 850 °C, 950 °C, and 1050 °C, respectively. The scale bar is 2 μm.

Pristine monolayer graphene has a G peak at 1580 cm⁻¹ with FWHM in the range of 20-30 cm⁻¹. A blueshift of the 2D peak in comparison to pristine graphene can be due to either doping or an enhanced number of layers. To eliminate the effect of layer dependence on Raman peaks, we only compared the Raman peaks from the monolayer only. The peak positions and FWHM of the G band and 2D band are given in Table 5.1. Raman peaks were fitted with the Lorentzian function and determined the positions, FWHM, layer number, and defect density for the films synthesized at different temperatures. The position for the G band of monolayer film is 1586.2 cm⁻¹, 1588.5 cm⁻¹, and 1590.4 cm⁻¹ for 850 °C, 950 °C, and 1050 °C, respectively. Compared to graphene, all the G peaks are shifted to higher wavenumbers, and this shift increases with increasing synthesis

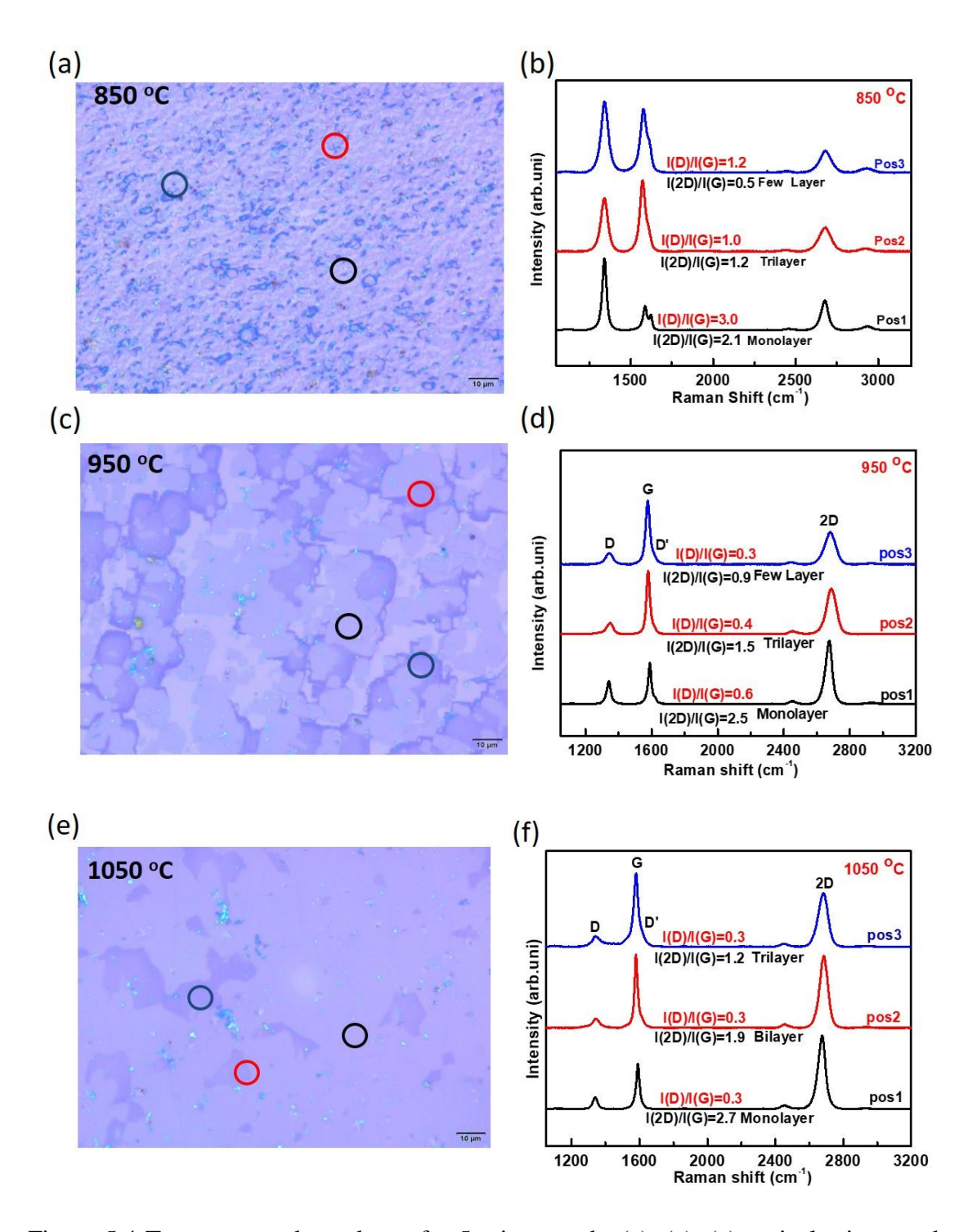


Figure 5.4 Temperature dependence for 5 min growth: (a), (c), (e) optical micrographs and (b), (d), (f) Raman spectra of films synthesized at temperatures 850 °C, 950 °C, and 1050 °C, respectively. The scale bar is 10 μm. Raman spectra were recorded after transferring the films on SiO₂ (300 nm)/Si substrate using a 532 nm laser. Raman spectra were recorded for each film from three positions with different thicknesses.

temperature. The FWHM of the G peak for the monolayer is also larger in comparison to pristine graphene. The blue shift of the G band can be attributed to electron and hole doping or tensile/compressive strain in the C-C bonds due to nitrogen atoms [31,32].

We also observe the D peak which is activated by defects such as edges/grain boundaries, in-plane substitution of heteroatoms, and vacancies. From the I(D)/I(G) ratios, we determined the concentration of defects/dopants in the films. We observe that the defect concentration in each layer is not the same. For the discontinuous film synthesized at 850°C, observe the highest amount of defects with I(D)/I(G)=3.0, 2.5, and 1.0 for monolayers, trilayer, and few layers. For the film synthesized at 950°C, we observe that defect concentration is highest for the monolayer, and it decreases with thickness with I(D)/I(G)=0.6,0.4 and 0.3 for monolayer, trilayer, and few layers. Compared to the films synthesized at 850°C, we observe the opposite trend, with the first layer and the second layer having the highest concentration of the defects I(D)/I(G)=0.3) while the third layer has a much lower amount of defect I(D)/I(G)=1. For the NDG film synthesized at 1050°C, we observe the lowest amount of defect I(D)/I(G)=0.3, and it is constant for all layers, indicating the uniformity in doping. The I(D)/I(G) is used for determining the in-plane-crystallite size, defect distance, and dopant density using the equation given below [33].

$$L_a(nm) = (2.4 \times 10^{-10}) \lambda^4 (I(D)/I(G))^{-1}$$
 - (1)

$$L_D = \sqrt{\frac{(2.4 \times 10^{-10})\lambda^4}{I(D)/I(G)}}$$
 - (2)

$$n_D = (2.4 \times 10^{22})\lambda^{-4}(I(D)/I(G))$$
 - (3)

Where λ is the excitation wavelength used for Raman measurements, where L_a is the crystallite size in nm, L_D is the distance between dopants, and n_D is the dopant density in cm⁻².

Equation (2) is only valid for low defect density point defects. The obtained values are shown in table 5.2. We can clearly see that with increasing synthesis temperature, the crystallite size increases, dopant density decreases, and the separation distance between dopants increases. The crystallite size is greatest for the samples synthesized at 1050°C. We sometimes also observe a small D' peak convoluted with the G peak. For the film synthesized at 850°C, the D' peak is very prominent, while for the films synthesized at 950°C and 1050°C, the D' peak is very small and just

produces an asymmetry in the G peak towards the higher wavenumber. The ratio of I(D')/I(D) gives information about the type of defects in the film.

Temperature	Pos	Layer	PosD	Pos G	Pos D'	Pos 2D
(°C) & time	or spot	Number	(cm ⁻¹)	(cm ⁻¹)	(cm ⁻¹)	(cm ⁻¹)
850, 5min	Pos1	Bilayer	1341.2	1587.6	1622.7	2675.6
	Pos2	Trilayer	1340.7	1572.9	1607.0	2677.1
	pos3	Few layer	1343.5	1588.2	1622.7	2679.9
950, 5min	pos1	Monolayer	1339.6	1588.5	1621.9	2675.7
	Pos2	Trilayer	1345.2	1578.8	1612.7	2688.6
	Pos3	Few layers	1342.3	1576.3	1610.7	2681.5
1050, 5min	Pos1	Monolayer	1338.7	1590.4	-	2673.4
	Pos2	Bilayer	1343.6	1579.7	1615.0	2685.0
	Pos3	Trilayer	1342.5	1579.2	1615.7	2683.5

Table 5.1 The peak positions of G, 2D, D, and D' bands of the NDG films synthesized at different temperatures. The uncertainty in the position is ± 0.1 cm⁻¹.

The thickness of the continuous films was also measured with AFM after transferring them to SiO₂/Si substrate. Figure 5.5 (a-c) shows the AFM image of the films synthesized at $1050\,^{\circ}$ C. AFM measurements were performed for the continuous film obtained at $1050\,^{\circ}$ C. Figure 5.5 (a) represents the AFM image at the edge of the film. The thickness of the film was measured at the edge film around ten places and took the average of it. The average thickness of the film shown in figure 5.5 (b) was found to be 1.0 ± 0.1 nm, which indicates the monolayer [23]. Fig. SI2 g is the AFM image of the center of the film. The continuity of the film is observed throughout the image. We can see the wrinkles in the image and the average height of these wrinkles is about 1.0 ± 0.2 nm. The bright spots in the images are the residual PMMA particles.

Temperature	Layer Number	I(D)/I(G)	La	L_{D}	$n_{\rm DX10}^{11}$
			nm	nm	cm ⁻²
850°C	Monolayer	3.0	6.4	8.1	9
	Few layers	1.0	19.2	13.8	3
	Few layers	2.5	7.7	9.2	7.5
950°C	Monolayer	0.6	32	17.8	1.8
	Tri-layer	0.4	48	21.9	1.2
	Few-Layer	0.3	64	25.5	0.9
1050°C	Monolayer	0.3	64	25.5	0.9
	Bilayer	0.3	64	25.5	0.9
	Tri-layer	0.3	96	31.4	0.9

Table 5.2 I(D)/I(G) ratio of NDG films synthesized for 5 min at 850°C, 950°C, and 1050°C. The ratios were used to calculate crystallite size, defect distance, and defect densities.

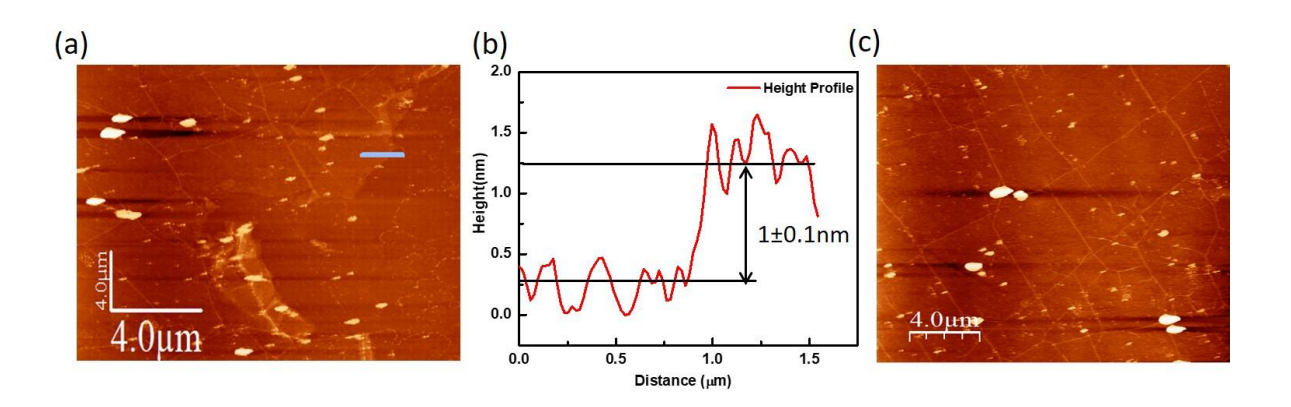


Figure 5.5 AFM measured thicknesses and topography of the NDG films. Thickness measured at the edge of the film (a) 1050 °C. (b) the thickness profile of the film. (c) the topography of the same film. The wrinkles thickness is found to be 1 ± 0.2 nm.

The films were further characterized with X-ray photoelectron spectroscopy to investigate the presence of nitrogen dopants, bonding configurations, and their concentration. The films that were grown at 850 °C, 950 °C, and 1050 °C for 5 minutes at 50 SCCM of Ar+H₂ flow were used for

XPS measurements. Figure 5.6 shows the XPS survey spectrum. Carbon and oxygen peaks can be clearly observed, but the N peak can be barely observed. The oxygen peak appears due to the film's defects (dopants, edges), which will act as hosts for the adsorption of oxygen moieties from the air and ambient moisture. We observe that the amount of nitrogen in the film decreases with increasing synthesis temperature.

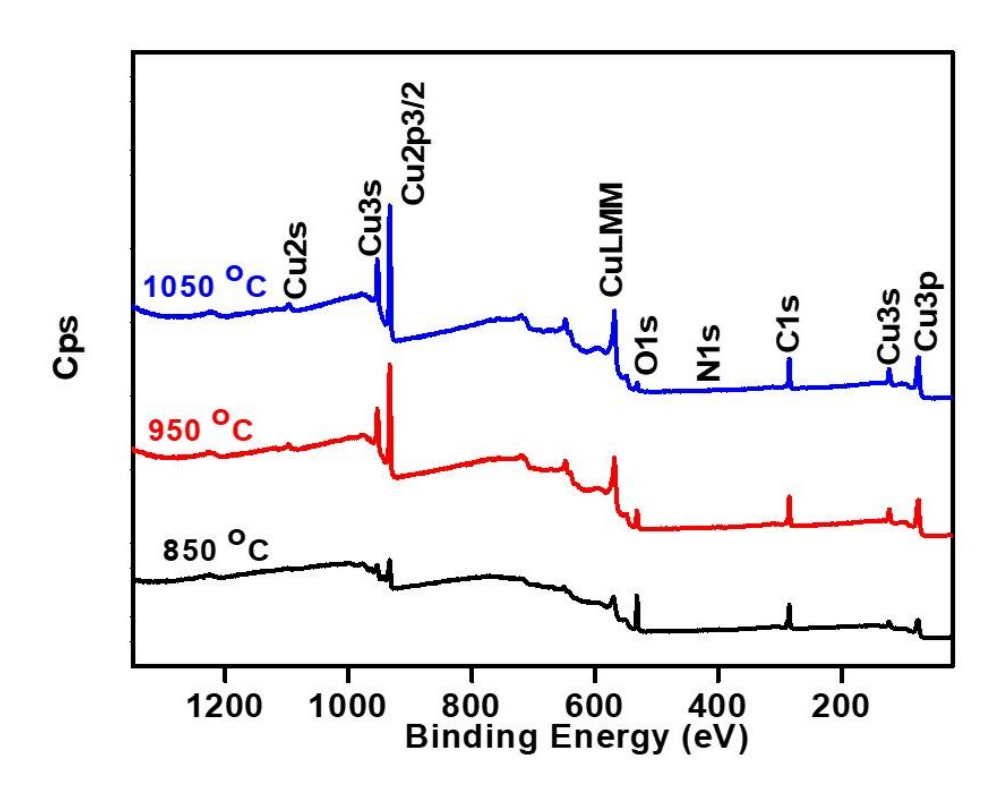


Figure 5. 6 XPS Survey spectrum of the NDG films that were synthesized at various temperatures 850 °C, 950 °C, and 1050 °C for 5 minutes.

High-resolution core-level XPS spectra of C1s is given in Fig.3a for temperatures 850 °C, 950 °C, and 1050 °C. C1s have been deconvoluted into peaks corresponding to sp² C=C, sp² C-N, sp³ C-N, and C=O groups. The peaks at 285.6±0.5 eV and 286.7±0.2 eV correspond to the sp² hybridized carbon atoms bonded to the nitrogen atoms (pyrrolic-N, graphitic-N, and pyridinic-N) (C-sp2-N) and sp³ hybridized carbon atoms (defected sp³-C bonds bonding to N atoms) bonding to nitrogen atoms respetively[34]·[32]. The last peak centered at 288.7±0.2 eV is C=O contributes to the oxygen bonding to Carbon atoms present at the defect sites [35].

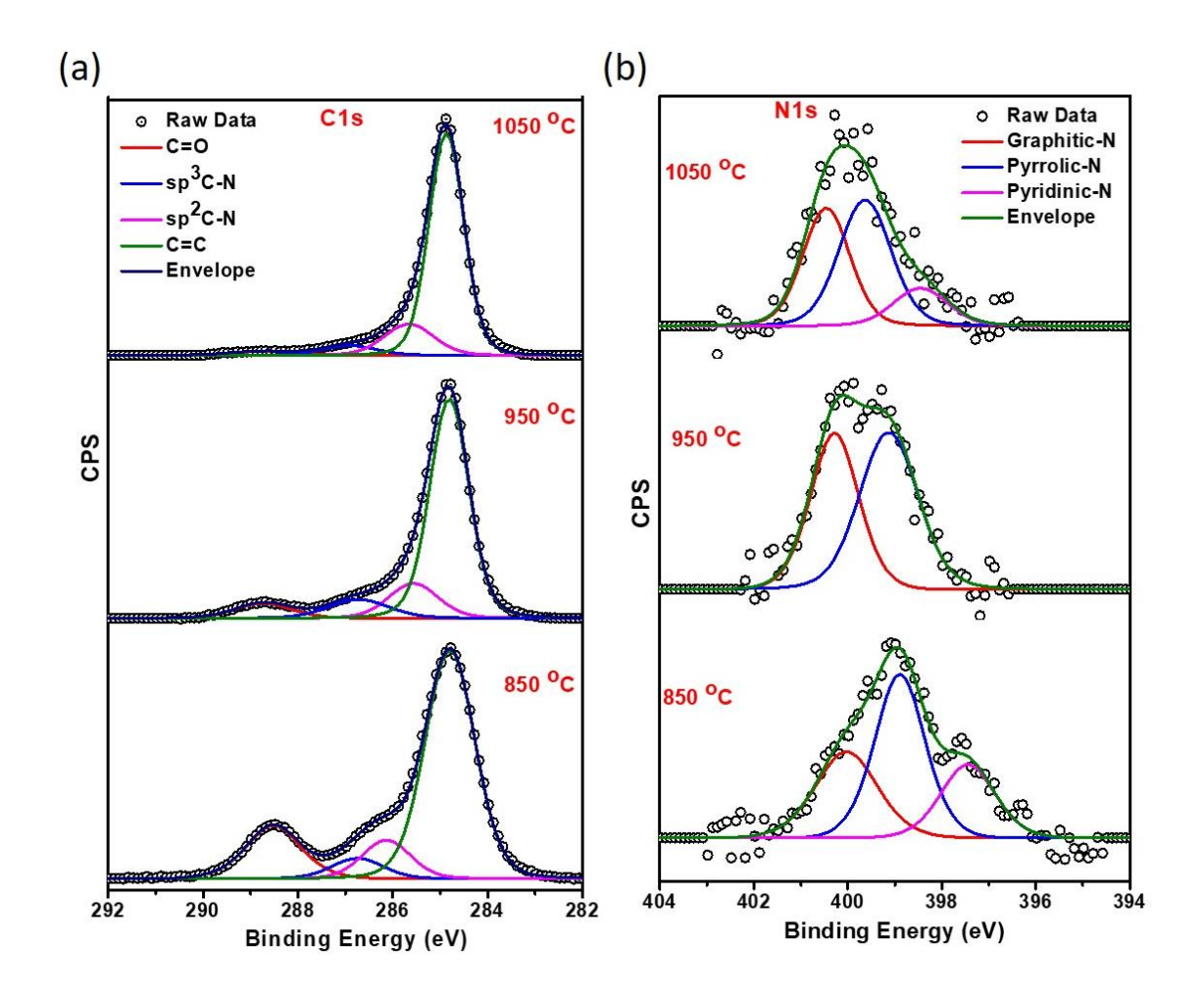


Figure 5.7 Evolution of C 1s and N 1s photoelectron peaks as a function of synthesis temperature: XPS measurements of NDG films on copper synthesized at 850 C, 950 C, and 1050 C for 5 min. High-resolution spectra of (a) C 1s and (b) N 1s

The N1s asymmetric peak can be deconvoluted into three distinctive individual peaks labeled as graphitic-N, pyrrolic-N, and pyridinic-N, as reported in the literature [16]. Graphitic-N has been assigned from 400.0 eV to 401.8 eV, and the pyridinic-N range exists between 398.1 eV and 399.3 eV [36,37]. The pyrrolic-N configuration binding energy lies between 399.0 eV and 399.7 eV[32]. With an increase in synthesis temperature, we observed a decrease in the nitrogen content. The C: N ratio is 1.4%, 0.8%, and 0.7% for 850°C, 950°C, and 1050°C, respectively. In addition, the type of nitrogen dopants also strongly depended on the synthesis temperature. At 850 °C, we get a mixture of graphitic (~23 at%), pyrrolic (~54 at%), and pyridinic nitrogen (~23 at%). At 950 °C, we get a nearly equal proportion of graphitic (~48 at%) and pyrrolic nitrogen (~48 at%). With

1050°C, we again see a small increase in the pyridinic nitrogen content. From the FESEM image in figure 5.3, we see that at 850 °C, we have many small grains with large numbers of edges, indicating that we would have the most pyridinic or pyrrolic type of nitrogen defects present. With the increase in grain size (area) at 950°C, the relative contribution of the graphitic type of nitrogen compared to pyridinic/pyrrolic nitrogen should increase. At 1050 °C, the etching due to the hydrogen in the carrier gas is more pronounced, which creates more edges which leads to a small increase in the pyridinic type of defects.

5.3.2 Time-dependent Nitrogen-doped graphene from Pc

We have also investigated the film morphology and composition evolution as a function of growth time (at fixed growth temperature). Figure 5.8 shows the FESEM and Raman spectra of the films synthesized at 850 °C for 5 min, 10 min, and 15 min, respectively. The isolated grains were observed for all the films, as shown in figure 5.8 (a, c, and e). Contrast variation of grains indicates the different thicknesses in the grains. The individual grains coalesced as time increased to 15 min and formed bigger grains. With increasing growth time, the grains become larger and more uniform in terms of thickness. These samples could not form continuous films as compared to the films synthesized at 1050 °C (discussed later) because the surface diffusion for the adsorbed reactive species is very low, which can be attributed to the lower growth temperature. The characteristic Raman bands G and 2D bands were observed, as shown in Figures 5.8 (b, d, and f). The defective peaks D and D' bands are also present in the spectra, indicating that the grains have defects (dopants, grain boundaries, sp³ carbons). Raman spectra of these films showed the variation in the layer number confirmed by the I(2D)/I(G) ratio and non-uniformity in the films deduced from the defect density (I(D)/I(G)). The layer number also has been reduced as the growth time increased from 5 min to 15 min. The defect density has also been decreased from 5 min to 15 min because the D band intensity is decreased.

Figure 5.9 shows the FESEM images and the Raman spectra of the films that were synthesized for 10 min and 15 min at 1050 °C. From the FESEM images and Raman spectra in figures 5.3 and 5.4, we observed that in the initial 5 min of growth at 1050 °C, the films were quite smooth with thickness variation monolayer, bilayer to trilayer. The FESEM image in figure 5.9 (a) shows that the film's surface morphology after 10 min growth is quite similar to that after 5 min growth. Now we also observe some very bright features of different sizes. Some of these bright features are

hexagonal in shape and have nice sharp facets, which may correspond to etched pits in the film (inset).

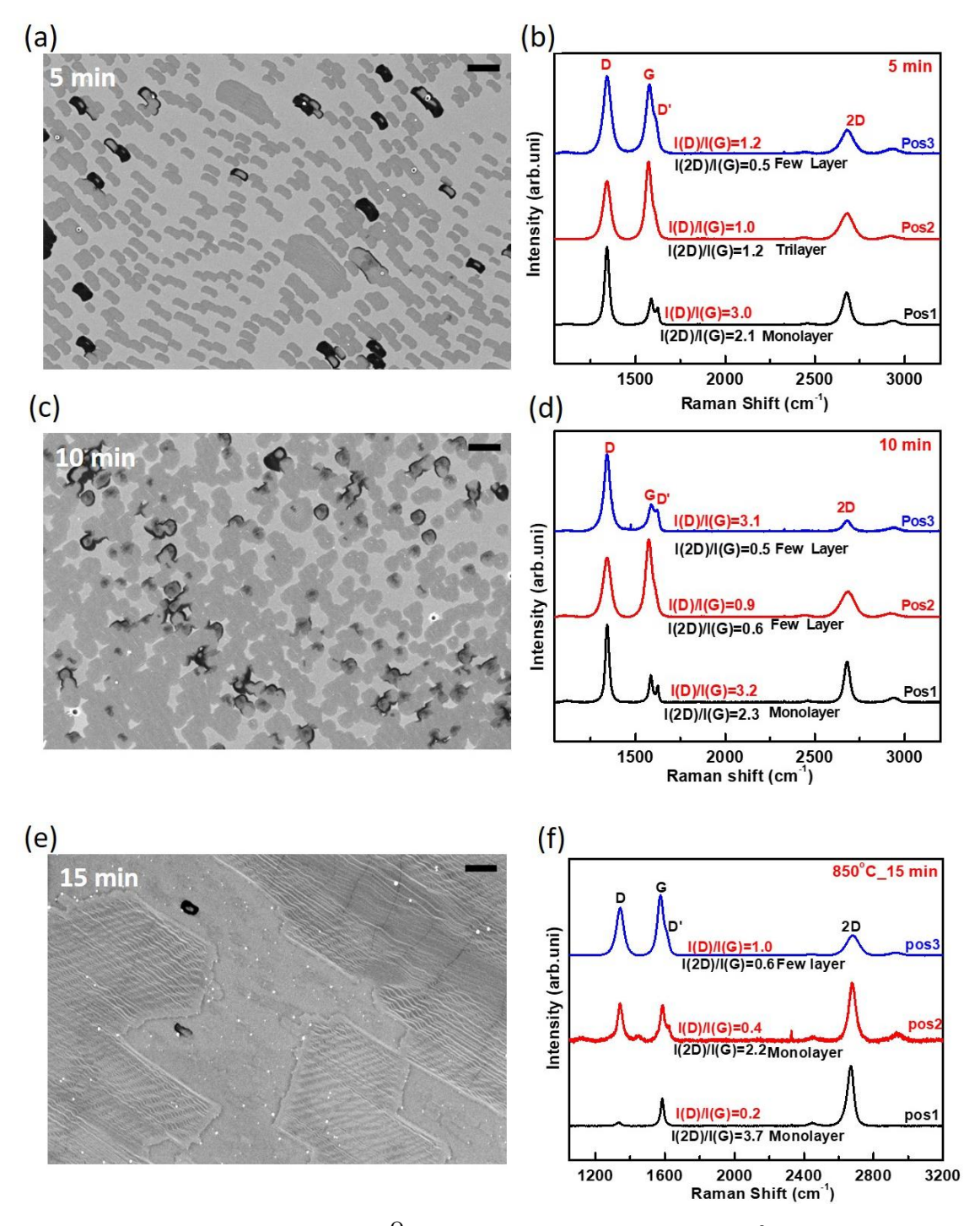


Figure 5.8 Time dependence at 850 $^{\circ}$ C. FESEM of NDG films at 850 $^{\circ}$ C for various time growths (a) 5 min, (c) 10 min, (e) 15 min. The scale bar is 10 μ m. Raman spectra of NDG films synthesized at 850 $^{\circ}$ C for different time growths (b) 5 min, (d) 10 min, and (f) 15 min.

In fact, the Raman spectrum in figure 5.9 (b) also shows that the film thickness has reduced, with only monolayers and bilayers present in the film. Increasing the growth time to 15 min resulted in increased etched pits, as shown in figure 5.9 (c). Figure 5.9 (d) shows the Raman spectra for 15 min having monolayers and bilayers similar to 10 min film. Table 5.3 lists the position and FWHM of the G peak and 2D peak as a function of growth time for films synthesized at 1050°C. The G peak and 2D peak position of the monolayer are similar for 5 min and 15 min growth, while for 10 min growth, the G peak shifts slightly by ~3 cm⁻¹ to higher wavenumbers, with similar behavior observed for the 2D peak. Also, the I(D)/I(G) peak ratio has increased, indicating the creation of more defects due to etching. However, for 15 min, we observe the D peak intensity and the FWHM

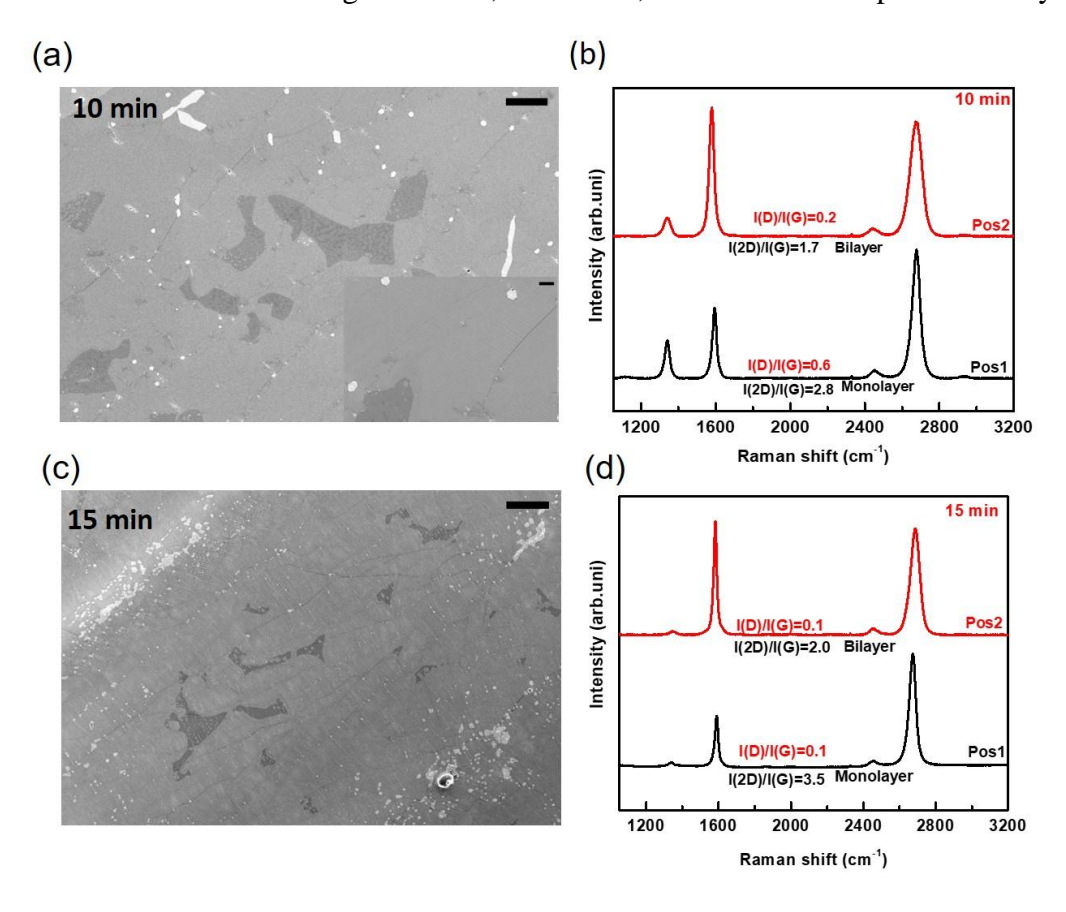


Figure 5.9 Time dependence for 1050 C growth: (a) and (c) FESEM micrographs of films synthesized at temperatures for 10 min and 15 min, respectively. The scale bar is $10 \, \mu m$. The inset FESEM image is a magnified image to show the hexagonal pits. The inset scale bar is $2 \, \mu m$. (b) and (d) Raman spectra of the films synthesized for 10 min and 15 min, respectively.

of the 2D peaks decreasing, indicating a decrease in the defect density and an improvement in the crystalline quality. The defect density/ nitrogen dopant concentration in the film continues to increase as long as sufficient mass transport of the precursor or precursor fragments still reach the substrate. Once all the precursor molecules are evaporated, mass transport, then the film gets etched by H₂ present in the carrier gas. It is quite possible for the 15 min growth, the film is getting etched more.

Temperature	Position	Layer	PosD	Pos G	Pos D'	Pos 2D
°C& time	or spot	Number	(cm ⁻¹)	(cm ⁻¹)	(cm ⁻¹)	(cm ⁻¹)
1050,10 min	Pos1	Monolayer	1339.6	1593.7	-	2675.9
	Pos2	Bilayer	1339.1	1578.3	-	2675.0
1050,15 min	Pos1	Monolayer	1338.2	1588.7	-	2671.8
	Pos2	Bilayer	1345.3	1581.4	-	2685.8

Table 5.3 The peak positions of G, 2D, D, and D' bands of the NDG films synthesized for 10 min and 15 min.

XPS spectra were recorded to investigate the evolution of defects with synthesis time. Figure 5.10 shows the high-resolution XPS spectra of the NDG films synthesized at 1050 °C for 10 min and 15 min. It was found that the % of nitrogen for 5 min, 10 min, and 15 min are 0.7 %, 1.0 %, and 0.6 %, respectively. The nitrogen content in the film increases for 10 min of growth, indicating the incorporation of more nitrogen in the film. This is consistent with the increase in dopant density observed in Raman spectra. Figure 5.10 (a) and c show the C1s high-resolution XPS spectra for 10 min and 15 min. The increase in C=C and decrease in the sp²C-N from 10 min to 15 min indicates the reduction in the N- content. The nitrogen dopant configurations were evaluated by the deconvolution of N1s high-resolution spectra shown in Figures 5.10 (b) and d. For the 10 min film, the graphitic nitrogen and pyrrolic Nitrogen content increased to 49.7% and 52.3 %, respectively, while the pyridinic nitrogen content became negligible. The absence of pyridinic-N indicates that it has been converted to either graphitic-N or pyrrolic-N or removed completely. Increasing the growth time to 15 minutes resulted in a further increase of graphitic-N to 76 % and

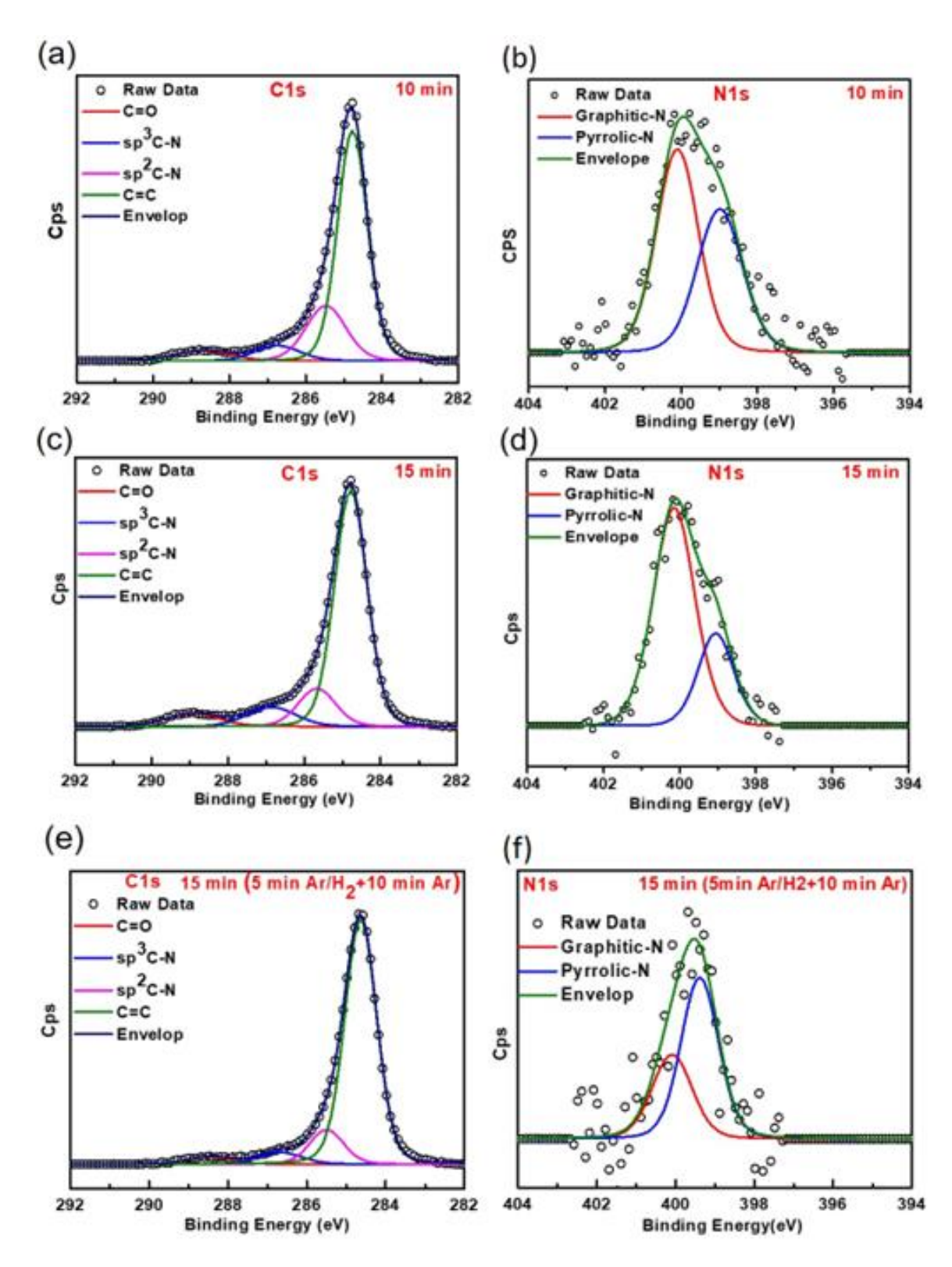


Figure 5.10 Evolution of C 1s and N 1s photoelectron peak with time at 1050 °C: high-resolution spectra of C 1s and N 1s for (a) and (b) 10 min in Ar/H2, (c) and (d) 15 min Ar +H2, and (e) and (f) for 15 min (Ar+H2 5 min +Ar 10 min), respectively.

while pyrrolic-N reduced to 24 %. It can be noticed that the graphitic-N has been increased and pyrrolic-N is decreased, which indicates that some amount of pyrrolic-N has been converted to Graphitc-N. This conversion of pyrrolic defects to graphitic defects can be stopped by removing H₂ from the carrier gas. We synthesized the nitrogen-doped films at 1050°C for 5 min and then replaced the Ar+H₂ with Ar gas and continued annealing the film in Ar gas for 10 more minutes. Figure 5.10 (e) and (f) show the high- resolution, XPS spectra of C1s and N1s of the film. Compared to the film synthesized for 15 min under Ar+H2 gas flow, this film had a higher content of pyrrolic defects than graphitic ones. The total N content for this film is 0.3% is lower than the 15 min films synthesized using Ar+H₂. The pyrrolic-N contribution is 64.1%, and graphitic-N is 35.9%. Further investigation is needed to elucidate the carrier gas's chemical potential's role in the precursor's decomposition and stabilization of nitrogen dopants.

5.3.3. Nitrogen-doped graphene (NDG) from CuPc

Nitrogen-doped graphene films have been synthesized using a wide variety of precursors, and in most of them, we get either pyridinic or graphitic-type nitrogen dopants. We also observed a mixture of pyrrolic and graphitic dopants using Pc precursor. When the precursor was changed to CuPc, we were able to get the dominant pyrrolic type of dopants. These films were synthesized at 1050°C for 5 min and 10 min.

Figure 5.11 (a) and (b) show the film morphology. For the 5 min growth, we only get the discontinuous film with hexagonal grains of size ~ 20 μm. From the contrast, it is evident that these grains are not of uniform thickness, and secondary nucleation has already started. For the 10 min growth, we observe that the grains have coalesced and nearly it formed continuous films. Compared to the films synthesized from Pc molecules under identical conditions, the growth rate of the film is slow (see figures 5.3 and 5.9). The XPS spectra of the film were recorded as shown in Fig. 6 (c) (d) (e) and (f). The C1s spectra have been deconvoluted into sp³ C-N,-sp² C-N, C=C, and C=O peaks. From the N1s spectrum, we observe that within the first 5 min growth, we get the predominantly pyrrolic type of defects, and with increasing growth time, we get a mixture of graphitic and pyrrolic-N defects. This indicates that the graphitic-N dopants are favoured while increasing the growth time.

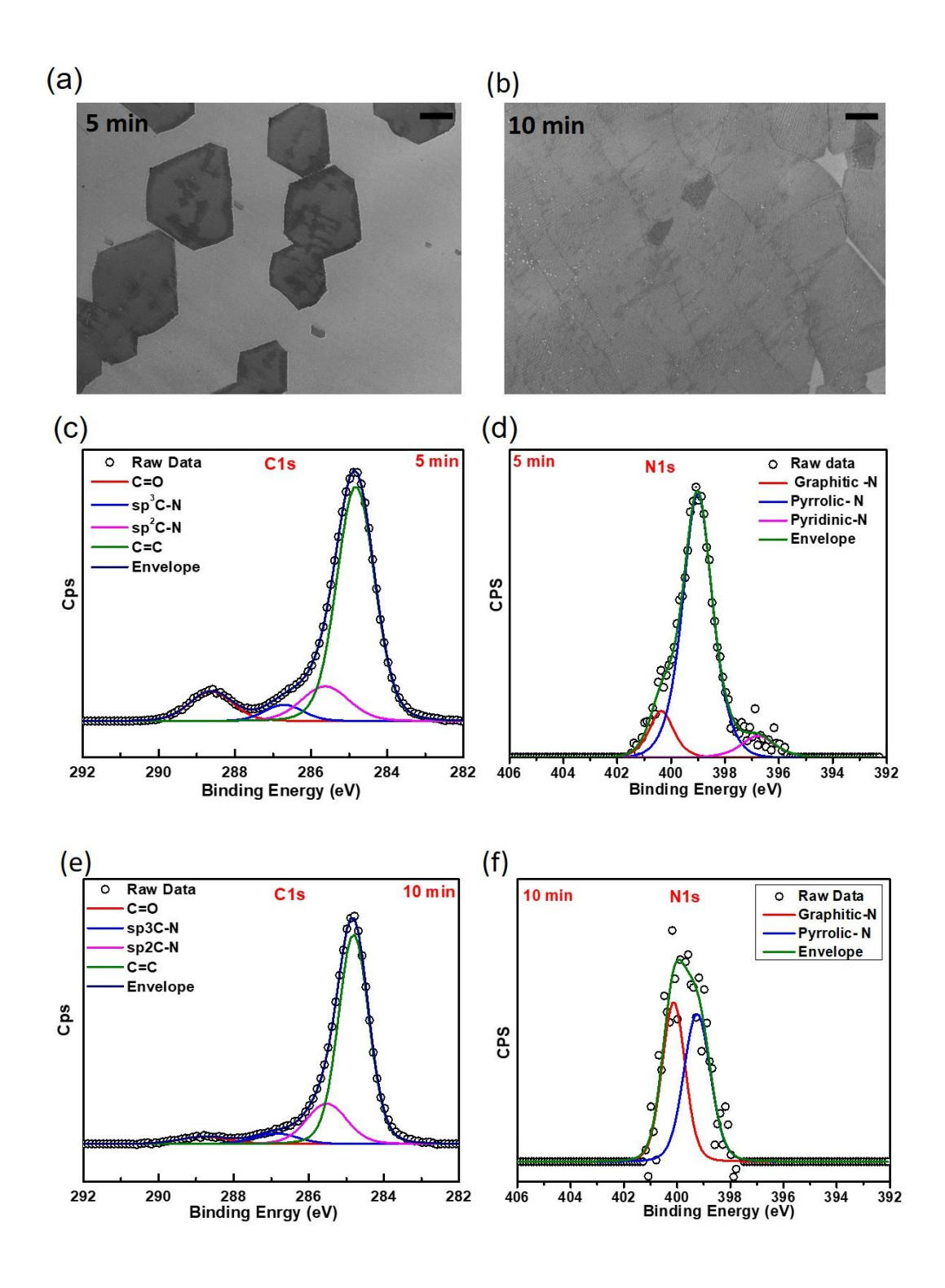


Figure 5.11 NDG films synthesized using CuPc. (a) and (b) FESEM micrographs NDG films synthesized at 1050°C for 5 min and 10 min. The scale bar is 10 um. (c) and (d) High-resolution XPS spectra of C1s and N1s photoelectron peak for 5 min synthesis. (e) and (f) High-resolution

XPS spectra of C1s and N1s photoelectron peaks for 10 min synthesis. CuPc powder is evaporated at 545 °C.

5.4 Conclusion

In our synthesis process, we used Pc and CuPc as the solid precursors for the synthesis of NDG films. We systematically investigated the growth of NDG films using these precursors and their properties. We demonstrated that the chemical nature of nitrogen defects depends strongly on the starting precursor and growth parameters. For the Pc precursor, at 1050 C growth temperature and 5-min growth duration, we observed a mixture of pyridinic and pyrrolic defects with a small percentage of graphitic kind of nitrogen. For CuPc precursor, we observed primarily pyrrolic type of defects under the same growth conditions. In both cases, if the growth time is increased, all the defects are converted to graphitic-type nitrogen defects. We also measured the electronic conductivity of the NDG films synthesized using Pc precursor and showed their dependence on the nature of defects. Our results suggest that we can tailor the chemical nature of nitrogen defects and corresponding electronic properties by selecting an appropriate starting precursor and carefully tuning the synthesis conditions.

5.5 References:

- [1] Schwierz F 2010 Graphene transistors *Nat. Nanotechnol.* **5** 487–96
- [2] Balandin A A, Ghosh S, Bao W, Calizo I, Teweldebrhan D, Miao F and Lau C N 2008 Superior thermal conductivity of single-layer graphene *Nano Lett.* **8** 902–7
- [3] Novoselov K S, Jiang Z, Zhang Y, Morozov S V., Stormer H L, Zeitler U, Maan J C, Boebinger G S, Kim P and Geim A K 2007 Room-temperature quantum hall effect in graphene *Science* (80-.). **315** 1379
- [4] Laref A, Ahmed A, Bin-Omran S and Luo S J 2015 First-principle analysis of the electronic and optical properties of boron and nitrogen doped carbon mono-layer graphenes *Carbon N. Y.* **81** 179–92
- [5] Wang X, Li X, Zhang L, Yoon Y, Weber P K, Wang H, Guo J and Dai H 2009 N-doping of graphene through electrothermal reactions with ammonia *Science* (80-.). **324** 768–71

- [6] Zhang L and Xia Z 2011 Mechanisms of oxygen reduction reaction on nitrogen-doped graphene for fuel cells *J. Phys. Chem. C* **115** 11170–6
- [7] Ayiania M, Hensley A J R, Groden K, Garcia-Perez M and McEwen J S 2019

 Thermodynamic stability of nitrogen functionalities and defects in graphene and graphene nanoribbons from first principles *Carbon N. Y.* **152** 715–26
- [8] Yutomo E B, Noor F A and Winata T 2021 Effect of the number of nitrogen dopants on the electronic and magnetic properties of graphitic and pyridinic N-doped graphene-a density-functional study *RSC Adv.* **11** 18371–80
- [9] Yang J, He W, Jiang Q, Chen Z, Ju H, Xue X, Xu Z, Hu P A and Yu G 2020 Hydrogen-dominated metal-free growth of graphitic-nitrogen doped graphene with n-type transport behaviors *Carbon N. Y.* **161** 123–31
- [10] Błoński P, Tuček J, Sofer Z, Mazánek V, Petr M, Pumera M, Otyepka M and Zbořil R 2017 Doping with Graphitic Nitrogen Triggers Ferromagnetism in Graphene J. Am. Chem. Soc. 139 3171–80
- [11] Liu Y, Zhao J and Cai Q 2016 Pyrrolic-nitrogen doped graphene: A metal-free electrocatalyst with high efficiency and selectivity for the reduction of carbon dioxide to formic acid: A computational study *Phys. Chem. Chem. Phys.* **18** 5491–8
- [12] Lin L, Li J, Yuan Q, Li Q, Zhang J, Sun L, Rui D, Chen Z, Jia K, Wang M, Zhang Y, Rummeli M H, Kang N, Xu H Q, Ding F, Peng H and Liu Z 2019 Nitrogen cluster doping for high-mobility/conductivity graphene films with millimeter-sized domains *Sci. Adv.* 5 1–10
- [13] Wei D, Liu Y, Wang Y, Zhang H, Huang L and Yu G 2009 Synthesis of n-doped graphene by chemical vapor deposition and its electrical properties *Nano Lett.* **9** 1752–8
- [14] Panchakarla L S, Subrahmanyam K S, Saha S K, Govindaraj A, Krishnamurthy H R, Waghmare U V. and Rao C N R 2009 Synthesis, structure, and properties of boron- and nitrogen-doped graphene *Adv. Mater.* **21** 4726–30
- [15] Deng D, Pan X, Yu L, Cui Y, Jiang Y, Qi J, Li W X, Fu Q, Ma X, Xue Q, Sun G and Bao

- X 2011 Toward N-doped graphene via solvothermal synthesis Chem. Mater. 23 1188–93
- [16] Zhang C, Fu L, Liu N, Liu M, Wang Y and Liu Z 2011 Synthesis of nitrogen-doped graphene using embedded carbon and nitrogen sources *Adv. Mater.* **23** 1020–4
- [17] Sheng Z H, Shao L, Chen J J, Bao W J, Wang F Bin and Xia X H 2011 Catalyst-free synthesis of nitrogen-doped graphene via thermal annealing graphite oxide with melamine and its excellent electrocatalysis *ACS Nano* **5** 4350–8
- [18] Wang H, Zhang C, Liu Z, Wang L, Han P, Xu H, Zhang K, Dong S, Yao J and Cui G 2011 Nitrogen-doped graphene nanosheets with excellent lithium storage properties *J. Mater. Chem.* **21** 5430–4
- [19] Guo B, Liu Q, Chen E, Zhu H, Fang L and Gong J R 2010 Controllable N-doping of graphene *Nano Lett.* **10** 4975–80
- [20] Li J, Ren Z, Zhou Y, Wu X, Xu X, Qi M, Li W, Bai J and Wang L 2013 Scalable synthesis of pyrrolic N-doped graphene by atmospheric pressure chemical vapor deposition and its terahertz response *Carbon N. Y.* **62** 330–6
- [21] Lv R, Li Q, Botello-Méndez A R, Hayashi T, Wang B, Berkdemir A, Hao Q, Eléas A L, Cruz-Silva R, Gutiérrez H R, Kim Y A, Muramatsu H, Zhu J, Endo M, Terrones H, Charlier J C, Pan M and Terrones M 2012 Nitrogen-doped graphene: Beyond single substitution and enhanced molecular sensing *Sci. Rep.* 2 1–8
- [22] Zabet-Khosousi A, Zhao L, Pálová L, Hybertsen M S, Reichman D R, Pasupathy A N and Flynn G W 2014 Segregation of sublattice domains in nitrogen-doped graphene *J. Am. Chem. Soc.* **136** 1391–7
- [23] Gao H, Song L, Guo W, Huang L, Yang D, Wang F, Zuo Y, Fan X, Liu Z, Gao W, Vajtai R, Hackenberg K and Ajayan P M 2012 A simple method to synthesize continuous large area nitrogen-doped graphene *Carbon N. Y.* **50** 4476–82
- [24] Wang Z, Li P, Chen Y, Liu J, Tian H, Zhou J, Zhang W and Li Y 2014 Synthesis of nitrogen-doped graphene by chemical vapour deposition using melamine as the sole solid source of carbon and nitrogen *J. Mater. Chem. C* **2** 7396–401

- [25] Usachov D, Vilkov O, Grüneis A, Haberer D, Fedorov A, Adamchuk V K, Preobrajenski A B, Dudin P, Barinov A, Oehzelt M, Laubschat C and Vyalikh D V. 2011 Nitrogendoped graphene: Efficient growth, structure, and electronic properties *Nano Lett.* 11 5401–7
- [26] Imamura G and Saiki K 2011 Synthesis of nitrogen-doped graphene on Pt(111) by chemical vapor deposition *J. Phys. Chem. C* **115** 10000–5
- [27] Basiuk V A, Bolivar-Pineda L M, Meza-Laguna V, Glushenkov A M, Murdoch B J and Basiuk E V. 2020 N-doped carbon nanofibers from pyrolysis of free-base phthalocyanine *Diam. Relat. Mater.* 105 107812
- [28] Milev A S, Tran N, Kannangara G S K, Wilson M A and Avramov I 2008 Polymorphic transformation of iron-phthalocyanine and the effect on carbon nanotube synthesis *J. Phys. Chem. C* **112** 5339–47
- [29] Casiraghi C, Pisana S, Novoselov K S, Geim A K and Ferrari A C 2007 Raman fingerprint of charged impurities in graphene *Appl. Phys. Lett.* **91** 1–4
- [30] Ni Z H, Yu T, Lu Y H, Wang Y Y, Feng Y P and Shen Z X 2008 Uniaxial strain on graphene: Raman spectroscopy study and band-gap opening *ACS Nano* **2** 2301–5
- [31] Das A, Chakraborty B, Piscanec S, Pisana S, Sood A K and Ferrari A C 2009 Phonon renormalization in doped bilayer graphene *Phys. Rev. B Condens. Matter Mater. Phys.* **79** 1–7
- [32] Matsoso B J, Ranganathan K, Mutuma B K, Lerotholi T, Jones G and Coville N J 2016 Time-dependent evolution of the nitrogen configurations in N-doped graphene films *RSC Adv.* **6** 106914–20
- [33] Caṇado L G, Takai K, Enoki T, Endo M, Kim Y A, Mizusaki H, Jorio A, Coelho L N, Magalhães-Paniago R and Pimenta M A 2006 General equation for the determination of the crystallite size la of nanographite by Raman spectroscopy *Appl. Phys. Lett.* **88** 1–4
- [34] Van Khai T, Na H G, Kwak D S, Kwon Y J, Ham H, Shim K B and Kim H W 2012 Significant enhancement of blue emission and electrical conductivity of N-doped

- graphene J. Mater. Chem. 22 17992–8003
- [35] Wang H, Maiyalagan T and Wang X 2012 Review on recent progress in nitrogen-doped graphene: Synthesis, characterization, and its potential applications *ACS Catal.* **2** 781–94
- [36] Susi T, Pichler T and Ayala P 2015 X-ray photoelectron spectroscopy of graphitic carbon nanomaterials doped with heteroatoms *Beilstein J. Nanotechnol.* **6** 177–92
- [37] Yanilmaz A, Tomak A, Akbali B, Bacaksiz C, Ozceri E, Ari O, Senger R T, Selamet Y and Zareie H M 2017 Nitrogen doping for facile and effective modification of graphene surfaces *RSC Adv.* **7** 28383–92

Chapter-6

Applications of Pristine Graphene & Nitrogen Doped

Graphene films

This chapter deals with the applications of CVD-grown pristine and nitrogen-doped Graphene (NDG) films in optical, electrical, Optoelectronic, and sensing fields. The transmittance, field effect transistor (FET), photodetector, and surface-enhanced Raman spectroscopic (SERS) measurements were investigated to show that these films can be utilized in the formerly mentioned applications. The values obtained for the transmittance and FET are compared with existing literature. The effect of the nitrogen dopant concentration and configuration on the properties have been studied. The photodetector device was fabricated by Graphene/MoS₂ heterostructure, in which graphene is employed as a charge collector was also investigated. The studies on surface-enhanced Raman spectroscopy of graphene and NDG film were discussed. The enhancement in the Raman bands of analyte molecules (organic dyes) was studied on graphene and NDG films and compared.

6.1 Introduction

Graphene has been subjected to the exploration of many practical applications such as FETs, sensors, flexible transparent conductors, photodetectors, solar cells, and batteries due to its exceptional properties such as high carrier mobilities, high transparency, zero bandgap, high ballistic transport, the large surface-to-volume ratio and high flexibility [1–7]. Continuous graphene films are needed to meet the electronic, optoelectronic, and sensing applications. It has been discussed that CVD is the most suitable technique to obtain continuous films. Most applications shown till now through CVD-grown graphene are synthesized from gaseous precursor methane. In this thesis work, graphene has been synthesized from the solid precursor PMMA. High-quality large-area continuous graphene film obtained with optimized parameters (2mg PMMA, 10 SCCM, 1050 °C, 20 minutes) mentioned in chapter 4 is utilized for various applications. Graphene employed in different applications is compared with methane-derived graphene. The nitrogen doping concentrations and configurations depend on the precursor choice in the in-situ CVD growth. The novel precursor phthalocyanines were used for the Nitrogen-doped

graphene synthesis. The grown films at 1050 °C for 5 minutes and 15 minutes, having the majority of pyrrolic-N and graphitic-N configuration dopants, respectively, are used for different applications in this chapter. The effect of these dopants on different applications is analyzed. Here, we employed the graphene and NDG films on the optical and FET measurements. Graphene was utilized in optoelectronic applications with MoS₂, a semiconducting material. Both graphene and NDG films have also been explored in surface-enhanced Raman spectroscopic applications. All these applications that have been studied are discussed in the next section.

6.2 Applications

6.2.1 Transparency of the Graphene and NDG films

Graphene, being only one atomic thick, is transparent, flexible with high strain strength, and conductive, making it suitable for the flexible transparent conductor. Graphene has become an alternative to the Indium Tin oxide (ITO) material used for touch screen manufacturing [8]. The theoretically calculated optical transmittance value for pristine monolayer graphene is 97.7%. It absorbs 2.3% of the incident white light, which can be attributed to its unique electronic structure. The opacity of the pristine suspended graphene is defined by the fine structure constant $\alpha = e^2/\hbar c \approx 1/137$, where c is the speed of light [9]. The transmittance depends on the number of layers, each absorbing 2.3 % visible light. Therefore, it can be considered that the optical absorption increases linearly as the number of layers increases. In multilayer graphene, each layer can be considered a two-dimensional electron gas, with small perturbations due to adjacent layers that make it optically equivalent to a superposition of almost a non-interacting single-layer graphene [10].

Graphene and NDG films grown on copper were transferred onto quartz substrates using PMMA assisted wet transfer method to evaluate the optical transparency of the films. UV-Vis-IR spectrometer was employed to measure the optical absorbance. Only visible light (400 nm-800 nm) was used as the incident light. The optical transmittance of high-quality, large-area continuous pristine monolayer graphene film is shown in figure 6.1 (a). At 550 nm wavelength, the obtained transmittance value is 97.4%, slightly deviating from the expected value of 97.7% [9]. It also indicates that the film absorbed 2.6 % of the incident visible light. The slight deviation of the transmittance value from the actual value is attributed to the PMMA residues [11]. Figure 6.1 (b)

shows the optical transmittance of the nitrogen-doped Graphene (NDG) films. The Graphitic-N dominated configuration of NDG film exhibited a transmittance value of 97.3% at 550 nm wavelength. Pyrrolic-N-dominated NDG film showed a transmittance value of 97.1 %. The slight decrease in the transmittance value from graphitic-N to the pyrrolic-N configuration can be attributed to increased defects in the NDG film, as the pyrrolic-N configuration creates more defects in the film. Overall, it can be inferred from the transmittance of Graphene and NDG films that the as the defects increased in the film, the transmittance value decreased. Therefore, the pristine monolayer graphene has more transmittance value than the monolayer NDG films.

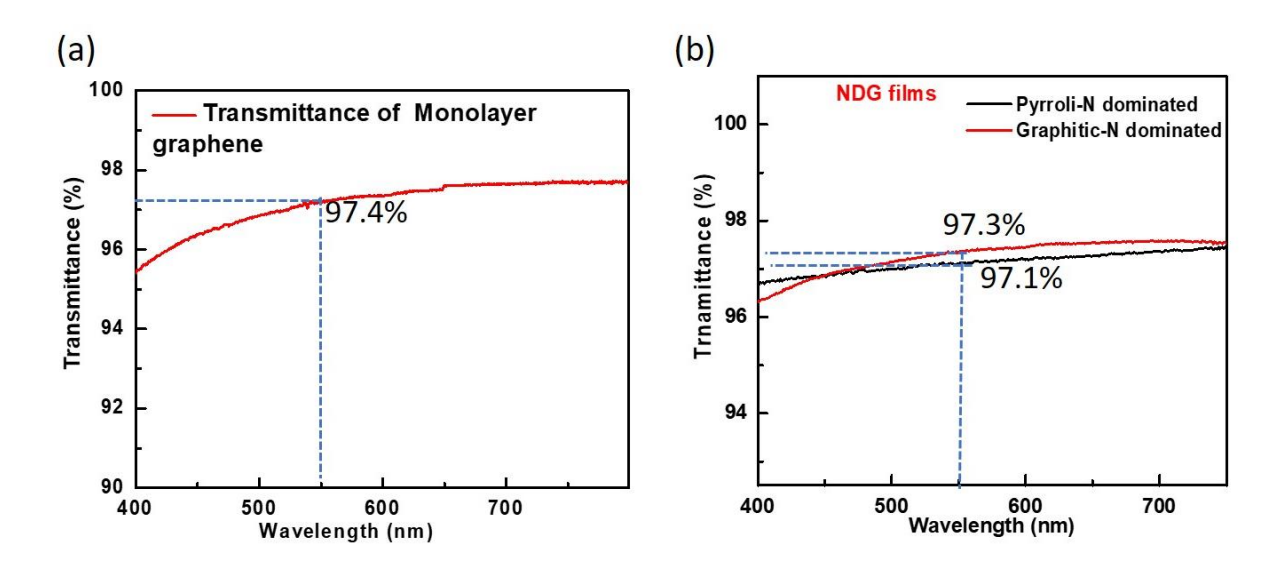


Figure 6.1 Optical transmittance of continuous films (a) pristine graphene (b) nitrogen-doped graphene; pyrrolic-N dominated and graphitic-N dominated configurations.

6.2.2 Graphene and NDG Field Effect Transistors (FETs)

The core of modern electronics is to control the material's electronic properties by applying external voltage. Indeed, an electric field's effect changes the carrier concentration in the semiconducting device, thus changing the electric current. When the FET's channel width is reduced to the nanoscale resulting in low device performance due to the quantum effects, and the source to drain tunneling would also be high, leading to less gate control. In this scenario, graphene was found to be a potential alternative candidate for nanoelectronics and other applications that can address the issues related to bulk counterparts.

Graphene has become a promising material for FET devices because of its high ballistic transport properties and high mobilities, which were demonstrated at room temperature. Graphene FETs show unique current-voltage (I-V) characteristics compared to the other popular semiconductors (silicon, germanium). It exhibits an ambipolar behavior, meaning that both charge carrier types contribute to conductivity, as shown in figure 6.2 (a). The charge carrier density is proportional to the external applied potential difference and its polarity between the gate voltage (VGS) and graphene channel. Electron density is increased with the positive gate voltages, and the channel becomes n-type. The negative gate voltage increases the hole density, and the channel turns to ptype [12][13]. The minimum conductivity point that separates these two regions is called the Dirac point (charge neutral point). Theoretically, the Dirac point denotes the zero charge carrier density, and the density of states is zero, where the conduction band and valence band touch each other. However, the intrinsic charge carrier concentration is observed experimentally at the Dirac point due to the charge impurities and puddles originating from the underlying substrate and the rippling of graphene [14]. Both electron and hole conductivities show linear behavior around the Dirac point. The ambipolar behavior of graphene has been utilized in electronic circuits such as highperformance frequency doublers, digital moderators, and radio frequency mixers [15,16].

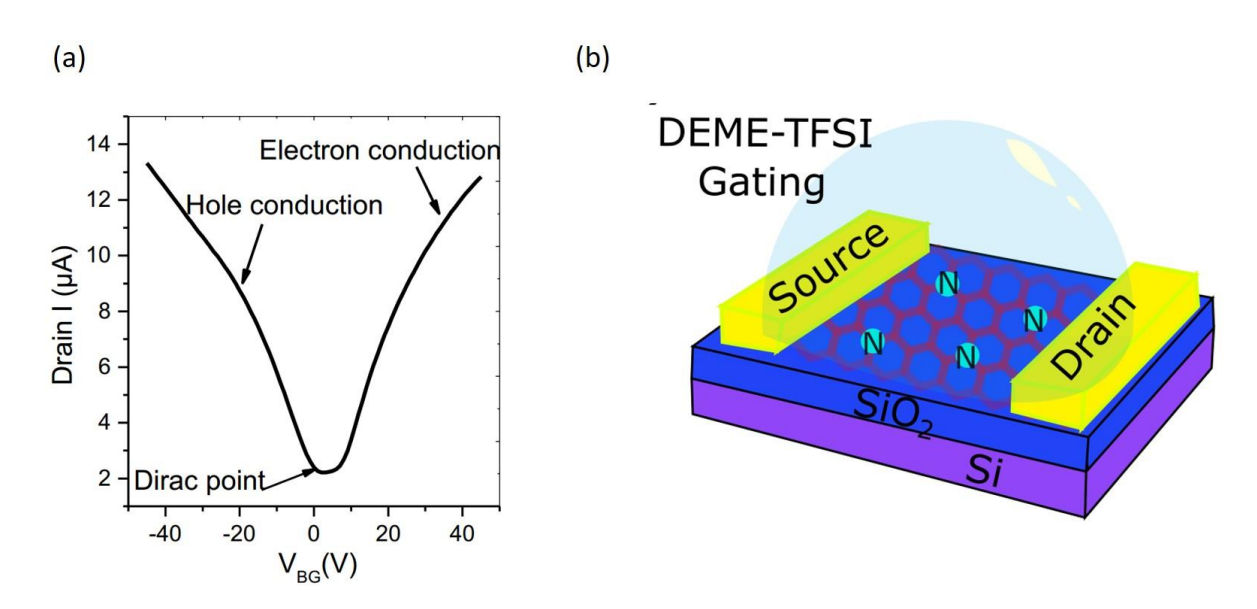


Figure 6.2 (a) Typical ambipolar behavior of graphene field effect transistor under an applied external gate bias voltage. (b) Schematics of electrolyte gated field effect transistor, where DEME-TFSI is used as an electrolyte.

Field effect transistor devices have different architectures with respect to the position of the gate, like back-gated, top-gated, and top-/back-gated FETs. Every architecture has its pros and cons regarding fabrication methodology and desired applications. The performance of the device depends on its architecture [17]. Here, we employed a top-gated FET device for the graphene electrical measurements. An electrolyte DEME-TFSI was used for top gating. This topology is called an electrolyte-gated FET, and its schematics are shown in figure 6.2 (b). The SiO₂ (300 nm)/Si substrate was used for depositing source and drain electrodes using standard lithographic techniques as mentioned chapter-3. On top of the pre-patterned electrodes, the graphene was transferred using the PMMA-assisted wet transfer method. The graphene/NDG channel interconnects the drain and source. The electrolyte was drop-casted onto the Graphene or NDG films, and the transport characteristics of the device were measured at room temperature. The gate is isolated from the channel by the gate dielectric, where the electrolyte acts as the dielectric material. The graphene/NDG channel is characterized by its width (W) and length (L). A current (I_{DS}) flows through the channel from the drain to the source for applied drain-source voltage (V_{DS}) . By applying gate voltage (V_{GS}) , this current can be tuned by adjusting the charge of the channel through the induced electric field. The mobilities were calculated using the peak transconductance method for electrons and holes;

The hole and electron mobility are calculated using the formula:

$$\mu_{e,h} = \frac{L}{WC_{ox}V_{ds}} \left(\frac{dI_{ds}}{dV_{gs}}\right)_{e,h},$$
 -(6.1)

where L (40 µm) and W (20 µm) are the length and width of the channel, C_{ox} is the capacitance of dielectric material (7.2 µFcm⁻²), and $\left(\frac{dI_{ds}}{dV_{gs}}\right)_{e,h}$ is the slope of the I_{DS} vs. V_{GS} curve in a linear region [18].

The CVD-grown continuous graphene film was used for the FET measurements. The measured transport characteristics of electrolyte-gated graphene FET are shown in figure 6.3. Transfer characteristics are shown in figure 6.3 (a), in which the drain current (I_{DS}) curve is obtained by varying the gate voltage (V_{GS}) from -1 V to 1 V at different fixed V_{DS} (0.1 V and 0.2 V).

Characteristic v-shaped ambipolar behavior was obtained. The Dirac points for fixed V_{DS} =0.2 V is 0.9 V. The minimum conductivity at Dirc points is attributed to the unintentional doping to the graphene sample [19]. The negative and positive V_{GS} region denotes the hole and electron transport, respectively. The Dirac point at 0.9 eV indicates that the graphene film is p-type doped. The average electron and hole mobility was determined to be 65.4 cm²V⁻¹s⁻¹ and 94.8 cm²V⁻¹s⁻¹, respectively, at V_{DS} =0.2V and comparable to the reported mobilities with electrolyte-gated FET for exfoliated graphene in the literature [20]. The low mobility of the electrolyte-gated FET compared to the back-gated FET can be attributed to two effects. One is the residues of PMMA polymer leftover on the surface of the graphene due to transfer which is in direct contact with the drop-casted electrolyte. The other is the graphene film's surface roughness, where the graphene/electrolyte interface is rougher than the graphene/ SiO₂ interface [20]. The output characteristics are shown in figure 6.3 (b), where the I_{DS} was obtained by varying the drain voltage (V_{DS}) at a fixed gate voltage (V_{GS}) of 0.2V. The conductivity shows that it follows the linear behavior due to graphene's semi-metallic nature.

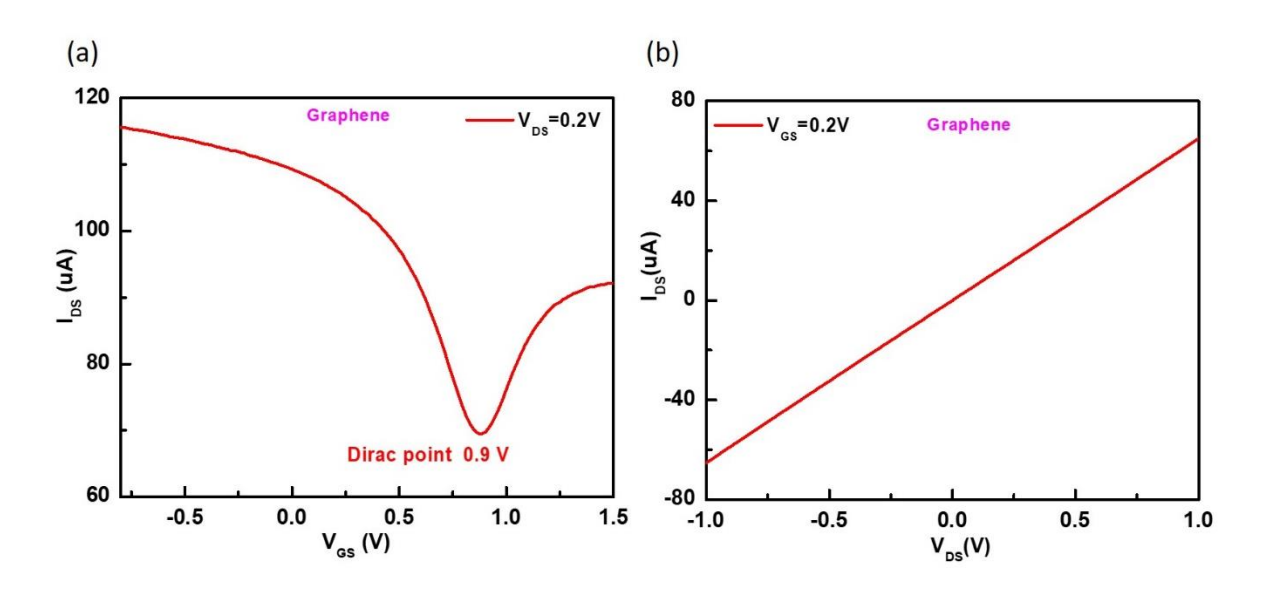


Figure 6.3 Electrolyte-gated FET measurements of the CVD-grown graphene film from PMMA.

(a) transfer characteristics and (b) Output characteristics of conductivity.

FET measurements were performed using the NDG films synthesized from phthalocyanine. FET devices were fabricated for pyrrolic-N and graphitic-N dominated configuration films. The pyrrolic-N dominated configuration NDG films have ~ 0.7 % nitrogen dopants, while the Graphitic-N dominated NDG film has ~ 0.6 % concentration. Figure 6.4 (a) shows the I-V curve

for both pyrrolic-N and graphitic-N dominated NDG films. The pyrrolic-N and graphitic-N NDG samples show resistivity of \sim 8.2 Ω -cm and \sim 3.75 Ω -cm, respectively. This reduction of resistivity for the Graphitic-N dominated configuration NDG film can be due to a decrease in the number of dopants and type of configuration in the film. Figure 6.4 (b) shows the transfer curve for both films at 0.1 V V_{DS} . The graph shows a typical ambipolar nature of NDG with a minimum conductivity point associated with the Dirac point. The presence of the Dirac point at positive gate voltages indicates p-type charge carrier transport. FETs based on exfoliated graphene supported on SiO₂/Si usually exhibit p-type charge transport due to substrate doping. Even though we cannot completely rule out doping due to the substrate or ambient contaminants, the shift of the Dirac point from 1V for the pyrrolic-N NDG to 0.6V for the graphitic-N NDG film indicates that the film with graphitic dopants is more n-type than the film with pyrrolic dopants.

The calculated mobility for holes and electrons is 13.3 and 10.7 cm²V⁻¹s⁻¹ for the pyrrolic-N dominated NDG film, and 62.8 and 40.4 cm²V⁻¹s⁻¹ for graphitic-N dominated NDG film. The increase in the mobility for the graphitic-N dominated film compared with the pyrrolic-N dominated film can be attributed to the domination of the graphitic-N dopants, which act as less scattering centers.

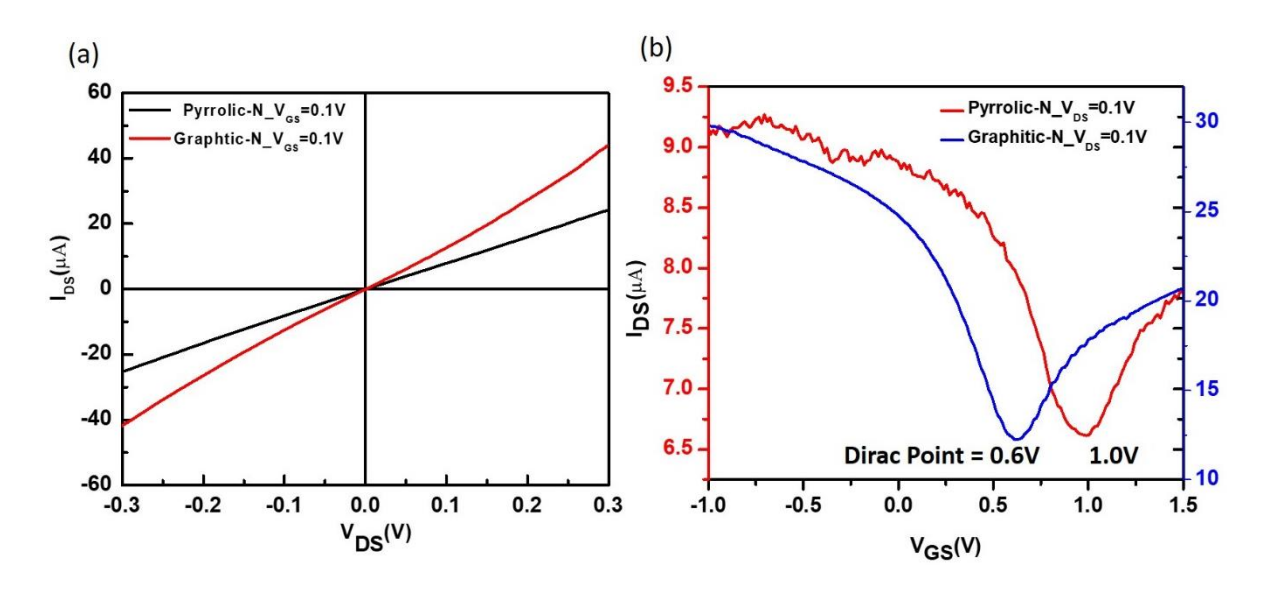


Figure 6.4 Conductivity measurements of NDG Electrolyte-gated FET devices. (a) comparison of the output characteristics of NDG films for pyrrolic-N dominated and graphitic-N dominated at a

fixed gate voltage of 0.1 V. (b) comparison of the transfer characteristics of pyrrolic-N dominated and graphitic-N dominated NDG films at a fixed drain-source voltage of 0.1 V.

The charge concentration, n_{2D} , for NDG can be calculated using the parallel plate capacitor model by the formula:

$$n_{2D} = \frac{c_{ox} \Delta V_{gs}}{e}, \qquad -(6.2)$$

where C_{ox} is the parallel plate capacitance of dielectric, $\Delta V_{gs} = V_{gs} - V_{th} (V_{gs})$ is any voltage in On state), and e is the elementary charge, 1.602 x 10^{-19} C [21]. At $V_{gs} = 1.5$ V, the electron density from the n branch of the curve is found to be 4.05×10^{13} and 2.25×10^{13} cm⁻² in graphitic-N dominated and pyrrolic-N dominated NDG films. This significant reduction in electron density clearly shows that the pyrrolic-N dominated is more p-type compared to the graphitic-N dominated NDG film. The effect of growth time on the fermi level can be understood by calculating the work function difference between the two samples using the formula for change in work function ($\Delta \Phi$):

$$\Delta \Phi = \Phi_{\text{pyrrolic-N}} - \Phi_{\text{graphitic-N}} = ln(\frac{n_{2D,\text{pyrrolic-N}}}{n_{2D,\text{graphitic-N}}}), \qquad -(6.3)$$

Where, $\Phi_{\text{graphitic-N}}$ and $\Phi_{\text{pyrrolic-N}}$ are work functions of the graphitic-N and the pyrrolic-N dominated NDG films, respectively [22]. n_{2D} is the carrier density extracted from FET measurements, as discussed above. The shift comes out to be -0.58 eV. This shows that the fermi level shifts down in pyrrolic-N dominated NDG film compared to graphitic-N dominated NDG film by 580 meV, making it to be more p-type material. The obtained mobilities for both configurations were compared with the reported mobilities in the literature and shown in table 6.1. The mobilities of the films produced in our work are in the range of reported mobilities. Overall, from FET measurements of graphene and NDG films, we can infer that the mobility has decreased from Graphene to NDG owing to the introduction of dopants in the NDG film, which acts as scattering centers.

Precursor	Substra te	Growth temp.	Total N content	Defect configuratio	Type of FET	Mobility (cm ² V ⁻¹ s ⁻¹)	Dirac point	Ref.
		(°C)	(%)	n				
Melamine	Cu	990	5.6	Graphitic-N	Back gate	72	-25	[23]
Pyridine	Cu	1000	2.4	Pyridinic-N	Back gate	5	-10	[24]
1,3,5- Triazine	Cu	700	5.6	Pyrrolic-N	Back gate	11.7	-1.5	[25]
PMMA + Melamine	Cu	1000	2	Pyrrolic-N	Back gate	<10	-8	[26]
Pyridine	Cu	300	16.7	Graphitic-N	Back gate	53-74	-26	[27]
Phthalocya nine	Cu	1050	0.7	Pyrrolic-N	Electrolyte -gate	13.6	1.0	Our work
Phthalocya nine	Cu	1050	0.6	Graphitic-N	Electrolyte -gate	62.8	0.6	Our work

Table 6.1 Comparison of mobility of Nitrogen-doped Graphene.

6.2.3 Graphene/Molybdenum Disulfide (MoS₂) heterostructure as a photodetector

Heterostructures are synthetic materials that can be fabricated with two or more materials, either stacking vertically (vertical heterostructure) or in-plane stitching (lateral heterostructure) to obtain desired functionalities [28]. New artificial materials formed from heterostructures provide synergistic properties and applications compared to the individual components. Here, we employed two 2D materials, MoS₂ and Graphene, stacked vertically to form a heterostructure. MoS₂ is an inorganic compound of the transition metal dichalcogenides (TMDs) series, containing one molybdenum atom and two sulfur atoms, connected by covalent bonding. MoS₂ is a semiconducting material with a band gap of 1.8 eV, which changes from an indirect bandgap to a direct bandgap when it reaches the monolayer. Monolayer MoS2 is a suitable material for optoelectronic applications (photodetector) because the direct band gap would allow a high absorption coefficient and efficient generation of electron-hole pairs under photoexcitation [29]. Another 2D material with great carrier mobility and quick response time is graphene, which is particularly appealing for optoelectronic applications. The properties mentioned above of both materials can be utilized together in a heterostructure to obtain an efficient photoconductive behavior compared to the individual component's photoconductive behavior. In this heterostructure, the MoS₂ acts as a light-sensitive material that promotes the generation of photogenerated carriers and the role of graphene as a conductive material that improves the device's carrier transmit speed.

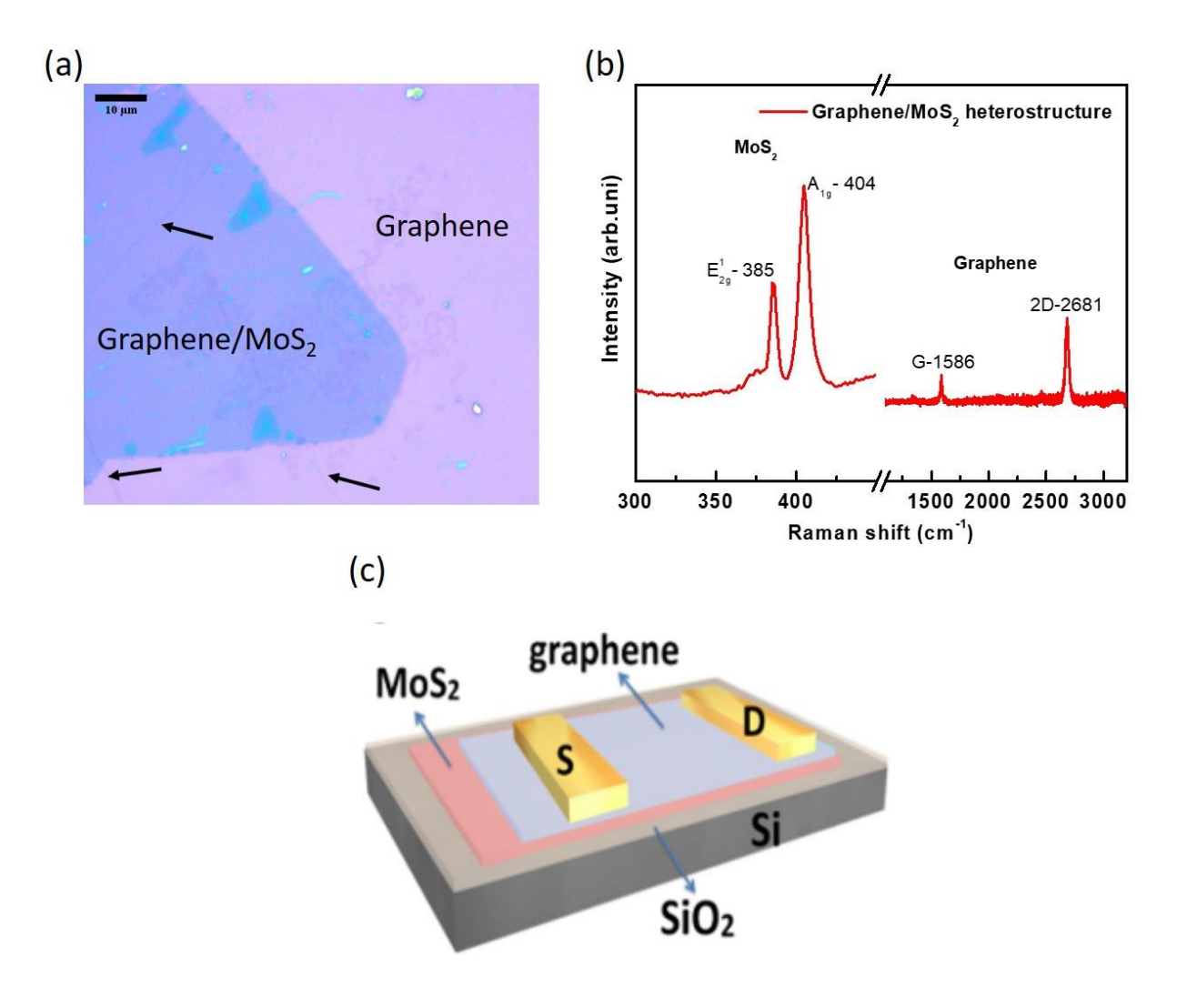


Figure 6.5 (a) optical micrograph and (b) Raman spectrum of graphene/MoS2 heterostructure, laser excitation used was 532 nm for Raman measurements. (c) schematic representation of graphene (Gr)/MoS2 photodetector [30].

MoS₂ was grown on SiO2(300 nm)/Si by using molybdenum trioxide (MoO₃) and sulfur (S) precursors via APCVD [31]. The synthesized graphene on copper from PMMA via APCVD. Graphene/MoS₂ heterostructure was obtained by transferring them onto SiO₂ (300 nm)/Si using PMMA assisted wet transfer method. The optical micrograph of the graphene/ MoS₂ vertical heterostructure is shown in figure 6.5 (a). The arrows (black color) indicate the wrinkles of graphene on the MoS₂ and SiO₂ substrate. Thus, it can be corroborated that the graphene is covered

MoS₂ completely. Then, the Raman measurements were performed on the heterostructure with a 532 nm excitation wavelength. Figure 6.5 (b) shows the Raman spectrum of graphene/MoS₂ heterostructure. The peak positions at 385 cm⁻¹ and 404 cm⁻¹ indicate the MoS₂ material, and 1586 and 2681 cm⁻¹ positions represent the G and 2D bands, respectively, which are the characteristic bands of the graphene. Figure 6.5 (c) represents the graphene (Gr)/MoS₂ heterostructure photodetector device, where the channel is formed between the source and drain metal electrodes. Then, Photoconductivity measurements were performed on the graphene/MoS₂ device.

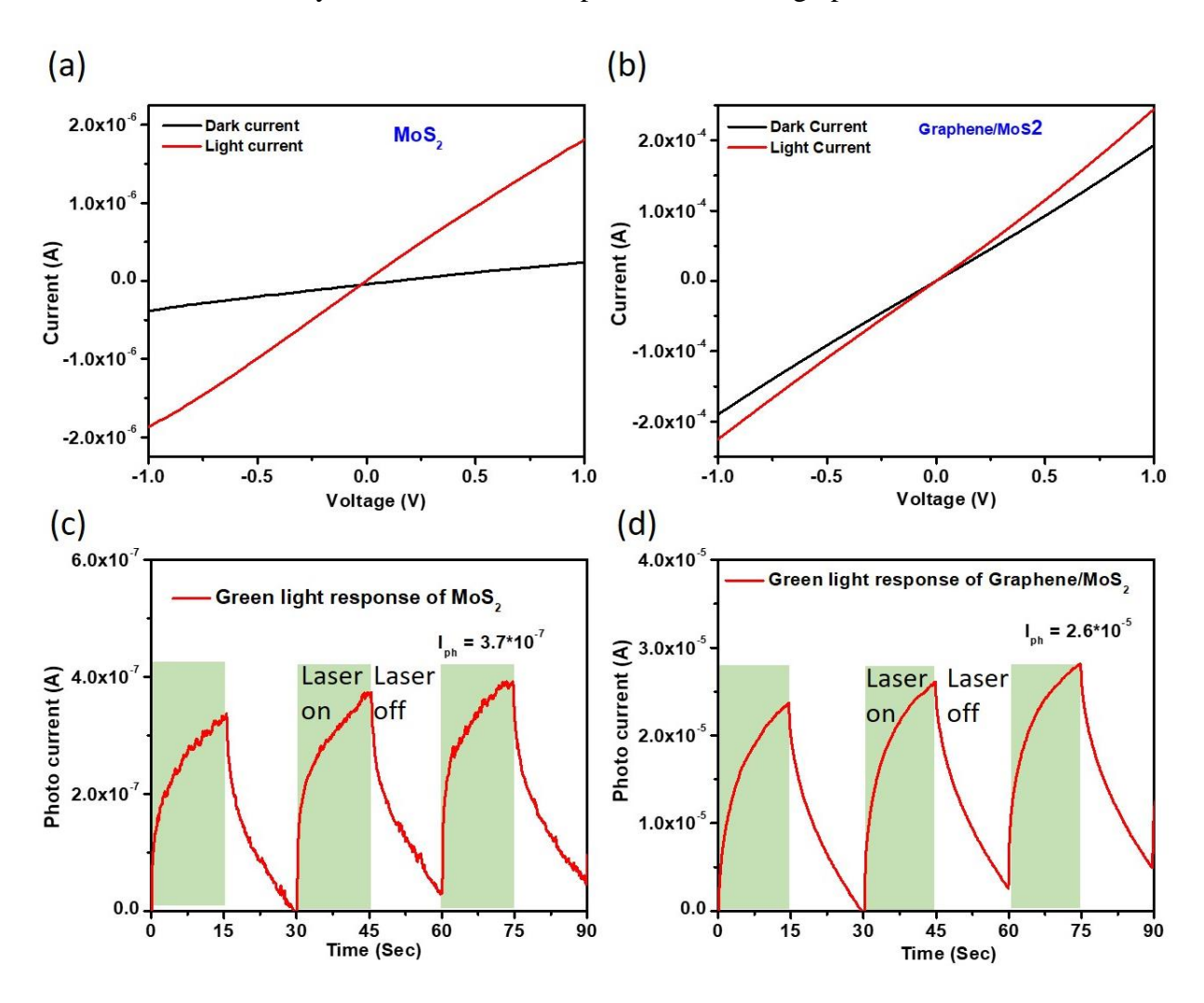


Figure 6.6 Photoresponse measurements using 532 nm green light source. Dark and light current of (a) MoS_2 (b) Gr/MoS_2 . Transient photoresponse of (c) MoS_2 and (d) Gr/MoS_2 for green light (532 nm laser) at constant $V_{ds} = 0.5 \text{ V}$.

Generally, the process of light detection starts when the absorbed incident light energy is greater than the bandgap energy of photoactive material. Then, the photogenerated electron/hole pairs are separated by the applied voltage (V_{ds}), and the separated holes and electrons are collected at the electrodes. Photoresponse measurements were performed using a green light source of 532 nm. The energy of the source is 2.3 eV, which is higher than the MoS_2 bandgap energy, which results in the activation of the generation of photocarriers. MoS_2 and $Graphene/MoS_2$ both the devices showed enhancement in current from dark to light, shown in figure 6.6 (a) and (b). The transient photoresponsivity of both devices with green light was studied at constant $V_{ds} = 0.5 \text{ V}$, shown in Figures 6.6 (c) and (d). The photoconductive switching behavior with 15 second green light pulse is shown for both devices. The photocurrent response has repeatability and stability for all cycles (laser on and off). The value of photocurrent ($I_{ph} = I_{light} - I_{dark}$) was calculated from the graphs and found to be 3.7×10^{-7} for MoS_2 , whereas 2.6×10^{-5} for Gr/MoS_2 . The increment of photocurrent is due to the higher conductivity of graphene. The photoresponsivity (R) of the devices is calculated using the formula given in equation 6.4 [32].

$$R = \frac{I_{Ph}}{P \times A} \tag{6.4}$$

Where I_{ph} is the photocurrent, P is the power density, and A is the effective area of the device. The values of power density (P) and active area (A) used in the measurements are 5 mW/cm² and 100 μ m x 10 μ m, respectively. The obtained responsivity values for MoS₂ and Gr/MoS₂ are 7.4 A/W and 520 A/W, respectively. The increase in photoresponsivity (R) for Gr/MoS₂ compared to the MoS₂ device is due to the presence of graphene, where the transit time of photoexcited carriers through graphene is low and the long recombination time ($\tau_{lifetime}$) of electron-hole pairs [33]. Therefore, using the heterostructures formed with the graphene can enhance the figures of merit (photocurrent, photoresponsivity) that characterize a photodetector.

6.2.4 Surface-enhanced Raman spectroscopy of Graphene and NDG

Surface-enhanced Raman spectroscopy (SERS) technique has become an alternative to Raman spectroscopy, where it cannot obtain the fingerprints of molecular vibrations of some compounds with low Raman signals because of their low Raman scattering cross-section [34]. The SERS is a highly sensitive, reusable, and fast-detecting platform for the analyte (probe) molecules, which can be traced down to a single molecule level [35]. When the probe molecules are adsorbed onto the

SERS substrates, the Raman signals of probe molecules are enhanced, with which they can be sensed. In normal Ramal spectroscopy/scattering, the Raman signal arises mainly due to the interaction between the photons and matter molecules. In contrast, there is a complex mechanism behind the enhancement of the Raman signal in SERS. Broadly, two widely accepted mechanisms for SERS are the electromagnetic enhancement mechanism (EM) and the chemical enhancement mechanism (CM). The enhancement in EM is attributed to two reasons: the local electric field enhancement around the rough metallic substrate surfaces induced by the surface plasmon effect and the re-radiation enhancement effect [36]. The EM can provide an enhancement factor up to 10^8 to 10^{11} , and it does not depend on the nature of probe molecules. The Raman signal amplifies in the CM due to the charge transfer effect between the substrates and probe molecules. Resonant charge transfer chemical and non-resonant chemical effects are the two possibilities in the charge transfer effect that contribute to the CM [36]. The enhancement factor in CM is less than the EM enhancement factor and is dependent on the interaction of the probe molecule with the SERS substrate. However, the substrate is pivotal in the SERS enhancement irrespective of which mechanism it follows.

The conventional substrates used in SERS are roughened noble metals (gold, silver, etc.) because of their high enhancement factors operated through the EM effect. For these metals, the EM effect is so dominant that the presence of the CM effect vanishes. However, the metallic substrates have some disadvantages, such as the deformation of the adsorbate because of the strong adsorbate-metal interaction, the catalytic effect of metals inducing side-reactions to the adsorbates, and the low oxidation resistance of metals and photobleaching effect. Therefore, there is a need to explore non-metallic substrates, which could overcome the limitations of metal substrates. Recently, 2D materials like graphene and hexagonal boron nitride (h-BN) have been found to be an effective alternatives as they provide uniform, clean, and repeatable enhanced Raman signals [37]. 2D materials exhibit unique properties like high oxidation resistance and chemical inertness, large specific surface area, high flexibility and thermal conductivity, and good biocompatibility. These properties can be considered desirable features for SERS substrates. These materials showed intriguing prospects as Raman enhancement substrates, such as (1) easy control of probe molecule orientation, (2) ability to combine with conventional SERS substrates, (3) chemical mechanism dominance than the electromagnetic mechanism, and (4) suitable as flexible substrates [38]. The

enhancement factor (EF) in 2D materials depends on the probe molecule type, orientation, concentration, substrate type, and laser excitation wavelength [39].

In our work, pristine graphene and Nitrogen-doped graphene have been utilized as SERS substrates. Raman signal enhancement by graphene is called graphene-enhanced Raman spectroscopy (GERS). It was reported that the graphene could quench the fluorescence besides enhancing the Raman signals of probe molecules [40]. It was reported that the graphene systems follow the chemical enhancement mechanism [41]. Recently, there were attempts to use doped graphene as a SERS substrate and found that the enhancement is far better than the graphene. Nitrogen doping to graphene results in additional charge carriers and modifications in the electronic properties, which can be utilized in the GERS applications. Until now, not much research has been done on the effect of nitrogen doping configuration on the enhancement of Raman signals. We employed three organic dyes as probe molecules. They are methylene blue (MB), crystal violet (CV), and Nile blue (NB.), and their structures are shown in figure 6.7 (a-c) [42,43]. The obtained enhanced Raman signals for graphene and NDG were analyzed and compared with the literature. We also investigated the reproducibility and repeatability of the SERS behavior of graphene and NDG films.

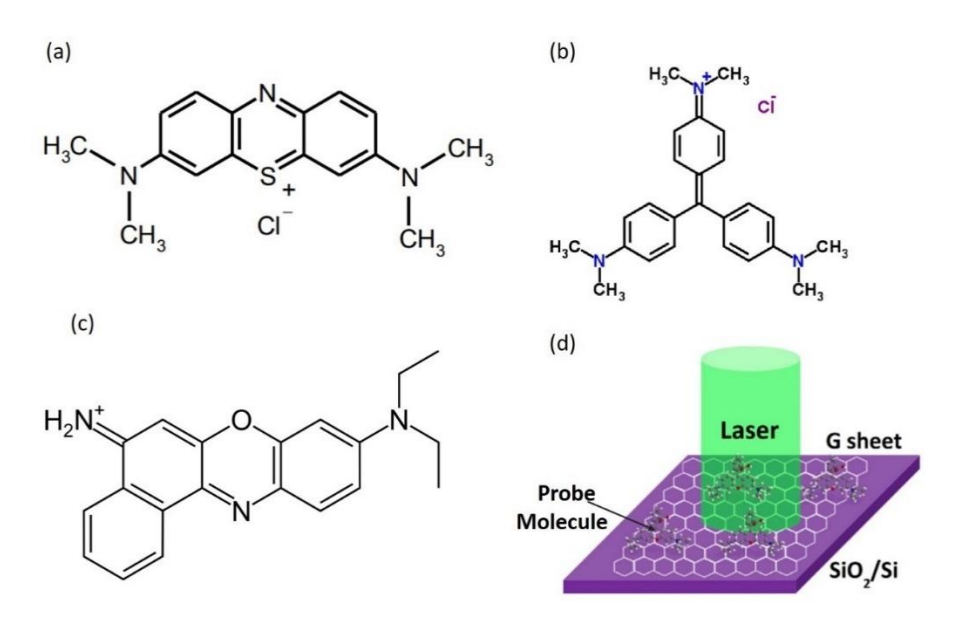


Figure 6.7 The molecular structure of (a) methyl blue, (b) Crystal violet, and (c) Nile blue, which are used as probe molecules [42,43]. (d) schematic representation of the SERS experimental setup [44].

The SERS measurements were performed on CVD-grown graphene and NDG films by using organic dyes as probe molecules. In NDG, the pyrrolic-N and graphitic-N dominated configuration films were used. The schematics of the SERS experiment are shown in figure 6.7 (d) [44]. The Raman spectra were acquired using In via Renishaw spectrometer using 633 nm and 532 nm excitation wavelength, 100 X objective lens, laser power 1 mW, and laser spot size 1 um. All parameters were kept constant throughout the measurements. The different concentrations (in molar) from 10⁻⁸ M to 10⁻¹ M of MB, CV, and NB were prepared in methanol. The grown graphene and NDG samples were transferred onto SiO₂(300 nm)/ Si substrates with a PMMA-assisted wet transfer technique. The transferred Graphene and NDG films were immersed in the different concentrations for 5 minutes and dried for 15 minutes. Then, the Raman measurements were recorded. All measurements were performed with a 633 nm wavelength. Wherever another wavelength was used is mentioned, especially in a future discussion.

(A) Methylene Blue (MB)

First of all, the SERS behavior was investigated for pyrrolic-dominated NDG film with a concentration of 1x 10⁻⁵ M of MB. Raman spectra of MB on SiO2/Si and pyrrolic-N NDG film are shown in figure 6.8. The sharp G-band (1591 cm⁻¹) and 2D band (2635 cm⁻¹) are the characteristic bands of monolayer graphene, and the presence of the peak at 1325 cm⁻¹ with small intensity is the D band that arose due to the nitrogen dopants. Thus, the Raman spectrum denotes the monolayer nitrogen-doped graphene on SiO₂/Si. The Raman spectrum of 10⁻⁵ M concentration on SiO₂/Si is shown in the same figure. It was reported that the MB has distinguishable different Raman bands between 250 cm⁻¹ and 1750 cm⁻¹, in which the strongest band at 1624 cm⁻¹ arises due to C-C stretching. The single peak was not observed in the spectrum due to the high fluorescence that suppressed all the bands and the weak Raman scattering cross-section. In contrast, the Raman bands of MB were observed when it was on the Pyrrolic-N NDG film, shown in the same figure. The Raman bands of MB are denoted with *, and the strongest band is at 1623 cm⁻¹, confirming the Methylene blue (MB). We can observe that the fluorescence has been quenched (not completely), and the Raman signals have been enhanced. The enhancement of Raman signals of MB when it is on pyrrolic-N NDG film can be attributed to the charge transfer between the MB and pyrrolic-N NDG substrate [44,45]. We can eliminate the contribution of the EM mechanism because of excitation wavelength used is in the visible region, which does not interact with the

wavelength of surface plasmon resonance of NDG as it is about $2.73~\mu m$ [46]. It can be corroborated from the Raman enhancement of MB that our grown films are exhibiting SERS behavior. After that, the three substrates, graphene, pyrrolic-N NDG, and graphitic-N NDG films, were used as SERS substrates for further analysis of SERS measurements.

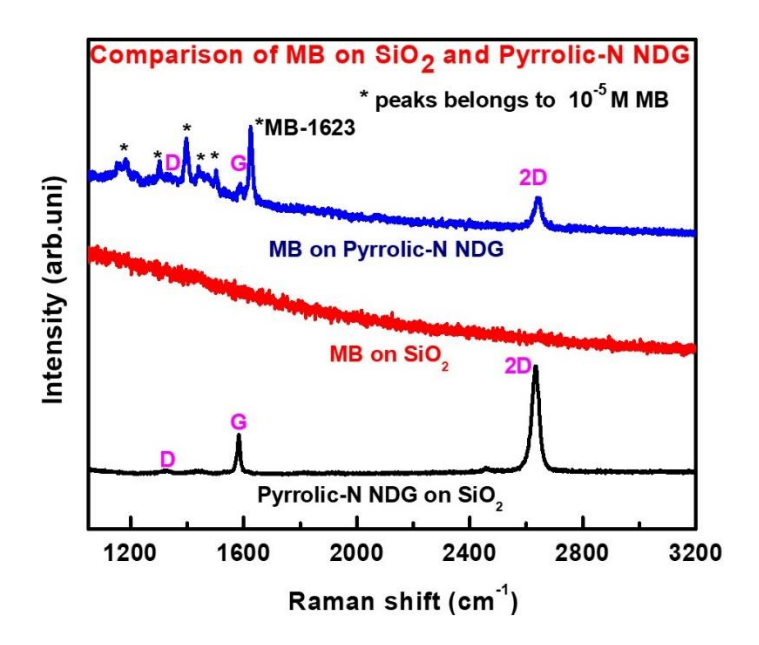


Figure 6.8 Raman spectra of Pyrrolic-N NDG film (a) and the methylene blue (MB) on the SiO2 (300 nm)/Si (b) and Pyrrolic-N NDG films (c). The laser excitation wavelength used was 633 nm.

The MB molecules were investigated on the pyrrolic-N NDG, graphitic-N NDG, and graphene substrates for the enhancement of Raman signals and also verified their reproducibility. The strongest peak of MB located at 1623 cm⁻¹ was opted to use as SERS enhanced Raman signal for further measurements. The variation in the Raman signal intensity with increasing the concentration of MB on pyrrolic-N NDG film is shown in figure 6.9 (a). We can observe that as the concentration of MB from 10⁻⁸ M to 10⁻³ M increases, the Raman signal at 1623 cm⁻¹ peak increases. The least concentration of MB that has been detected on pyrrolic-N NDG substrate is 10⁻⁸ M, as the prominent Raman band 1623 cm⁻¹ is clearly visible in the spectrum. The Raman band 1623 cm⁻¹ peak intensity was plotted against the concentration of MB is shown in figure 6.9 (b). It shows that 1623 cm⁻¹ peak intensity is linearly dependent on the concentration in the logarithmic scale. The correlation coefficient (R²) is 0.98, indicating that the pyrrolic-N NDG substrate has notable sensitivity [47]. The reproducibility of the SERS signal of 1 x 10⁻⁵ M MB on

pyrrolic-N NDG was evaluated by recording the MB Raman spectra at 10 random positions, and the spectra are shown in figure 6.9 (c). For all 10 different sites, the presence of the SERS signal of MB at 1623 cm⁻¹ indicates the availability of MB all over the substrate. The histogram plot was drawn for the variation in the intensity of the 1623 cm⁻¹ peak with different sites on pyrrolic-N NDG substrate, shown in figure 6.9 (d). The root means square deviation (RSD) of the Raman peak at 1623 cm⁻¹ was calculated to be 20.36 %, indicating that the pyrrolic-N NDG has good reproducibility.

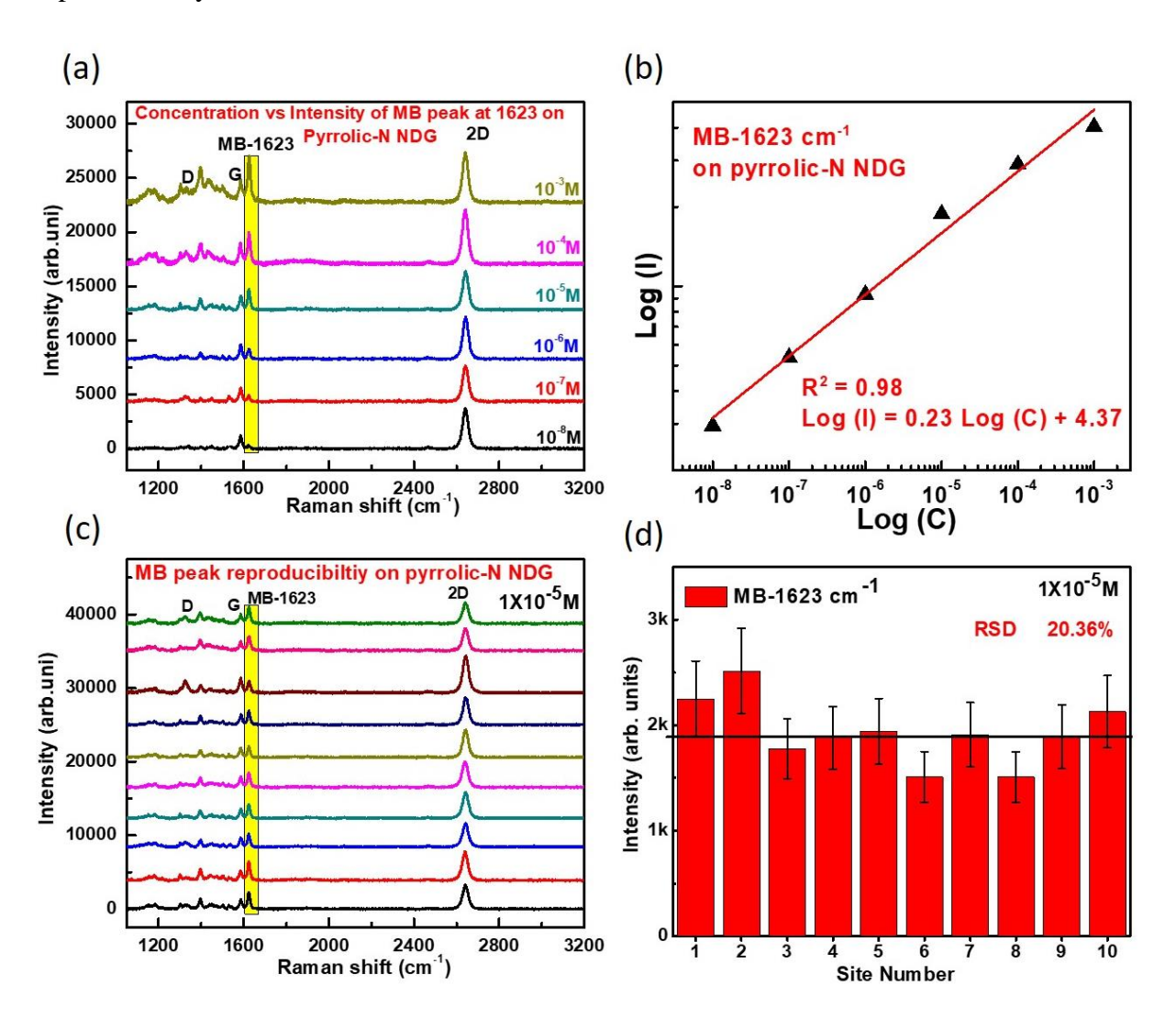


Figure 6.9 (a) SERS spectra of MB with its varied concentration on pyrrolic-N NDG. (b) variation of MB peak (1623 cm⁻¹) with concentration variation. (c) SERS spectra of 1 x 10⁻⁵ MB were recorded at various positions. (d) Histogram plot of the MB SERS signal intensity at 1623 cm⁻¹ peak recorded at 10 sites.

The SERS signal of MB was measured on the graphitic-N NDG substrate. The intensity of the SERS signal of MB with a variation of concentration of MB was investigated, and it is shown in figure 6.10 (a). It was found that the intensity of the SERS signal of MB increased as the concentration increased. The lowest concentration detected is 10⁻⁸ M MB, but its intensity is relatively lower than when it is pyrrolic-N NDG. The Raman intensity of MB at 1623 cm⁻¹ was plotted against the concentration variation, as shown in figure 6.10 (b), and it was shown that they hold a linear relationship in the logarithmic scale. The R² is 0.99, which indicates that graphitic-N NDG has more sensitivity. The reproducibility of the SERS signal of MB was probed on the

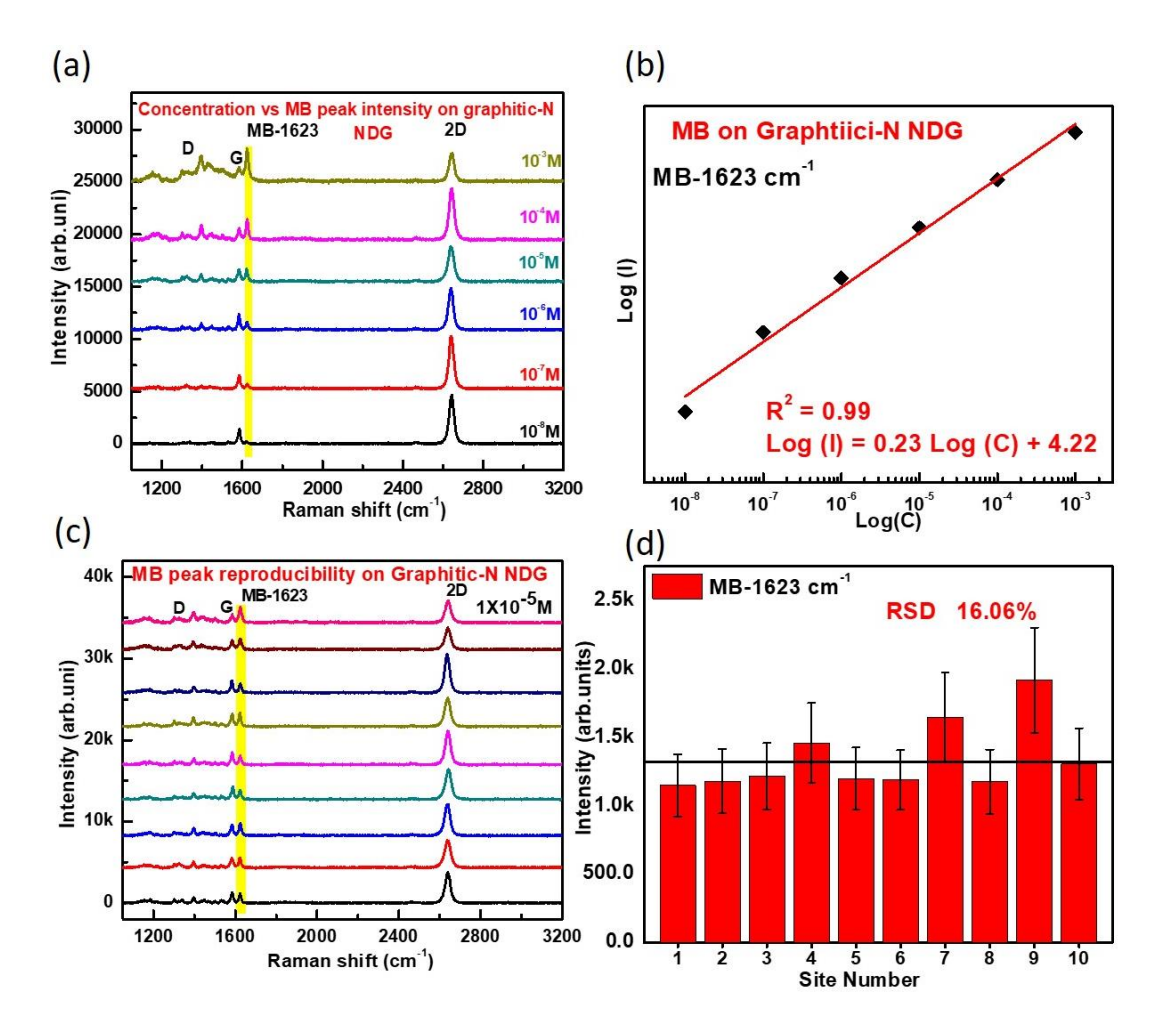


Figure 6.10 (a) SERS spectra of MB with its varied concentration on graphitic-N NDG. (b) variation of MB peak (1623 cm⁻¹) with concentration variation. (c) SERS spectra of 1 x 10⁻⁵ MB were recorded at various sites on graphitic-N NDG. (d) The histogram plot of the MB SERS signal intensity at 1623 cm⁻¹ peak was recorded at 10 sites.

graphitic-N NDG. The Raman spectra shown in figure 6.10 (c) show that the strong peak of MB at 1623 cm⁻¹ is present in all the spectra. The Histogram of the intensity variation of the 1623 cm⁻¹ band was plotted with different sites on graphitic-N NDG substrate, shown in figure 6.10 (d). The RSD of the 1623 cm⁻¹ peak was obtained at 16.06%, which is lower compared to the RSD value on pyrrolic-N NDG. This might be due to the decrease of the nonuniform adsorption of MB on the graphitic-N NDG, as it has fewer defects in the film. The decrease in the RSD indicates the increase in the uniformity of the enhanced Raman signal of MB.

Similarly, the Raman signal enhancement of MB was studied on graphene. The dependence of enhancement of the Raman signal of MB on concentration has been investigated and depicted in figure 6.11 (a). It can be observed that the enhancement of the Raman signal increases as the concentration increases. The lowest concentration of MB detected on graphene is 10⁻⁶ M MB. The decrease in the detection of the lowest concentration of MB by graphene substrate compared to the NDG substrate can be attributed to the absence of defects (Nitrogen dopants) in graphene. The Raman enhanced signal of 1623 cm⁻¹ intensity is varied with concentration, as shown in figure 6.11 (b), and found that they hold the linear relationship in the logarithmic scale.

The Raman spectra of 1x10⁻⁵ M concentration of MB on graphene were recorded at 10 locations, and it is shown in figure 6.11 (c). It can be noticed that the Raman-enhanced signal existed everywhere, indicating the presence of MB all over the sample. The Histogram of the Raman band 1623 cm⁻¹ intensity variation of MB was investigated with different sites on graphene. The RSD was calculated to be 12.75%, indicating that the graphene has good reproducibility. The 12.75% is lower than the values (20.26% & 16.06%) obtained for NDG films, indicating that the graphene can produce a uniform Raman-enhanced signal. It can be attributed to the uniform deposition of MB molecules over graphene and the same amount of charge transfer between graphene and MB molecules all over the sample.

The Raman-enhanced signal of 1x10⁻⁵ M concentration of MB has been compared for all substrates (pyrrolic-N NDG, graphitic-N NDG, and graphene), and it is shown in figure 6.12 (a). It can be noticed that the intensity of Raman enhanced signal of 1623 cm⁻¹ peak is relatively decreasing from the pyrrolic-N NDG to graphene. To quantify the enhancement effect of these SERS substrates on MB probe molecules, the enhancement factor (EF) was calculated using equation 6.5.

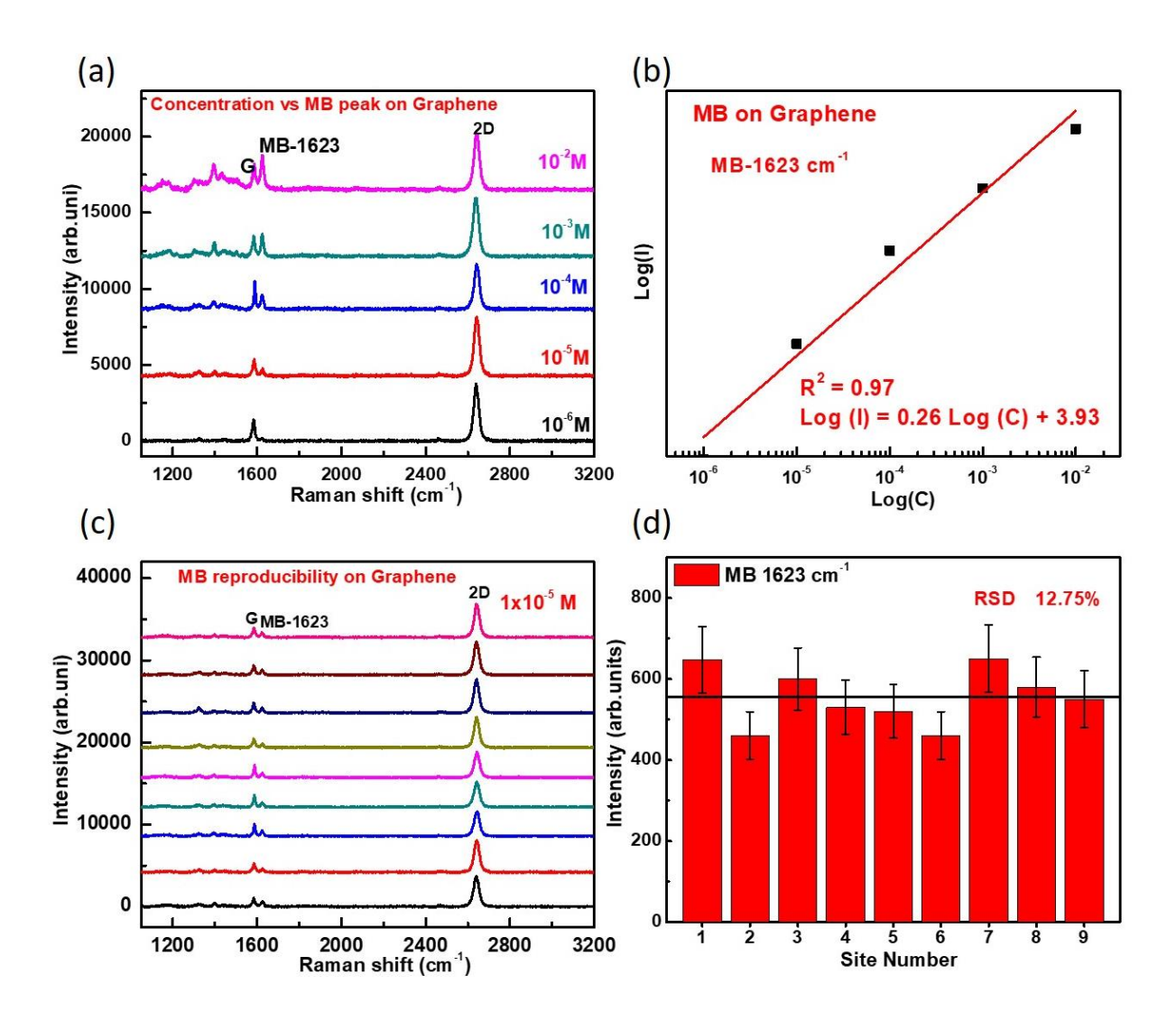


Figure 6.10 (a) SERS spectra of MB with its varied concentration on graphene. (b) variation of MB peak (1623 cm⁻¹) with concentration variation. (c) SERS spectra of 1 x 10⁻⁵ MB recorded at various sites on graphene. (d) Histogram plot of the MB SERS signal intensity at 1623 cm⁻¹ peak recorded at 10 sites.

$$EF = \frac{I_{SERS} X C_{Raman}}{I_{Raman} X C_{SERS}}$$
 -(6.5)

Where I_{Raman} is the Raman intensity of the probe molecule on a reference substrate (SiO₂/Si)

 C_{Raman} is the corresponding concentration of the probe molecule in methanol

 I_{SERS} is the Raman intensity of the probe molecule on the SERS substrate

 C_{SERS} is the corresponding concentration of the probe molecule in methanol.

The obtained enhancement factors of MB for pyrrolic-N NDG, graphitic-N NDG, and graphene SERS substrates are 7.0X10⁵, 4.8X10⁵, and 5.0X10³, respectively. The enhancement factor for NDG substrates is in 10⁵ order, while graphene has 10³. The increase in the EF for NDG is due to the nitrogen dopants that contribute to the additional charge carriers in the film that result in a further increase of charge transfer between probe molecules and the SERS substrate, which in turn increases the polarizability of vibrational mode at 1623 cm⁻¹. Thus, it can be confirmed that NDG is a better SERS substrate than graphene. The EF for pyrrolic-N is more than graphitic-N, even though the order of EF is the same. It is due to the pyrrolic-N NDG having more N-dopants than the graphitic-N that increases the charge transfer. There is also a possibility that more adsorption of MB molecules on the pyrrolic-N NDG as it creates more defects in the film compared to the graphitic-N NDG substrate. So, it can be understood that the different configurations and concentrations of NDG determine the enhancement of Raman signals of probe molecules.

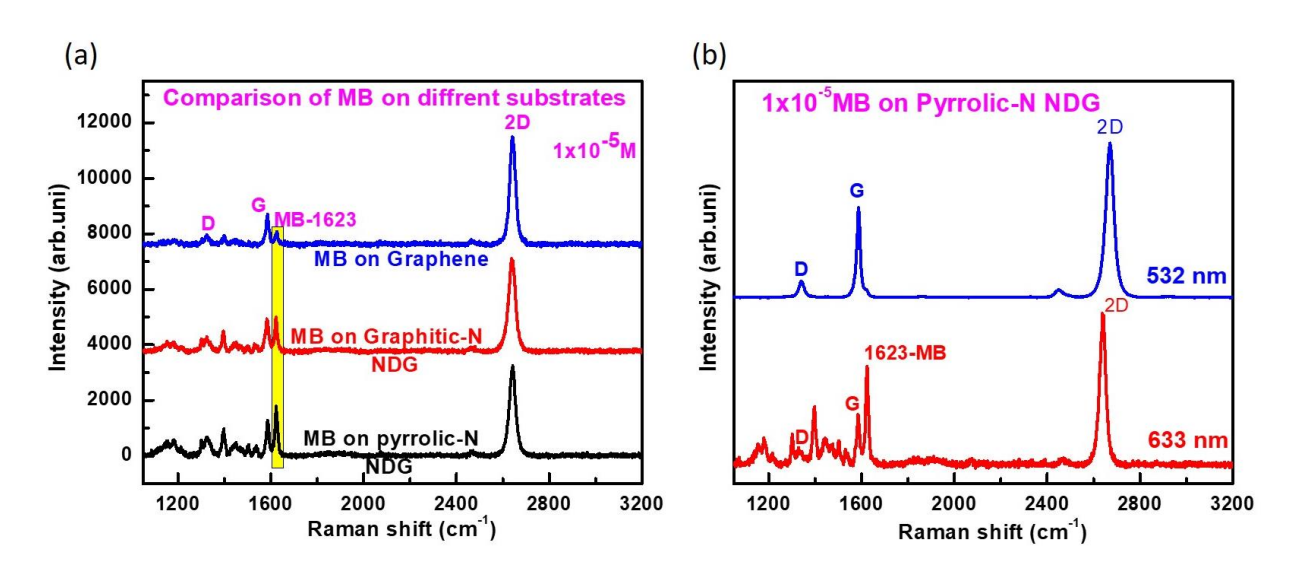


Figure 6.12 (a) Comparison of SERS spectra of 1x 10⁻⁵ M concentration of MB for all substrates (pyrrolic-N NDG, graphitic-N NDG, and graphene). (b) Laser excitation wavelength dependence on the SERS spectra of 1x 10⁻⁵ M concentration of MB on pyrrolic-N NDG substrate.

We used the pyrrolic-N NDG as a SERS substrate for further studies, as it showed more EF than all other substrates. Till now, 633 nm has been used as an excitation wavelength for SERS studies. The laser excitation wavelength dependence has been investigated for 1x 10⁻⁵ M MB concentration with 633 nm and 532 nm. The SERS spectra of MB on pyrrolic-N NDG with 532 nm and 633 nm are shown in figure 6.12 (b). The D, G, and 2D bands shown in the spectra belong to the NDG

substrate, and the 1623 cm⁻¹ band belongs to MB. The shift in the 2D band for both laser wavelengths is because of its dispersive nature. We can observe from the figure that the 633 nm wavelength shows the Raman signal enhancement of MB, and the 532 nm wavelength does not show any enhancement. It implies that for certain laser wavelengths, the Raman intensity of MB on pyrrolic-N NDG meets the Raman resonance condition [48]. At this condition, the energy of the laser excitation wavelength is close to the energy of the electronic transition of MB on pyrrolic-N NDG, which results in more charge transfer giving rise to the enhanced Raman signal. So, we can conclude that the SERS behavior of graphene and NDG substrates depend on the laser excitation wavelength. Here, the 633 nm excitation wavelength meets the resonance condition for MB when it is on NDG or graphene. But, for the same case, when the MB was on SiO₂(300 nm)/Si substrate, excited with 633 nm, there was no Raman signal enhancement, shown in figure 6.8. Thus, it can be corroborated that the enhancement of the Raman signal is not only due to the resonance condition but also the substrate that makes the probe molecule (MB) attain the resonance condition.

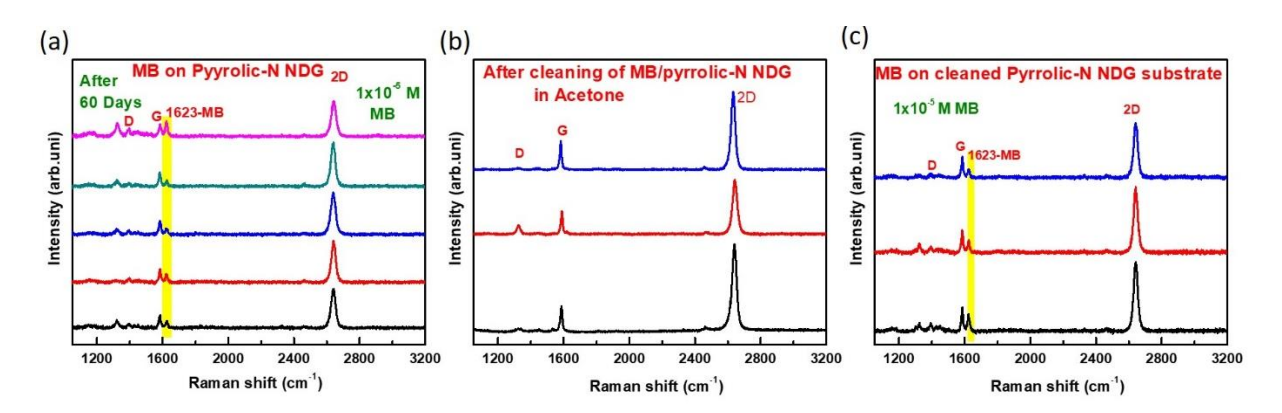


Figure 6.13 (a) SERS spectra of $1x10^{-5}$ M MB on pyrrolic-N NDG recorded after 60 days. (b) Raman spectra were recorded after cleaning the MB/pyrrolic-N NDG in acetone. (c) SERS spectra of $1x10^{-5}$ M MB redeposited on cleaned pyrrolic-N NDG.

The reusability and stability are the figures of merit for SERS substrates besides the enhancement factor for choosing them for commercial use. Here, $1x10^{-5}$ M MB concentration on Pyrrolic-N NDG sample was stored for 60 days in ambient conditions. The SERS spectra were recorded after 60 days shown in figure 6.13 (a). We can observe the D, G, and 2D bands representing the pyrrolic-N NDG substrate, and the peak at 1623 cm-1 belongs to the MB. We can notice that the Raman signal enhancement is there, but it is lower than the freshly prepared sample (figure 6.9 (c)). The

decrease in the Raman-enhanced signal after 60 days can be attributed to the adsorption of moisture and oxygen functionalities on the sample.

The reusability of the pyrrolic-N NDG film as a SERS substrate has been investigated. The sample for which SERS spectra of MB on pyrrolic-N NDG were recorded after 60 days was immersed in the acetone for 10 minutes to remove the MB from pyrrolic-N NDG. The Raman spectra of the cleaned sample are shown in figure 6.13 (b). Only D, G, and 2D bands are the characteristic bands of NDG. The absence of MB bands in the spectra indicates that the MB molecules have been removed from the sample. After that, MB molecules were redeposited by immersing the cleaned pyrrolic-N NDG substrate in 1x10⁻⁵ M concentration. The SERS spectra of MB are shown in figure 6.13 (c). We can observe an enhanced Raman signal of MB at 1623 cm⁻¹ besides the D, G, and 2D bands, indicating the presence of MB all over the sample. We can notice that the enhanced signal intensity is smaller than the freshly prepared sample (figure 6.9 (c)). This can be attributed to the degradation of pyrrolic-N NDG film due to its aging.

(B) Crystal violet (CV)

The different concentrations of CV were prepared in methanol. The pyrrolic-N NDG samples were immersed in all solutions for 5 minutes and dried for 15 minutes. The SERS measurements were performed with a 633 nm excitation wavelength for all the samples. The CV has Raman bands between 400 to 1800 cm⁻¹, and it has the strongest peak at 1620 cm⁻¹ [49]. We did not observe any Raman band of CV till 10⁻³ M concentration. The Raman spectrum of 1x 10⁻² M concentration CV on pyrrolic-N NDG is shown in figure 6.14, for which the CV peak has been observed. The D, G, and 2D bands observed in the spectrum indicate NDG film. The peak appeared at the higher wavenumber side of the G band as a kink. It is located at 1620 cm-1 and belongs to the CV molecule. We can clearly see it as the prominent peak in the inset of the figure. We can conclude that there is no enhancement of the Raman signal for CV with a 633 nm wavelength, as the 633 nm is not a resonant excitation wavelength. It was reported in the literature that the CV exhibits the resonant condition on NDG film at 514 nm wavelength [48].

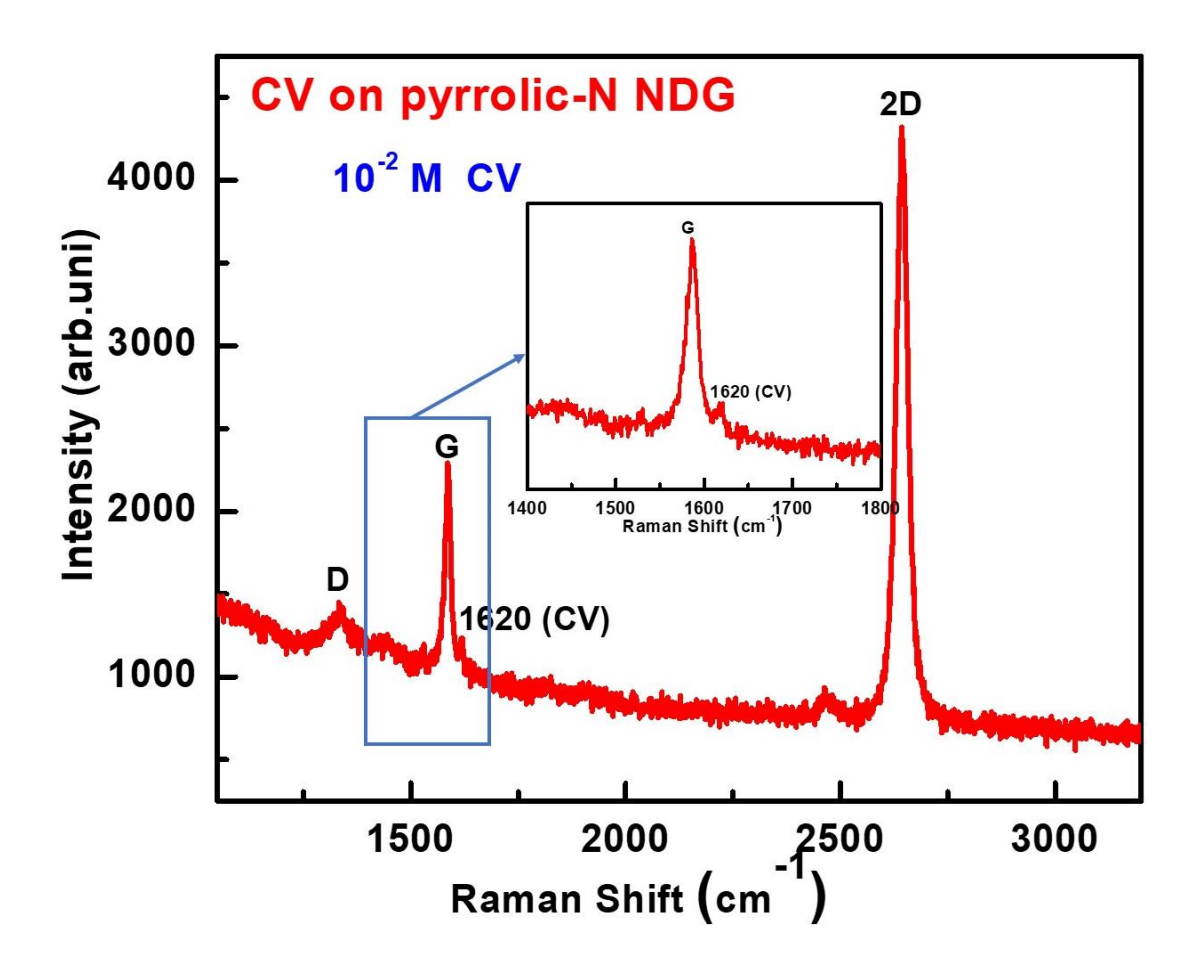


Figure 6.14 The Raman spectra of $1x10^{-2}$ M concentration of CV on pyrrolic-N NDG substrate, excited with 633 nm wavelength.

(C) Nile Blue (NB)

The SERS behavior of pyrrolic-N NDG and graphene was studied using a nile blue organic molecule. The different concentrations of NB were prepared using a similar procedure as mentioned earlier. The 1x10⁻⁵ M concentration of NB was chosen to investigate the SERS studies. The Raman bands of NB reported in the literature are from 400 to 1600 cm⁻¹ [50]. The band at 592 cm⁻¹ is the strongest peak for nile blue. All the SERS measurements were recorded with a 633 nm excitation wavelength. Figure 6.15 (a) shows the SERS spectra 1x10⁻⁵ M concentration of NB on pyrrolic-N NDG. The D, G, and 2D bands in the spectra represent the NDG. The enhanced Raman signal at 592 cm⁻¹ belongs to NB. The presence of NB SERS signal in each spectrum

indicates that the NB is all over the sample, and pyrrolic-N NDG has good reproducibility. Similarly, The NB SERS measurements have been investigated on the graphene, shown in figure 6.15 (b). The SERS signal of NB exists in every spectrum, indicating the presence of NB all over the sample and the good reproducibility of graphene. The enhancement in the Raman signal of NB can be ascribed to the charge transfer between the NB and SERS substrates. The NB peak has more intensity than the 2D peak of both substrates denotes good enhancement. The obtained enhancement factors (EF) for NB on pyrrolic-N NDG and graphene SERS substrates are 2.4×10^6 and 3.7×10^4 , respectively. The 633 nm wavelength exhibits the resonance condition for NB on both SERS substrates. It was reported that the NDG could show an EF of up to 10^6 for resonance conditions [46,48].

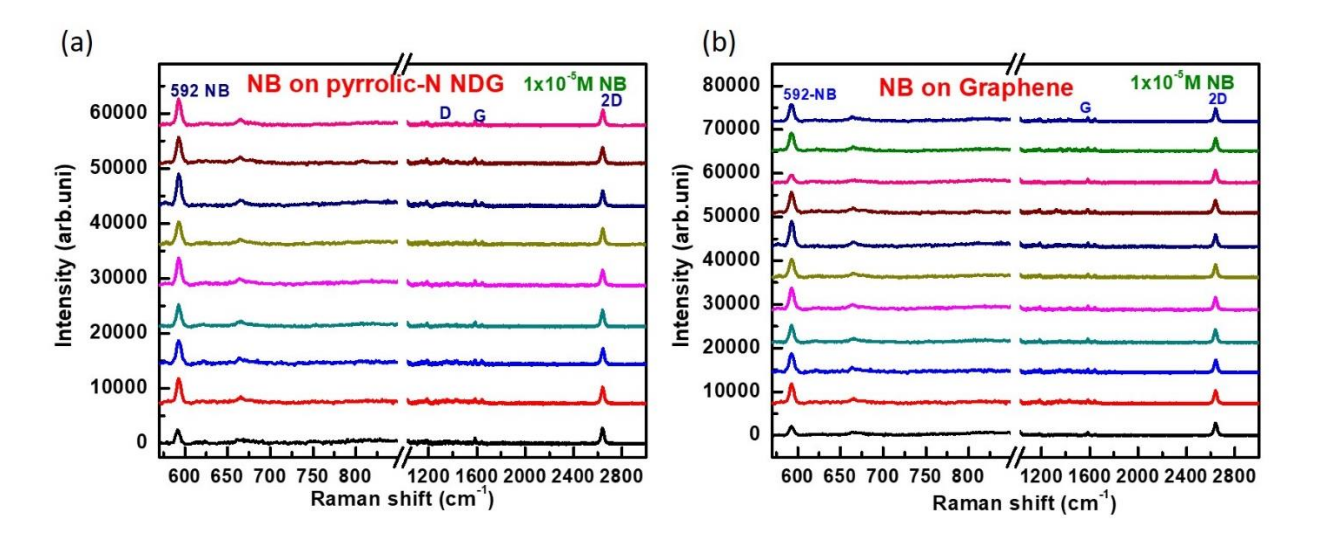


Figure 6.15 SERS spectra of 1 x 10^{-5} MB were recorded at various positions on pyrrolic-N NDG (a) and graphene (b).

Overall, we can infer from the SERS studies by graphene and NDG on MB, CV, and NB that the SERS behavior is dependent on the laser excitation wavelength and also on the substates. The enhancement factor (EF) for NDG is two orders more than the graphene EF. The pyrrolic-N NDG showed more EF than the graphitic-N NDG.

6.4 Conclusion

CVD-grown graphene and NDG films have been utilized to study the different applications. The synthesized two dominant configurations within the NDG films, pyrrolic-N NDG and graphitic-N

NDG, have also been used in applications to understand their impact on the applications. The studies on the transparency of all films have been evaluated, and the transmittance values (97.4% - 97.1 %) were found to be near the values of exfoliated graphene. All the films were utilized for electronic applications. The electrolyte-gated FETs were fabricated using these films. The mobilities and Dirac points were determined for all the films and found that the graphene has higher mobility (94.8 cm²V⁻¹s⁻¹) than the NGD films. The effect of configuration on the mobility and Dirac point was studied and compared with the existing literature. The heterostructure of graphene/MoS₂ has been prepared for a photodetector device. The role of graphene in the photodetector has been studied. The photoresponsivity is 520 A/W for the graphene/MoS₂ device is higher than the responsivity (7.2 A/W) of the MoS₂ device. Surface-enhanced Raman spectroscopic (SERS) behavior of all films was studied. Three different organic dye molecules, methylene blue (MB), crystal violet (CV), and nile blue (NB), were used as analyte molecules. The effect of nitrogen dopant configurations and concentrations on SERS was evaluated. The SERS behavior was shown to depend on the laser excitation wavelength. All films showed the SERS effect on the MB and NB dyes, with a 633 nm excitation wavelength, which is a resonant excitation wavelength. No SERS was observed for CV dye. The enhancement factors (EF) for NDG reached up to 10⁶ and for graphene 10⁴. There is no change in the order of EF for pyrrolic-N NDG and graphitic0N NDG, but the former showed higher EF than the latter.

6.5 References:

- [1] Ranjan P, Gaur S, Yadav H, Urgunde A B, Singh V, Patel A, Vishwakarma K, Kalirawana D, Gupta R and Kumar P 2022 2D materials: increscent quantum flatland with immense potential for applications *Nano Converg.* **9**
- [2] Krsihna B V, Ravi S and Prakash M D 2021 Recent developments in graphene based field effect transistors *Mater. Today Proc.* **45** 1524–8
- [3] Malesevic A, Kemps R, Vanhulsel A, Chowdhury M P, Volodin A and Van Haesendonck C 2008 Field emission from vertically aligned few-layer graphene *J. Appl. Phys.* **104** 1–6
- [4] Wang X, Zhi L and Müllen K 2008 Transparent, conductive graphene electrodes for dyesensitized solar cells *Nano Lett.* **8** 323–7

- [5] Bonaccorso F, Sun Z, Hasan T and Ferrari A C 2010 Graphene photonics and optoelectronics *Nat. Photonics* **4** 611–22
- [6] Schedin F, Geim A K, Morozov S V., Hill E W, Blake P, Katsnelson M I and Novoselov K S 2007 Detection of individual gas molecules adsorbed on graphene *Nat. Mater.* **6** 652–5
- [7] Mazar Atabaki M and Kovacevic R 2013 Graphene composites as anode materials in lithium-ion batteries *Electron. Mater. Lett.* **9** 133–53
- [8] Esteghamat A and Akhavan O 2022 Graphene as the ultra-transparent conductive layer in developing the nanotechnology-based flexible smart touchscreens *Microelectron*. *Eng*. 267–268 111899
- [9] Nair R R, Blake P, Grigorenko A N, Novoselov K S, Booth T J, Stauber T, Peres N M R and Geim A K 2008 Fine structure constant defines visual transparency of graphene *Science* (80-.). **320** 1308
- [10] Pang S, Hernandez Y, Feng X and Müllen K 2011 Graphene as transparent electrode material for organic electronics *Adv. Mater.* **23** 2779–95
- [11] Seo T H, Lee S, Cho H, Chandramohan S, Suh E K, Lee H S, Bae S K, Kim S M, Park M, Lee J K and Kim M J 2016 Tailored CVD graphene coating as a transparent and flexible gas barrier *Sci. Rep.* **6** 1–8
- [12] K. S. Novoselov et al 2016 Electric Field Effect in Atomically Thin Carbon Films **306** 666–9
- [13] Zhang Y, Tan Y W, Stormer H L and Kim P 2005 Experimental observation of the quantum Hall effect and Berry's phase in graphene *Nature* **438** 201–4
- [14] Wojtaszek M 2009 Graphene: a two type charge carrier system *Transport* 81
- [15] Vigneswar A 2016 The Graphene Field Effect Transistor: A Large Scale Integration Approach
- [16] Wang Z X, Zhang Z Y and Peng L M 2012 Graphene-based ambipolar electronics for

- radio frequency applications *Chinese Sci. Bull.* **57** 2956–70
- [17] Jmai B, Silva V and Mendes P M 2021 2D electronics based on graphene field effect transistors: Tutorial for modelling and simulation *Micromachines* **12**
- [18] Liang Y, Liang X, Zhang Z, Li W, Huo X and Peng L 2015 High mobility flexible graphene field-effect transistors and ambipolar radio-frequency circuits *Nanoscale* 7 10954–62
- [19] Kim S, Nah J, Jo I, Shahrjerdi D, Colombo L, Yao Z, Tutuc E and Banerjee S K 2009 Realization of a high mobility dual-gated graphene field-effect transistor with Al2O3 dielectric *Appl. Phys. Lett.* **94**
- [20] Kim B J, Jang H, Lee S K, Hong B H, Ahn J H and Cho J H 2010 High-performance flexible graphene field effect transistors with ion gel gate dielectrics *Nano Lett.* **10** 3464–6
- [21] Dontschuk N, Stacey A, Tadich A, Rietwyk K J, Schenk A, Edmonds M T, Shimoni O, Pakes C I, Prawer S and Cervenka J 2015 A graphene field-effect transistor as a molecule-specific probe of DNA nucleobases *Nat. Commun.* **6**
- [22] Song S M, Park J K, Sul O J and Cho B J 2012 Determination of work function of graphene under a metal electrode and its role in contact resistance *Nano Lett.* **12** 3887–92
- [23] Wang Z, Li P, Chen Y, Liu J, Tian H, Zhou J, Zhang W and Li Y 2014 Synthesis of nitrogen-doped graphene by chemical vapour deposition using melamine as the sole solid source of carbon and nitrogen *J. Mater. Chem. C* **2** 7396–401
- [24] Jin Z, Yao J, Kittrell C and Tour J M 2011 Large-scale growth and characterizations of nitrogen-doped monolayer graphene sheets *ACS Nano* **5** 4112–7
- [25] Lu Y F, Lo S T, Lin J C, Zhang W, Lu J Y, Liu F H, Tseng C M, Lee Y H, Liang C Te and Li L J 2013 Nitrogen-doped graphene sheets grown by chemical vapor deposition:

 Synthesis and influence of nitrogen impurities on carrier transport *ACS Nano* **7** 6522–32
- [26] Sun Z, Yan Z, Yao J, Beitler E, Zhu Y and Tour J M 2010 Growth of graphene from solid carbon sources *Nature* **468** 549–52

- [27] Xue Y, Wu B, Jiang L, Guo Y, Huang L, Chen J, Tan J, Geng D, Luo B, Hu W, Yu G and Liu Y 2012 Low temperature growth of highly nitrogen-doped single crystal graphene arrays by chemical vapor deposition *J. Am. Chem. Soc.* **134** 11060–3
- [28] Wang H, Liu F, Fu W, Fang Z, Zhou W and Liu Z 2014 Two-dimensional heterostructures: Fabrication, characterization, and application *Nanoscale* **6** 12250–72
- [29] Lopez-Sanchez O, Lembke D, Kayci M, Radenovic A and Kis A 2013 Ultrasensitive photodetectors based on monolayer MoS 2 *Nat. Nanotechnol.* **8** 497–501
- [30] Zhang W, Chuu C P, Huang J K, Chen C H, Tsai M L, Chang Y H, Liang C Te, Chen Y Z, Chueh Y L, He J H, Chou M Y and Li L J 2015 Ultrahigh-Gain Photodetectors Based on Atomically Thin Graphene-MoS2 Heterostructures *Sci. Rep.* **4** 1–8
- [31] Sharma R, Sharma P, Sahoo K R, Sankar S, Awana V P S, Kumar M and Narayanan T N 2021 Giant photoresponsivity of transfer free grown fluorographene MoS2 heterostructured ultra-stable transistors *Mater. Today* **50** 69–78
- [32] Nur R, Tsuchiya T, Toprasertpong K, Terabe K, Takagi S and Takenaka M 2020 High responsivity in MoS2 phototransistors based on charge trapping HfO2 dielectrics *Commun. Mater.* **1** 1–9
- [33] Roy K, Padmanabhan M, Goswami S, Sai T P, Ramalingam G, Raghavan S and Ghosh A 2013 Graphene-MoS 2 hybrid structures for multifunctional photoresponsive memory devices *Nat. Nanotechnol.* **8** 826–30
- [34] Langer J, de Aberasturi D J, Aizpurua J, Alvarez-Puebla R A, Auguié B, Baumberg J J, Bazan G C, Bell S E J, Boisen A, Brolo A G, Choo J, Cialla-May D, Deckert V, Fabris L, Faulds K, Javier García de Abajo F, Goodacre R, Graham D, Haes A J, Haynes C L, Huck C, Itoh T, Käll M, Kneipp J, Kotov N A, Kuang H, Le Ru E C, Lee H K, Li J F, Ling X Y, Maier S A, Mayerhöfer T, Moskovits M, Murakoshi K, Nam J M, Nie S, Ozaki Y, Pastoriza-Santos I, Perez-Juste J, Popp J, Pucci A, Reich S, Ren B, Schatz G C, Shegai T, Schlücker S, Tay L L, George Thomas K, Tian Z Q, van Duyne R P, Vo-Dinh T, Wang Y, Willets K A, Xu C, Xu H, Xu Y, Yamamoto Y S, Zhao B and Liz-Marzán L M 2020 Present and future of surface-enhanced Raman scattering *ACS Nano* 14 28–117

- [35] Naqvi T K, Bajpai A, Bharati M S S, Kulkarni M M, Siddiqui A M, Soma V R and Dwivedi P K 2021 Ultra-sensitive reusable SERS sensor for multiple hazardous materials detection on single platform *J. Hazard. Mater.* **407** 124353
- [36] Pilot R, Signorini R, Durante C, Orian L, Bhamidipati M and Fabris L 2019 A review on surface-enhanced Raman scattering *Biosensors* 9
- [37] Ling X, Xie L, Fang Y, Xu H, Zhang H, Kong J, Dresselhaus M S, Zhang J and Liu Z 2010 Can graphene be used as a substrate for Raman enhancement? *Nano Lett.* **10** 553–61
- [38] Ling X, Fang W, Lee Y, Araujo P T, Zhang X, Rodriguez-nieva J F, Lin Y, Zhang J, Kong J and Dresselhaus M S 2014 Raman Enhancement E ff ect on Two-Dimensional Layered Materials: 2005–8
- [39] Ling X, Wu J, Xu W and Zhang J 2012 Probing the effect of molecular orientation on the intensity of chemical enhancement using graphene-enhanced Raman spectroscopy *Small* 8 1365–72
- [40] Liu M, Zhao H, Quan X, Chen S and Fan X 2010 Distance-independent quenching of quantum dots by nanoscale-graphene in self-assembled sandwich immunoassay *Chem. Commun.* **46** 7909–11
- [41] Xia M 2018 A Review on Applications of Two-Dimensional Materials in Surface-Enhanced Raman Spectroscopy *Int. J. Spectrosc.* **2018** 1–9
- [42] Ghosh R K, Ray D P, Debnath S, Tewari A and Das I 2019 Optimization of process parameters for methylene blue removal by jute stick using response surface methodology *Environ. Prog. Sustain. Energy* **38** 620–34
- [43] Goksu A and Tanaydin M K 2017 Adsorption of hazardous crystal violet dye by almond shells and determination of optimum process conditions by taguchi method *Desalin*. *Water Treat.* **88** 189–99
- [44] Lv R, Li Q, Botello-Méndez A R, Hayashi T, Wang B, Berkdemir A, Hao Q, Eléas A L, Cruz-Silva R, Gutiérrez H R, Kim Y A, Muramatsu H, Zhu J, Endo M, Terrones H, Charlier J C, Pan M and Terrones M 2012 Nitrogen-doped graphene: Beyond single

- substitution and enhanced molecular sensing Sci. Rep. 2 1–8
- [45] Ling X, Moura L G, Pimenta M A and Zhang J 2012 Charge-transfer mechanism in graphene-enhanced Raman scattering *J. Phys. Chem. C* **116** 25112–8
- [46] Wu Z, Zeng P, Zhao W, Wang W, Zheng P, Zheng H, Zheng L, Yao X, Huo D, Ni Z and Zhang Y 2021 Synthesis of Single- And Few-Layer Nitrogen-doped Graphene and Layer-Dependent Surface-Enhanced Raman Scattering Properties *J. Phys. Chem. C* 125 17831–40
- [47] Byram C, Rathod J, Moram S S B, Mangababu A and Soma V R 2022 Picosecond Laser-Ablated Nanoparticles Loaded Filter Paper for SERS-Based Trace Detection of Thiram, 1,3,5-Trinitroperhydro-1,3,5-triazine (RDX), and Nile Blue *Nanomaterials* **12** 1–16
- [48] Feng S, Cristina dos Santos M, Carvalho B R, Lv R, Li Q, Fujisawa K, Elías A L, Lei Y, Perea-López N, Endo M, Pan M, Pimenta M A and Terrones M 2016 Ultrasensitive molecular sensor using N-doped graphene through enhanced Raman scattering *Sci. Adv.* 2 1–13
- [49] Mao A, Jin X, Gu X, Wei X and Yang G 2012 Rapid, green synthesis and surface-enhanced Raman scattering effect of single-crystal silver nanocubes *J. Mol. Struct.* **1021** 158–61
- [50] Rajesh Y, Bharati M S S, Rao S V and Krishna M G 2021 ZnO nanowire arrays decorated with titanium nitride nanoparticles as surface-enhanced Raman scattering substrates *Appl. Phys. A Mater. Sci. Process.* **127** 1–8

Chapter 7

Conclusion and Future scope

In this chapter, all the results of the research work shown in the previous chapters are summarized. The conclusions drawn are briefed in this chapter. The possibility of extending this work in different directions is proposed in the future scope.

7.1 Summary & Conclusion

The research work has been summarized in pictorial form and is shown in figure 7.1. Graphene systems (graphene & Nitrogen-doped graphene(NDG)) have been synthesized using solid precursors by employing a chemical vapor deposition technique. The grown films were explored for different applications, such as field effect transistors (FETS), Surface-enhanced Raman spectroscopy (SERS), and photodetector.

Graphene has to be grown over a large area at a large scale with a low cost to industrialize and realize the potential applications. Some of the challenges can be overcome by employing the chemical vapor deposition (CVD) technique to synthesize graphene systems where we can obtain large-area continuous, high-quality graphene films. The most used precursor for graphene's CVD growth is methane gas which is poisonous, highly explosive, and the decomposition temperature is very high. Solid precursors were found to be alternative precursors that pose less threat than methane gas, and their decomposition temperature is also low, which results in low-temperature growth of graphene. However, the graphene has been grown from solid precursors by post-annealing the deposited solid carbon precursor's film on a substrate in the reduced atmosphere, which does not have any control over the nucleations and grain boundaries. Therefore, we used the solid precursor Polymethymethacryalte (PMMA) for the growth of graphene by employing a method where the PMMA is evaporated and transported to the copper substrate with carrier gas assistance.

The graphene has been synthesized successfully over copper foil at 1050 °C via APCVD using PMMA. The evaporation temperature of PMMA has been optimized to get low evaporation, with which the lowest number of nucleations is obtained. The growth parameters, such as flow rate and growth time, have been optimized to obtain nucleations, isolated crystals, and continuous film. A large-sized isolated graphene single crystal of around 180 µm is obtained. It was found that the PMMA is evaporating and polymerizing simultaneously, leading to the

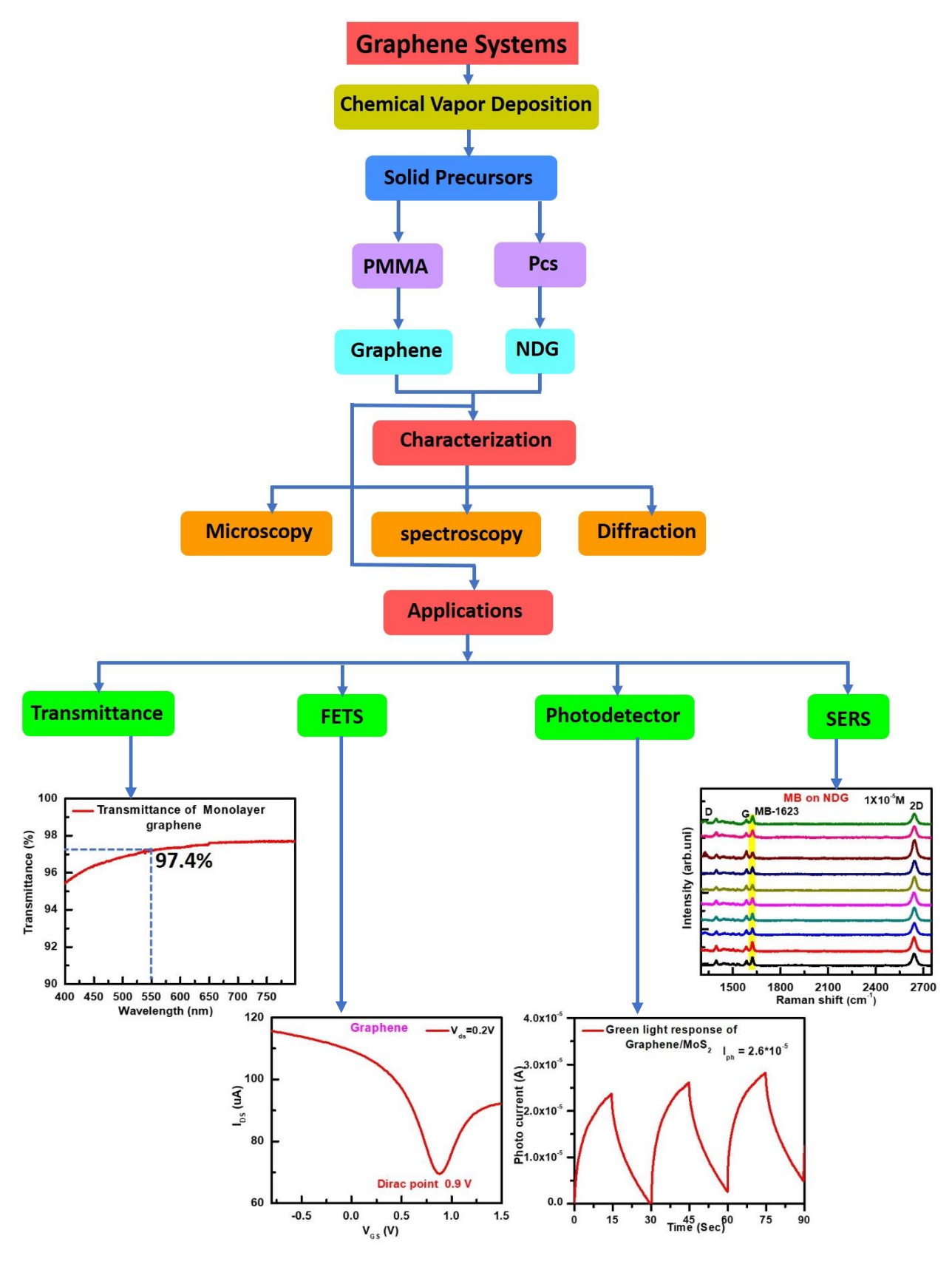


Figure 7.1 Pictorial demonstration of summary of the research work.

arrest of PMMA vapor after some time. The amount of PMMA has been optimized to get the large-area, high-quality continuous film. The thickness of the monolayer graphene obtained around 0.5 nm. The temperature-dependent growth graphene has been investigated and obtained nanocrystalline graphene film at 650 °C temperature.

The doping of graphene can be utilized to tune its physicochemical properties besides inducing a band gap. Nitrogen is doped with graphene, which is very near the carbon atom's size. The nitrogen doping concentration and its configurations depend on the precursor choice and the growth parameters such as temperature, flow rate, time, and pressure. Thus, it is very important to explore the novel precursors and tune the growth parameters for attaining the required nitrogen concentration and configurations.

We explored Phthalocyanine as a solid precursor for synthesizing NDG films and compared them with NDG grown from copper phthalocyanine (CuPc). We systematically investigated the growth of NDG films using these precursors and their properties. We demonstrated that the chemical nature of nitrogen defects depends strongly on the starting precursor and growth parameters. For the Pc precursor, at 1050 °C growth temperature and 5-min growth duration, we observed a mixture of pyridinic and pyrrolic defects with a small percentage of graphitic nitrogen dopants. For CuPc precursor, we observed pyrrolic type of defects primarily under the same growth conditions. In both cases, if the growth time is increased, all the defects are converted to graphitic-type nitrogen defects. We can arrest the conversion of pyrrolic-N dopants into graphitic-N dopants by switching the Ar/H₂ gas to the sole Ar gas. Our results suggest that we can tailor the chemical nature (configurations & concentrations) of nitrogen defects by selecting an appropriate starting precursor and carefully tuning the synthesis conditions.

CVD-grown graphene and NDG films have been utilized to study the different applications. The studies on the transparency of all films have been evaluated, and the transmittance values (97.4% - 97.1 %) were found to be near the values of exfoliated graphene. The mobilities and Dirac points were determined for all the films and found that the graphene has higher mobility (94.8 cm²V⁻¹s⁻¹) than the NGD films. The effect of configuration on the mobility and Dirac point was studied and compared with the existing literature. The heterostructure of graphene/MoS₂ has been prepared for a photodetector device. The role of graphene in the photodetector has been studied. The photoresponsivity is 520 A/W for the graphene/MoS₂ device is higher than the responsivity (7.2)

A/W) of the MoS₂ device. Surface-enhanced Raman spectroscopic (SERS) behavior of all films was studied. The effect of nitrogen dopant configurations and concentrations on SERS was evaluated. The SERS behavior was shown to depend on the laser excitation wavelength. All films showed the SERS effect on the MB and NB dyes, with a 633 nm excitation wavelength, which is a resonant excitation wavelength. No SERS was observed for CV dye. The enhancement factors (EF) for NDG reached up to 10⁶ and for graphene 10⁴ for resonant excitation wavelength. There is no change in the order of EF for pyrrolic-N NDG and graphitic-N NDG, but the former showed higher EF than the latter.

7.2 Scope for Future work

The work carried out in this thesis can be extended to future work in many directions. The size of the graphene-isolated crystals has to be increased further to reduce grain boundaries when they coalesce to form a continuous film. The temperature-dependent growth of graphene can be studied further using PMMA, as it has a low decomposition temperature compared to methane gas. In the case of NDG, the role of the central metal atom of meal phthalocyanine precursors such as CuPc should be investigated. If we could retain the metal atom in the NDG, the film would become a metal co-doped NDG, which can be applied to different applications depending on the doping of the metal to the NDG. Suppose other precursors, such as Iron phthalocyanine (FePc) produce Iron co-doped NDG that may exhibit ferromagnetic behavior. Gold phthalocyanine (AuPc) can produce gold-co-doped NDG (Au-NDG), which can be utilized in the SERS application. There is a possibility that Au-NDG can eliminate the laser dependence of NDG on SERS. Platinum phthalocyanine (Pt) produces Pt-NDG, which can be utilized as a single metal catalyst in oxygen reduction reactions. At last, we can foresee that these phthalocyanines can open up new directions for NDG and broaden their applications.

List of Publications:

- 1. Shyaga N, Sharma R, Hassan N, Alam B and Parmar A S 2022 Influence of growth parameters on the dopant configuration of nitrogen-doped graphene synthesized from phthalocyanine molecules J. Mater. Sci. Mater. Electron 33, 19361-19375 (2022) https://doi.org/10.1007/s10854-022-08733-x
- 2. Harshita Trivedi, Gaganpreet, Arash Boochani, Naresh Shagya, Jayeeta Lahiri, Zohreh Ghorannevis, Avanish S. Parmar, Investigating optical, structural and morphological properties of polycrystalline CdTe thin-film deposited by RF magnetron sputtering, Materials Letters: X https://doi.org/10.1016/j.mlblux.2021.100087
- 3. One-Dimensional Hollow Structures of 2O-PdS2 Decorated Carbon for Water Electrolysis. Anku Guha, Rahul Sharma, Krishna Rani Sahoo, Anand B. Puthirath, Naresh Shyaga, Pulickel M. Ajayan, and T. N. Narayanan. ACS Applied Energy Materials 2021 4 (9), 8715-8720

https://doi.org/10.1021/acsaem.1c01703

4. Selenium Coupled Reduced Graphene Oxide as Single Atom Site Direct Four Electron Oxygen Reduction Reaction Catalyst. Shubhadeep Pal, Sumit Bawari, Vineesh T. V., Naresh Shyaga, and T. N. Narayanan. ACS Appl. Energy Mater. 2019, 2, 5, 3624–3632. https://doi.org/10.1021/acsaem.9b00364

Conferences & Workshops Attended:

- 1. Poster presentation at International Conference on Functional Nanomaterials 22-25 February 2019, Department of Physics, IIT (BHU), and Varanasi.
- 2. Participated in SSPro-2019 Winter School on Surface Science & Probes.
- 3. Poster presentation at "International Conference on Advances in Biological Systems and Material Science in Nanoworld" -2017 at IIT BHU
- 4. Participated in INUP Hands-on Training Workshop on Nanofabrication Technologies 2017.

Studies on Pristine Graphene and Nitrogen Doped Graphene Films Grown by Chemical Vapour Deposition for Electronic and Sensing Applications

by Naresh Shyaga

Submission date: 03-Feb-2023 03:23PM (UTC+0530)

Submission ID: 2005442430

File name: Naresh Shyaga.docx (12.71M)

Word count: 41153

Character count: 218887

Librarian

UNIVERSITY OF HYDERABAD

Central University P.O. HYDERABAD-500 046.

Studies on Pristine Graphene and Nitrogen Doped Graphene Films Grown by Chemical Vapour Deposition for Electronic and **Sensing Applications**

ORIGINALITY REPORT

SIMILARITY INDEX

INTERNET SOURCES

PUBLICATIONS

STUDENT PAPERS

PRIMARY SOURCES

"Handbook of Graphene", Wiley, 2019 Publication

Naresh Shyaga, Rahul Sharma, Nurul Hassan, Md Bayazeed Alam, Avanish Singh Parmar, Jayeeta Lahiri. "Influence of growth parameters on the dopant configuration of nitrogen-doped graphene synthesized from phthalocyanine molecules", Journal of Materials Science: Materials in Electronics, 2022

Publication

coek.info Internet Source

Fred A. Stevie, Carrie L. Donley. "Introduction to x-ray photoelectron spectroscopy", Journal of Vacuum Science & Technology A, 2020 Publication

5

Nabil A. Abdel Ghany, Safaa A. Elsherif, Hala T. Handal. "Revolution of Graphene for different

applications: State-of-the-art", Surfaces and Interfaces, 2017

Publication

6	Submitted to University of Hyderabad, Hyderabad Student Paper	<1%
7	www.nature.com Internet Source	<1%
8	Geetanjali Deokar, Junjie Jin, Udo Schwingenschlögl, Pedro M. F. J. Costa. "Chemical vapor deposition-grown nitrogen- doped graphene's synthesis, characterization and applications", npj 2D Materials and Applications, 2022 Publication	<1%
9	"Springer Handbook of Nanotechnology", Springer Science and Business Media LLC, 2017 Publication	<1%
10	pubs.rsc.org Internet Source	<1%
11	hdl.handle.net Internet Source	<1 %
12	Dacheng Wei, Yunqi Liu, Yu Wang, Hongliang Zhang, Liping Huang, Gui Yu. "Synthesis of N- Doped Graphene by Chemical Vapor	<1%

Deposition and Its Electrical Properties", Nano Letters, 2009

Publication

13	Yuqing Song, Wentao Zou, Qi Lu, Li Lin, Zhongfan Liu. "Graphene Transfer: Paving the Road for Applications of Chemical Vapor Deposition Graphene", Small, 2021 Publication	<1%
14	pure.manchester.ac.uk Internet Source	<1%
15	rua.ua.es Internet Source	<1%
16	www2.avs.org Internet Source	<1%
17	documentserver.uhasselt.be Internet Source	<1%
18	"Springer Handbook of Nanomaterials", Springer Science and Business Media LLC, 2013 Publication	<1%
19	escholarship.mcgill.ca Internet Source	<1%
20	s1.iran-mavad.com Internet Source	<1%
21	www.ncbi.nlm.nih.gov Internet Source	<1%

22	Marcelo de Assumpção Pereira-da-Silva, Fabio A. Ferri. "Scanning Electron Microscopy", Elsevier BV, 2017 Publication	<1%
23	Submitted to University of Auckland Student Paper	<1%
24	eprints.kfupm.edu.sa Internet Source	<1%
25	scholarcommons.usf.edu Internet Source	<1%
26	tesisenred.net Internet Source	<1%
27	vtechworks.lib.vt.edu Internet Source	<1%
28	Submitted to Indian Institute of Technology, Madras Student Paper	<1%
29	Submitted to The University of Manchester Student Paper	<1%
30	Submitted to Wright State University Student Paper	<1%
31	www.mdpi.com Internet Source	<1%
32	www.researchgate.net Internet Source	<1%

33	Huasheng Lai, Fugang Xu, Yue Zhang, Li Wang. "Recent progress on graphene-based substrates for surface-enhanced Raman scattering applications", Journal of Materials Chemistry B, 2018 Publication	<1%
34	Submitted to Queen Mary and Westfield College Student Paper	<1%
35	Submitted to Universiti Sains Malaysia Student Paper	<1%
36	hal.archives-ouvertes.fr Internet Source	<1%
37	www.science.gov Internet Source	<1%
38	Submitted to Savitribai Phule Pune University Student Paper	<1%
39	Submitted to University of Sri Jayewardenepura Nugegoda Sri Lanka Student Paper	<1%
40	Jayewardenepura Nugegoda Sri Lanka	<1 %

www.politesi.polimi.it
Internet Source

41

		<1%
42	"Electrochemistry of Carbon Electrodes", Wiley, 2015 Publication	<1%
43	"Graphene", Wiley, 2012 Publication	<1%
44	D. Usachov, O. Vilkov, A. Grüneis, D. Haberer et al. "Nitrogen-Doped Graphene: Efficient Growth, Structure, and Electronic Properties", Nano Letters, 2011 Publication	<1%
45	Haibo Wang, Thandavarayan Maiyalagan, Xin Wang. "Review on Recent Progress in Nitrogen-Doped Graphene: Synthesis, Characterization, and Its Potential Applications", ACS Catalysis, 2012	<1%
46	Submitted to Nanyang Technological University, Singapore Student Paper	<1 %
47	Submitted to SASTRA University Student Paper	<1%
48	Submitted to Universiti Malaysia Perlis Student Paper	<1%

49	Wonbong Choi, Indranil Lahiri, Raghunandan Seelaboyina, Yong Soo Kang. "Synthesis of Graphene and Its Applications: A Review", Critical Reviews in Solid State and Materials Sciences, 2010 Publication	<1%
50	"Handbook of Materials Characterization", Springer Science and Business Media LLC, 2018 Publication	<1%
51	B. Krauss, T. Lohmann, DH. Chae, M. Haluska, K. von Klitzing, J. H. Smet. "Laser-induced disassembly of a graphene single crystal into a nanocrystalline network", Physical Review B, 2009 Publication	<1%
52	Govindaraj, Achutharao, and C.N.R. Rao. "Doping of Graphene by Nitrogen, Boron, and Other Elements", Functionalization of Graphene, 2014. Publication	<1%
53	Submitted to University of Wollongong Student Paper	<1%
54	www.fulviofrisone.com Internet Source	<1%

Exclude quotes On Exclude matches < 14 words

Exclude bibliography On